MATERIAL AND COMPOSITION SCREENING APPROACHES IN ELECTROCATALYSIS AND BATTERY RESEARCH

EDITED BY: Kai S. Exner, Jun Huang, Jianping Xiao, Thomas Kadyk and Hideshi Ooka

PUBLISHED IN: Frontiers in Energy Research

frontiers Research Topics

frontiers

ISSN 1664-8714
ISBN 978-2-88966-983-7
DOI 10.3389/978-2-88966-983-7

About Frontiers

Frontiers is more than just an open-access publisher of scholarly articles: it is a pioneering approach to the world of academia, radically improving the way scholarly research is managed. The grand vision of Frontiers is a world where all people have an equal opportunity to seek, share and generate knowledge. Frontiers provides immediate and permanent online open access to all its publications, but this alone is not enough to realize our grand goals.

Frontiers Journal Series

The Frontiers Journal Series is a multi-tier and interdisciplinary set of open-access, online journals, promising a paradigm shift from the current review, selection and dissemination processes in academic publishing. All Frontiers journals are driven by researchers for researchers; therefore, they constitute a service to the scholarly community. At the same time, the Frontiers Journal Series operates on a revolutionary invention, the tiered publishing system, initially addressing specific communities of scholars, and gradually climbing up to broader public understanding, thus serving the interests of the lay society, too.

Dedication to Quality

Each Frontiers article is a landmark of the highest quality, thanks to genuinely collaborative interactions between authors and review editors, who include some of the world's best academicians. Research must be certified by peers before entering a stream of knowledge that may eventually reach the public - and shape society; therefore, Frontiers only applies the most rigorous and unbiased reviews.
Frontiers revolutionizes research publishing by freely delivering the most outstanding research, evaluated with no bias from both the academic and social point of view. By applying the most advanced information technologies, Frontiers is catapulting scholarly publishing into a new generation.

What are Frontiers Research Topics?

Frontiers Research Topics are very popular trademarks of the Frontiers Journals Series: they are collections of at least ten articles, all centered on a particular subject. With their unique mix of varied contributions from Original Research to Review Articles, Frontiers Research Topics unify the most influential researchers, the latest key findings and historical advances in a hot research area! Find out more on how to host your own Frontiers Research Topic or contribute to one as an author by contacting the Frontiers Editorial Office: frontiersin.org/about/contact

MATERIAL AND COMPOSITION SCREENING APPROACHES IN ELECTROCATALYSIS AND BATTERY RESEARCH

Topic Editors:
Kai S. Exner, Sofia University, Bulgaria
Jun Huang, Central South University, China
Jianping Xiao, Dalian Institute of Chemical Physics, China
Thomas Kadyk, Julich-Forschungszentrum, Germany
Hideshi Ooka, Riken, Japan

Citation: Exner, K. S., Huang, J., Xiao, J., Kadyk, T., Ooka, H., eds. (2021). Material and Composition Screening Approaches in Electrocatalysis and Battery Research. Lausanne: Frontiers Media SA. doi: 10.3389/978-2-88966-983-7

Table of Contents

frontiers in Energy Research

EDITORIAL
published: 14 May 2021
doi: 10.3389/fenrg.2021.699376

Editorial: Material and Composition Screening Approaches in Electrocatalysis and Battery Research

*Thomas Kadyk[1,2], Jianping Xiao[3], Hideshi Ooka[4], Jun Huang[5] and Kai S. Exner[6,7,8]**

[1]Theory and Computation of Energy Materials (IEK-13), Institute of Energy and Climate Research, Forschungszentrum Jülich GmbH, Jülich, Germany, [2]Jülich Aachen Research Alliance, JARA Energy, Jülich, Germany, [3]State Key Laboratory of Catalysis, Dalian Institute of Chemical Physics, Chinese Academy of Sciences, Dalian, China, [4]Center for Sustainable Resource Science (CSRS), RIKEN, Wako, Japan, [5]Institute of Theoretical Chemistry, Ulm University, Ulm, Germany, [6]Faculty of Chemistry, Theoretical Inorganic Chemistry, University Duisburg-Essen, Essen, Germany, [7]Cluster of Excellence RESOLV, Bochum, Germany, [8]Center for Nanointegration (CENIDE) Duisburg-Essen, Duisburg, Germany

Keywords: materials screening, electrocatalysis, solid-state batteries, electrolyte composition, machine learning

Editorial on the Research Topic

Material and Composition Screening Approaches in Electrocatalysis and Battery Research

In light of the global effort to transform the energy supply away from fossil fuels toward renewables, electrochemical devices have emerged as key technologies to store and convert energy as well as to convert waste products such as CO_2 into high-value chemicals. Progress in advancing these technologies (i.e., fuel cells, batteries, electrolyzers, or CO_2 conversion cells) hinges on the development and improvement of key materials, especially electrocatalysts and charge storage materials as well as electrolytes and transport materials. The complexity of the structure and composition of the state-of-the-art materials synthesized in recent years has made the search for new materials challenging. Trial-and-error-based screening of new materials is becoming less effective, as there are too many material combinations, synthesis parameters and processing routes to try experimentally. Hence, effective screening methods to designate experimental targets are required to advance the discovery of next-generation materials in an effective way. The development of advanced screening methods has led scientists on the hunt for the understanding of underlying relationships (e.g., structure-property-performance), and guiding principles (like the Sabatier principle). Additionally, the use of ever-more-powerful computational methods to avoid cumbersome, expensive experiments, as well as the utilization of machine learning and artificial intelligence techniques to re-create in-silico the intuition and experience of an experimenter, leads to a further increase of the efficiency of materials screening methods.

The articles comprised in this special issue highlight a broad range of applications, in which materials and composition screening is used. They range from advanced battery technologies (Dillenz et al.; Tichter et al.; Kowalski et al.), to water splitting (Mukouyama and Nakanishi; Lim et al.; Zeradjanin et al.) and CO_2 reduction (Malek et al.; Verma et al.) to general electrocatalysis (Kox et al.; Ooka et al.). The applied methods span the whole spectrum from computational methods like density functional theory (Dillenz et al.; Kowalski et al.; Lim et al.; Verma et al.) and ab-initio molecular dynamics simulations (Kox et al.), continuum modeling (Mukouyama and Nakanishi), artificial intelligence (Malek et al.), as well as the interplay of theory and experiment (Mukouyama and Nakanishi; Tichter et al.).

Apart from the 8 Original Research articles, this special issue contains 2 review articles. Our editors Ooka, Huang and Exner have reviewed the famous Sabatier principle within the context of electrocatalysis. They have highlighted its limitations and challenges, and in doing so, have showed how moving beyond its current thermodynamic framework might lead to next-generation

Edited and Reviewd by:
Sheng S. Zhang, United States Army Research Laboratory, United States

****Correspondence:***
Kai S. Exner
kai.exner@uni-due.de

Specialty section:
This article was submitted to Electrochemical Energy Conversion and Storage, a section of the journal Frontiers in Energy Research

Received: *23 April 2021*
Accepted: *30 April 2021*
Published: *14 May 2021*

Citation:
Kadyk T, Xiao J, Ooka H, Huang J and Exner KS (2021) Editorial: Material and Composition Screening Approaches in Electrocatalysis and Battery Research. Front. Energy Res. 9:699376. doi: 10.3389/fenrg.2021.699376

electrocatalysts. In the second review, Zeradjanin et al. have reviewed the current understanding of activity and stability trends of oxides for the anodic oxygen evolution reaction (OER). Their review brilliantly highlights that the topic is far from being concluded and ends with remaining fundamental questions and eight suggestions for future research directions.

Lim et al. partially followed one of the suggested directions by tuning the OER activity of transition-metal oxides via the strategic formation of a heterostructure with another transition metal oxide. They screened 11 transition metal oxides on a TiO_2 substrate using DFT, finding that these heterostructures follow the universal scaling relationship of metal oxides, thereby confirming RuO_2 and IrO_2 as highly active OER catalysts.

Staying in the field of electrochemical water splitting, Mukouyama and Nakanishi investigated the hydrogen evolution reaction and highlighted the importance of quantifying the surface pH. They developed and demonstrated an effective continuum model, which converts partial differential equations to ordinary differential equations, allowing the surface pH to be estimated in a computationally efficient way. The resulting model explains measured experimental voltammograms of both the hydrogen evolution as well as the more complex hydrogen peroxide reduction reaction.

Another work focusing on the catalyst-electrolyte interface is presented by Kox et al. Using ab-initio molecular dynamics simulations, they unraveled the effect of water and solvation on the structure and reactivity of Co_3O_4 (001) A-type and B-type surface terminations.

Moving to the application in batteries, Tichter et al. have investigated the electro-oxidation of VO^{2+} on glassy carbon electrodes, as encountered in redox-flow batteries. They performed stationary and rotating linear sweep voltammetry, which they combined with Koutecký-Levich analysis. While the observed concentration dependence of the ordinate intercept in the Koutecký-Levich plots was so far unexplained by the theory, they introduced a concept of finite rate constants leading to a theory that captures mass transport limitations, Butler-Volmer kinetics, and finite heterogenous kinetics simultaneously.

In solid-state lithium ion batteries, Kowalski et al. gave an overview and discussed the role of atomistic modeling in accurately predicting thermodynamic properties of Li_xFePO_4 orthophosphates as well as fluorite- and pyrochlore-type zirconates, key materials for energy storage and solid-state ion conduction. Dillenz et al. also used periodic density functional theory calculations to screen the migration of various charge carriers in spinel-type $MgSc_2Se_4$, a potential candidate for solid electrolytes in Mg-ion batteries. Screening the diffusion barriers of different ions in this material allowed disentangling structural and chemical factors in ion mobility. Not only the size and charge of the ion determines its mobility, but also charge redistribution and rehybridization caused by the migration of multivalent ions increase the resulting migration barriers.

Tackling the challenge to find suitable electrocatalysts for CO_2 reduction to CO, Verma et al. used computational screening of doped graphene electrodes. After establishing thermodynamically stable electrode materials, the CO_2 reduction reaction in alkaline media was studied. It was found that the CO_2 electrosorption and associated charge transfer along the decoupled proton and electron transfer mechanism significantly impacts the electrochemical performance, leading to their discovery of metal-doped 3 nitrogen-coordinated graphene as highly active electrodes.

Malek et al. made use of computational and experimental materials data in an artificial intelligence-based material recommendation and screening framework. This framework utilizes high-level technical targets, advanced data extraction, and categorization as well as data analytics and property-matching algorithms to recommend the most viable materials and reveal correlations that govern catalyst performance. This framework is demonstrated for certain classes of electrocatalyst materials for low or high temperature CO_2 reduction.

Overall, we thank all authors for their excellent, broad and multi-facetted contributions that highlight the importance and widespread application of diverse materials screening approaches and show up pathways for future energy materials discovery.

AUTHOR CONTRIBUTIONS

TK drafted the editorial. All authors discussed, reviewed, and approved the submission of this editorial.

Conflict of Interest: The authors declare that the research was conducted in the absence of any commercial or financial relationships that could be construed as a potential conflict of interest.

frontiers in Energy Research

ORIGINAL RESEARCH
published: 08 October 2020
doi: 10.3389/fenrg.2020.00155

Finite Heterogeneous Rate Constants for the Electrochemical Oxidation of VO^{2+} at Glassy Carbon Electrodes

Tim Tichter[1]*, *Jonathan Schneider*[1] and *Christina Roth*[2]

[1] Angewandte Physikalische Chemie, Freie Universität Berlin, Berlin, Germany, [2] Lehrstuhl für Werkstoffverfahrenstechnik, Universität Bayreuth, Bayreuth, Germany

The electrochemical oxidation of VO^{2+} at planar glassy carbon electrodes is investigated via stationary and rotating linear sweep voltammetry as well as via chronoamperometry. It is demonstrated that introducing finite kinetic rate constants into the Butler-Volmer equation captures the experimentally observed concentration dependence of the ordinate intercept in Koutecký-Levich plots that cannot be explained by using the classical model. This new concept leads to a three-term Koutecký-Levich equation considering mass transport limitations, Butler-Volmer kinetics, as well as finite heterogeneous kinetics simultaneously. Based on these findings it is pointed out that stationary linear sweep voltammetry followed by an irreversible Randles-Ševčík analysis is not sufficient for deducing the electrode kinetics of the VO^{2+}-oxidation. In contrast, it is verified experimentally and theoretically that a Tafel analysis will still provide reasonable values of $k^0 = 1.35 \cdot 10^{-5}$ cm/s and $\alpha = 0.38$, respectively. Finally, it is shown that introducing the concept of finite heterogeneous kinetics into the theory of stationary linear sweep voltammetry also explains the failure of the irreversible Randles-Ševčík relation leading to an extension of the classical model and providing insight into the electrochemical oxidation reaction of VO^{2+}.

Keywords: vanadium redox-flow batteries, rotating disc electrode, linear sweep voltammetry, Koutecký-Levich analysis, Tafel analysis

OPEN ACCESS

Edited by:
Kai S. Exner,
Sofia University, Bulgaria

Reviewed by:
Aaron Marshall,
University of Canterbury, New Zealand
Aleksandar Zeradjanin,
Max Planck Institute for Chemical Energy Conversion, Germany

***Correspondence:**
Tim Tichter
t.tichter@fu-berlin.de

Specialty section:
This article was submitted to Electrochemical Energy Conversion and Storage, a section of the journal Frontiers in Energy Research

Received: *27 March 2020*
Accepted: *22 June 2020*
Published: *08 October 2020*

Citation:
Tichter T, Schneider J and Roth C (2020) Finite Heterogeneous Rate Constants for the Electrochemical Oxidation of VO^{2+} at Glassy Carbon Electrodes. Front. Energy Res. 8:155. doi: 10.3389/fenrg.2020.00155

1. INTRODUCTION

In vanadium redox flow battery (VRFB) research, stationary[1] linear sweep voltammetry (S-LSV) and stationary cyclic voltammetry (S-CV) are the most prevalent techniques used for the fast assessment of the kinetic performance of surface-modified carbon felt electrodes, and numerous studies have been published on that topic (Flox et al., 2013a,b; Gao et al., 2013; Hammer et al., 2014; Suárez et al., 2014; Liu et al., 2015; Park and Kim, 2015; He et al., 2016, 2018; Kim et al., 2016; Park et al., 2016; Ryu et al., 2016; Zhang et al., 2016; Zhou et al., 2016; González et al., 2017; Jiang et al., 2017; Ghimire et al., 2018; Xiang and Daoud, 2019; Yang et al., 2019). However, regarding the complex diffusion domain inside a felt electrode, the common approach of relating the peak-to-peak separation of an S-CV curve to the electrodes' kinetics (valid for a planar electrode in semi-infinite diffusion space only; Matsuda and Ayabe, 1954; Nicholson and Shain, 1964; Nicholson, 1965) does not seem to be appropriate. Applying the irreversible Randles-Ševčík relation for deducing the intrinsic kinetics of a felt electrode is also not possible since (a) the

[1] Stationary refers to an electroanalytical experiment without any forced convection of the electrolyte.

electrochemically active electrode area of the fiber network is unknown or at least uncertain and (b) the variation of the peak height with respect to the potential sweep rate becomes ambiguous when non-planar electrodes are involved (Aoki et al., 1983, 1984, 1985; Aoki, 1988). Since the majority of publications are dedicated to felt electrodes and respective diffusion domain effects rarely receive sufficient attention (Menshykau and Compton, 2008; Smith et al., 2015; Peinetti et al., 2016; Tichter et al., 2019a), literature values of the intrinsic vanadium redox kinetics might spread over orders of magnitude, as discussed recently in the paper by Friedl and Stimming (2017). Unfortunately, studies involving planar electrodes providing a well-defined, semi-infinite diffusion domain are unpopular in case of the VRFB system and a quantification of the intrinsic kinetics of novel electrode materials usually remains untested (Oriji et al., 2004; Han et al., 2011; Li et al., 2011, 2012, 2013, 2014; Jin et al., 2013; Dai et al., 2017). Compared to S-CV/LSV measurements at planar electrodes, studies using a rotating disc electrode (RDE) are even more unpopular (Zhong and Skyllas-Kazacos, 1992; Oriji et al., 2004). This is somewhat astonishing since they are well established in other fields of energy conversion (e.g., the fuel cell community) and can provide valuable information on the proceeding electrode reactions. With this paper we present a recent and comprehensive study on the oxidation reaction of VO^{2+} at electrochemically activated glassy carbon electrodes involving stationary and rotating linear sweep voltammetry as well as chronoamperometry. It is demonstrated that a Koutecký-Levich analysis of the RDE limiting currents yields a theoretically unexpected non-zero ordinate intercept proportional to the inverse VO^{2+} concentrations. Furthermore, it is shown that interpreting S-LSV data in terms of the irreversible Randles-Ševčík relation leads to values in the electron transfer coefficient α that contradict the findings from Tafel analysis of RDE data. We account for these two unexpected features simultaneously by introducing finite heterogeneous kinetic rate constants into the Butler-Volmer equation. Based on this idea, a three-term Koutecký-Levich equation is derived, allowing for unraveling mass transport, Butler-Volmer electrode kinetics and finite heterogeneous electron transfer kinetics. In this manner, the maximum heterogeneous rate constant for the oxidation reaction of VO^{2+} is found to be $k_{max} = 2.6 \cdot 10^{-2}$ cm/s. By including the estimated maximum rate constant into the theory of stationary linear sweep voltammetry, we also propose a model that captures the deviations of the experimental S-LSV data from the ideal irreversible Randles-Ševčík behavior. Finally, it is shown mathematically that the classical Tafel analysis of RDE data is unaffected by the limited electron transfer kinetics and should therefore be preferred for kinetic characterization.

2. EXPERIMENTAL SECTION

2.1. Electrochemical Measurements

The oxidation of VO^{2+} was investigated at electrochemically activated glassy carbon surfaces. The electrochemical activation was performed according to the conditioning given in **Table 1**. As an electrolyte solution, 2 M H_2SO_4 (ROTIPURAN® Ultra 95%, Carl Roth) with different concentrations of VO^{2+} [0.00, 0.02, 0.04, 0.06, and 0.08 M, Vanadium(IV) sulfate oxide hydrate, 99.9% (metals basis), Alfa Aesar] was used. All measurements were performed in a three electrode setup consisting of a Ag/AgCl reference (saturated, 198 mV vs. SHE), a Pt-mesh counter electrode, and a glassy carbon disc (7 mm diameter, embedded into a PEEK cylinder) working electrode. Data was acquired using a PalmSens Em-Stat potentiostat (PalmSens). The working electrode was connected to a control panel (MetrohmAutolab® RDE-2) to adjust the rotation speed during the measurements.

TABLE 1 | Overview of all linear sweep (LSV) and chronoamperometry (CA) measurements with corresponding pretreatments.

	Stationary-LSV	Rotating-LSV	Stationary-CA
ω / rpm	0	100, 123, 156, 204, 278, 400, 625	0
ν / mV s^{-1}	70, 60, 50, 40, 30, 20, 10	20	0
E vs. $E_{Ag/AgCl}$ / V	1–1.7	1–1.7	1.65
Conditioning	15 s, −0.2 V 30 s break 20 s, 0.7 V	15 s, −0.2 V at 1,600 rpm 30 s break, 5 s 0.7 V	15 s, −0.2 V at 1,600 rpm, 60 s break

2.2. Pretreatment of the Electrode

Prior to each measurement, the glassy carbon electrode was polished in two successive steps (step 1: 1.0 micron, BUEHLER 40-10081 and step 2: 0.05 micron, BUEHLER 40-10083). Electrochemical activation was performed under rotation in a chronoamperometric three-step sequence (step 1: 2 V vs. E_{Ref} for 15 s, step 2: −1 V vs. E_{Ref} for 5 s, step 3: 2 V vs. E_{Ref} for 5 s, each step at $\omega = 1{,}600$ rpm). Subsequently, S-LSV, R-LSV, and S-CA measurements were performed as given in **Table 1**.

3. RESULTS AND DISCUSSION

3.1. RDE Measurements

The desired reaction of this study, the electrochemical oxidation of VO^{2+}, can be formulated as

$$VO^{2+} + H_2O \xrightarrow{-e^-} VO_2^+ + 2H^+ \tag{1}$$

and has a standard electrode potential of $E^0 - E_{SHE} = 0.995$ V. To eliminate errors resulting from parasitic reactions such as the carbon corrosion or the oxygen evolution reaction, the datasets obtained for vanadium containing electrolytes were corrected by the corresponding vanadium-free baselines in pure 2 M sulfuric acid. This entirely subtractive correction is based on the assumption that any parasitic reactions proceed in parallel and do not impair the desired oxidation

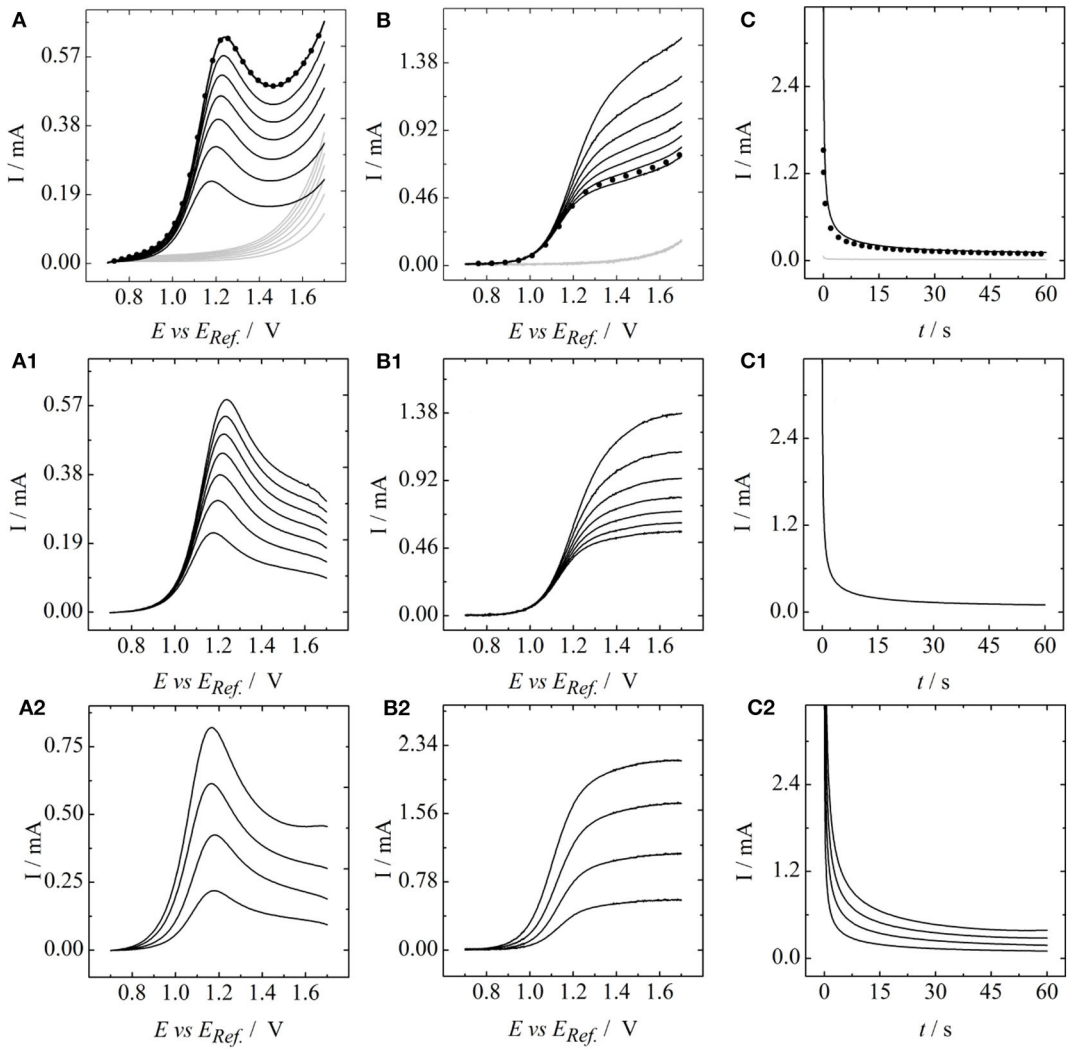

FIGURE 1 | (A) Stationary and **(B)** rotating linear sweep as well as **(C)** chronoamperometric measurements at a glassy carbon surface. Gray lines: 2 M sulfuric acid as a baseline, black lines: vanadyl sulfate containing 2 M sulfuric acid, black dots: repetition of initial measurements to check experimental reproducibility. **(A1–C1)** Represent baseline corrected data at a VO^{2+} concentration of 0.02 M for **(A1)** varying scanrates and **(B1)** varying rotation rates. **(A2–C2)** Represent baseline corrected data for varying concentrations of VO^{2+} at **(A2)**: a fixed scanrate of 10 mV/s and **(B2)**: a fixed rotation rate of 100 rpm. Potentials were referred to a saturated Ag/AgCl reference.

of VO^{2+}. Furthermore, it holds only under the presumption that the electrode area is independent of the applied electrode potential. These assumptions are considered reasonable as long as the upper potential limit does not allow for the formation of gaseous oxygen, which was ensured throughout the entire study. This correction is illustrated for the electrolyte containing 0.02 M vanadyl sulfate in **Figure 1A**: stationary and **Figure 1B**: rotating linear sweep as well as the **Figure 1C**: chronoamperometric measurements. Gray lines represent the baseline in pure 2 M sulfuric acid solution and black lines the measurements in 2 M sulfuric acid containing 0.02 M vanadyl sulfate. The corresponding baseline corrected curves are shown in **Figures 1A1–C1**. Baseline corrected data at the different vanadyl sulfate concentrations are depicted in **Figures 1A2–C2**. In the S-LSV measurements (**Figure 1A2**) a potential sweep rate of $\nu = 10$ mV/s was used. The rotation rate in the R-LSV experiments in **Figure 1B2** was set to $\omega = 100$ rpm.

It can be seen that increasing the scan rate (**Figure 1A1**) or the rotation rate (**Figure 1B1**) at fixed VO_2^+-concentration results in a set of curves starting at the same kinetic origin. In contrast, an increase in the concentrations, as shown in **Figures 1A2,B2**, results in a negative shift of the entire LSV curves. This is expected, as the exchange current is proportional to the analyte concentration. In case of the S-LSVs a peak current with constant peak position is obtained for the different concentrations, whereas in case of the R-LSVs the limiting current scales linearly with respect to the concentrations. The

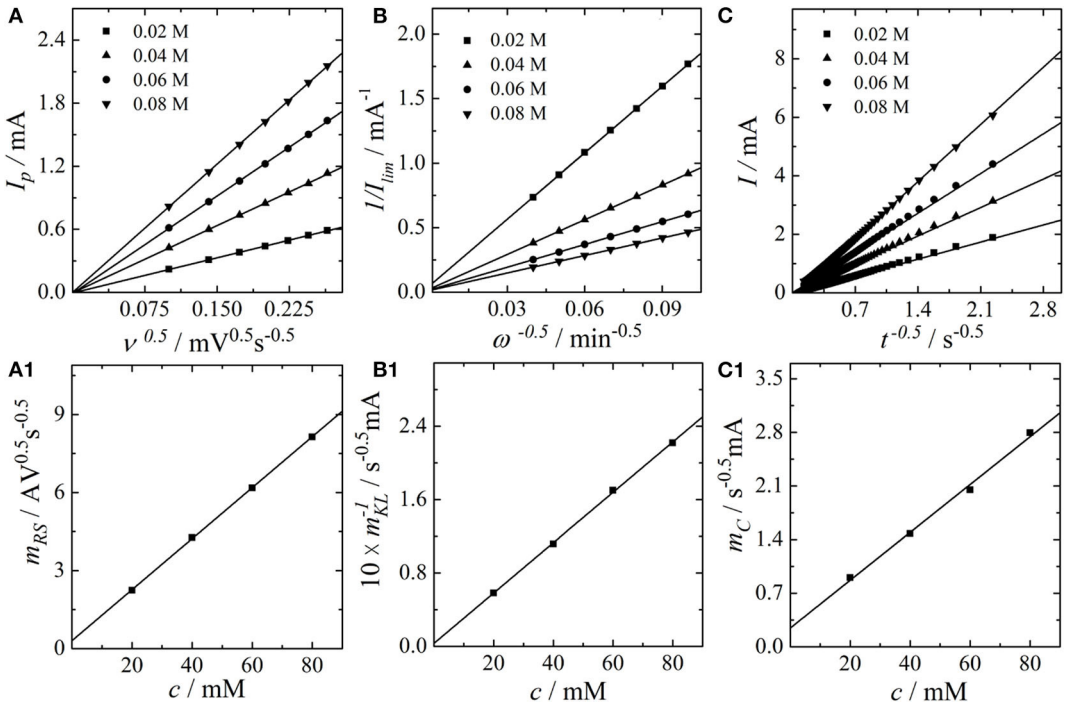

FIGURE 2 | (A) Randles-Ševčík-Plot of the peak currents vs. the square root of the scan rate, **(B)** Koutecký-Levich plot of the inverse limiting currents vs. the inverse square root of the electrode rotation rate, and **(C)** Cottrell plot of the current vs. the inverse square root of the experiment duration. **(A1)** plot of the Randles-Ševčík slopes vs. the concentrations, **(B1)** plot of the inverse Koutecký-Levich slopes vs. the concentrations, and **(C1)** plot of the Cottrell slopes vs. the concentrations.

chronoamperometric measurements of **Figure 1C2** also show a linear scaling of the current with the concentrations. Based on the datasets of **Figures 1**, **2A** shows a Randles-Ševčík plot, **Figure 2B** a Koutecký-Levich plot and **Figure 2C** a Cottrell plot for the different concentrations of VO^{2+}. In all cases straight lines are obtained. At this point we want to draw the reader's attention to the experimentally observed ordinate intercepts in the Koutecký-Levich plots in particular. These are not expected from a theoretical point of view and will be discussed in detail in section 3.2. Based on the data of **Figures 2A–C,A1,C1** depict the slopes obtained from the analysis in **Figures 2A,C**, plotted versus the corresponding concentrations of VO^{2+}. A plot of the inverse slope of **Figure 2B** versus the analyte concentration leads to **Figure 2B1**. In all cases a linear concentration dependence is obtained, providing a slope that corresponds to the second partial derivatives of the Koutecký-Levich eq. 3, the irreversible Randles-Ševcík eq. 2 and the Cottrell equation eq. 4, respectively.

$$I_R'' = \frac{\partial^2 I_R}{\partial c \partial \nu^{1/2}} \tag{2}$$

$$I_K'' = \frac{\partial^2 I_K}{\partial c \partial \omega^{1/2}} \tag{3}$$

$$I_C'' = \frac{\partial^2 I_C}{\partial c \partial t^{-1/2}} \tag{4}$$

These second partial derivatives are used in the following section for further analysis.

By combining the second partial derivative of the Cottrell equation with the second partial derivative of the Koutecký-Levich equation, we obtain the diffusion coefficient of the VO^{2+}-ion via

$$D = 489\eta \left(\frac{I_K''}{I_C''} \right)^6 . \tag{5}$$

Compared to the classical Koutecký-Levich or Cottrell analysis, this expression appears to be superior in estimating diffusion coefficients since (a) it does not depend on the active electrode area (which might differ from the geometric area) and (b) it accounts for different analyte concentrations as well. Furthermore, it is not necessary to know the value of n a priori. Following this strategy, we determine the diffusion coefficient of the VO^{2+}-cation in 2 M H_2SO_4 to a value of $2.26 \cdot 10^{-6}$ cm^2/s, in good agreement with the average value given in Zhong and Skyllas-Kazacos (1992) and slightly smaller than the value reported in our recent study (Tichter et al., 2019b), which was obtained from S-CV fitting of a felt electrode. A similar combination of the second partial derivative of the irreversible Randles-Ševčík equation obtained from **Figure 2A1** with the second partial derivative of the Cottrell

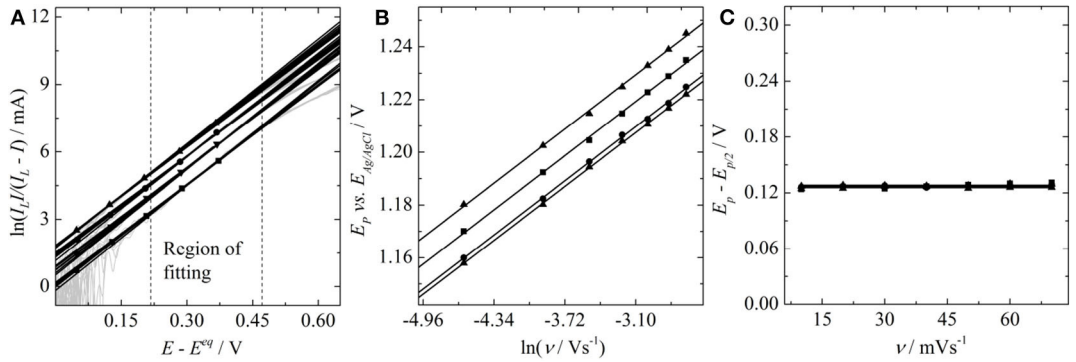

FIGURE 3 | (A) Tafel plots (dashed lines are the limits of the fitting region), **(B)** plot of the peak position vs. the logarithm of the scan rate, and **(C)** peak-shape analysis for the oxidation of vanadyl sulfate in concentrations of 0.02 M (square), 0.04 M (down-triangle), 0.06 M (circle), and 0.08 M (up-triangle) at a glassy carbon electrode in 2 M H_2SO_4.

equation allows for a determination of the electron transfer coefficient as

$$\alpha = 1.294\frac{RT}{nF}\left(\frac{I_P''}{I_C''}\right)^2. \tag{6}$$

Nevertheless, it has to be noted that this expression requires the values of n to be known (in the present case it is assumed that $n = 1$). Via Equation (6), we estimate the electron transfer coefficient for the electrochemical oxidation of VO^{2+} at the glassy carbon electrode to $\alpha = 0.32$. At this stage we highlight the importance of the baseline correction as shown in **Figure 1**, which was necessary in order to remove additively scaling parasitic currents. However, we refer to an alternative way for estimating α, which is independent of the current magnitude and is outlined in the early findings of Matsuda and Ayabe (1954). There, the authors propose that it is possible to obtain the electron transfer coefficient for an electrochemically irreversible reaction (taking place at a planar electrode in semi-infinite diffusion space) by analyzing the peak shape and the peak position of a S-LSV curve via Equations (7) and (8) only. Also in this context, however, the value of n has to be known.

$$\alpha = \frac{1.85RT}{nF(E_p - E_{p/2})} \tag{7}$$

$$\alpha = \frac{RT}{2nF}\left(\frac{\partial I_P}{\partial ln(\nu)}\right)^{-1} \tag{8}$$

Another, and probably the most straightforward way for obtaining the electron transfer coefficient is given in terms of a Tafel-analysis of RDE data (Equation 9).

$$\alpha = \frac{RT}{nF}\left(\frac{\partial ln(\frac{II_L}{I_L - I})}{\partial(E - E^{eq})}\right) \tag{9}$$

TABLE 2 | Values of the electron transfer coefficient α, estimated from Tafel-, Randles-Ševčík-, and Matsuda-Ayabe analysis.

	0.02 M	0.04 M	0.06 M	0.08 M
α(A)	0.381	0.383	0.375	0.381
α(B)	0.385	0.385	0.385	0.386
α(C)	0.371	0.376	0.371	0.368

In order to deduce α, **Figure 3A**: a Tafel plot, **Figure 3B**: a plot of the peak position versus the logarithm of the scan rate and **Figure 3C**: the peak shape analysis for the oxidation of vanadyl sulfate at a glassy carbon electrode. The values of the electron transfer coefficient are listed in **Table 2**.

All the values of α given in **Table 2** are close to $\alpha = 0.38$ and therefore diverge significantly from the value of $\alpha = 0.32$ determined by Equation (6). No dependence of α on the concentrations is observed. Consequently, the average of the α value is taken for all individual concentrations. Thus, analyzing the dependence of the peak-potential on the logarithm of the scan rate according to Equation (7) yields $\alpha = 0.385$, the shape analysis according to Equation (8) leads to $\alpha = 0.372$, and a Tafel analysis provides $\alpha = 0.38$. Furthermore, a Tafel analysis provides the standard heterogeneous rate constant to $k^0 = 1.35 \cdot 10^{-5}$ cm/s. The significant deviation in the α values given in **Table 2** from the findings involving Equation (6) as well as the unexpected non-zero ordinate intercepts in Koutecký-Levich analysis will be discussed in the following subsections.

3.2. Concept of Finite Heterogeneous Kinetics

The experimentally observed non-zero ordinate intercepts obtained in Koutecký-Levich plots are the main motivation for the following considerations. Such a behavior cannot be explained with the classical Koutecký-Levich model (Equation 10), since a limiting current, or better, a hydrodynamic limiting current caused by mass transfer limitations—corresponds to infinitely fast reaction kinetics forcing $I_{kin}^{-1} \rightarrow 0$. Consequently,

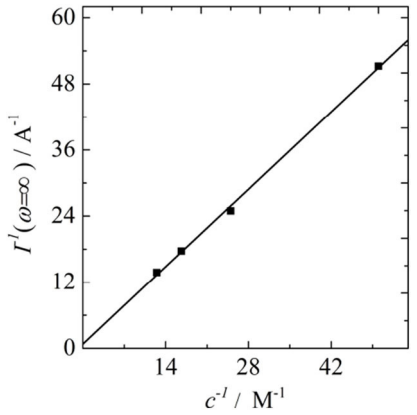

FIGURE 4 | Plot of the ordinate intercepts of the Koutecký-Levich plots at different concentrations of vanadyl sulfate vs. the inverse concentrations.

the extrapolation to infinite rotation rate will actually give a zero-ordinate intercept.

$$\frac{1}{I_K} = \frac{1}{I_{kin}} + \frac{1}{0.201nFAcD^{2/3}\eta^{-1/6}\sqrt{\omega}} \tag{10}$$

However, we propose that a current plateau, usually associated with the hydrodynamic limiting current, can also be reached by a limitation of the heterogeneous reaction kinetics itself. Thus, the term I_{kin}^{-1} will become small and constant, but it will not approach zero. The current plateau achieved under these circumstances will always be lower than the hydrodynamic limiting current, which is indeed what is observed experimentally. By calculating the hydrodynamic limiting current with the classical Koutecký-Levich equation using the previously obtained value of D, the estimated hydrodynamic limiting current values are always larger than their experimentally measured analogs. Thus, we suggest that for implementing the concept of a maximum kinetic current into the Koutecký-Levich equation, a third and additively scaling inverse current term that does neither depend on the overpotential, nor on the rotation rates is required. Subsequently, it needs to be clarified whether or not this extra quantity will depend on the analyte concentrations. By thoroughly examining the Koutecký-Levich plots for the different concentrations of VO^{2+} we found a linear relation between the ordinate intercepts and the inverse analyte concentration, which is depicted in **Figure 4**. Consequently, we propose that the maximum kinetic current has to be considered as a linear function of the concentration. Assuming that the slope of the line in **Figure 4** can be expressed in terms of the maximum kinetic current, which we define by $I_{max} = nFAck_{max}$, we obtain a maximum heterogeneous rate constant of $k_{max} = 0.026$ cm/s. This hypothetic limit is the starting point for further considerations, where the idea of finite kinetics will be introduced into the Butler-Volmer equation.

3.3. Theoretical Discussion

First, we recall the classical Butler-Volmer equation as

$$I = nFAk^0\left(c_{red,s}e^{\alpha\xi} - c_{ox,s}e^{-(1-\alpha)\xi}\right), \tag{11}$$

where $\xi = nF(E - E^0)/RT$ denotes the dimensionless electrode potential and $c_{red,s}$ and $c_{ox,s}$ denote the surface concentrations of the electrochemically active species. Other variables have their usual meaning. An introduction of a maximum achievable rate constant k_{max} yields

$$I = nFAk^0\left(c_{red,s}\frac{k_{max}e^{\alpha\xi}}{k_{max} + k^0e^{\alpha\xi}} - c_{ox,s}\frac{k_{max}e^{-(1-\alpha)\xi}}{k_{max} + k^0e^{-(1-\alpha)\xi}}\right). \tag{12}$$

It is readily seen that Equation (12) reduces to Equation (11) when k_{max} becomes very large which corresponds to the case of no kinetic limitations. In contrast, if k_{max} is comparably small, the effect of kinetic limitations can be expected to be more prominent. Equation (12) is the starting point for all further considerations.

3.3.1. Rotating Electrode Polarography With Finite Kinetics

Introducing the above definition of the maximum kinetic current as

$$I_{max} = nFAc_bk_{max}, \tag{13}$$

where the index b represents the bulk concentration, as well as the exchange current as

$$I^{eq} = nFAk^0c_{red,b}e^{\alpha a} = nFAc_{ox,b}k^0e^{-(1-\alpha)a}, \tag{14}$$

where $a = nF(E^{eq} - E^0)/RT$ is the dimension-less equilibrium potential, we get

$$I = I^{eq}\left(\frac{c_{red,s}}{c_{red,b}}\frac{I_{max,an}e^{\alpha(a-\xi)}}{I_{max,an} + I^{eq}e^{\alpha(a-\xi)}} - \frac{c_{ox,s}}{c_{ox,b}}\frac{I_{max,ca}e^{-(1-\alpha)(a-\xi)}}{I_{max,ca} + I^{eq}e^{-(1-\alpha)(a-\xi)}}\right). \tag{15}$$

For a rotating electrode we substitute the steady state formalism $c_{red,s}/c_{red,b} = 1 - I/I_{L,an}$ and $c_{ox,s}/c_{ox,b} = 1 - I/I_{L,ca}$ with $I_{l,an}$ and $I_{l,c}$ being the anodic and cathodic limiting currents expressed by the Levich equation. Since the backward reaction can be neglected at absolute overpotentials larger than $118/n$ mV, Equation (15) can be simplified for an exemplary anodic reaction to

$$I = I^{eq}\left(\left(1 - \frac{I}{I_{L,an}}\right)\frac{I_{max,an}e^{\alpha(a-\xi)}}{I_{max,an} + I^{eq}e^{\alpha(a-\xi)}}\right) \tag{16}$$

This expression can be rearranged to give the following desired three-term Koutecký-Levich equation

$$\frac{1}{I} = \frac{1}{I_{kin}} + \frac{1}{I_{L,an}} + \frac{1}{I_{max}}. \tag{17}$$

The first two terms in Equation (17) form the classical Koutecký-Levich equation, whereas the third term $1/I_{max}$ contains the maximum rate constant and is therefore responsible for the non-zero ordinate intercept in Koutecký-Levich plots. As k_{max} tends to infinity, the third term vanishes, and Equation (17) reduces to the classical expression. Unifying the term of the hydrodynamic limiting current with the maximum kinetic current, the latter two terms in Equation (17) provide the measured limiting current $I_{lim,me}$ as

$$I_{lim,me} = \frac{I_{lim,an} I_{max,an}}{I_{lim,an} + I_{max,an}}. \tag{18}$$

Consequently, the unlimited kinetic current can be obtained from measured data as

$$ln(I_{kin}) = ln\left(\frac{I_{lim,me} I}{I_{lim,me} - I}\right) = ln(I^{eq}) + \frac{\alpha n F(E - E^{eq})}{RT}, \tag{19}$$

which is in principle just a rearranged version of Equation (18) as well as an alternative form of the conventional *"mass transfer correction"* described by Equation (9). This underlines that even if the heterogeneous kinetics are finite, the value of α and I^{eq} (and thus k^0) can still be determined by using Tafels law if the current gets normalized properly to its limiting value.

3.3.2. Stationary Electrode Polarography With Finite Kinetics

If the model of finite kinetic rate constants is valid for a rotating electrode, it has to apply also to stationary measurements. In analogy to the limiting currents of an RDE experiment it can be assumed that the finite electrode kinetics will reduce the peak height in a S-LSV curve, which would in turn explain the misleading results of α obtained from the classical Randles-Ševčík analysis. To support this assumption, the theory of stationary electrode polarography, accounting for finite heterogeneous kinetics, will be re-derived in this paragraph. Starting again with Equation (12) and replacing the surface activities by their known expressions of the convoluted current for semi-infinite planar diffusion as

$$c_{red,s} = c_{red,b} - \frac{1}{nFA\sqrt{\pi D}} \int_0^t \frac{I(\tau)}{\sqrt{t-\tau}} d\tau \tag{20}$$

$$c_{ox,s} = c_{ox,b} + \frac{1}{nFA\sqrt{\pi D}} \int_0^t \frac{I(\tau)}{\sqrt{t-\tau}} d\tau \tag{21}$$

we obtain

$$\frac{I(t)}{nFAk^0 k_{max}} = \frac{c_{red,b} e^{\alpha\xi(t)}}{k_{max} + k^0 e^{\alpha\xi(t)}} - \frac{c_{ox,b} e^{-(1-\alpha)\xi(t)}}{k_{max} + k^0 e^{-(1-\alpha)\xi(t)}} - \frac{1}{nFA\sqrt{\pi D}} \left[\frac{e^{\alpha\xi(t)}}{k_{max} + k^0 e^{\alpha\xi(t)}} + \frac{e^{-(1-\alpha)\xi(t)}}{k_{max} + k^0 e^{-(1-\alpha)\xi(t)}}\right] \int_0^t \frac{I(\tau)}{\sqrt{t-\tau}} d\tau. \tag{22}$$

Defining a new constant $k_{fin} = k^0/k_{max}$ and taking the definition of the dimensionless rate constant and the dimensionless current as

$$\Lambda = \frac{k^0\sqrt{RT}}{\sqrt{nF\nu D}} \tag{23}$$

$$\chi(\xi) = \frac{I(\xi)}{nFAc_{red,b}\sqrt{\frac{nF\nu D}{RT}}} \tag{24}$$

we obtain the following integral equation (Equation 25).

$$\frac{\chi(\xi)}{\Lambda} \frac{1 + k_{fin}(e^{\alpha\xi} + e^{-(1-\alpha)\xi}) + k_{fin}^2 e^{\xi(2\alpha-1)}}{e^{\alpha\xi} + e^{-(1-\alpha)\xi} + 2k_{fin} e^{\xi(2\alpha-1)}} = \frac{(1 - e^{a-\xi}) + k_{fin}(1 + e^{a}) e^{-(1-\alpha)\xi}}{1 + e^{-\xi} + 2k_{fin} e^{-(1-\alpha)\xi}} - \frac{1}{\sqrt{\pi}} \int_0^\xi \frac{\chi(\xi)}{\sqrt{\xi - \zeta}} d\zeta \tag{25}$$

The desired dimension-less current function $\chi(\xi)$ can be evaluated accurately as Riemann-Stieltjes integral after eliminating the singularity in the denominator similar to Nicholson and Shain (1964). In case of no kinetic limitations it is obvious that $k_{max} \to \infty$ and thus $k_{fin} \to 0$. Therefore, Equation (25) condenses to the expression (Equation 26) of (Matsuda and Ayabe, 1954):

$$\frac{\chi(\xi)}{\Lambda} \frac{1}{e^{\alpha\xi} + e^{-(1-\alpha)\xi}} = \frac{(1 - e^{a-\xi})}{1 + e^{-\xi}} - \frac{1}{\sqrt{\pi}} \int_0^\xi \frac{\chi(\xi)}{\sqrt{\xi - \zeta}} d\zeta. \tag{26}$$

3.3.3. Simulation of Data

In this section, Equation (25) is used for simulating stationary LSV responses that are subsequently evaluated using the irreversible Randles-Ševčík relation as well as Equations (7) and (8) in order to reproduce the experimentally observed error. For the simulation we took $\alpha = 0.38$ and $k^0 = 1.35 \cdot 10^{-5}$ cm/s as extracted from the Tafel plots of **Figure 3A** and $k_{max} = 0.026$ cm/s as extracted from **Figure 4** as well as the estimated value of $D = 2.26 \cdot 10^{-6}$cm^2/s. Simulations were performed using our in-house developed software Polarographica (Tichter and Schneider, 2019). The calculated voltammogramms as well as the corresponding Randles-Ševčík plot, conducted peak-shape analysis, and plotted the dimensionless peak potential vs. the scan rate, as shown in **Figure 5**.

Analyzing the simulated dataset of **Figure 5** gives $\alpha = 0.343$ for the Randles-Ševčík analysis, $\alpha = 0.371$ for the peak shape analysis and $\alpha = 0.378$ for the plot of the peak potential vs. the logarithm of the scan rate. This confirms our expectation, that significant deviations from the original α value are obtained as soon as finite kinetics are present. Furthermore, it shows that the largest error in α is obtained by the classical Randles-Ševčík analysis which captures the experimentally observed trend. Consequently, we conclude that, in stationary potential sweep

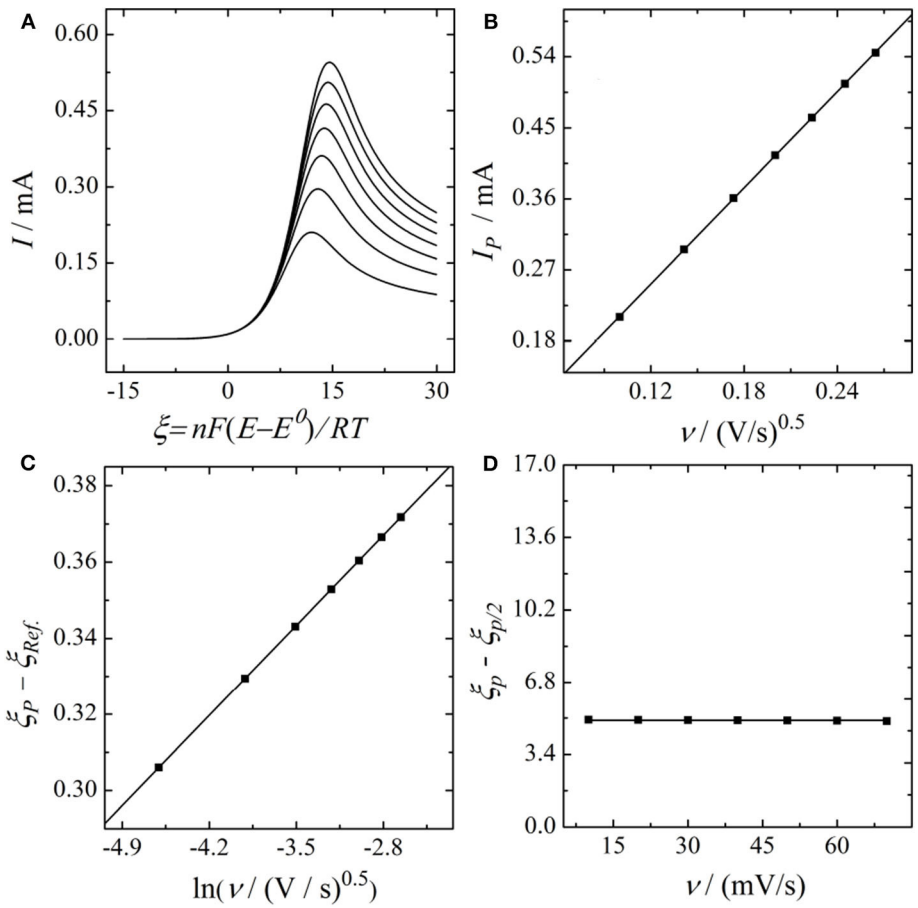

FIGURE 5 | (A) S-LSV curves, **(B)** Randles-Ševčík Plot, **(C)** Matsuda-Ayabe analysis, and **(D)** peak shape analysis of an electrochemical reaction (the oxidation of VO^{2+} with finite kinetics simulated for the set of parameters obtained previously via Tafel analysis and Kouteck-Levich analysis).

experiments, the finite heterogeneous kinetics predominantly affect the current magnitude. Nevertheless, it has to be noted that also the accuracy of the shape analysis and the plot of the peak potential vs. the scan rate are affected by the kinetic limitations, even if these deviations are minor. Based on these findings we finally conclude that S-LSV measurements are not well-suited for estimating the electrode kinetics in a straightforward way, even if planar electrodes are involved. In contrast, since Tafel analysis of RDE data is independent of the finite electrode kinetics, we refer it as a more reliable way for investigating electrode kinetics.

3.3.4. Practical Relevance of Finite Kinetics

In the previous sub-paragraphs, the experimental verification and theoretical treatment of finite heterogeneous electrode kinetics were introduced. However, so far, we have not yet discussed the practical relevance and the possible origin of such a limitation. When regarding an electrode reaction like the electrochemical oxidation of VO^{2+}, the classical analysis usually accounts for Butler-Volmer electron transfer kinetics coupled to mass transfer only. Consequently, no intermediate reaction steps are considered. Such additional reaction steps might be, however, responsible for the finiteness of the electrode reaction kinetics. In this context one might think of (a) an adsorption/desorption of the electrochemically active vanadium species preceding or following the electron transfer or (b) of rearrangements in the solvate shell of the vanadium ions which have to occur before an electrochemical reaction can proceed. However, since we do not have any experimental evidence for either scenario (a) or (b), we do no attempt to speculate about possible reaction mechanisms at this stage. In contrast, we want to underline that analyzing the kinetic limit of an electrochemical reaction with the strategy outlined in this paper can offer valuable insights in the intrinsic activity of novel catalyst materials, since an overpotential independent performance indicator is obtained. In this manner, our strategy might also lead to a better understanding of intermediate reaction steps. Therefore, it can be extraordinarily important for the experimentalists community when screening alternative catalyst materials for possible applications in a VRFB.

4. SUMMARY AND CONCLUSIONS

The kinetics of the $VO^{2+}/VO_2{}^{2+}$ redox couple was investigated at planar glassy carbon electrodes via rotating and stationary linear sweep voltammetry as well as stationary chronoamperometry. A combination of the Koutecký-Levich equation with the Cottrell equation allowed for a precise determination of the diffusion coefficient of the vanadyl cation, leading to $D = 2.26 \cdot 10^{-6}$ cm^2/s. A similar combination of the irreversible Randles-Ševčík equation with the Cottrell equation provided an electron transfer coefficient of $\alpha = 0.32$. Contrary, calculating the electron transfer coefficient via Tafel analysis of RDE data provided $\alpha = 0.38$. This deviation in the electron transfer coefficient as well as the experimentally observed non-zero ordinate intercepts in Koutecký-Levich plots, which cannot be explained by the classical model are explained simultaneously by introducing the concept of finite heterogeneous electron transfer kinetics into the Butler-Volmer equation. In this manner, a three term Koutecký-Levich type equation was derived, which allows for the determination of the maximum kinetic rate constant to $k_{max} = 0.026$ cm/s. By considering the modified Butler-Volmer equation as the boundary condition for stationary electrode polarography, the experimentally observed deviation in the electron transfer coefficients could be simulated as well. Based on the modified version of the Butler-Volmer equation it was shown that Tafel analysis of RDE data will not be affected by the finite heterogeneous kinetics. Therefore, we concluded that the Tafel analysis in a rotating disc electrode setup is the most accurate method to determine the kinetic parameters of a reaction.

DATA AVAILABILITY STATEMENT

The raw data supporting the conclusions of this article will be made available by the authors, without undue reservation.

AUTHOR CONTRIBUTIONS

TT carried out the data acquisition and conception, developed the theory, and wrote the manuscript. JS carried out the conception and scientific discussion and wrote the manuscript. CR carried out the scientific supervision and wrote the manuscript. All authors contributed to the article and approved the submitted version.

FUNDING

We acknowledge support from the Open Access Publication Initiative of Freie Universität Berlin.

REFERENCES

Aoki, K. (1988). Theory of irreversible cyclic voltammetry at microcylinder electrodes. *J. Electroanalyt. Chem.* 247, 17–27. doi: 10.1016/0022-0728(88)80127-X

Aoki, K., Honda, K., Tokuda, K., and Matsuda, H. (1985). Voltammetry at microcylinder electrodes Part I. *Linear sweep voltammetry. J. Electroanalyt. Chem.* 182, 267–279. doi: 10.1016/0368-1874(85)87005-2

Aoki, K., Tokuda, K., and Matsuda, H. (1983). Theory of linear sweep voltammetry with finite diffusion space part I. *J. Electroanalyt. Chem.* 146, 417–424. doi: 10.1016/S0022-0728(83)29080601-9

Aoki, K., Tokuda, K., and Matsuda, H. (1984). Theory of linear sweep voltammetry with finite diffusion space part II. *J. Electroanalyt. Chem.* 160, 33–45. doi: 10.1016/S0022-0728(84)80113-8

Dai, L., Jiang, Y., Meng, W., Zhou, H., Wang, L., and Zhangxing, H. (2017). Improving the electrocatalytic performance of carbon nanotubes for VO^{2+}/VO^{2+} redox reaction by KOH activation. *Appl. Surface Sci.* 401, 106–113. doi: 10.1016/j.apsusc.2017.01.002

Flox, C., Rubio-Garcíia, J., Skoumal, M., Andreu, T., and Morante, J. R. (2013a). Thermo-chemical treatments based on NH_3/O_2 for improved graphite-based fiber electrodes in vanadium redox flow batteries. *Carbon* 60, 280–288. doi: 10.1016/j.carbon.2013.04.038

Flox, C., Skoumal, M., Rubio-Garcia, J., Andreu, T., and Ramón Morante, J. (2013b). Strategies for enhancing electrochemical activity of carbon-based electrodes for all-vanadium redox flow batteries. *Appl. Energy* 109, 344–351. doi: 10.1016/j.apenergy.2013.02.001

Friedl, J., and Stimming, U. (2017). Determining electron transfer kinetics at porous electrodes. *Electrochim. Acta* 227, 235–245. doi: 10.1016/j.electacta.2017.01.010

Gao, C.,Wang, N., Peng, S., Liu, S., Lei, Y., Liang, X., et al. (2013). Influence of Fenton's reagent treatment on electrochemical properties of graphite felt for all vanadium redox flow battery. *Electrochim. Acta* 88, 193–202. doi: 10.1016/j.electacta.2012.10.021

Ghimire, P. C., Schweiss, R., Scherer, G. G., Wai, N., Lim, T. M., Bhattarai, A., et al. (2018). Titanium carbide-decorated graphite felt as high performance negative electrode in vanadium redox flow atteries. *J. Mater. Chem. A* 6, 6625–6632. doi: 10.1039/c8ta00464a

González, Z., Flox, C., Blanco, C., Granda, M., Morante, J. R., Menéndez, R., et al. (2017). Outstanding electrochemical performance of a graphene-modified graphite felt for vanadium redox flow battery application. *J. Power Sources* 338, 155–162. doi: 10.1016/j.jpowsour.2016.10.069

Hammer, E.-M., Berger, B., and Komsiyska, L. (2014). Improvement of the performance of graphite felt electrodes for vanadium-redox-flow-batteries by plasma treatment. *Int. J. Renew. Energy Dev.* 3, 7–12. doi: 10.14710/ijred.3.1.7-12

Han, P., Wang, H., Liu, Z., Chen, X., Ma, W., Yao, J., et al. (2011). Graphene oxide nanoplatelets as excellent electrochemical active materials for VO^{2+}/VO^{2+} and V^{2+}/V^{3+} redox couples for a vanadium redox flow battery. *Carbon* 49, 693–700. doi: 10.1016/j.carbon.2010.10.022

He, Z., Jiang, Y., Zhou, H., Cheng, G., Meng, W., Wang, L., et al. (2016). Graphite felt electrode modified by square wave potential pulse for vanadium redox flow battery. *Int. J. Energy Res.* 41, 439–447. doi: 10.1002/er.3626

He, Z., Li, M., Li, Y., Zhu, J., Jian, Y., Meng, W., et al. (2018). Flexible electrospun carbon nanofiber embedded with TiO_2 as excellent negative electrode for vanadium redox flow battery. *Electrochim. Acta* 281, 601–610. doi: 10.1016/j.electacta.2018.06.011

Jiang, Y., He, Z., Li, Y., Zhu, J., Zhou, H., Meng, W., et al. (2017). Carbon layer-exfoliated, wettability enhanced, SO_3H-functionalized carbon paper: a superior positive electrode for vanadium redox flow battery. *Carbon* 127, 297–304. doi: 10.1016/j.carbon.2017.11.006

Jin, J., Fu, X., Liu, Q., Liu, Y., Wei, Z., Niu, K., et al. (2013). Identifying the active site in nitrogen-doped graphene for the VO^{2+}/VO^{2+} redox reaction. *ACS Nano* 7, 4764–4773. doi: 10.1021/nn3046709

Kim, K. J., Lee, H. S., Kim, J., Park, M.-S., Kim, J. H., Kim, Y.-J., et al. (2016). Superior electrocatalytic activity of a robust carbon-felt electrode with oxygen-rich phosphate groups for all-vanadium redox flow batteries. *ChemSusChem* 9, 1329–1338. doi: 10.1002/cssc.201600106

Li, B., Gu, M., Nie, Z., Wei, X., Wang, C., Sprenkle, V., et al. (2014). Nanorod niobium oxide and powerful catalysts for an all vanadium redox flow battery. *Nano Lett.* 14, 158–165. doi: 10.1021/nl403674a

Li, W., Liu, J., and Yan, C. (2011). Multi-walled carbon nanotubes used as an electrode reaction catalyst for VO^{2+}/VO^{2+} for a vanadium redox flow battery. *Carbon* 49, 3463–3470. doi: 10.1016/j.carbon.2011.04.045

Li, W., Liu, J., and Yan, C. (2012). The electrochemical catalytic activity of single-walled carbon nanotubes towards VO^{2+}/VO^{2+} and V^{2+}/V^{3+} redox pairs for an all vanadium redox flow battery. *Electrochim. Acta* 79, 102–108. doi: 10.1016/j.electacta.2012.06.109

Li, W., Liu, J., and Yan, C. (2013). Reduced graphene oxide with tunable C/O ratio and its activity towards vanadium redox pairs for an all vanadium redox flow battery. *Carbon* 55, 313–320. doi: 10.1016/j.carbon.2012.12.069

Liu, T., Li, X., Nie, H., Xu, C., and Zhang, H. (2015). Investigation on the effect of catalyst on the electrochemical performance of carbon felt and graphite felt for vanadium flow batteries. *J. Power Sources* 286, 73–81. doi: 10.1016/j.jpowsour.2015.03.148

Matsuda, H., and Ayabe, Y. (1954). Zur Theorie der Randles-Ševčík'schen Kathodenstrahl-Polarographie. *Z. Elektrochem.* 59, 494–503. doi: 10.1002/bbpc.19550590605

Menshykau, D., and Compton, R. G. (2008). The influence of electrode porosity on diffusional cyclic voltammetry. *Electroanalysis* 22, 2387–2394. doi: 10.1002/elan.200804334

Nicholson, R. S. (1965). Theory and application of cyclic voltammetry for measurement of electrode reaction kinetics. *Anal. Chem.* 37, 1351–1355. doi: 10.1021/ac60230a016

Nicholson, R. S., and Shain, I. (1964). Theory of stationary electrode polarography single scan and cyclic methods applied to reversible, irreversible, and kinetic systems. *Anal. Chem* 36, 706–723. doi: 10.1021/ac60210a007

Oriji, G., Katayama, Y., and Miura, T. (2004). Investigation on V(IV)/V(V) species in a vanadium redox flow battery. *Electrochim. Acta* 49, 3091–3095. doi: 10.1016/j.electacta.2004.02.020

Park, J. J., Park, J. H., Park, O. O., and Yang, J. H. (2016). Highly porous graphenated graphite felt electrodes with catalytic defects for high performance vanadium redox flow batteries produced via FNiO/Ni redox reactions. *Carbon* 110, 17–26. doi: 10.1016/j.carbon.2016.08.094

Park, S., and Kim, H. (2015). Fabrication of nitrogen-doped graphite felts as positive electrodes using polypyrrole as a coating agent in vanadium redox flow batteries. *J. Mater. Chem. A* 3, 12276–12283. doi: 10.1039/C5TA02674A

Peinetti, A., Gilardoni, R., Mizrahi, M., Requejo, F., Gonzalez, G., and Battaglini, F. (2016). Numerical simulation of the diffusion processes in nanoelectrode arrays using an axial neighbor symmetry approximation. *Analyt. Chem.* 88, 5752–5759. doi: 10.1021/acs.analchem.6b00039

Ryu, J., Park, M., and Cho, J. (2016). Catalytic effects of B/N-co-doped porous carbon incorporated with Ketjenblack nanoparticles for all-vanadium redox flow batteries. *J. Electrochem. Soc.* 163, 5144–5149. doi: 10.1149/2.0191601jes

Smith, R. E., Davies, T. J., Baynes, N. d. B., and Nichols, R. J. (2015). The electrochemical characterization of graphite felts. *J. Electroanalyt. Chem.* 747, 29–38. doi: 10.1016/j.jelechem.2015.03.029

Suárez, D. J., González, Z., Blanco, C., Granda, M., Menéndez, R., and Santamaría, R. (2014). Graphite felt modified with bismuth nanoparticles as negative electrode in a vanadium redox flow battery. *ChemSusChem* 7, 914–918. doi: 10.1002/cssc.201301045

Tichter, T., Andrae, D., Mayer, J., Schneider, J., Gebhard, M., and Roth, C. (2019a). Theory of cyclic voltammetry in random arrays of cylindrical microelectrodes applied to carbon felt electrodes for vanadium redox flow batteries. *Phys. Chem. Chem. Phys.* 21, 9061–9068. doi: 10.1039/C9CP00548J

Tichter, T., and Schneider, J. (2019). Polarographica program. Available online at: https://github.com/Polarographica/Polarographica_program.

Tichter, T., Schneider, J., Andrae, D., Gebhard, M., and Roth, C. (2019b). Universal algorithm for simulating and evaluating cyclic voltammetry at macroporous electrodes by considering random arrays of microelectrodes. *Chem. Phys. Chem.* 21, 428–441. doi: 10.1002/cphc.201901113

Xiang, Y., and Daoud, W. A. (2019). Investigation of an advanced catalytic effect of cobalt oxide modification on graphite felt as the positive electrode of the vanadium redox flow battery. *J. Power Sources* 416, 175–183. doi: 10.1016/j.jpowsour.2019.01.079

Yang, D.-S., Han, J. H., Jeon, J. W., Lee, J. Y., Kim, D.-G., Seo, D. H., et al. (2019). Multimodal porous and nitrogen-functionalized electrode based on graphite felt modified with carbonized porous polymer skin layer for all-vanadium redox flow battery. *Mater. Today Energy* 11, 159–165. doi: 10.1016/j.mtener.2018.11.003

Zhang, Z., Xi, J., Zhou, H., and Qiu, X. (2016). KOH etched graphite felt with improved wettability and activity for vanadium flow batteries. *Electrochim. Acta* 218, 15–23. doi: 10.1016/j.electacta.2016.09.099

Zhong, S., and Skyllas-Kazacos, M. (1992). Electrochemical behaviour of vanadium(V)/vanadium(IV) redox couple at graphite electrodes. *J. Power Sources* 39, 1–9. doi: 10.1016/0378-7753(92)85001-Q

Zhou, H., Shen, Y., Xi, J., Qiu, X., and Chen, L. (2016). ZrO_2-nanoparticle-modified graphite felt: bifunctional effects on vanadium flow batteries. *Appl. Mater. Interfaces* 8, 15369–15378. doi: 10.1021/acsami.6b03761

Conflict of Interest: The authors declare that the research was conducted in the absence of any commercial or financial relationships that could be construed as a potential conflict of interest.

frontiers in Energy Research

ORIGINAL RESEARCH
published: 22 October 2020
doi: 10.3389/fenrg.2020.584654

Screening of Charge Carrier Migration in the $MgSc_2Se_4$ Spinel Structure

Manuel Dillenz[1], *Mohsen Sotoudeh*[1], *Holger Euchner*[2] *and Axel Groß*[1,2]*

[1] *Institute of Theoretical Chemistry, Ulm University, Ulm, Germany,* [2] *Helmholtz Institute Ulm (HIU) for Electrochemical Energy Storage, Ulm, Germany*

Periodic density functional theory calculations have been performed to study the migration of various charge carriers in spinel-type $MgSc_2Se_4$. This compound exhibits low barriers for Mg ion diffusion, making it a potential candidate for solid electrolytes in Mg-ion batteries. In order to elucidate the decisive factors for the ion mobility in spinel-type phases, the diffusion barriers of other mono- and multivalent ions (Li^+, Na^+, K^+, Cs^+, Zn^{2+}, Ca^{2+}, and Al^{3+}) in the $MgSc_2Se_4$ framework have been determined as well. This allows for disentangling structural and chemical factors, showing that the ion mobility is not solely governed by size and charge of the diffusing ions. Finally, our results suggest that charge redistribution and rehybridization caused by the migration of the multivalent ions increase the resulting migration barriers.

Keywords: electrochemical energy storage, batteries, multivalent ions, ion mobility, ion radius, spinel, computational chemistry, density functional theory

OPEN ACCESS

Edited by:
Kai S. Exner,
Sofia University, Bulgaria

Reviewed by:
Syed Muhammad Alay-e-Abbas,
Government College University Faisalabad, Pakistan
Sang Kyu Kwak,
Ulsan National Institute of Science and Technology, South Korea

***Correspondence:**
Axel Groß
axel.gross@uni-ulm.de

Specialty section:
This article was submitted to Electrochemical Energy Conversion and Storage, a section of the journal Frontiers in Energy Research

Received: *17 July 2020*
Accepted: *15 September 2020*
Published: *22 October 2020*

Citation:
Dillenz M, Sotoudeh M, Euchner H and Groß A (2020) Screening of Charge Carrier Migration in the $MgSc_2Se_4$ Spinel Structure. Front. Energy Res. 8:584654. doi: 10.3389/fenrg.2020.584654

1. INTRODUCTION

Due to the combination of potentially high capacity, increased safety and beneficial environmental aspects, batteries with multivalent charge carriers represent a promising alternative to lithium-ion technology. Through the pairing of metal anodes with high voltage cathodes, energy densities which exceed the current limits of lithium-ion batteries are likely to become possible (Elia et al., 2016; Canepa et al., 2017b). In addition, multivalent ion batteries appear to exhibit a low tendency for dendrite formation (Aurbach et al., 2001; Matsui, 2011; Jäckle et al., 2018; Stottmeister and Groß, 2020). Nevertheless, there are obstacles which need to be overcome for making multivalent batteries a viable alternative to the state of the art lithium-ion technology. One of the greatest challenges is the search for high voltage cathode materials which offer sufficient ion mobility. In fact, multivalent ions like Mg^{2+}, Zn^{2+}, and Ca^{2+} show very different ion mobility in structurally identical materials, which leads to identifying the charge carrier site preference as a criterion for good ion conductivity (Rong et al., 2015). Furthermore, the fact that compounds with high lithium-ion mobility tend to show poor multivalent ion mobility (Levi et al., 2009) complicates the search for suitable cathode materials. Spinel type phases are a class of materials which shows promising multivalent ion mobility (Rong et al., 2015). While showing good lithium-ion mobility, the spinel structure, moreover, offers a topology that is particularly well-suited for magnesium ion conduction.

Reversible intercalation of magnesium ions into oxide spinels could be verified (Kim et al., 2015; Yin et al., 2017) and several spinel phases were identified as suitable cathode materials (Liu et al., 2015; Bayliss et al., 2019). Interestingly, the ion conductivity of spinel materials can be further increased by moving towards sulfide (Emly and Van der Ven, 2015; Liu et al., 2016; Sun et al., 2016; Kulish et al., 2017) and selenide based (Canepa et al., 2017a; Wang et al., 2019; Koettgen et al., 2020) spinels. The volume per anion increases in the order of $O^{2-} < S^{2-} < Se^{2-}$ and is connected to a rising polarizability, which is beneficial for the cation mobility (Canepa et al., 2017a). Thus, materials like

the $MgSc_2Se_4$ spinel phase could be identified, exhibiting excellent migration barriers for magnesium ions of less than 0.4 eV (Canepa et al., 2017a; Wang et al., 2019). It has to be noted that the increased ion mobility in sulfides and selenides comes at the expense of a significantly decreased insertion potential which consequently results in a lower energy density of the battery. Hence, many spinel chalcogenides are rather unsuited for the use as cathode materials, however, they are interesting candidates for solid ionic conductors to enable all-solid-state multivalent ion batteries. Spinel materials have been investigated as cathode materials for several different multivalent charge carriers (Liu et al., 2015; Rong et al., 2015; Liu et al., 2016; Kulish et al., 2017). However, the origin of the vastly different migration barriers is still not fully understood. While the size and charge of the migrating cation clearly play a role, these properties alone are not sufficient to explain the differences in the diffusion barriers. In this study, migration barriers for a series of selected charge carriers in the $MgSc_2Se_4$ spinel are determined using periodic density functional theory calculations, aiming to reveal the factors that determine the observed differences in the ion migration.

2. COMPUTATIONAL DETAILS

Periodic density functional theory (Hohenberg and Kohn, 1964; Kohn and Sham, 1965) calculations are well-suited to reveal microscopic details of structures and processes in battery materials (Hörmann et al., 2015; Groß, 2018). Here we have used them to study the ASc_2Se_4 (A = Li, Na, K, Cs, Mg, Ca, Zn, and Al) spinel structure with a particular focus on the migration of the respective charge carriers "A." Exchange and correlation are considered within the generalized gradient approximation, employing the functional form as introduced by Perdew, Burke, and Ernzerhof (Perdew et al., 1996). The electron-core interactions are accounted for by the Projector Augmented Wave (Blöchl, 1994) method as implemented in the Vienna *Ab Initio* Simulation Package (Kresse and Hafner, 1993; Kresse and Furthmüller, 1996; Kresse and Joubert, 1999). The migration barriers of the charge carriers were determined using the climbing image Nudged Elastic Band (NEB) (Sheppard et al., 2008) method in the conventional 56 atom $1 \times 1 \times 1$ cubic unit cell of the spinel structure which corresponds to the primitive $2 \times 2 \times 2$ supercell. Brillouin zone sampling was performed using a $2 \times 2 \times 2$ k-point grid. Test calculations with $3 \times 3 \times 3$ and $4 \times 4 \times 4$ k-point grids resulted in differences of less than 0.5 meV per atom. A plane wave cutoff energy of 520 eV has been chosen. The electronic structure was converged within 1×10^{-6} eV. As only spinel structures with the d^0 transition metal Sc have been studied, it has not been necessary to consider spin-polarization effects. The NEB calculations have been carried out with four distinct images and all forces on the atoms were converged within 0.05 eV $Å^{-1}$. The migrating ions are separated by a minimum distance of more than 10 Å across periodic boundaries to minimize the resulting interactions (Sheppard et al., 2008).

3. RESULTS AND DISCUSSION

Spinel compounds crystallize in space group $Fd\bar{3}m$ with their characteristic AB_2X_4 stoichiometry (see **Figure 1A**). The anions 'X" ($X = O^{2-}, S^{2-}, Se^{2-}$) form a face-centered cubic lattice with the cation "A" in one eighth of the tetrahedral AX_4 interstices and the cation "B" in half of the octahedral BX_6 interstices. The AX_4 tetrahedra are connected by empty octahedra forming a percolating network in three dimensions. In order to migrate from one tetrahedral environment to the next, the ion has to pass through the triangular face shared by the tetrahedron and the empty octahedron (**Figure 1B**) which in most cases corresponds to the transition state of the diffusion process. Migration barriers of multivalent ions are generally significantly larger than those of their monovalent counterparts like Li^+ and Na^+. In fact, the migration barrier is largely determined by two factors, namely, the migration path topology–including the connectivity between sites and the size of the diffusion channels and intercalants–and the interaction strength between the intercalant and the host structure (Liu et al., 2016; Euchner et al., 2020). In this work, we aim at disentangling the migration path topology from the interaction strength to determine the factors which govern the latter one.

For this purpose, the relaxed cubic unit cell of the $MgSc_2Se_4$ spinel is taken as the starting point for a screening of selected charge carriers, namely Li^+, Na^+, K^+, Cs^+, Mg^{2+}, Zn^{2+}, Ca^{2+}, and Al^{3+}. To allow for direct comparison of the diffusion properties of the different charge carriers, a special set up has been chosen as a model system. While this model system can hardly be realized in experiment, it allows us to directly compare the results for the various charge carriers in the spinel structure. Thus we are able to derive trends in the migration barriers as a function of the properties of the migrating ion und thus to gain a deeper understanding of the factors underlying the ion mobility in the spinel structures. One Mg vacancy is introduced in the $MgSc_2Se_4$ supercell, and the structure is subsequently relaxed. Then, one of the neighboring Mg atoms is replaced by one of the charge carriers of interest, and a NEB calculation for a fixed host lattice is performed. Since the migration path topology, being of the form tetrahedral-octahedral-tetrahedral (tet-oct-tet), is symmetric, only the path from tetrahedral to octahedral coordination needs to be calculated. The corresponding minimum energy paths, as obtained by the NEB method, are shown in **Figure 2**. The energies are given relative to the charge carrier in the initial tetrahedral coordination environment and are mirrored with respect to the octahedral site in order to represent the full tet-oct-tet migration path. The site preference of the respective charge carrier can be readily deduced from the difference in energy of the octahedral and tetrahedral site.

These results indicate that Mg^{2+} and Li^+ show good ionic mobility with barriers below 0.5 eV, while the other charge carriers exhibit significantly higher barriers. Nevertheless, it should be noted that these barriers are obtained for fixed geometry, which allows for accessing the interaction type and strength of the different charge carriers with the host structure. In an actual compound, the host structure can adapt to the ion's

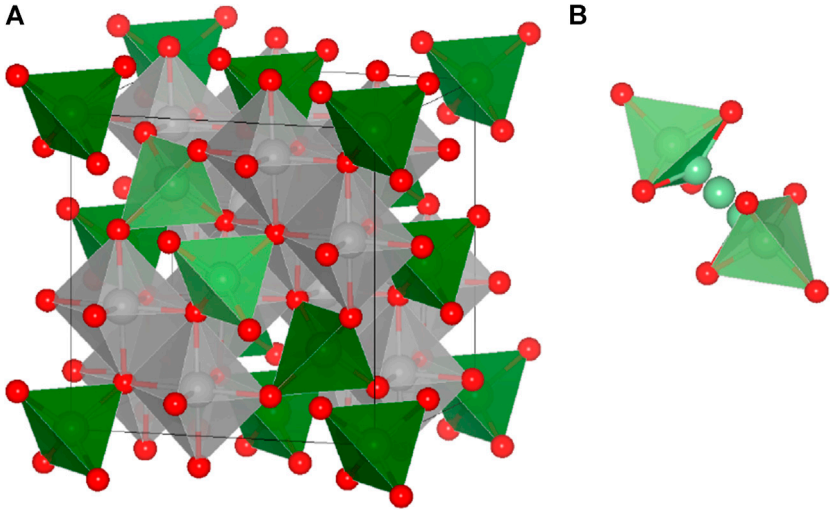

FIGURE 1 | (A) The AB_2X_4 spinel structure. The "X" anions (red) form a face-centered cubic lattice, the "B" cations (gray) are octahedrally coordinated, and the "A" cations (green) occupy tetrahedrally coordinated sites and **(B)** the schematic representation of a diffusion path between two adjacent tetrahedral sites (tet-oct-tet). The migration path of an exemplary tet-oct-tet diffusion event is indicated by the light green atoms.

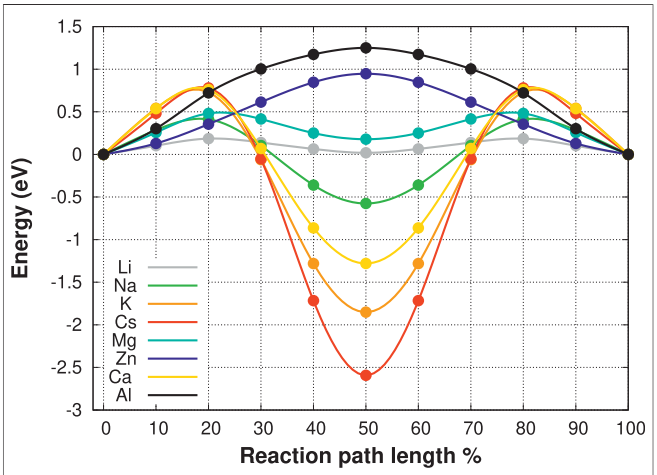

FIGURE 2 | The tet-oct-tet migration of possible charge carriers in the fixed $MgSc_2Se_4$ spinel structure without ionic relaxation. The energies are taken relative to the energy of the charge carrier in the tetrahedral coordination.

TABLE 1 | Lattice constants *a* and charge carrier selenium distances A-Se of the ASc2Se4 spinel structures. Crystal ionic radii for the charge carriers in tetrahedral environment are listed (Cs and Ca are typically not observed in tetrahedral coordination). For comparison the values for octahedral environment are given in brackets.

Spinel	*a* (Å)	A-Se (Å)	Crystal ionic radius (Shannon, 1976) (Å)
$LiSc_2Se_4$	11.11	2.53	0.73 (0.90)
$NaSc_2Se_4$	11.49	2.77	1.13 (1.16)
KSc_2Se_4	11.92	3.02	1.51 (1.52)
$CsSc_2Se_4$	12.24	3.21	–(1.81)
$AlSc_2Se_4$	11.03	2.44	0.53 (0.675)
$ZnSc_2Se_4$	11.08	2.49	0.74 (0.88)
$MgSc_2Se_4$	11.23	2.58	0.71 (0.860)
$CaSc_2Se_4$	11.59	2.79	–(1.14)

movement, and consequently the barriers are likely to decrease. Interestingly, our results show significant differences in the activation barriers and site preferences of the different charge carriers. Notably, for most charge carriers the difference in energy between the tetrahedral and octahedral coordination, responsible for the respective site preference, contributes significantly to the overall migration barrier. In the following this contribution is referred to as the static part of the migration barrier. Furthermore, apart from the static barrier the transition state energy varies significantly for the various charge carriers which can be interpreted as the kinetic contribution to the overall barrier. Both contributions need to be taken into account to fully understand the ion migration. First, we will focus on the dominant static barriers described by the site preference of the respective ion. In fact, the ratio of the cation to the Se^{2-} anion radii can be identified to exert a significant impact on the site preference. Large cations, such as Cs^+, K^+, and Ca^{2+}, strongly favor octahedral coordination, whereas small ions like Zn^{2+} and Al^{3+} prefer a tetrahedral environment. On the other hand, Zn^{2+}, Mg^{2+} and Li^+ exhibit very similar ionic radii but Zn^{2+} favors the tetrahedral site significantly while Mg^{2+} only shows a slight tetrahedral site preference.

As already stated, the size of the charge carrier ions can be quantified by their ionic radii (Koettgen et al., 2020). However, these ionic radii are obtained by employing a set of assumptions, including independence of the structure type. Furthermore, an ionic radius can only be assigned correctly if the respective ion shows purely ionic interactions with its surrounding. Therefore, the standard values for ionic radii are not necessarily an ideal quantity to reflect the bonding situation for a certain ion in a particular

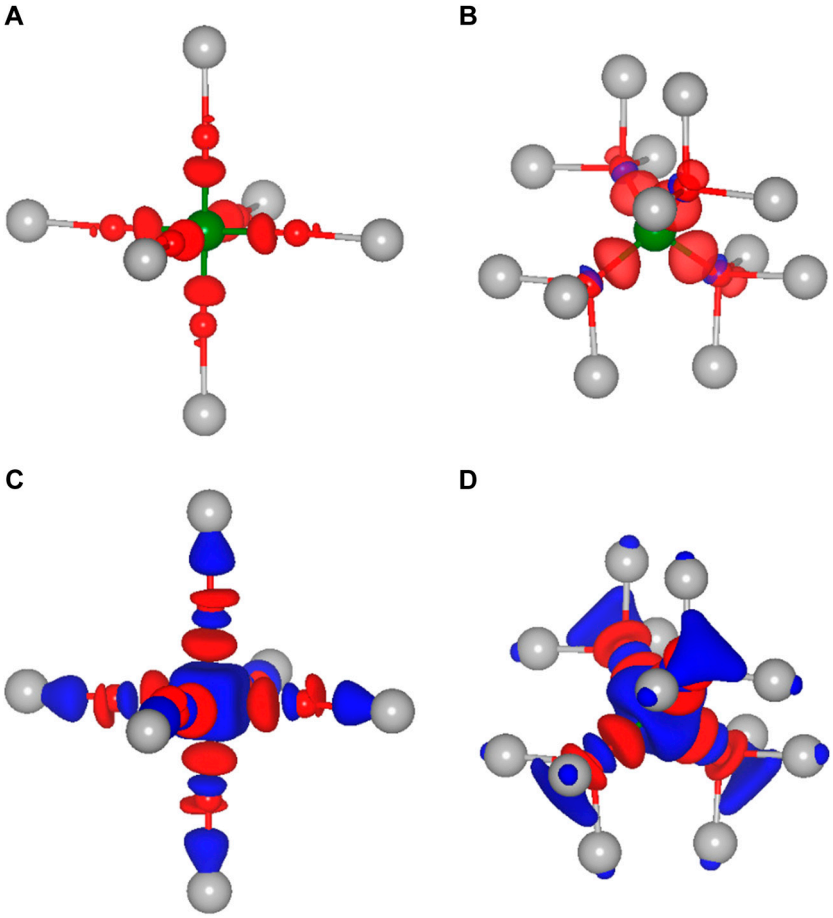

FIGURE 3 | Isosurfaces of the charge density difference of $MgSc_2Se_4$ structures in side view with the charge carrier **(A)** Li, **(C)** Al in octahedral coordination and **(B)** Li, **(D)** Al in tetrahedral coordination. Areas of charge depletion are shown in blue and areas of charge accumulation are shown in red.

structure. In order to get a better understanding of the true size of the charge carriers of interest in the spinel structure, the lattice constants for the full charge carrier spinels have been calculated. The obtained lattice constants and charge carrier selenium (A-Se) distances are given in **Table 1**. Indeed, the A-Se distances, which follow the same trend as the lattice constants, are in accordance with the site preference of the charge carriers observed in **Figure 2**. Here, the comparison between Mg^{2+} and Zn^{2+} is of particular interest. While the ionic radii are very similar for both ions, the actual A-Se distances are notably different. In fact, the Mg compound shows a significantly larger lattice constant and consequently larger A-Se distances. Furthermore, comparing the A-Se distances of Li^{+} and Mg^{2+} indicates that Li^{+} appears to be smaller and therefore an octahedral site preference for the Mg^{2+} ion should be expected. However, Mg^{2+} favors the tetrahedral site by about 0.2 eV. This points to the fact that apart from the dominating ion size, the charge and electronic structure additionally affect the site preference and therefore also the corresponding static contribution to the barriers. Nevertheless, if properly defined, the ion size strongly dominates the site preference and hence the resulting migration barriers. However, it has to be noted that all ASc_2Se_4 spinels, except for the Al and Zn spinel, show a certain degree of trigonal distortion that increases with the ion size. The trigonal distortion does not affect the coordination tetrahedron of the charge carrier "A" and only translates in a distortion of the coordination octahedron of the charge carrier "A" and the transition metal, respectively. This might have an influence on the lattice constant but leaves the A-Se distance essentially unaffected.

As already mentioned, not only the cation size is a crucial parameter for the site preference and therefore for the static part of the migration barriers, but obviously also the charge of the respective ion plays a vital role. Indeed, ions of almost the same size but different charge, e.g., Li^{+} and Mg^{2+} or Na^{+} and Ca^{2+}, differ significantly in their migration barrier. Higher charged ions show increased static contributions to the activation barriers for migration, which is mostly due to a significant energy difference between the tetrahedral and octahedral site. In order to understand the direct impact of the charge, it is necessary to obtain a better insight into the underlying interactions between the charge carriers and the surrounding anions. While most arguments are typically based on a fully ionic interaction between the charge carrier and the anion, many interactions actually have a considerable covalent component. To gain more insight into the chemistry of the A-X bonds, charge density

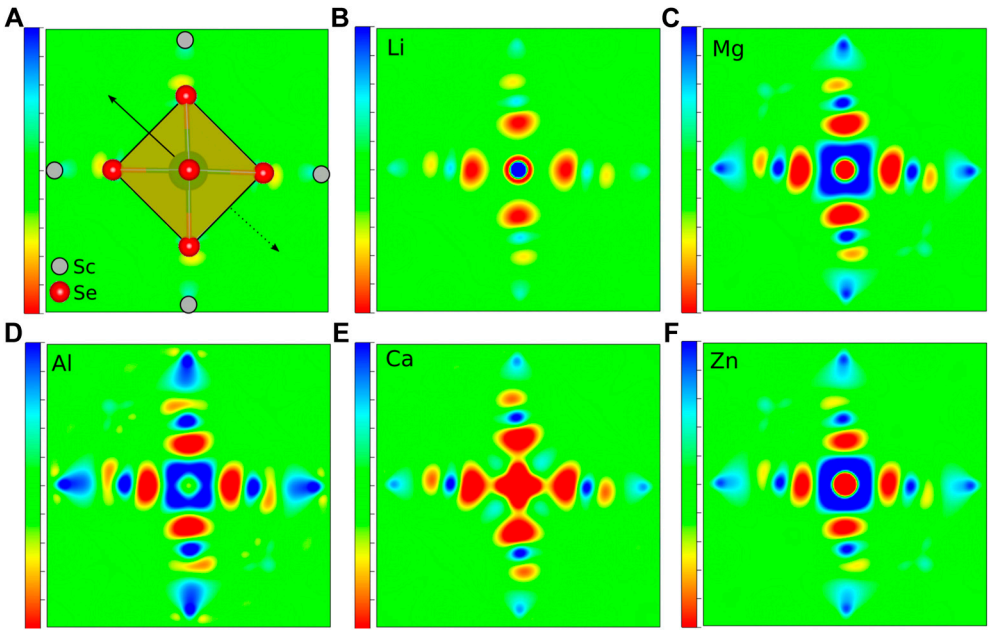

FIGURE 4 | Charge density difference contour plots of $MgSc_2Se_4$ structures with **(A)** a schematic presentation, **(B)** Li, **(C)** Mg, **(D)** Al, **(E)** Ca, and **(F)** Zn atoms in octahedral coordination. Areas of charge depletion are shown in blue and areas of charge accumulation are shown in red. The solid arrow indicates the displacement of the upper Se atom, while the dashed arrow shows the opposing shift of the Se atom below the plane.

difference plots have been created. The latter ones are obtained by subtracting both, the charge density of the isolated host structure and of the selected charge carrier from the charge density of the combined system. In order to illustrate the charge density differences, we have plotted isosurfaces for selected octahedral and tetrahedral environments in **Figure 3**. Moreover, **Figure 4** depicts contour plots of the octahedrally coordinated sites, showing the plane connecting four atoms of the Se octahedron, as illustrated in panel A. Only the most stable sites at high charge carrier concentration are considered, i.e., the tetrahedral and octahedral sites. Areas of charge depletion are shown in blue, and areas of charge accumulation are shown in red. It should be noted that the appearance of the isosurface plots depends strongly on the selected isosurface level (see **Supplementary Figure S1**). To allow for comparison, the same isosurface value was chosen for all panels in **Figure 3**. The charge densities are slightly distorted and do not show the full octahedral symmetry. This is a consequence of the trigonal distortion of the $MgSc_2Se_4$ spinel which slightly displaces the Se atoms in front of and behind the plane depicted in **Figure 4A**. Li is known to show mostly ionic interaction in the spinel structure, as can be inferred from **Figures 3**A,B**, 4**B.

Furthermore, the other alkaline metals show charge density differences very similar to the one of Li (**Supplementary Figures S2, S3**), with the charge density difference for K being even further smeared out. These charge density difference plots show mostly ionic bonding for the alkaline metals at the octahedral site, however, with a possibly increasing covalent character for the larger and softer ions. These findings are essentially the same for the tetrahedral site, as shown for the case of Li in **Figure 3B**.

In the case of the divalent charge carriers Mg and Zn, the same slight distortion is visible, however, additional strong charge depletion is observed in the vicinity of the charge carriers, as depicted in **Figures 4C, F**. For Ca, the isosurfaces are qualitatively very similar to the other divalent ions (**Supplementary Figure S4**). However, the charge depletion areas are less pronounced in the plane depicted in the contour plot, such that only a slight charge depletion is visible inside the octahedron, shown in light blue in **Figure 4E**. For Al, even more pronounced charge depletion is present (see **Figures 3C, D, 4D**). The charge depletion in the vicinity of the octahedron center, as observed for the multivalent ions, may be associated with the formation of an ionic bond and a greater interaction strength with the host lattice. This results in an increased oxidation of the Se atoms of the coordination octahedron upon deintercalation of the charge carrier. Essentially the same trend in terms of charge depletion around the charge carrier position is seen for the tetrahedral site, meaning additional charge depletion in the tetrahedron center for multivalent ions.

Most importantly, for the charge carrier at the octahedral site, the multivalent ions cause a significant charge depletion in the vicinity of the Sc atom next to the octahedron corners, however, without changing the Sc oxidation state. At the same time, a corresponding charge accumulates close to the Se atoms of the coordination octahedron. Hence, this may be understood as a polarization of the charge density of the Sc-Se bond due to the presence of the charge carrier. In contrast to the multivalent charge carriers, the alkaline metals hardly polarize the charge distribution of the Sc-Se bond, and therefore, at the transition metal. This is best seen when comparing the 3D plots for Li and Al (see **Figure 3**). In the case of multivalent ions, the charge distribution at the transition metal is strongly changed when

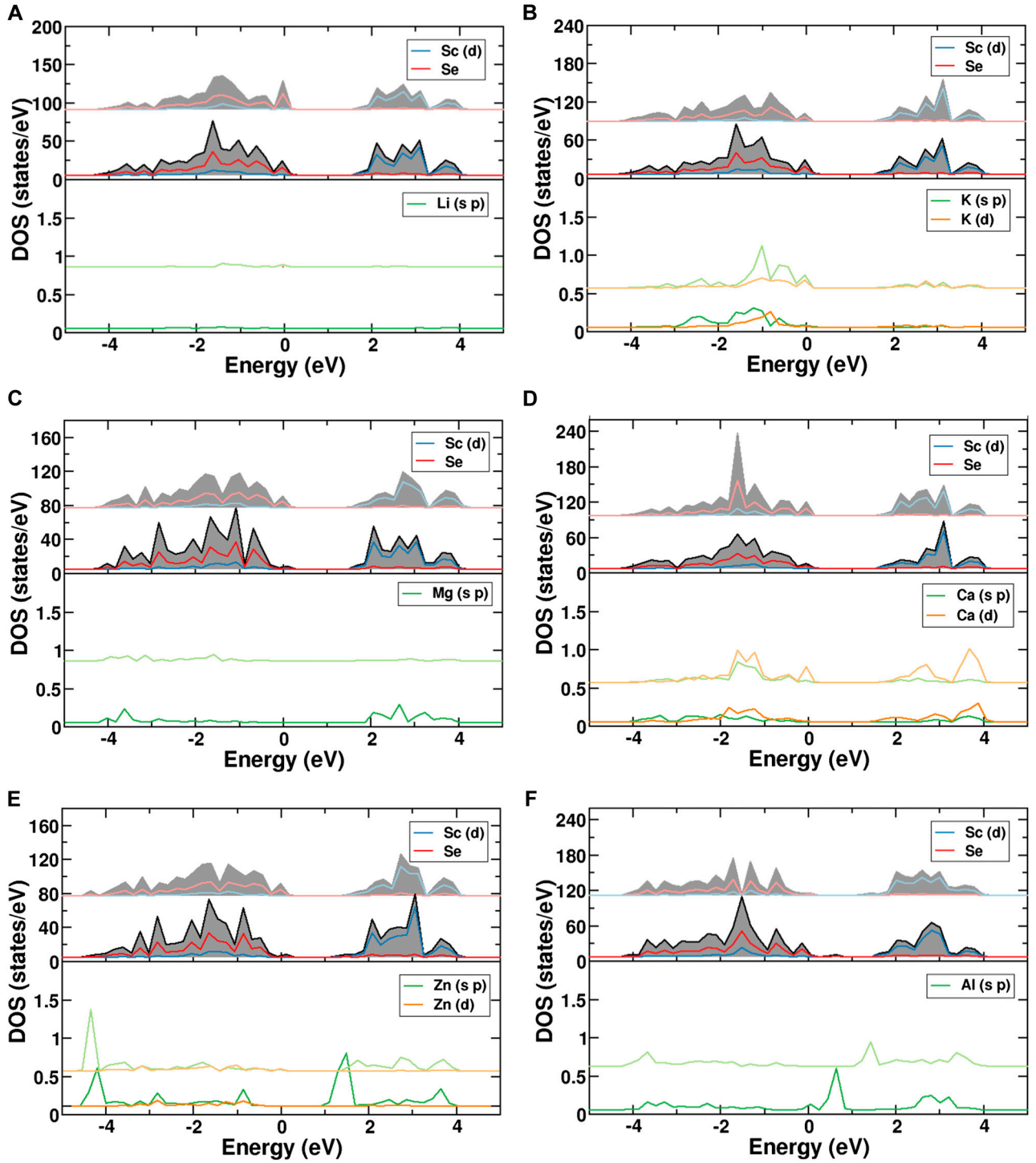

FIGURE 5 | PDOS of $MgSc_2Se_4$ with **(A)** Li, **(B)** K, **(C)** Mg, **(D)** Ca, **(E)** Zn, and **(F)** Al atoms in octahedral and tetrahedral coordination. The DOS of the ion in tetrahedral coordination (light color) is shifted upwards relative to the DOS of the ion in octahedral coordination (dark color).

moving from octahedral to tetrahedral coordination (see **Figures 3C, D**), and the charge depletion distributes over the twelve Sc atoms neighboring the tetrahedral site. For Al, an additional charge depletion between each Se atom of the tetrahedron and its three neighboring Sc atoms is observed. In general, this means that for the multivalent ions a strong charge redistribution takes place when moving from tetrahedral to octahedral site. Indeed, this confirms the findings of Levi et al. (2009) and Emly and Van der Ven (2015), that the reduced multivalent ion mobility in the spinel structure is not only a consequence of the ionic interaction

alone. Instead, the observed charge redistribution accompanied by rehybridization significantly increases the migration barriers.

Further understanding can be obtained from the partial density of states of the atoms divided into the respective *s*-, *p*- and *d*-components. The calculated density of states (DOS) for the investigated charge carriers on the octahedral and tetrahedral sites are shown in **Figure 5**. The filled valence band, which extends from −4 to 0 eV, is predominantly of Se-*p* character (red) with some contribution of Sc-*d* orbitals (blue). They represent the Sc-Se bonding states. The Sc-*d* states are located 1–4 eV above the valence band. The subfigures show the projected density of states for the migrating single-ion in the fixed framework. For the case of Li^+, **Figure 5A** reveals a negligible contribution of the cation to the valence band, confirming the purely ionic character. The same is true for Na^+ (see **Supplementary Figure S5**), whereas the other alkali metals show increasing contributions to the valence bands, confirming that the bonds become partially covalent. For instance, the DOS of K^+ indeed reveals an increased covalency as already suggested by the charge density differences (see **Figure 5B**). The same trend is observed in the case of Cs^+. Mg^{2+} on the other hand again shows only very small covalent contributions, while it increases for Ca^{2+}, such that the covalent character seems to increase with the ion size. Interestingly, the DOS for K^+ and Ca^{2+} show similar covalent contributions, while Na^+ and Mg^{2+} are almost fully ionic, thus pointing to the impact of the chemical character for elements in the same row. A similar tendency is again observed for Al^{3+} and Zn^{2+} which are small in size and show almost no or only small covalent interaction, respectively. Furthermore, it is interesting to note that for Al^{3+} (**Figure 5F**) and Zn^{2+} (**Figure 5E**), the projected density of states of the migrating ion depends on the coordination number. The lower coordination number shifts the *p*-orbital contributions near the Fermi level downwards. This displacement of the states means that the tetrahedral sites show increased hybridization and stronger bonding compared to the octahedral sites. This electronic rearrangement contributes to the fact, that Zn^{2+} and Al^{3+} ions strongly favor tetrahedral coordination.

So far, we have focused on the site preference and the respective static barrier as the dominating part of the overall migration barrier. Yet, also the transition state dominated kinetic part contributes significantly to the overall migration barrier. As already mentioned earlier, the transition state constitutes a threefold coordination environment of the ion, making it the bottleneck of the migration. While readily describing the site preference, the ion size also shows a strong impact on the energy of the transition state. For the small ions Zn^{2+} and Al^{3+} the threefold coordination environment does not strongly influence the energetics of the ion migration and the difference between octahedral and tetrahedral site readily determines the overall barrier. The energy of the transition state of the other investigated charge carriers, with respect to the tetrahedral site energy, mostly increases with the size of the ion. However, further in-depth examination of the transition state energy reveals that the charge and the electronic structure have a significant influence on the kinetic part of the migration barrier. Thus, relative to the tetrahedral site, Mg^{2+} and the much larger Na^+ ions show similar transition state energies and so do Ca^{2+} and the much larger K^+ and Cs^+ ions.

In order to conclude our thorough study on the charge carrier mobility in the spinel structure, we compare our findings with the materials design rules for multivalent ion mobility developed by Rong et al. (2015). These guidelines state that high multivalent ion mobility is, in first order, determined by the site preference of the charge carrier. However, they conclude that the ion size described by the respective ionic radii is not a useful descriptor to estimate the ion mobility. Our findings strongly support the importance of the site preference for multivalent ion mobility, yet, show that a properly defined ion size actually is a good descriptor for the site preference. In addition, our findings indicate that multivalent ions show a certain degree of covalency, which causes rehybridization and charge redistribution along the migration path, resulting in increased overall migration barriers. Thus, the importance of the site preference remains undoubtful and is predominantly influenced by the ion size. Additionally, the ion size affects the transition state energy and thus small ions are favorable. At last the covalent character of the interactions increases the barriers and mostly ionic interaction is highly favorable. Comparing our results for the various charge carriers indicates that Zn^{2+} and Al^{3+} are of small size and only show very limited covalent character. Thus if the site preference of these charge carriers could be positively affected, e.g., by doping the Sc gate sites by other (transition) metals (Xiao et al., 2018), a high ion mobility for the Zn^{2+} ion seems possible.

4. CONCLUSION

In this work, we have investigated the migration barriers for various mono and multivalent ions (Li^+, Na^+, K^+, Cs^+, Zn^{2+}, Ca^{2+}, and Al^{3+}) in the spinel-type $MgSc_2Se_4$ phase. We find that both the size and the charge of the cations strongly influence the height of the migration barriers. However, our findings indicate that crystal ionic radii are not suitable to describe the ion size in the spinel structure, instead A-Se distances are suggested for a more accurate description. Using this descriptor, the ion size is found to determine the site preference of the ion and the resulting diffusion barrier in first order. However, the transition state energy is also influenced by the ion size, but here the impact of the charge and bonding characteristics appears to be more pronounced. Indeed, calculated charge density distributions and electronic densities of state reveal the essence of the bonding character which is necessary to be taken into account to fully understand the migration barriers. We find that Li^+ and Na^+ are purely ionic in this framework, while other ions show different degrees of partially covalent bonding. Our results indicate that the ion size, when properly defined, indeed can be applied to estimate the order of the migration barriers in the spinel structure. Nevertheless, an in-depth understanding can only be obtained when the influence of the charge and the electronic structure are incorporated. Thus, the simple concept of purely ionic charge carriers only yields limited understanding of the multivalent ion migration in the spinel structure, additionally rehybridization and the charge density redistribution that modify the migration

barriers need to be considered. Furthermore, our results indicate that tuning the site preference of Zn^{2+} could lead to superior ion mobility in the spinel structure. Specifically, we shed light on the role of the ionic size, the charge and the bonding character of the mobile ions. Therefore, our calculations identified factors that are applicable to fast ion migration in a broad range of energy storage techniques.

DATA AVAILABILITY STATEMENT

The raw data supporting the conclusions of this article will be made available by the authors, without undue reservation.

AUTHOR CONTRIBUTIONS

MD performed the bulk of the DFT calculations, additional calculations were performed by MS who was also instrumental in the analysis of the computational output. AG designed and together with HE supervised the project. MD, MS, and HE wrote the first version of the manuscript. All authors revised the manuscript, and read and approved the submitted version.

FUNDING

Computer time provided by the state of Baden-Württemberg through the bwHPC project and the German Research Foundation (DFG) through grant no INST 40/467-1 FUGG (JUSTUS cluster) is gratefully acknowledged. This work contributes to the research performed at Center for Electrochemical Energy Storage Ulm-Karlsruhe (CELEST) and was funded by the German Research Foundation (DFG) under Project ID 390874152 (POLiS Cluster of Excellence).

ACKNOWLEDGMENTS

MD thanks Sung Sakong and Mohnish Pandey for fruitful discussions.

SUPPLEMENTARY MATERIAL

The Supplementary Material for this article can be found online at: https://www.frontiersin.org/articles/10.3389/fenrg.2020.584654/full#supplementary-material

REFERENCES

Aurbach, D., Cohen, Y., and Moshkovich, M. (2001). The study of reversible magnesium deposition by *in situ* scanning tunneling microscopy. *Electrochem. Solid State Lett.* 4, A113. doi:10.1149/1.1379828

Bayliss, R. D., Key, B., Sai Gautam, G., Canepa, P., Kwon, B. J., Lapidus, S. H., et al. (2019). Probing mg migration in spinel oxides. *Chem. Mater.* 32 (2), 663–670. doi:10.1021/acs.chemmater.9b02450

Blöchl, P. E. (1994). Projector augmented-wave method. *Phys. Rev. B* 50, 17953–17979. doi:10.1103/physrevb.50.17953

Canepa, P., Bo, S. H., Gautam, G. S., Key, B., Richards, W. D., Shi, T., et al. (2017a). High magnesium mobility in ternary spinel chalcogenides. *Nat. Comm.* 8, 1–8. doi:10.1038/s41467-017-01772-1

Canepa, P., Sai Gautam, G., Hannah, D. C., Malik, R., Liu, M., Gallagher, K. G., et al. (2017b). Odyssey of multivalent cathode materials: open questions and future challenges. *Chem. Rev.* 117, 4287–4341. doi:10.1021/acs.chemrev.6b00614

Elia, G. A., Marquardt, K., Hoeppner, K., Fantini, S., Lin, R., Knipping, E., et al. (2016). An overview and future perspectives of aluminum batteries. *Adv. Mater.* 28 (35), 7564–7579. doi:10.1002/adma.201601357

Emly, A., and Van der Ven, A. (2015). Mg intercalation in layered and spinel host crystal structures for mg batteries. *Inorg. Chem.* 54, 4394–4402. doi:10.1021/acs.inorgchem.5b00188

Euchner, H., Chang, J. H., and Groß, A. (2020). On stability and kinetics of Li-rich transition metal oxides and oxyfluorides. *J. Mater. Chem.* 8, 7956–7967. doi:10.1039/d0ta01054e

Groß, A. (2018). Fundamental challenges for modeling electrochemical energy storage systems at the atomic scale. *Top. Curr. Chem.* 376, 17. doi:10.1007/s41061-018-0194-3

Hohenberg, P., and Kohn, W. (1964). Inhomogeneous electron gas. *Phys. Rev.* 136, B864–B871. doi:10.1103/PhysRev.136.B864

Hörmann, N. G., Jäckle, M., Gossenberger, F., Roman, T., Forster-Tonigold, K., Naderian, M., et al. (2015). Some challenges in the first-principles modeling of structures and processes in electrochemical energy storage and transfer. *J. Power Sources* 275, 531–538. doi:10.1016/j.jpowsour.2014.10.198

Jäckle, M., Helmbrecht, K., Smits, M., Stottmeister, D., and Groß, A. (2018). Self-diffusion barriers: possible descriptors for dendrite growth in batteries?. *Energy Environ. Sci.* 11 (12), 3400–3407. doi:10.1039/C8EE01448E

Kim, C., Phillips, P. J., Key, B., Yi, T., Nordlund, D., Yu, Y.-S., et al. (2015). Direct observation of reversible magnesium ion intercalation into a spinel oxide host. *Adv. Mater.* 27, 3377–3384. doi:10.1002/adma.201500083

Koettgen, J., Bartel, C. J., and Ceder, G. (2020). Computational investigation of chalcogenide spinel conductors for all-solid-state mg batteries. *Chem. Commun.* 56, 1952–1955. doi:10.1039/c9cc09510a

Kohn, W., and Sham, L. J. (1965). Self-consistent equations including exchange and correlation effects. *Phys. Rev.* 140, A1133–A1138. doi:10.1103/PhysRev.140.A1133

Kresse, G., and Furthmüller, J. (1996). Efficient iterative schemes forab initiototal-energy calculations using a plane-wave basis set. *Phys. Rev. B* 54, 11169–11186. doi:10.1103/PhysRevB.54.11169

Kresse, G., and Hafner, J. (1993). Ab initiomolecular dynamics for liquid metals. *Phys. Rev. B* 47, 558–561. doi:10.1103/PhysRevB.47.558

Kresse, G., and Joubert, D. (1999). From ultrasoft pseudopotentials to the projector augmented-wave method. *Phys. Rev. B* 59, 1758–1775. doi:10.1103/PhysRevB.59.1758

Kulish, V. V., Koch, D., and Manzhos, S. Aluminium and magnesium insertion in sulfur-based spinels: a first-principles study (2017). *Phys. Chem. Chem. Phys.* 19, 6076–6081. doi:10.1039/c6cp08284j

Levi, E., Levi, M. D., Chasid, O., and Aurbach, D. A review on the problems of the solid state ions diffusion in cathodes for rechargeable Mg batteries (2009). *J. Electroceram.* 22, 13–19. doi:10.1007/s10832-007-9370-5.

Liu, M., Jain, A., Rong, Z., Qu, X., Canepa, P., Malik, R., et al. (2016). Evaluation of sulfur spinel compounds for multivalent battery cathode applications. *Energy Environ. Sci.* 9, 3201–3209. doi:10.1039/c6ee01731b

Liu, M., Rong, Z., Malik, R., Canepa, P., Jain, A., Ceder, G., et al. (2015). Spinel compounds as multivalent battery cathodes: a systematic evaluation based on ab initio calculations. *Energy Environ. Sci.* 8, 964–974. doi:10.1039/c4ee03389b

Matsui, M. (2011). Study on electrochemically deposited mg metal. *J. Power Sources* 196, 7048–7055. doi:10.1016/j.jpowsour.2010.11.141

Perdew, J. P., Burke, K., and Ernzerhof, M. (1996). Generalized gradient approximation made simple. *Phys. Rev. Lett.* 77, 3865–3868. doi:10.1103/PhysRevLett.77.3865.

Rong, Z., Malik, R., Canepa, P., Sai Gautam, G., Liu, M., Jain, A., et al. (2015). Materials design rules for multivalent ion mobility in intercalation structures. *Chem. Mater.* 27, 6016–6021. doi:10.1021/acs.chemmater.5b02342

Shannon, R. D. (1976). Revised effective ionic radii and systematic studies of interatomic distances in halides and chalcogenides. *Acta. Cryst.* A32, 751–767. doi:10.1107/s0567739476001551

Sheppard, D., Terrell, R., and Henkelman, G. (2008). Optimization methods for finding minimum energy paths. *J. Chem. Phys.* 128, 134106. doi:10.1063/1.2841941

Stottmeister, D., and Groß, A. (2020). Strain dependence of metal anode surface properties. *ChemSusChem* 13, 3147–3153. doi:10.1002/cssc.202000709

Sun, X., Bonnick, P., Duffort, V., Liu, M., Rong, Z., Persson, K. A., et al. (2016). A high capacity thiospinel cathode for mg batteries. *Energy Environ. Sci.* 9, 2273–2277. doi:10.1039/c6ee00724d

Wang, L. P., Zhao-Karger, Z., Klein, F., Chable, J., Braun, T., Schür, A. R., et al. (2019). MgSc 2 Se 4 -A magnesium solid ionic conductor for all-solid-state Mg batteries?. *ChemSusChem* 12, 2286–2293. doi:10.1002/cssc.201900225

Xiao, W., Xin, C., Li, S., Jie, J., Gu, Y., Zheng, J., et al. (2018). Insight into fast Li diffusion in Li-excess spinel lithium manganese oxide. *J. Mater. Chem.* 6, 9893–9898. doi:10.1039/c8ta01428k

Yin, J., Brady, A. B., Takeuchi, E. S., Marschilok, A. C., and Takeuchi, K. J. (2017). Magnesium-ion battery-relevant electrochemistry of $MgMn_2O_4$: crystallite size effects and the notable role of electrolyte water content. *Chem. Commun.* 53, 3665–3668. doi:10.1039/c7cc00265c

Conflict of Interest: The authors declare that the research was conducted in the absence of any commercial or financial relationships that could be construed as a potential conflict of interest.

frontiers in Energy Research

ORIGINAL RESEARCH
published: 26 November 2020
doi: 10.3389/fenrg.2020.604799

Impact of Solvation on the Structure and Reactivity of the Co_3O_4 (001)/H_2O Interface: Insights From Molecular Dynamics Simulations

T. Kox[1]*, *E. Spohr*[1,2]* and *S. Kenmoe*[1]*

[1]Department of Theoretical Chemistry, University of Duisburg-Essen, Essen, Germany, [2]Center of Computational Science and Simulation, University of Duisburg-Essen, Essen, Germany

The spinel Co_3O_4 has many beneficial properties for potential use in catalysis. In operando, water is always present and alters the properties of the catalyst. We have used ab initio molecular dynamics to understand the effect of water and solvation on the structure and reactivity of the Co_3O_4 (001) A-type and B-type surface terminations. Water adsorbs on both terminations via a partial dissociative mode, and the A-termination is seen to be more reactive. On this surface, a higher degree of dissociation is observed in the topmost layers of the crystal in contact with water. Water dissociates more frequently on the Co^{2+} sites (about 75%) than on the adjacent Co^{3+} sites, where the degree of dissociation is about 50%. Increasing water coverage does not change the degree of water dissociation significantly. OH^- adsorption on the Co^{2+} sites leads to a reduction of the amount of reconstruction and relaxation of the surface relative to the clean surface at room temperature. Proton transfer within the water films and between water molecules and surface has localized character. The B-terminated interface is less dynamic, and water forms epitactic layers on top of the Co^{3+} sites, with a dissociation degree of about 25% in the contact layer.

Keywords: solvation, reactivity, ab initio molecular dynamics, surface termination, coordination number, Cobalt oxide, Spinel

OPEN ACCESS

Edited by:
Jun Huang,
Central South University, China

Reviewed by:
Mohammad J. Eslamibidgoli,
Forschungszentrum Jülich, Germany
Zhengda He,
Helmholtz Association of German Research Centers (HZ), Germany

***Correspondence:**
T. Kox
tim.kox@uni-due.de
E. Spohr
eckhard.spohr@uni-due.de
S. Kenmoe
stephane.kenmoe@uni-due.de

Specialty section:
This article was submitted to Electrochemical Energy Conversion and Storage, a section of the journal Frontiers in Energy Research

Received: *10 September 2020*
Accepted: *21 October 2020*
Published: *26 November 2020*

Citation:
Kox T, Spohr E and Kenmoe S (2020) Impact of Solvation on the Structure and Reactivity of the Co_3O_4 (001)/H_2O Interface: Insights From Molecular Dynamics Simulations. Front. Energy Res. 8:604799. doi: 10.3389/fenrg.2020.604799

INTRODUCTION

Recent years have witnessed a rise of interest for heterogeneous catalysis in the liquid phase. Its paramount importance in industrial chemical process technology has prompted intense efforts to gain an atomistic-level understanding of the fundamental process steps. Due to their abundance, the use of transition metal oxides as heterogeneous catalysts is seen as an important low-cost alternative to costly noble metal-based ones. Unlike in the latter case, deep insight into the interplay of factors defining the activity and selectivity of metal oxide catalysts is still missing. More knowledge is still required about the different factors governing their efficiency in order to allow their rational design and application. Several metal oxides have been found relevant for catalysis, and their interactions with water have captured particular attention as water is always present in operando. Co_3O_4 is one of them, as it shows electronic, magnetic and redox properties that make it a potential candidate for many catalytic reactions. For example, Co_3O_4 nanoparticles have been successfully used for water and carbon monoxide oxidation, selective 2-propanol oxidation, or steam reforming of ethanol (Llorca et al., 2004; Deng and Tüysüz, 2014; Anke et al., 2019; Cai et al., 2019).

Zasada and co-workers combined DFT calculations and high resolution scanning transmission electron microscopy (HRSTEM) to investigate the structure and shape of cobalt spinel nanostructures (Zasada et al., 2011). Their calculations of surface energies predicted the following order of stability for the low index facets: (001) >(111) >(110), in agreement with Montoya et al., (2011) who came to the same conclusion in a separate DFT study. Based on these surfaces energies, a Wulff construction was applied to predict the shape of nanoparticles. They showed rhombicuboctahedral grains exposing mainly the (001) and (111) facets, with a percentage of exposure of 48% and 41%, respectively, and the (101) facet with a minor percentage of 11%. These predictions compared well with HRSTEM images of synthesized spinel nanocrystals. The impact of the vapor pressure of water on the equilibrium shape of the nanoparticles was studied by Zasada et al. (2010). Their study reports no faceting transformation upon water adsorption, and the percentage of exposure of the least stable (110) facet is slightly increased to 14%. The presence of water (in the submonolayer and monolayer regime) slightly changes the relative abundance of exposure between the (001) and (111) facets to 39% and 47%, respectively. However, as mentioned in the same study, the (001) facet remains the most attractive to catalyse liquid phase processes. The reason is that on the (111) facet, because of the highly unsaturated nature of the surface Co ions, water molecules do not desorb even at elevated temperatures of more than 450°C, which implies that water may block active sites and inhibit catalytic processes taking place at lower temperatures.

To enhance the catalytic response of Co_3O_4 nano-catalysts, several recipes have been proposed over the years to allow a selective exposure of the more reactive crystal facets for particular catalytic reactions(Sun et al., 2013). Depending on the recipe, Co_3O_4 nanoparticles assume the shapes of nanocubes, octahedrons, or nanorods, exposing, respectively, the (001), the (111), or the (101) facets only. These nanoparticle shapes were proven to be beneficial for many catalytical reactions such as hydrodesulfurization of carbonyl sulfide (Wang et al., 2011) or ethylene oxidation(Ma et al., 2010). For these reactions, the least-exposed (110) facet was found to be the most reactive one, and, therefore, the reaction was found to be selectively promoted on nanorods. Observations of this nature have motivated studies on the interaction between this particular facet and water (Xu and Li, 2011; Chen and Selloni, 2012; Creazzo et al., 2019), which have provided some atomistic understanding of the water monolayer regime (Chen and Selloni, 2012) and, very recently, also the inferface with liquid water (Creazzo et al., 2019), under electrochemical conditions.

Unlike for the (110) surface, atomic-level information for the (001)/H_2O interface of Co_3O_4 is scarce, although this facet is reported as being the most stable one and the most relevant for many catalytical reactions. To our knowlegde, only an early attempt by Zasada et al. has been made to understand the water sub- and monolayer adsorption regime on an oxygen-poor Co_3O_4 surface(Zasada et al., 2010). Thus, several open issues need to be addressed for the (001) surface. The current paper aims at providing insight into the structure and reactivity of the (001) surface upon water adsorption. We use ab initio molecular dynamics simulations to study the following properties of interfacial water: 1) the active binding sites, 2) the adsorption mode, 3) the degree of dissociation, 4) the fundamental interactions that stabilize the adsorption layer, 5) the structural response of the substrate and 6) the hydrogen bond network. Specifically, we have studied the impact of increasing water content between 16 and 32 water molecules on the A-terminated surface, which contains 16 formal Co^{3+} and eight formal Co^{3+} ions, and on the B-terminated surface with 16 formal Co^{2+} ions, and we compared these simulations with room temperature simulations of the water-free systems.

COMPUTATIONAL DETAILS

Co_3O_4 crystallises in a spinel structure with a face-centered cubic unit cell. The primitive unit cell contains 14 atoms (2 Co^{2+}, 4 Co^{3+}, and 8 O^{2-}). Four such primitive cells form the conventional face-centered cubic unit cell of the antiferromagnetic spinel structure (Chen et al., 2011), consisting of 56 atoms (8 Co^{2+}, 16 Co^{3+}, and 32 O^{2-} ions). When cutting the bulk in the (001) direction, two (001) surfaces are possible for different termination layers. A surface layer of 16 Co^{3+} ions forms the B-terminated structure. Slightly above this layer, an additional layer containing 8 Co^{2+} ions forms the A-termination. **Figure 1** shows side-views of the two terminations. Note the exposed (green) Co^{2+} ions on the A-terminated surface (top figure), whereas the Co^{3+} ions (purple) are, on both ideal surfaces, embedded in the top-most oxygen layer.

The Co_3O_4 (001) surfaces were modeled as slabs of 11 and 13 atomic layers for A- and B-termination, respectively. The choice of non-stoichiometric slabs with an odd number of layers was motivated by the requirement that two equivalent surfaces on top and bottom minimize the dipole moment within the supercell, at least in the water-free case. The atoms in the bottom five or six slab layers were kept immobile at their bulk positions for A- and B-termination (see **Figure 1**). All other atoms were free to move. Orthorhombic supercells with (2 × 2) periodicity in the lateral directions (x,y) and dimensions 16.18 Å × 16.18 Å × 24.9 Å and 16.18 Å × 16.18 Å × 27.2 Å for the A- and B-terminated surfaces, respectively, were used to study the interaction of water films with the slabs. Water molecules were adsorbed asymmetrically only on the (mobile) top surface and an additional vacuum region of at least 10 Å thickness was introduced, resulting in the box dimensions as given above. All calculations were performed at the Γ point. Because of the asymmetry imposed by adsorption and the constrained atoms in the bottommost layers, a dipole correction was applied to cancel the electric field gradient in the vacuum.

Spin polarized Born-Oppenheimer molecular dynamics (MD) simulations were performed using the CP2K/Quickstep package (The CP2K developers group, 2016). The Generalized Gradient Approximation (GGA) within its PBE formulation (Perdew et al., 1996) was used to treat the exchange correlation effects. For a more efficient description of dispersion interactions, particularly in the water films, the Grimme D3 correction was added to the PBE exchange-correlation functional (Grimme et al., 2010). A

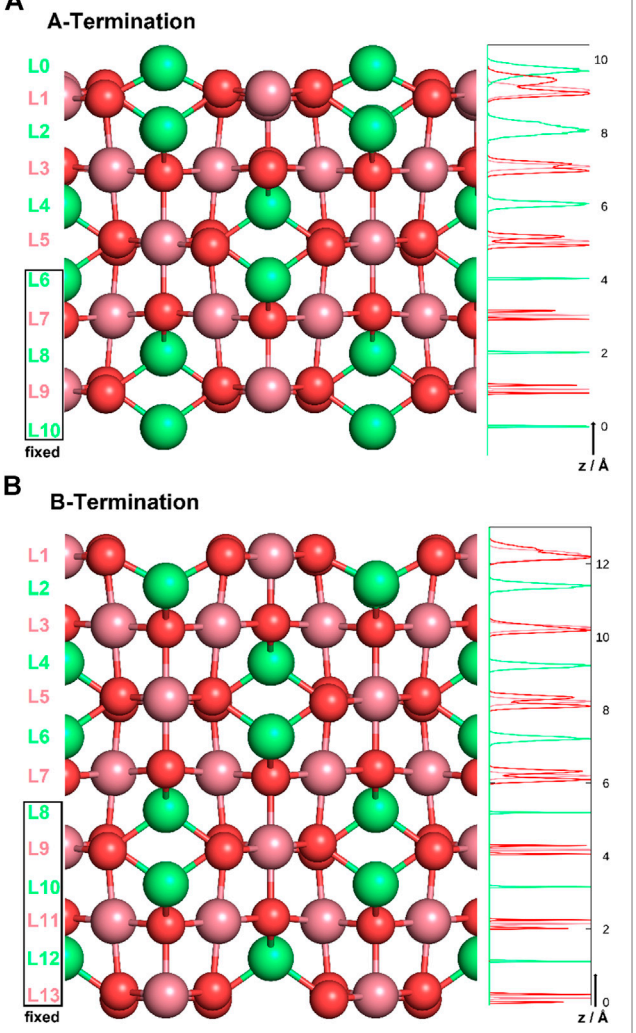

Figure 1 | A- (top) and B-terminations (bottom) of the Co_3O_4 (001) surface. Co^{2+} ions are shown in green, Co^{3+} in purple, oxygen in red. On the left, various layers are defined, and atom density profiles along the z axis are shown on the right. Layers L6-L10 and L8-L13 were kept rigid in all studies of A- and B-terminated surfaces, respectively.

Hubbard correction (Hubbard and Flowers, 1963) term (U) was added for a correct description of Co 3d states. In a previous study, different U values have been used for Co_3O_4. These values strongly depend on the computational procedure (Chen et al., 2011; Montoya et al., 2011; Chen and Selloni, 2012; Creazzo et al., 2019). For our system, the Hubbard correction was set to $U = 2$ eV. With this value, the calculated band gap (1.6 eV) agrees well with experiment (Kim and Park, 2013; Shinde et al., 2006). The 3 s, 3 p, 3 d, and 4 s electrons of Co atoms and the 2 s and 2 p electrons of O atoms were considered as valence electrons, and the Goedecker-Teter-Hutter (GTH) pseudopotentials were utilized to treat the core electrons. The mixed-repesentation basis sets consist of double-ζ quality local basis functions with one set of polarization functions (DZVP), together with plane waves with a cutoff of 500 Ry.

A Nosé-Hoover thermostat with a target temperature of 300 K and a time constant of 1 ps was used to impose NVT conditions on the system. A time step of 0.5 fs was used to propagate the Born-Oppenheimer molecular dynamics trajectories. Total simulation time was 20 ps for the water-covered films (after which the system reaches thermal equilibrium, see **Supplementary Figure S1**) and 10 ps for the water-free systems.

RESULTS AND DISCUSSIONS

Water-Induced Relaxation

We first studied the structural response of the A- and B-terminated substrates to water adsorption. The clean surfaces were taken as references. **Figure 2** shows each clean surface termination before and after a 10 ps MD run at room temperature.

A-Termination

Figure 2 shows that the A-terminated water-free surface undergoes reconstruction at room temperature. The relaxation to the final structure is almost instantaneous at the begin of the simulation. The reconstructed A-terminated surface evolves from the unreconstructed one by (green) Co^{2+} ions moving along the diagonal rows in the direction to one of the empty sites. The occupation of these four-fold hollow sites has already been reported by Montoya et al. (2011). **Figure 3A** shows the radial distribution function (RDF) of the surface oxygen atoms (those in the L1 layer) to the outermost Co^{2+} ions in layer L0 (see **Figure 1**). At 300 K, the first maximum of the RDF shifts towards larger distances from the corresponding bulk crystal value of 1.95 Å (black curve). The shift is largest for the clean surface (grey), and is smaller, when water is present. In the presence of water, the reconstruction of the A-terminated surface (**Figure 2B**) is lifted and the final surface positions look similar to the ones in **Figure 2A** again (not shown), with some minor relaxations. On all A-terminated surfaces, the RDF in **Figure 3A** shows a diffuse distance spectrum in the range up to about 3 Å, irrespective of actual degree of relaxation and reconstruction, and independent of water coverage. The RDF between surface oxygens and Co^{3+} ions in layer L1 (**Figure 3B**) shows a similar behavior of the first peak on the surface relative to the bulk, namely a broadening and large shift in the water-free case and smaller shifts and broadening in the hydrated case, with no significant dependence on water content.

The calculated average coordination numbers (defining the cut-off distance as 2.3 Å and averaging over the last half of the simulations, see **Supplementary Figure S2** for illustration) of Co^{2+} ions in L0 and Co^{3+} ions in L1 reveal the reason for the lifting of the reconstruction upon water adsorption. Relative to the ideal bulk lattice, coordination in the L0 layer of the water-free surface increases from 2 to 3.5, while the coordination in L1 (Co^{3+}) is reduced slightly from 5 to 4.9. With the adsorption of 16 water molecules, which mostly (see below) solvate the Co^{3+} ions in L1, the coordination number in L1 increases to 5.6, at the expense of a slight reduction of the average coordination in L0

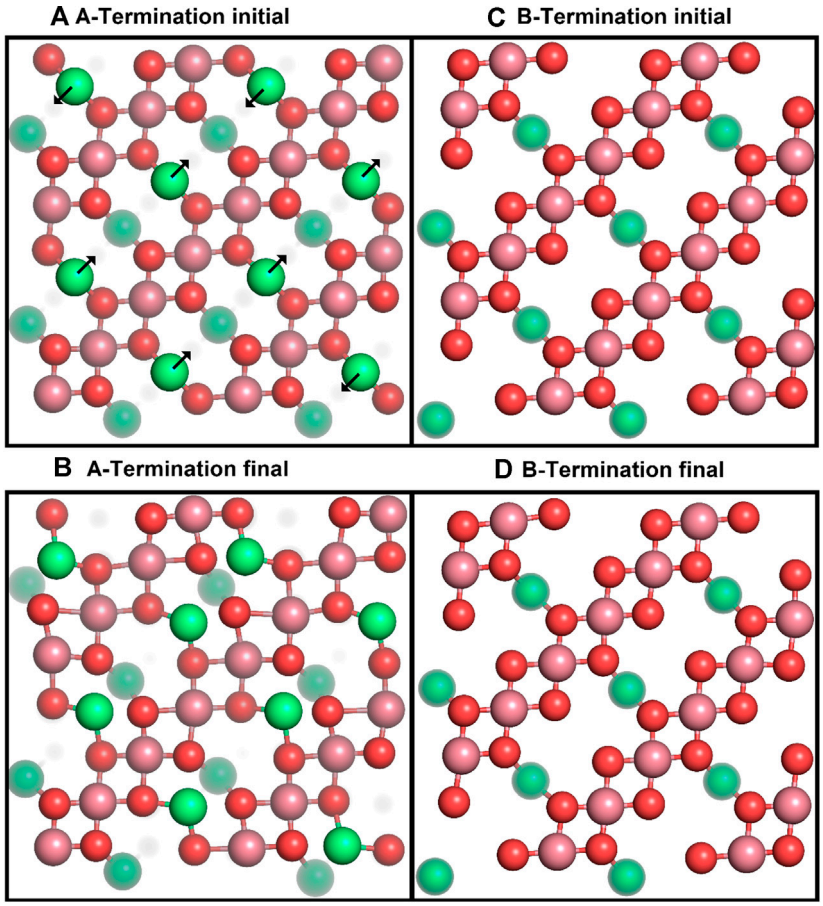

Figure 2 | Top views of the initial (top row) and final (after 10 ps; bottom row) surface structures for A- (left) and B-terminated water-free Co_3O_4 (001) surfaces, with atom colouring (Co^{2+}: green, Co^{3+}: purple, O: red) as in **Figure 1**. Co^{2+} ions below the top surface layers are partially grayed out.

from 3.5 to 3.0, indicative also of the lifting of the reconstruction addressed above. Increasing water content to 24 molecules solvates the L0 layer, by increasing the average coordination number of Co^{2+} to 3.7, while hardly changing the average coordination number in the L1 layer from 5.6 to 5.5. Increasing the water content to 32 water molecules leads to a very minor increase in the coordination number of Co^{2+} ions in the L0 layer to 3.8, while the coordination number in the L1 layer is stable at 5.5. Taken together with the snapshots in **Figure 2**, the results indicate that water adsorption leads to an (expected) increase in overall cobalt coordination number, which alleviates the need for reconstruction (driven by an increase in average coordination number), thereby reducing the strain energy of the crystal.

B-Termination

The free B-terminated surface shows no reconstruction during the 10 ps molecular dynamics runs, as can be observed by comparing **Figures 2C, D**. Relaxation effects are less prounounced than on the A-termination. The maximum of the RDF for Co^{3+} ions (layer L1) in **Figure 3C** shifts towards smaller distance on the free surface and is sharper than for the A-termination, where the shift is in the opposite direction (**Figure 3B**). Water adsorption reduces this shift relative to the bulk, which can be interpreted as the additional solvation of surface Co^{3+} ions, which increases their coordination number from 5 towards 6, thereby creating a more bulk-like local oxygen environment for the surface ions.

The Structure of Interfacial Water

Figure 4 shows top, front and side views of the final snapshots of the simulated water films with 16, 24, and 32 molecules on the A- and B-terminated Co_3O_4 (001) surfaces. On both terminations, it is seen that, for all coverages, water adsorbs via a partial dissociative mode; the dissociation degree within the contact layer is by and large independent of water content. To gain some statistical insights into the varying properties of the water layers, their interfacial bonds and hydrogen bond network, we analyse density profiles, characteristic radial distribution functions and OH orientations of adsorbed species on the different surface terminations.

A-Termination

On the A-termination, water can bind either to the Co^{2+} ions in layer L0 or to the Co^{3+} surface ions in the adjacent L1 layer. Altogether, 32 possible adsorption sites are, thus, present in the

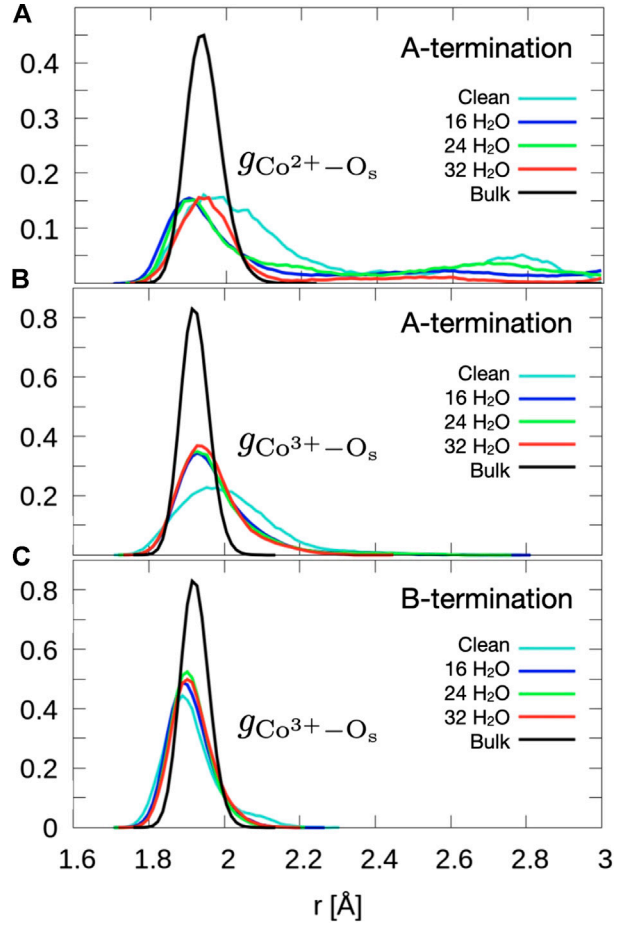

Figure 3 | Radial distribution functions of surface oxygens to outermost (A) Co^{2+} of the A-termination (layer L0), (B) Co^{3+} of the A-termination (L1) and (C) the Co^{3+} of the B-termination (L1). Data are obtained by averaging over the last 10 ps.

2 × 2 cell (2 per Co^{2+} and one per Co^{3+} ion). Hence, 16, 24 and 32 adsorbed water molecules correspond, respectively, to 0.5, 0.75 and 1 ML coverage. **Figure 5A** shows the out-of-plane density profiles of water oxygen (thick lines) and hydrogen atoms (thin lines) at different coverages. All oxygen densities have two maxima, one around 2 Å and another one around 2.5 Å from the position of the L1 layer, indicating a buckled water overlayer. At the coverage of 0.5 ML the majority of the water molecules are found in the lower sublayer. As the first 16 water molecules have been found to preferentially solvate the Co^{3+} ions in the L1 layer, one possible explanation for the bimodality might be that the closer sublayer solvates Co^{3+} and the more distant sublayer solvates Co^{2+} ions. Integrating the density peak from 0 to 2.3 Å and from 2.3 to 3.0 Å yields on average approximately 12.8 water molecules or hydroxide species in the closer and 3.2 molecules in the more distant sublayer, which does not agree well with the visual inspection of the interface (see also **Figure 6**), which leads to an estimate of about six molecules interacting with the Co^{2+} ions in the L0 layer. Thus, it is quite likely that, in addition to the difference between Co^{3+} and Co^{2+} solvation, the intrinsic (static and dynamic) inhomogeneity of the L0 layer itself may contribute to the observed oxygen density (see discussion of **Figure 7**). Increasing water coverage to 0.75 ML increases the contribution of the closer subpeak of the oxygen density only slightly to 12.9, whereas most of the additional water molecules are found in the more distant sublayer, in agreement with the progressive solvation of Co^{2+} ions in L0. Even further increase of water content to 1 ML coverage yields 12.6 and 15.7 molecules solvating the closer and more distant layers, respectively. Thus, in summary, these data and coordination numbers suggest that at 1 ML coverage most Co^{3+} ions are solvated by one water molecule or hydroxy group, whereas on average more than 1.5 water molecules or hydroxy species interact with each Co^{2+} ion directly. The remaining water molecules at the higher water coverages are located in the diffuse range beyond 3 Å.

The hydrogen density profiles show a peak centered around 1 to 1.1 Å, which corresponds to protons transferred from water molecules to the oxide ions. By integrating this peak one can conclude that on average 10.9, 12.0, and 14.0 water molecules transfer a proton to the oxygen atoms in the crystal lattice for 0.5, 0.75, and 1 ML coverage, respectively. The second hydrogen peak (clearly visible around 2.2-2.3 Å for the two lower coverages) indicates that the hydroxyl species formed from the water oxygen atoms are oriented on average at a substantial angle to the surface normal with the oxygen atom pointing down, which can be seen from the fact that this peak is further away than the oxygen peak (at around 2 Å). At the highest coverage (red line), the H peak starts rising at approximately the same distance from the reference surface, but the maximum is shifted further away from the surface, probably because the distribution of hydrogen atoms from OH overlaps with the distribution of water hydrogen atoms. Integrating this second hydrogen peak over the range from 1.7 to 2.6 Å yields 15.4, 18.9, and 25.0 hydrogen atoms. This also supports the conclusion that water and OH hydrogens are part of this second peak.

Figure 6 shows trajectory traces of surface cobalt ions (Co^{2+}: green, Co^{3+}: purple) and oxygen atoms from hydroxyl groups (red: O originally from water, orange: O originally from oxide) and from undissociated water molecules (grey, shifted upwards by 0.5 Å for better discernibility). First one notes, in agreement with the conclusions drawn before, that there is no visible reconstruction of the A-sites. Most oxygen traces for the A-terminated surface (left column) are localized, indicating a relatively immobile water/hydroxy overlayer. Already at 0.5 ML coverage (**Figure 6**) one notes a substantial amount of dissociated water molecules that transfer a proton to an (orange-colored) oxygen atom in the lattice and produce a second (red) hydroxy group. Undissociated water molecules are visible in grey. In line with the coordination numbers discussed above, many water molecules or hydroxy groups are attached to the Co^{3+} ions. However, not all of the Co^{3+} and not all of the Co^{2+} ions interact with these oxygen species. With increasing water content (**Figure 6**), all cobalt ions become solvated at 1 ML (32 water molecules), with the exception of a single Co^{3+} ion (at the upper right corner). Also note that there are several traces where red hydroxy and grey water traces are located roughly at the same spot, indicating proton equilibria

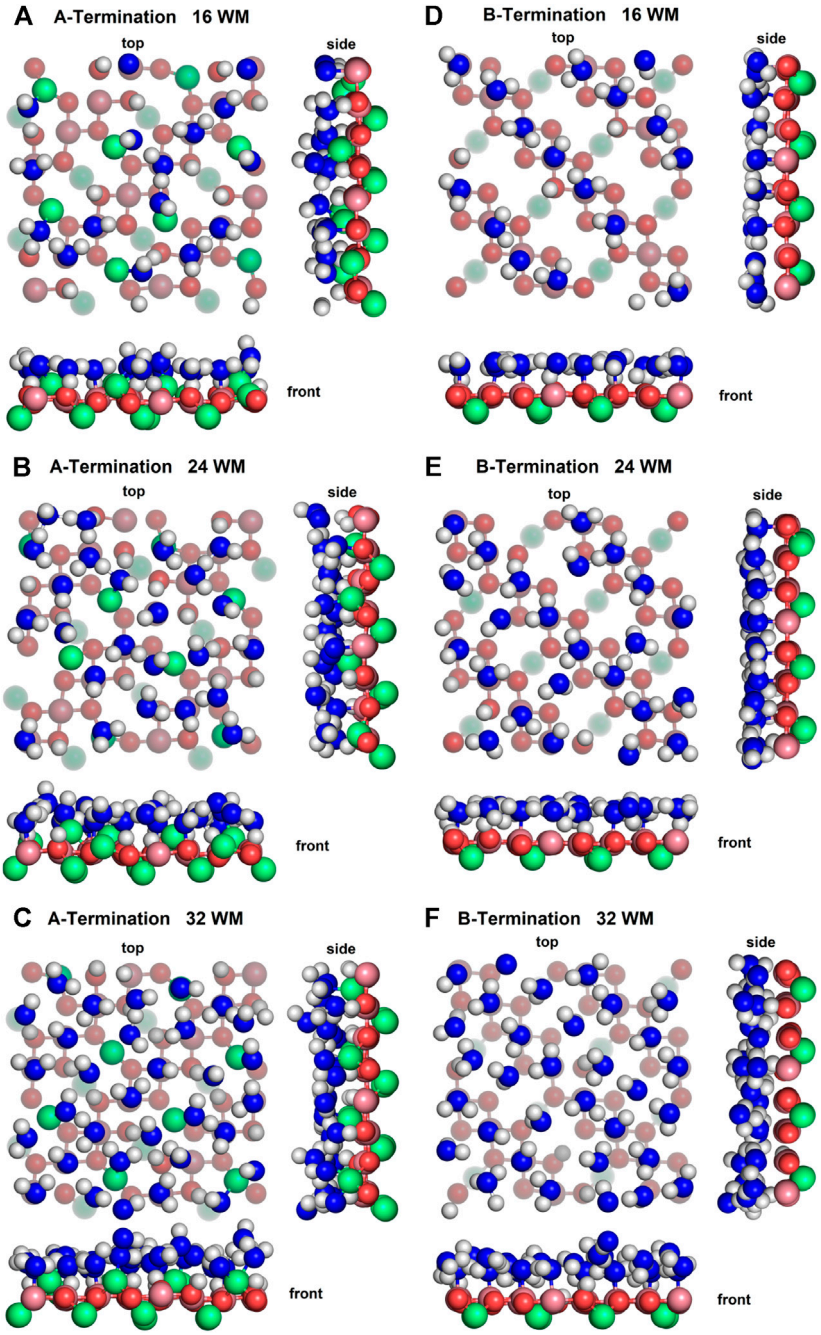

Figure 4 | Snapshots of final configurations of each simulation. Co^{2+}: green, Co^{3+}: purple, slab oxygens: red, water/hydroxide oxygen: blue, hydrogen: white. Greyed-out atoms are located in lower layers.

between OH and H_2O species. At 1 ML coverage, Co^{2+} ions are not fully solvated from the top but tend to have one or two patches of OH in the off-normal direction, indicating that also these ions are well solvated, often by two OH groups and/or water molecules.

As shown in **Figure 7**, the structure of the topmost Co^{2+} ion layer (L0) is not uniform. The density profiles are bimodal with two maxima separated by about 0.6 Å. The bistable nature of the Co^{2+} density has no obvious origin: While there is a larger tendency for ions solvated by a water molecule to be closer to the surface and a tendency for ions solvated by two hydroxide ions to be further from the surface, all other configurations can also be observed, at least at one of the three coverages. In addition, several ions dynamically switch from an oscillatory motion around one of the configurations to one around the other for extended periods of time. Certainly, the Co^{2+} ions and their

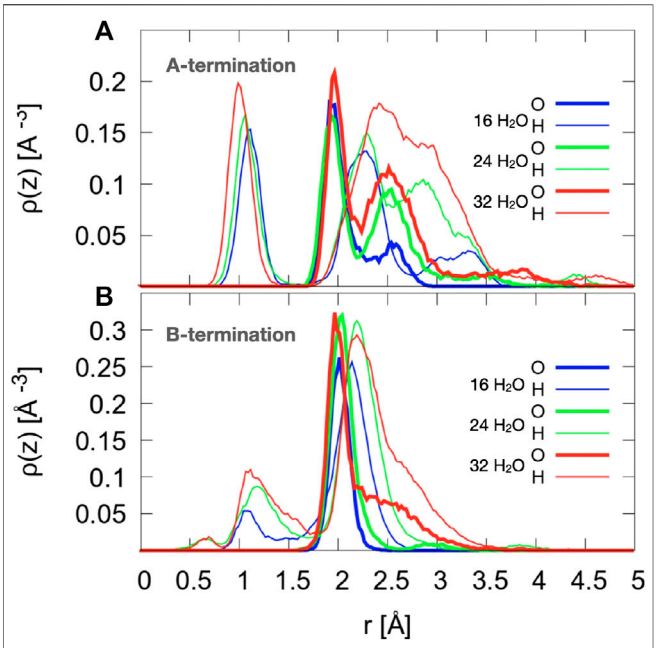

Figure 5 | Density profiles of oxygen atoms of water and hydroxide species (thick lines) and all hydrogen atoms (thin lines), averaged over the last 10 ps. The center of mass of layer L1 (see **Figure 1**) is taken as reference.

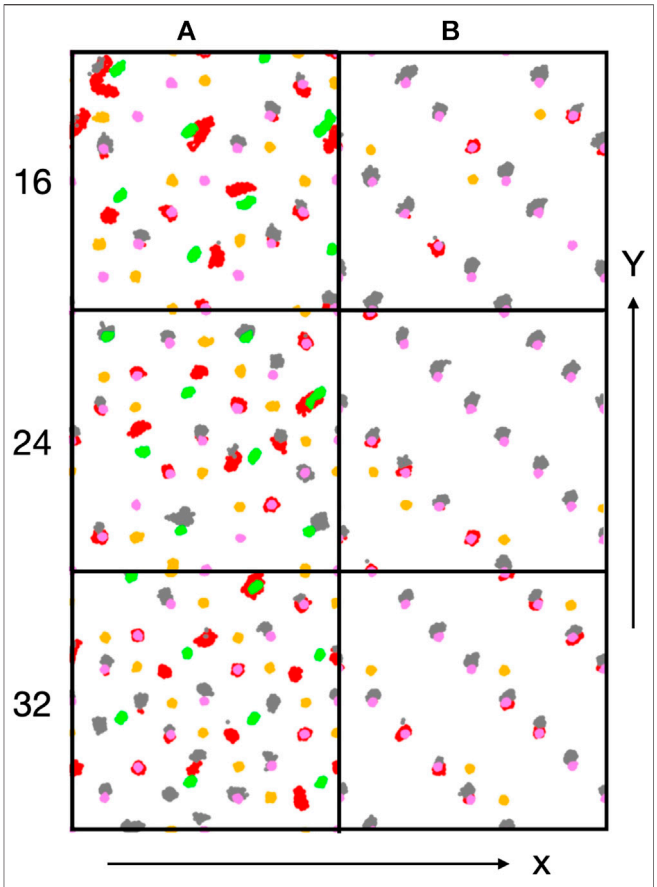

Figure 6 | Trajectory traces of interfacial Co ions (Co^{2+}: green, Co^{3+}: purple) and oxygen atoms of hydroxyl groups (red: oxygen originally from water molecule, orange: oxygen original from lattice) and water oxygen atoms (grey). Water oxygen atoms have been shifted upwards (along the y-direction) by 0.5 Å for better discernibility.

environment form the most dynamic part of the A-terminated interface.

Proton transfer takes place both from water films to the surface and within the water films. In the former case, the dissociated H atoms are transferred to surface oxygens across the neighboring trench which are bound to Co^{2+} ions underneath. In the latter case, proton transfer is made via Grothuss mechanism between water molecules binding to the surface and the ones bridging two such molecules. This mechanism is more likely to occur with increasing coverage, as more bridging molecules are present on the surface. However, the high dissociation degree in the contact Co^{2+} layer remains almost the same (see **Figures 4B,C**).

Figure 8A shows the radial distribution functions of Co^{2+} ions in layer L0 at the surface and oxygen atoms of water and hydroxide molecules. At 0.5 ML, the Co^{2+}-O_w radial distribution function shows a sharp peak centered at 1.85 Å (**Figure 8A**), as only hydroxide molecules coordinate the Co^{2+} sites, with short bond lengths. With increasing water coverage, the peak broadens, and its center shifts to 2.1 Å due to the coexistence of molecular water in the solvation shell (**Figure 8A**). On the Co^{3+} sites below (in layer L1; **Figure 8B**), both intact water molecules and OH groups are present at 0.5 ML in the peak at 1.9 Å, which extends up to 2.2 Å. As water coverage increases, a second peak, centered at 2.4 Å, arises. This can be attributed to additional water molecules that physisorb close to Co^{3+} sites, since the shape and height of the first Co^{3+}-O_w peak barely changes.

Figure 9 shows the distribution of the cosine of the angle θ between the surface normal and the OH vector of intact water molecules, (top), OH groups formed from water molecules (center) and OH groups formed from the proton transferred from water to an oxygen atom of the surface (bottom). The plane of molecular water which adsorbs at 0.5 ML on Co^{3+} lies mostly parallel to the surface. Increased water coverage increases the number of configurations with protons pointing slightly towards the surface. In addition, some OH groups point almost straight up or straight down towards the surface. The predominantly flat orientation allows for optimum hydrogen bonding at the limited water coverage, even at 1 ML coverage.

Hydroxide species, which are formed by proton detachment of an added water molecule, show a double maximum in their angular distribution (**Figure 9B**). One maximum in the range $0.8 < \cos\theta \leq 1$ shows OH groups pointing more or less perpendicularly away from the surface, whereas another set of OH groups points away from the surface at an oblique angle. The OH groups formed from the transferred water proton and a surface oxygen atom only take on the almost perpendicular configurations (**Figure 9C**), which forms when an oxygen bridge in the surface layers is broken up by protolysis. With increasing water coverage, the average orientation deviates increasingly from the normal direction, probably to facilitate

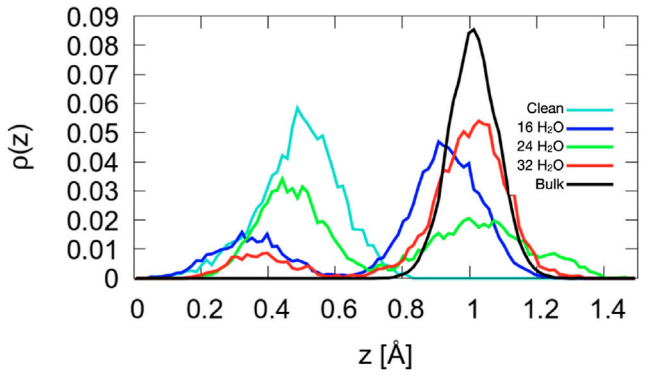

Figure 7 | Density profiles of the Co^{2+} atoms for A-terminated surfaces. The center of mass of layer L1 (see **Figure 1**) is taken as reference position $z = 0$.

the incorporation of these OH groups into the growing hydrogen bonding network. From the differences in **Figure 9B** (relative to c) one may arrive at the conclusion that, in addition to OH groups perpendicular to the surface, there is another set of OH that solvates cobalt ions in a more sideways fashion. From an inspection of **Figure 6** one may conclude that these ions are predominantly Co^{2+} ions. This is further supported by the fact that, with increasing water content, the relative abundance of the tilted configurations increases, when simultaneously the Co^{2+} ions become more strongly solvated (see above). The majority of OH groups that point perpendicularly away from the surface bridge, as a detailed analysis shows, two Co^{3+} sites and are preferentially located close to the sites that do not contain Co^{2+} ions in layer L0. These bridging OH groups form many of the orange traces in **Figure 6** that bridge two purple traces at a right angle, where no green trace of Co^{2+} can be found.

B-Termination

On the B-termination only Co^{3+} sites are available for adsorption and 16 potential adsorption sites are available in the 2 × 2 supercell. The adsorption of 16, 24, and 32 water molecules thus corresponds to 1, 1.5, and 2 ML coverage, respectively. As seen from **Figures 4D-F**, water films are partially dissociated in the contact layers at all coverages, and the dissociation degree is 25% on average. Proton transfer occurs here also on unsaturated surface oxygen atoms that are not connected to an adjacent Co^{2+} in the lower (L2) layer, but less frequently than on those connected to the Co^{2+} in the top (L0) layer in the case of the A-termination. As is also visible in **Figure 6**, at 1 ML the lateral distributions in the (x, y) plane of topmost Co^{3+} ions (L1) show mostly water molecules in an epitactic layer binding on top of the Co^{3+} ions, while a few OH groups bridge them in a manner similarly as on the A-terminated surface.

Figure 5B indicates the formation of an almost flat water layer at 1 ML as illustrated by the oxygen density peaks at 2.1 Å and the hydrogen peaks at 2.3 Å. This feature is still present at 1.5 ML; at 2 ML the onset of the formation of a diffuse region can be seen as the appearance of tails at larger distances. Transferred protons which are bound to surface oxygen atoms are also present, like on

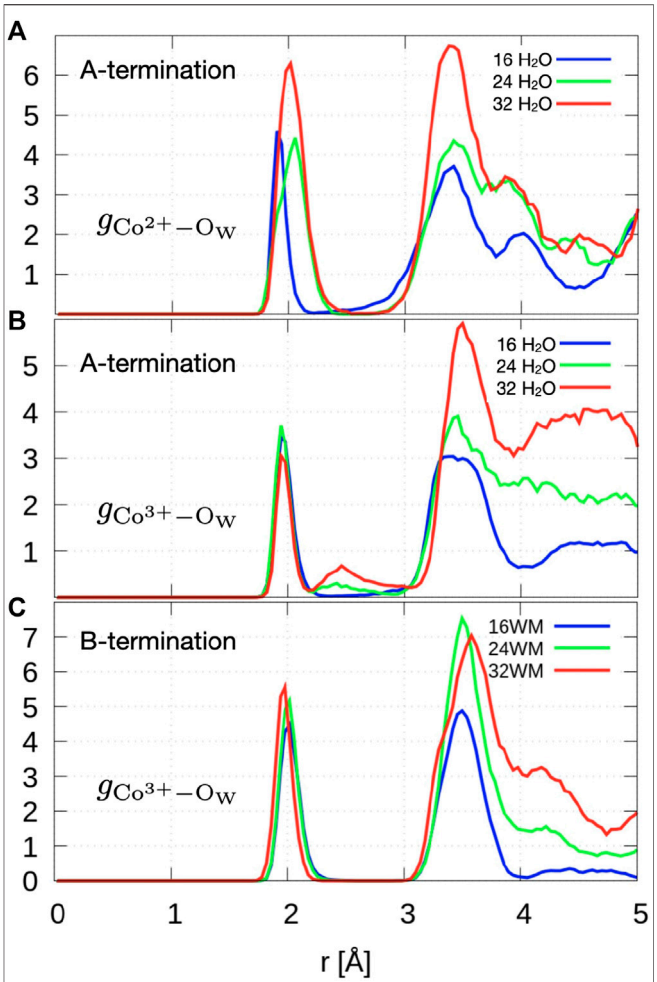

Figure 8 | Radial distribution function of topmost Co^{2+}/Co^{3+} to oxygen atoms of water and hydroxide ions.

the A- termination, but in lower proportion, as illustrated by the small peaks centered at 1.1 Å.

The radial distribution function of Co^{3+}-O_w (**Figure 8C**) shows a first peak centered around 1.9 Å that extends up to 2.2 Å, which illustrates the presence of intact water molecules and OH groups that bind via a strong bond. At higher coverage, the width of the peak does not change, which indicates that the rigidity of the contact layer is almost independent of the water content in the range studied here.

Water molecules at small surface coverage are oriented almost parallel to the surface (**Figure 9D**). With increasing water content additional configurations occur where one OH points towards the surface while the other points at a small angle away from the surface. This behaviour is indicative of a growing hydrogen bond network. Hydroxide ions created from water molecules by proton transfer to the surface are strongly tilted (**Figure 9E**), with the OH vector almost parallel to the surface at low water coverage. With increasing coverage, the OH direction is more parallel to the surface normal. This behavior may also be associated with the fact that there is substantial proton exchange between OH species and

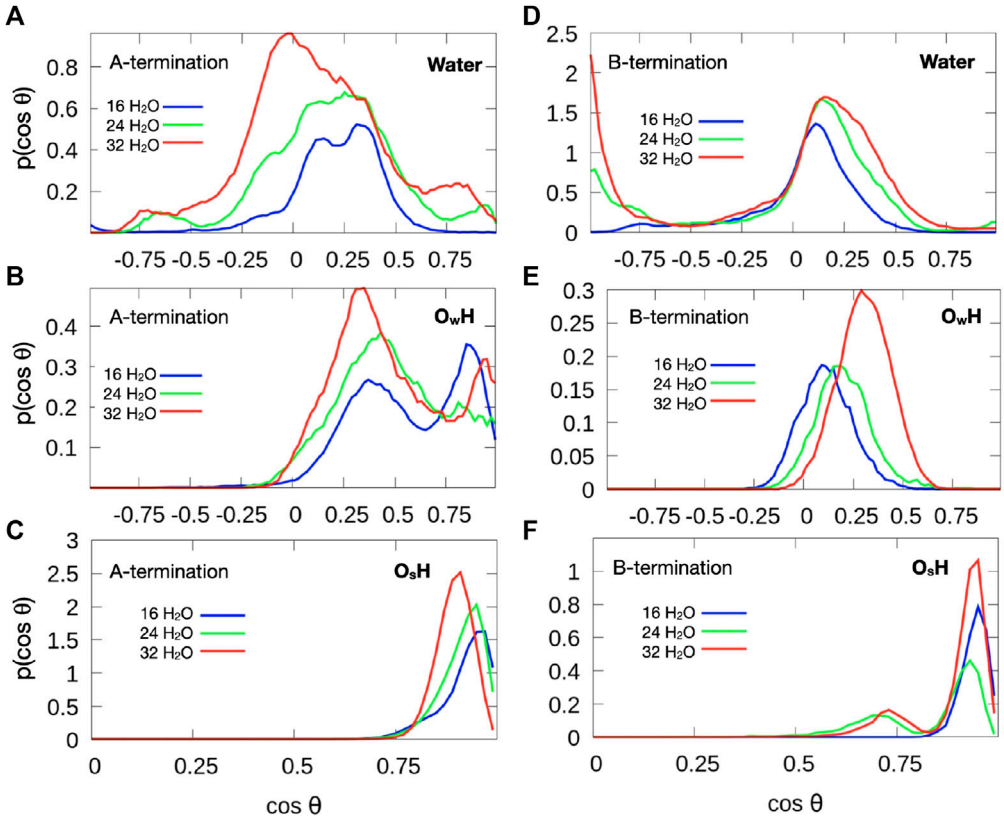

Figure 9 | Orientation of OH vectors of water molecules (top), hydroxide species with oxygen from water molecule (O_W; middle) and hydroxide species formed from the proton transferred from a water molecule to a surface oxygen atom O_S (bottom).

water molecules (see red and grey spots in **Figure 6**). Most OH groups originating from a surface oxygen atom (**Figure 9F**), however, point almost upward, similarly to the A-terminated surface, although a few OH groups are also substantially tilted (at $\cos\theta \approx 0.7$). Please note that the distribution functions in **Figure 9** are not normalized to one, but the area is proportional to the number of OH vectors contributing to the distribution functions.

Proton Transfer

Water dissociation into OH species and subsequent proton transfer to the surface is a frequent scenario on both surface terminations. Both surfaces are strongly hydroxylated. On the A-terminated surface, on average 5.5 of the 16 water molecules at the 0.5 ML coverage remain undissociated, while about 21 OH groups exist on average. With increasing water content the average number of OH groups increases to 23.5 and 28.0 for the simulations at 0.75 and 1.0 ML, respectively. The number of water molecules also increases from about 5.5 to 12 to 18 for 0.5, 0.75, and 1 ML, respectively. For the B-terminated surface, the number of OH groups increases only moderately from 6.0 to 6.2 and 10.1 and the number of water molecules from 13 to 20.9 to 26.8 (at 1, 1.5 and 2 ML, respectively).

CONCLUSION

Ab initio molecular dynamics simulations have shown that water adsorbs on both terminations of the Co_3O_4 (001) surface via a partially dissociative mode. The dissociation degree on the A-termination in contact with a water layer is significantly higher than on the B-termination.

On the A-terminated surface, water fully dissociates on or near all sites and thereby breaks up bridging oxygen atoms, mostly between Co^{3+} sites, but also near Co^{2+}. One can even observe coadsorption of intact and dissociated water molecules on the same Co^{2+} ion. OH^- adsorption promotes a bulk-like geometry of the reconstructed clean surface. The degree of dissociation on the adjacent Co^{3+} sites is 50% and remains constant with increasing water coverage. The interface is dynamic with frequent, localised proton transfers between water molecules and hydroxide species via a Grotthuss mechanism. Nevertheless, the oxygen arrangement in the water layer is quite rigid.

On the B-termination, a similar behaviour is observed. However, the interface is less reactive. Here, water forms epitactic layers on top of Co^{3+} sites and the dissociation degree is less than 25% in the contact layer at all coverages.

Proton transfer within the water film and towards the surface is also observed, but with lower probability than on the A-terminated surface.

Both surfaces are strongly hydroxylated with rigid oxygen layers but mobile and disordered proton subsystems. Overall, water solvates the A-terminated surface more strongly. It is also noteworthy that on the A-terminated surface, if water is present, the surface reconstruction observed on the clean surface is released again, due to the ability of water to increase the coordination number of the Co^{2+} ions substantially *without* moving them along the rows.

In summary, the larger degree of water dissociation on the A-terminated surface and the higher local abundance of OH groups (relative to water molecules) around Co^{2+} ions as compared to Co^{3+} ions is consistent with thermal desorption experiments which show high-temperature desorption peaks most probably due to OH groups. These difficult to displace tightly bound OH groups may be at the origin of the observed low oxidation activity on the A-terminated (001) surface.

DATA AVAILABILITY STATEMENT

The raw data supporting the conclusions of this article will be made available by the authors, without undue reservation.

AUTHOR CONTRIBUTIONS

We have contributed equally to the work: planning, discussions and writting.

ACKNOWLEDGMENTS

This study was funded by the Deutsche Forschungsgemeinschaft (DFG, German Research Foundation) – 388390466 – TRR 247 within the work of Project A6. The authors gratefully acknowledge computing time granted by the Center for Computational Sciences and Simulation (CCSS) of the Universität of Duisburg-Essen and provided on the supercomputer magnitUDE (DFG grants INST 20876/209-1 FUGG, INST 20876/243-1 FUGG) at the Zentrum für Informations- und Mediendienste (ZIM). We would also like to thank Rossitza Pentcheva and her group (TRR 247 Project B4) for helpful discussions and optimised oxide structures.

SUPPLEMENTARY MATERIAL

The Supplementary Material for this article can be found online at: https://www.frontiersin.org/articles/10.3389/fenrg.2020.604799/full#supplementary-material

REFERENCES

Anke, S., Bendt, G., Sinev, I., Hajiyani, H., Antoni, H., Zegkinoglou, I., et al. (2019). Selective 2-propanol oxidation over unsupported Co3O4 spinel nanoparticles: mechanistic insights into aerobic oxidation of alcohols. *ACS Catal.* 9(7): 5974–5985 doi:10.1063/1.5053729.

Cai, Y., Xu, J., Guo, Y., and Liu, J. (2019). Ultrathin, polycrystalline, two-dimensional Co3O4 for low-temperature co oxidation. *ACS Catal.*, 9(3): 2558–2567 doi:10.1021/acscatal.8b04064.

Chen., J., and Selloni, A.. Water adsorption and oxidation at the Co3O4 (110) surface. (2012). *J. Phys. Chem. Lett.* 3(19):2808–2814. doi:10.1016/j.cplett.2010.12.015.

Chen, J., Wu, X., and Selloni, A. (2011). Electronic structure and bonding properties of cobalt oxide in the spinel structure. *Phys. Rev. B.* 83:245204. doi:10.1103/physrevlett.77.3865.

Creazzo, F., Ruth Galimberti, D., Pezzotti, S., and Gaigeot, M.-P. (2019). DFT-MD of the (110)-Co3O4 cobalt oxide semiconductor in contact with liquid water, preliminary chemical and physical insights into the electrochemical environment. *J. Chem. Phys.* 150(4):041721. doi:10.1063/1.5053729

Deng, X., and Tüysüz, H. (2014). Cobalt-oxide-based materials as water oxidation catalyst: recent progress and challenges. *ACS Catal.* 4(10):3701–3714. doi:10.1021/acscatal.9b01048.

Grimme, S., Antony, J., Ehrlich, S., and Krieg, H. (2010). A consistent and accurate ab initio parametrization of density functional dispersion correction (DFT-D) for the 94 elements H-Pu. *J. Chem. Phys.*, 132(15):154104.

Hubbard, J., and Flowers, B. H. Electron correlations in narrow energy bands. (1963). *Proc. Roy. Soc. Lond. Math. Phys. Sci.* 276(1365):238–257. doi:10.1021/jp109264b.

Kim, K. J. and Park, Y. R. (2003). Optical investigation of charge-transfer transitions in spinel Co3O4. *Solid State Commun.*, 127(1):25–28. doi:10.1021/jp200581s.

Llorca, J. P., Dalmon, J.-A., and Homs, N. (2004). Transformation of Co3O4 during ethanol steam-re-forming. activation process for hydrogen production. *Chem. Mater.* 16(18):3573–3578. doi:10.1021/cs500713d.

Ma, C. Y., Mu, Z., Li, J. J., Jin, Y. G., Cheng, J., Lu, G. Q., et al. (2010). Mesoporous Co3O4 and au/Co3O4 catalysts for low-temperature oxidation of trace ethylene. *J. Am. Chem. Soc.*, 132(8):2608–2613. doi:10.1021/cm049311p.

Montoya, A., and Haynes, B. S. (2011). Periodic density functional study of Co3O4 surfaces. *Chem. Phys. Lett.* 502(1):63–68. doi:10.1063/1.3382344

Perdew, J. P., Burke, K., and Ernzerhof, M. (1996). Generalized gradient approximation made simple. *Phys. Rev. Lett.* 77:3865–3868. doi:10.1039/c3ta12960h.

Shinde, V. R., Mahadik, S. B., Gujar, T. P., and Lokhande, C. D. (2006). Supercapacitive cobalt oxide (Co3O4) thin films by spray pyrolysis. *Appl. Surf. Sci.* 252(20):7487–7492. doi:10.1016/j.apsusc.2005.09.004

Sun, H., Ang, H. M., Tadé, M. O., and Wang, S. (2013). Co3O4 nanocrystals with predominantly exposed facets: synthesis, environmental and energy applications. *J. Mater. Chem.* 1:14427–14442. doi:10.1039/C3TA12960H

The CP2K developers group. CP2K is freely available from: http://www.cp2k.org/, (2016).

Wang, X., Ding, L., Zhao, Z., Xu, W., Meng, B., and Qiu, J. (2011). Novel hydrodesulfurization nano-catalysts derived from Co3O4 nanocrystals with different shapes. *Catal. Today* 175(1):509–514. doi:10.1016/j.cattod.2011.02.052

Xu, X. L., and Li, J. Q. (2011). DFT studies on H2O adsorption and its effect on CO oxidation over spinel Co3O4 (110) surface. *Surf. Sci.* 605(23):1962–1967. doi:10.1021/ja906274t.

Zasada, F., Piskorz, W., Cristol, S., Paul, J.-F., Kotarba, A., and Sojka, Z. (2010). Periodic density functional theory and atomistic thermodynamic studies of cobalt spinel nanocrystals in wet environment: molecular interpretation of water adsorption equilibria. *J. Phys. Chem. C.* 114(50):22245–22253. doi:10.1021/jp109264b

Zasada, F., Piskorz, W., Stelmachowski, P., Kotarba, A., Paul, J.-F., Płociński, T., et al. (2011). Periodic DFT and HR-STEM studies of surface structure and morphology of cobalt spinel nanocrystals. retrieving 3D shapes from 2D images. *J. Phys. Chem. C.* 115(14):6423–6432. doi:10.1021/jp109264b

Conflict of Interest: The authors declare that the research was conducted in the absence of any commercial or financial relationships that could be construed as a potential conflict of interest.

frontiers in Energy Research

ORIGINAL RESEARCH
published: 23 December 2020
doi: 10.3389/fenrg.2020.582284

An Ordinary Differential Equation Model for Simulating Local-pH Change at Electrochemical Interfaces

Yoshiharu Mukouyama[1,2]* *and Shuji Nakanishi*[2,3]*

[1]Division of Science, College of Science and Engineering, Tokyo Denki University, Hatoyama, Japan, [2]Research Center for Solar Energy Chemistry, Osaka University, Toyonaka, Japan, [3]Graduate School of Engineering Science, Osaka University, Toyonaka, Japan

The local pH value at an electrochemical interface (pH^S) inevitably changes during redox reactions involving the transfer of H^+ or OH^- ions. It is important to quantitatively estimate pH^S during polarization, as this parameter has a significant impact on the activity and selectivity of electrochemical reactions. Numerical simulation is an effective means of estimating pH^S because it is not subject to experimental constraints. As demonstrated in a number of studies, pH^S can be estimated by solving partial differential equations that describe diffusion process. In the present work, we propose a method to consider the process by using ordinary differential equations (ODEs), which can significantly reduce the computational resources required for estimating pH^S values. In the ODE-based model, the description of the diffusion process was achieved by considering the reaction plane in the diffusion layer over which the H^+ and OH^- concentrations are balanced while assuming that the concentration profiles in the layer are in a steady state. The resulting model successfully reproduces experimental voltammograms characterized by local pH changes in association with the hydrogen evolution and hydrogen peroxide reduction reactions.

Keywords: electrochemistry, local pH simulation, hydrogen evolution, hydrogen peroxide reduction, electrocatalysts

OPEN ACCESS

Edited by:
Hideshi Ooka, RIKEN, Japan

Reviewed by:
Marc Koper, Leiden University, Netherlands
Joel Ager, University of California, Berkeley, United States

***Correspondence:**
Yoshiharu Mukouyama
mukoyama@mail.dendai.ac.jp
Shuji Nakanishi
nakanishi@chem.es.osaka-u.ac.jp

Specialty section:
This article was submitted to Electrochemical Energy Conversion and Storage, a section of the journal Frontiers in Energy Research

Received: *11 July 2020*
Accepted: *09 October 2020*
Published: *23 December 2020*

Citation:
Mukouyama Y and Nakanishi S (2020) An Ordinary Differential Equation Model for Simulating Local-pH Change at Electrochemical Interfaces. Front. Energy Res. 8:582284. doi: 10.3389/fenrg.2020.582284

INTRODUCTION

Electrochemical interfaces are regions in which electrical energy is directly converted to chemical energy or vice versa. Many important reactions closely related to energy and environmental issues, including hydrogen evolution/oxidation, oxygen reduction/evolution, carbon dioxide reduction, nitrate reduction and organic oxidation reactions, involve the transfer of H^+ and OH^- ions, which inevitably changes the electrode surface pH (pH^s). As a consequence, the pH^s can be more than 3 units different from the bulk pH (pH^b) even in a buffered electrolyte. This modification of pH^s can be particularly pronounced in the case that the current density is increased as a result of the use of gas diffusion or roughened/porous electrodes (Sen et al., 2014; Hall et al., 2015; Ma et al., 2016; Yoon et al., 2016; Yang et al., 2017; Song et al., 2019). Interestingly, the pH^s value determines both the kinetics and thermodynamics of various reactions, and thus affects the activity and selectivity of such processes. Therefore, it is important to determine pH^s during electrochemical polarization so as to understand and design electrocatalysts.

The pH^s value can be experimentally obtained in some specific cases. As an example, the reaction activity and selectivity are known to depend on pH during electrochemical carbon dioxide reduction

(Kas et al., 2015; Singh et al., 2015; Singh et al., 2016; Varela et al., 2016; Billy and Co, 2017; Ooka et al., 2017). Thus, pH^s can be quantified by monitoring the ratio of CO_3^{2-} to HCO_3^- (which will vary with pH) using attenuated total reflectance surface-enhanced infrared absorption spectroscopy (Ayemoba and Cuesta, 2017; Dunwell et al., 2018). A rotating ring-disc electrode assembly can also be used to determine pH^s if the electrochemical activities of reaction intermediates and/or products vary with pH (Zhang and Co, 2020). Even if a system does not exhibit these specific characteristics, pH^s may still be found by using pH probes together with appropriate analytical techniques. Deligianni and Romankiw developed an in-situ technique for measuring pH^s during Ni and NiFe electrodeposition on a gold mesh cathode. The technique made use of a flat-bottomed glass pH electrode positioned at the back of the cathode (Deligianni and Romankiw, 1993). Ji et al. modified this useful technique to conduct a further study of the Ni electrodeposition (Ji et al., 1995). Ryu et al. established the pH^s values associated with the hydrogen oxidation reaction by adding *cis*-2-butene-1,4-diol, which undergoes pH-dependent selective conversions to 1,4-butandiol (at higher pH) or *n*-butanol (at lower pH), to the reaction system (Ryu et al., 2018). Some groups demonstrated the spatiotemporal visualization of changes in pH^s based on the use of pH-responsive fluorescent dyes in conjunction with laser scanning confocal microscopy (Suzurikawa et al., 2010; Leenheer and Atwater, 2012; Fuladpanjeh-Hojaghan et al., 2019).

Another effective approach to the quantitative estimation of pH^s is to conduct a numerical simulation, which has the added benefit of being free from experimental constraints. As an example, Mayrhofer's group established the fundamental physicochemical relationship between current density and the total diffusive flux of ions within a diffusion layer (Auinger et al., 2011; Katsounaros et al., 2011). In this prior work, increases in pH^s during the hydrogen evolution reaction (HER) were estimated from the current density, and the electrode potential was calculated by substituting the calculated pH^s values into the Nernst equation. This same study also calculated ion distributions in the diffusion layer. Carneiro-Neto et al. also simulated the HER based on the Volmer-Tafel (V-T) and Volmer-Heyrovský mechanisms, in which the pH^s change during reactions was taken into consideration (Carneiro-Neto et al., 2016). In this work, equations were solved numerically employing a finite element method. Grozovski et al. studied the HER on a Ni rotating disc electrode in unbuffered electrolyte solutions with mildly acidic pH values (Grozovski et al., 2017) and also conducted finite element simulations, assuming that the concentration profiles of H^+ and OH^- ions were stationary during the HER. These simulations indicated that OH^- ions could have an infinite diffusion rate.

pH^s values can be simulated by solving mathematical equations representing diffusion process. When the diffusion process is described as a function of several independent variables, a numerical method to solve partial differential equations (PDEs) is required. This approach successfully provides spatial distributions of pH^s values (Rudd et al., 2005; Leenheer and Atwater, 2012). To obtain reliable pH^s data through numerical simulations, it is essential to accurately represent the possible reactions as differential equations. However, in the case that the system of interest consists of multiple reactions, the number of coupled differential equations inevitably increases, and consequently requires greater computational resources. Herein, we report an alternative method based on ordinary differential equations (ODEs) that can be employed to calculate simulated pH^s values. In this simplified model, the introduction of a new parameter that describes the plane in which the H^+ and OH^- concentrations are balanced (referred to as the "reaction plane") enables a representation of the temporal variations of pH^s using ODEs. This newly developed model is simple, yet it is able to reproduce the essential characteristics of voltammograms that appear due to changes in pH^s. In this ODE model, pH^s can be predicted simply by establishing the balance between H^+ and OH^-, even if the reactants and/or products vary in a pH^s-dependent manner. In the present work, we demonstrate the validity and generality of this approach by simulating the HER and hydrogen peroxide (H_2O_2) reduction reaction (HPRR). Notably, our model succeeds in reproducing even the features of the complex HPRR system, in which H_2O_2 dissociates in a pH-dependent manner ($H_2O_2 \rightleftharpoons HO_2^- + H^+$; $pK_a \approx 11.7$).

It should be noted that our model can be regarded as an expansion of the ODE model originally developed by Koper and Sluyters (Koper and Sluyters, 1991). Their model was based both on a Randles-type equivalent circuit (see **Figure 3**) and on the Nernst diffusion layer model where the concentration profile of electroactive species near the electrode is assumed to be in a steady state. Interestingly, their model can simulate even the essential features of dynamic behavior such as spontaneous current oscillations, because the concentrations of electroactive species at the electrode surface is treated as a time-dependent variable. This is a significant advantage of the model over the calculation performed under steady-state assumption. In our prior works (Mukouyama et al., 1999; Mukouyama et al., 2001; Mukouyama et al., 2015; Mukouyama et al., 2017a), by means of the model, we simulated spontaneous current and potential oscillations as well as cyclic voltammograms. We anticipate that the ODE model developed in the present work will provide valuable insights into dynamic changes of pH^s during electrocatalytic reactions.

MATERIALS AND METHODS

The electrochemical measurements in this work were performed using a three-electrode system at room temperature, in conjunction with a polycrystalline Pt or Ag working electrode (WE). A Pt wire was used as the counter electrode and a saturated mercury–mercurous sulfate electrode (MSE, 0.64 V vs. a standard hydrogen electrode (SHE) at 25°C) was used as the reference electrode. Throughout this paper, all potentials are referred to relative to a SHE.

RESULTS AND DISCUSSION

Experimental Results for the Hydrogen Evolution Reaction and Hydrogen Peroxide (H_2O_2) Reduction Reaction

Here, it is helpful to briefly discuss the electrochemical formation and desorption of hydrogen atoms on a Pt electrode. It is known that there are two types of adsorbed hydrogen atoms: under-potentially-deposited hydrogen (upd-H) and on-top H. These are generated at potentials more positive and negative than the onset potential of the HER, respectively. The corresponding reactions are as follows.

$$\mathrm{Pt} + \mathrm{H^+} + \mathrm{e^-} \underset{k_{-1}}{\overset{k_1}{\rightleftharpoons}} \mathrm{Pt\text{-}H\,(upd\text{-}H)} \quad (1)$$

$$\mathrm{Pt} + \mathrm{H^+} + \mathrm{e^-} \underset{k_{-2}}{\overset{k_2}{\rightleftharpoons}} \mathrm{Pt\text{-}H\,(on\text{-}topH)} \quad (2)$$

In an acidic medium, the HER is known to proceed via the V-T mechanism (Lamy-Pitara et al., 2000; Schmickler and Santos, 2010; Skúlason et al., 2010), with on-top H as the reaction intermediate. The associated reaction is provided below.

$$2\,\mathrm{Pt\text{-}H\,(on\text{-}top\ H)} \overset{k_3}{\rightarrow} \mathrm{H_2} \quad (3)$$

In each of the above equations, k_i (i = 1, −1, 2, −2 or 3) is the corresponding rate constant. In contrast, in a basic medium, water molecules are directly reduced via the process in the following reaction.

$$2\mathrm{H_2O} + 2\mathrm{e^-} \rightarrow \mathrm{H_2} + 2\mathrm{OH^-} \quad (4)$$

The onset potential of the HER follows Nernstian behavior (that is, changes according to the ratio −0.059 V/pH) over a wide pH range. The standard redox potentials of the HER in acidic media at pH of 0 and basic media with a pH of 14 are 0 and −0.828 V (vs. SHE), respectively, at 25°C.

Figure 1 presents the *I*–*U* curves previously reported for Pt and Ag electrodes in H_2SO_4 solutions (Mukouyama et al., 2008; Mukouyama et al., 2014). The characteristics of these curves are determined both by the concentration of the H_2SO_4 solution and by the presence or absence of Na_2SO_4. In the absence of Na_2SO_4, the absolute value of the HER current increases linearly as U decreases when the H_2SO_4 concentration is 0.07 M or higher. However, at lower concentrations (the red curve in **Figure 1A**), the *I*–*U* relationship exhibits a plateau over the potential region between −0.9 and −1.7 V, i.e., the current is almost constant in the region. Our prior work established that this plateau appears because of a limitation related to the diffusion of H^+. At more negative potentials (U < −1.7 V), the reduction current again increases as U decreases. Specifically, the limited H^+ supply eventually leads to an increase in pH^s, which in turn results in the reduction of H_2O (as in **Eq. 4**) at U < −1.7 V.

In the presence of Na_2SO_4, the plateau effect is observed even in 0.1 M H_2SO_4 (**Figures 1B,C**). In addition, the reduction of water occurs at potentials more negative than the potential of the plateau, indicating that the local environment at the electrochemical

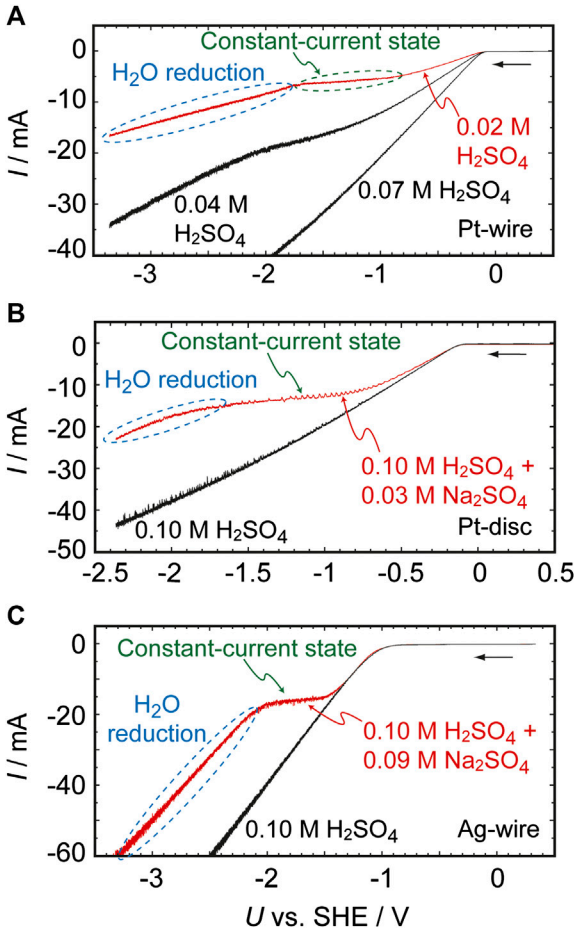

FIGURE 1 | Current (*I*)–potential (*U*) curves for H_2SO_4 solutions and H_2SO_4 + Na_2SO_4 solutions as obtained under controlled potential conditions at a scan rate of 0.01 V s^{-1}. The working electrodes were **(A)** a 0.5 mm diameter, 4 mm long Pt wire, **(B)** a 2 mm diameter Pt disc, and **(C)** a 0.5 mm diameter, 4 mm long Ag wire.

interface becomes basic even though the bulk electrolyte is strongly acidic (with a pH of approximately 1). It should be noted that, in negative potentials, the curve coincides with that obtained for a 0.1 M NaOH solution, as shown in **Supplementary Figure S1**. This result clearly indicates that a pH^s of approximately 13 is obtained at U = −1.8 V. Significant increases in pH^s were also confirmed when other salts, such as Li_2SO_4 and K_2SO_4, were added to the electrolyte, and when perchlorate ions are present in the solution instead of (bi)sulfate ions (**Supplementary Figure S2**). Although the mass transport of H^+ to the electrode surface is generally driven by diffusion, convection and electromigration, the migration of H^+ is suppressed in the presence of these salts because alkaline metal cations diminish the migration process. For this reason, pH^s becomes significantly higher in the presence of these salts. This is strongly supported by the fact that the essentially same behavior is observed when the concentration of the salts is remarkably high, e.g., 0.2 M (**Supplementary Figure S3**), and hence the migration process is negligible. Importantly, these effects are observed not only on Pt but also with various other

metals, including Ag, Au, Cu, Fe, Ni, W, and Zn, providing further evidence that the increase in pH^s during these reactions has a physical origin.

It is also helpful to examine the pH^s increase during the HPRR with a Pt electrode in an H_2SO_4 solution (Mukouyama et al., 2017a; Mukouyama et al., 2017b). As shown in **Figure 2A**, using a solution containing 0.1 M H_2SO_4 and 0.1 M H_2O_2 as the electrolyte, the HPRR current begins at 0.75 V and the HER occurs at U = −0.15 V. Because the HPRR proceeds via the potential-independent dissociative adsorption of H_2O_2 to generate adsorbed OH (Pt-OH) (**Eqs. 5** and **6**), a constant current flows over the wide potential range of 0.6 to −0.1 V. The associated reactions are provided below.

$$2\,Pt + H_2O_2 \xrightarrow{k_5} 2\,Pt\text{-}OH \quad (5)$$

$$Pt\text{-}OH + H^+ + e^- \xrightarrow{k_6} Pt + H_2O \quad (6)$$

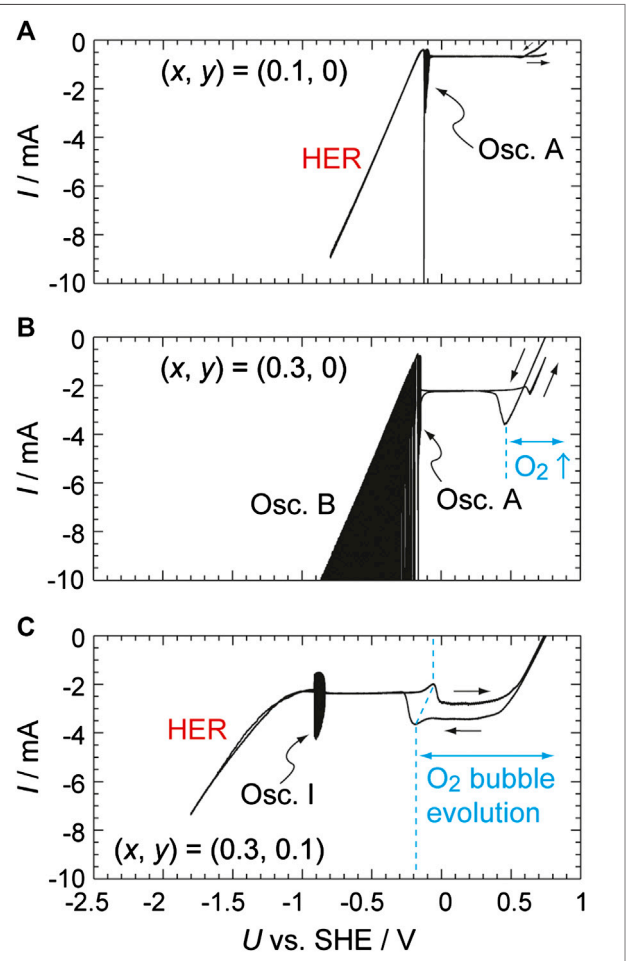

FIGURE 2 | *I–U* curves obtained using a Pt disc electrode (2 mm in diameter) in 0.1 M H_2SO_4 + x M H_2O_2 + y M Na_2SO_4, where (x, y) = (0.1, 0) (0.3, 0) and (0.3, 0.1) going from top to bottom, under controlled potential conditions at a sweep rate of 0.01 V s^{-1}.

The HPRR was suppressed at around −0.1 V by the formation of upd-H, and consequently a current oscillation (named oscillation A) appeared. When the concentration of H_2O_2 was increased to 0.3 M (**Figure 2B**), another type of oscillation (named oscillation B) appeared in the potential region of the HER. Note that pH^s was still acidic though H^+ was efficiently consumed by the HPRR. The mechanisms of the oscillations have been already clarified (Mukouyama et al., 1999; Mukouyama et al., 2001) and these phenomena are not in the scope of the present work.

Just as was the case for the HER data presented in **Figure 1**, when a sufficient quantity of Na_2SO_4 is added to the solution (**Figure 2C**), pH^s increases during the HPRR, resulting in the disappearance and appearance of H^+ reduction and H_2O reduction currents, respectively. Depending on the Na_2SO_4 concentration, another type of current oscillation (named oscillation I) appeared at around −0.9 V due to the formation of upd-H. Furthermore, since the pK_a value of H_2O_2 is approximately 11.7, the first step of the HPRR is altered as follows.

$$2\,Pt + HO_2^- + H_2O \xrightarrow{k_{5a}} 2\,Pt\text{-}OH + OH^- \quad (5a)$$

We have previously demonstrated that the generation of O_2 bubbles via the disproportionation reaction of H_2O_2 leads to hysteresis in the potential region of 0.6 V to −0.2 V. However, because this phenomenon has no relation to the scope of the present work, it is not discussed further in the present work.

Ordinary Differential Equation Modeling

The ion-product constant of water, $K_W = C_H C_{OH}$, is 1.0×10^{-20} at 25°C, where C is the concentration of each species. In this paper, C is in units of mol cm^{-3} and the superscripts "s" and "b" when applied to concentrations (that is, C_H^s and C_H^b) indicate values at the electrode surface and in the solution bulk, respectively. Note that the value of K_W changes to 1.0×10^{-14} if concentration units of mol L^{-1} are employed. In our earlier work (Mukouyama et al., 2015; Mukouyama et al., 2017a), the experimental results shown in **Figure 2A** were simulated employing a Randles-type equivalent circuit (**Figure 3**), just like the original model developed by Koper and Sluyters (1991). The applied potential (U) was treated as a controlled parameter while E was a time-dependent variable. The rate constants for the associated electrochemical reactions, which are functions of the true electrode potential (E), can be described using the Butler-Volmer equations below.

$$k_i = k_i^0 \exp\left[-\alpha_i nF\left(E - E_i^0\right)/RT\right] \text{ for reduction reactions} \quad (7)$$

$$k_i = k_i^0 \exp\left[(1-\alpha_i)nF\left(E - E_i^0\right)/RT\right] \text{ for oxidation reactions} \quad (8)$$

Here, E_i^0 is the equilibrium redox potential, k_i^0 is the rate constant at $E = E_i^0$, α_i is the transfer coefficient, n is the number of transferred electrons (with a value of 1), F is the Faraday constant (96,500 C mol^{-1}), R is the gas constant (8.31 J K^{-1} mol^{-1}), and T is the absolute temperature. The kinetics of the HER based on the V-T mechanism can be

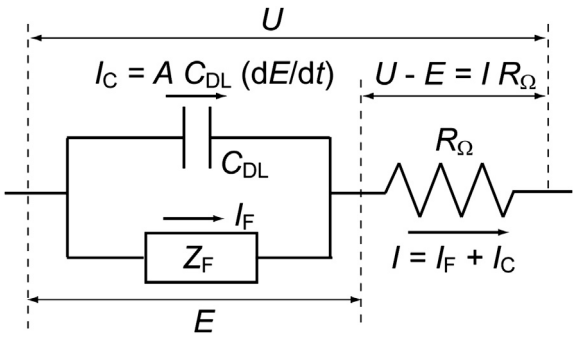

FIGURE 3 | The equivalent circuit from which the time dependence of the true electrode potential (dE/dt) is derived. The total current from the electrode (I) is the sum of the Faraday current (I_F) and the charging current of the electric double layer at the electrode surface (I_C). Here, U is the applied potential, E the true electrode potential, A the electrode area, Z_F the Faraday impedance, C_{DL} the double layer capacitance, and R_Ω the solution resistance between the working and reference electrodes.

expressed using the coverage of on-top H (Θ_H) and C_H^s as time-dependent variables. Hence, the following ODEs can be derived for dE/dt and $d\Theta_H/dt$.

$$\frac{dE}{dt} = \frac{U-E}{AC_{DL}R_\Omega} - \frac{I_F}{AC_{DL}} \tag{9}$$

$$I_F = AF\left[-k_2 C_H^s (1-\Theta_H) + k_{-2}\Theta_H\right] \tag{10}$$

$$N_0 \frac{d\Theta_H}{dt} = k_2 C_H^s (1-\Theta_H) - k_{-2}\Theta_H - 2k_3 \Theta_H^2 \tag{11}$$

Here, A is the electrode area, C_{DL} is the double layer capacity, R_Ω is the solution resistance between the working and reference electrodes, I_F is the Faraday current, and N_0 is the total number of surface sites per unit area (2.2×10^{-9} mol cm^{-2} for a Pt surface). The HER current is much larger than that due to Reaction 1 (associated with the formation of upd-H and the oxidation of this species), and so the latter process is not included in **Eq. 10**. It should also be noted that **Eqs. 10** and **11** reflect the Nernstian behavior of the HER because it contains C_H^s (Mukouyama et al., 1999).

When considering the pH^s change, both the kinetics at the electrochemical interface and the diffusion process must be taken into account. As an example, Grozovski et al. developed a diffusion layer model that is divided into two regimes for the numerical simulation of the HER on a Ni electrode (Grozovski et al., 2017). These regimes are separated by a reaction plane over which the local concentrations of H^+ and OH^- (C_{OH}^s) generated by direct H_2O reduction are balanced. In this model, OH^- can be present in the region close to the electrode surface whereas H^+ is present further away from the surface.

The present simulations aimed to establish an ODE-based model that can estimate increases in pH^s and incorporated both the reaction plane concept developed by Grozovski and the conventional Nernst diffusion layer model to simulate diffusion processes for $pH^s > 7$ and $pH^s \leq 7$, respectively. Based on the fact that the pH^s increase is enhanced by limited transportation of H^+, as has been described, the following three assumptions are made: (1) the electromigration of ions is neglected, (2) the thickness of the diffusion layer remains constant due to solution convection, and (3) the concentration profiles of H^+ and OH^- in the layer are linear (i.e., a stationary state is assumed). Note that the third assumption does not require that C_H^s is constant.

In the case of $pH^s \leq 7$ (i.e., when $C_H^s \geq C_{OH}^s$ ($= K_w/C_H^s$), **Figure 4A**), the quantity of OH^- is negligible and thus the diffusion of H^+ to the electrode surface can be simply expressed by the Nernst diffusion layer model. In contrast, at $pH^s > 7$ (i.e., when $C_H^s < C_{OH}^s$, **Figure 4B**), OH^- and H^+ ions diffuse to a reaction plane from the electrode surface and from the solution bulk, respectively, and C_H and C_{OH} are balanced (such that $C_H = C_{OH} = \sqrt{K_w} = 1.0 \times 10^{-10}$ mol cm^{-3}) in this plane. By introducing a parameter, β ($0 < \beta < 1$), that determines the position of the reaction plane, the thickness of the OH^- diffusion region and that of the H^+ diffusion region can be written as $(1-\beta)\delta$ and $\beta\delta$,

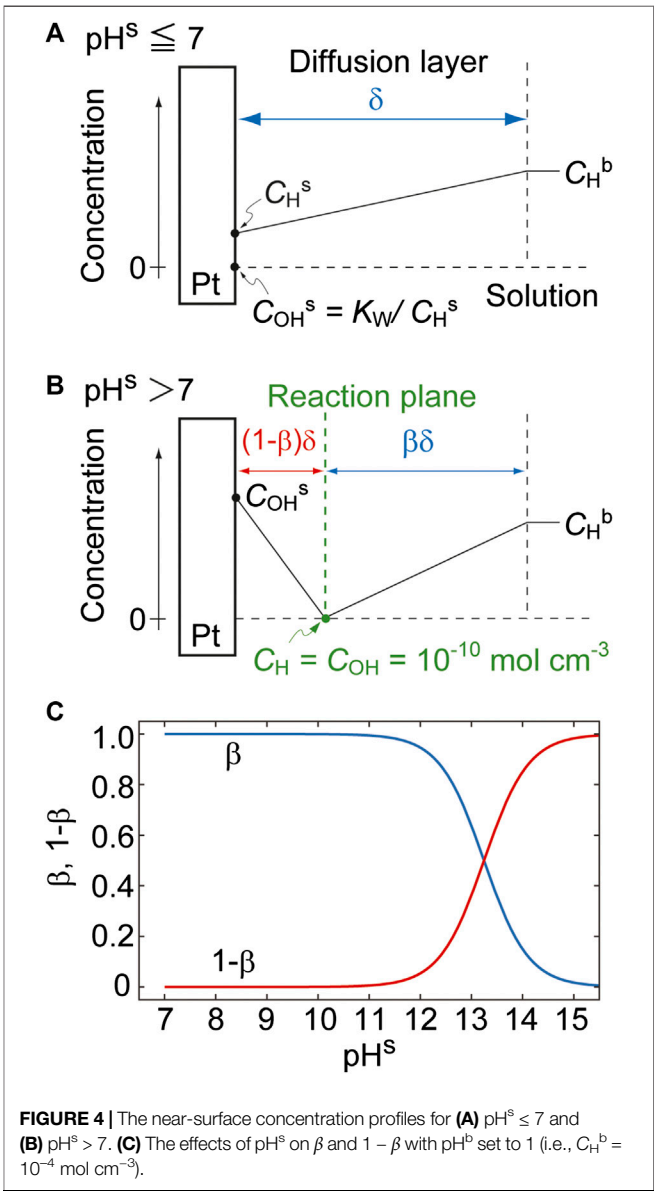

FIGURE 4 | The near-surface concentration profiles for **(A)** $pH^s \leq 7$ and **(B)** $pH^s > 7$. **(C)** The effects of pH^s on β and $1-\beta$ with pH^b set to 1 (i.e., $C_H^b = 10^{-4}$ mol cm^{-3}).

respectively. This parameter is derived by considering that the flux of OH^- to the plane is equal to that of H^+, such that we can write the following.

$$D_{OH}\frac{C_{OH}^{s}-\sqrt{K_w}}{(1-\beta)\delta}=D_H\frac{C_H^{b}-\sqrt{K_w}}{\beta\delta} \tag{12}$$

Here, D_H is the diffusion coefficient of H^+ (9.31×10^{-5} cm^2 s^{-1}) and D_{OH} that of OH^- (5.30×10^{-5} cm^2 s^{-1}). From **Eq. 12**, β and its derivative with respect to C_H^s, $d\beta/dC_H^s$, can be formulated as follows.

$$\beta=\frac{D_H\left(C_H^{b}-\sqrt{K_w}\right)}{D_H\left(C_H^{b}-\sqrt{K_w}\right)+D_{OH}\left(C_{OH}^{s}-\sqrt{K_w}\right)}$$
$$=\frac{D_H\left(C_H^{b}-\sqrt{K_w}\right)C_H^{s}}{\left[D_H\left(C_H^{b}-\sqrt{K_w}\right)-D_{OH}\sqrt{K_w}\right]C_H^{s}+D_{OH}K_w} \tag{13}$$

$$\frac{d\beta}{dC_H^{s}}=\frac{D_HD_{OH}\left(C_H^{b}-\sqrt{K_w}\right)K_w}{\left\{\left[D_H\left(C_H^{b}-\sqrt{K_w}\right)-D_{OH}\sqrt{K_w}\right]C_H^{s}+D_{OH}K_w\right\}^2} \tag{14}$$

Figure 4C shows the effect of pH^s on β and $1-\beta$ for a pH^b value of 1. As expected, the thicknesses of the OH^- (red curve) and H^+ (blue curve) regions increase and decrease with increases in pH^s, respectively. Note that β is defined at $pH^s > 7$.

The derivative of C_H^s with respect to time, dC_H^s/dt, can be derived by considering a small change in the amount of H^+ in the diffusion layer. Assuming a stationary state, such changes can be considered equivalent to the area of the shaded triangles in **Figure 5**, where ΔC_H^s and ΔC_{OH}^s indicate small increases in C_H^s and C_{OH}^s over a short time interval, Δt, respectively. In the case that $pH^s \le 7$, the area of the triangle is determined by both the H^+ diffusion and the reaction of H^+. As such, we have the following equations.

$$\frac{\delta}{2}\Delta C_H^{s}=\frac{D_H}{\delta}\left(C_H^{b}-C_H^{s}\right)\Delta t+r_H\Delta t \tag{15}$$

$$r_H=-k_2C_H^{s}\left(1-\Theta_H\right)+k_{-2}\Theta_H \tag{16}$$

The variable r_H is referred to as the reaction term and has the opposite sign but the same magnitude to the net consumption rate of H^+ at the electrode surface. The introduction of r_H provides a generic model that is applicable to various reactions, as discussed further on. Thus, dC_H^s/dt can be expressed by the following ODE.

$$\frac{dC_H^{s}}{dt}=\frac{2}{\delta}\left[\frac{D_H}{\delta}\left(C_H^{b}-C_H^{s}\right)+r_H\right] \tag{17}$$

In contrast, at $pH^s > 7$, the reaction plane moves towards the electrode as C_{OH}^s decreases and C_H^s increases. In other words, the thickness of the H^+ diffusion region ($\beta\delta$) increases along with increases in C_H^s. It should also be noted that ΔC_{OH}^s is negative when ΔC_H^s is positive. Consequently, the area of the triangle can be expressed by considering the thickness increase, $\delta\Delta\beta$, over the time interval Δt, as shown below.

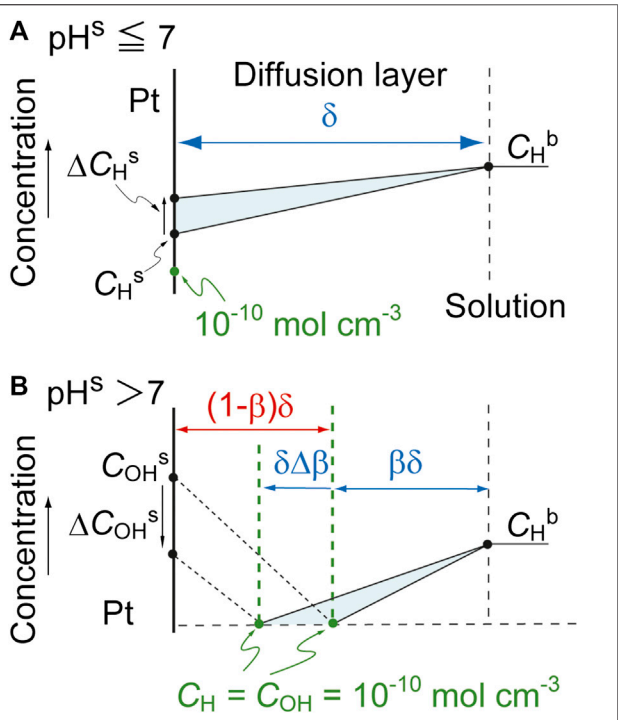

FIGURE 5 | Changes in the near-surface concentration profiles for **(A)** $pH^s \le 7$ and **(B)** $pH^s > 7$. Here, ΔC^s is a small change in C^s over a brief time interval, Δt, and ΔC_H^s is assumed to be positive.

$$\frac{1}{2}\left(C_H^{b}-\sqrt{K_w}\right)\delta\Delta\beta=\frac{D_H}{\beta\delta}\left(C_H^{b}-\sqrt{K_w}\right)\Delta t+r_H\Delta t$$

This can be transformed to the following equations.

$$\frac{1}{2}\left(C_H^{b}-\sqrt{K_w}\right)\delta\left(\frac{d\beta}{dt}\right)=\frac{D_H}{\beta\delta}\left(C_H^{b}-\sqrt{K_w}\right)+r_H$$
$$\frac{1}{2}\left(C_H^{b}-\sqrt{K_w}\right)\delta\left(\frac{d\beta}{dC_H^{s}}\frac{dC_H^{s}}{dt}\right)=\frac{D_H}{\beta\delta}\left(C_H^{b}-\sqrt{K_w}\right)+r_H$$

Finally, dC_H^s/dt can be described as follows.

$$\frac{dC_H^{s}}{dt}=\frac{2}{\left(C_H^{b}-\sqrt{K_w}\right)\delta}\frac{1}{\frac{d\beta}{dC_H^{s}}}\left[\frac{D_H}{\beta\delta}\left(C_H^{b}-\sqrt{K_w}\right)+r_H\right] \tag{18}$$

Numerical Simulation of the Hydrogen Evolution Reaction

We attempted to verify the validity of the above ODE-based model by simulating the *I–U* curve obtained from a Pt electrode in a solution containing 0.1 M H_2SO_4 and 0.03 M Na_2SO_4 (**Figure 6**). This simulation was performed using MATLAB (MathWorks) and the parameter values used are summarized in the figure caption. The second dissociation of H_2SO_4 was ignored in these calculations because the second dissociation constant is much smaller than the first one, and so C_H^b was set to 10^{-4} mol cm^{-3}. This simulation used δ, a fitting parameter having

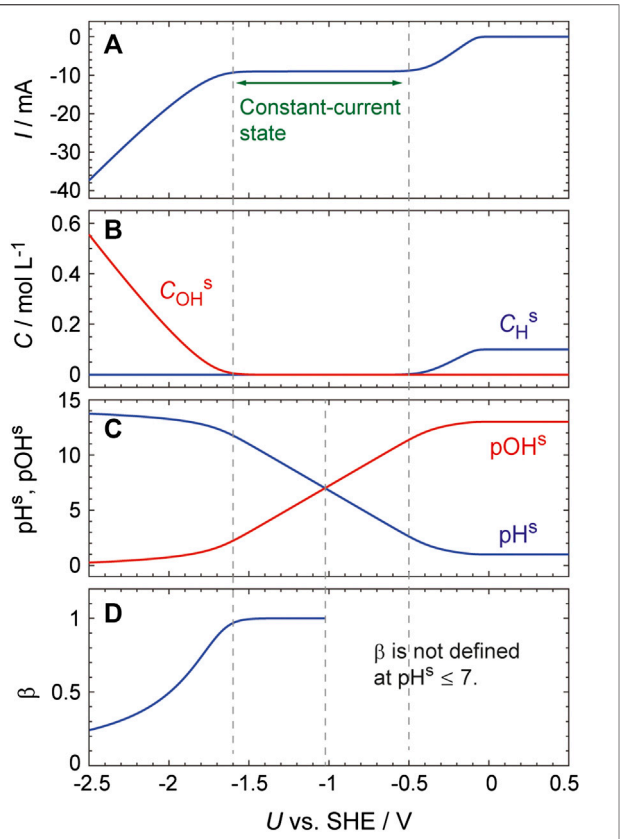

FIGURE 6 | Simulated curves generated with U being scanned at a rate of 0.01 Vs^{-1} from 0.5 V. The parameter values used were: C_H^b = 1.0 × 10^{-4} mol cm^{-3}, δ = 0.01 cm, T = 300 K, N_0 = 2.2 × 10^{-9} mol cm^{-2}, C_{DL} = 2.0 × 10^{-5} F cm^{-2}, A = 0.1 cm^2, R_Ω = 20 Ω, $E_2^0 = E_{-2}^0$ = −0.08 V vs. SHE, k_2^0 = 5.0 × 10^{-3} cm s^{-1}, k_{-2}^0 = 5.0 × 10^{-6} mol cm^{-2} s^{-1}, k_3^0 = 5.0 × 10^{-6} mol cm^{-2} s^{-1}, $\alpha_2 = \alpha_{-2}$ = 0.5.

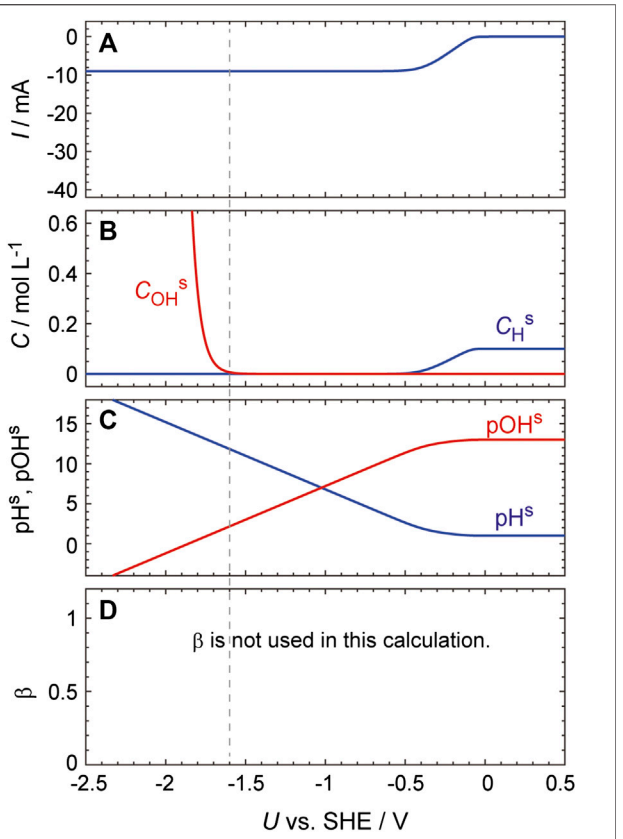

FIGURE 7 | Simulated curves generated using the same process as described in the caption to **Figure 6** except that **Eq. 17** was used to calculate dC_H^s/dt.

a value of 0.01 cm. This value was considered reasonable because, during the actual experiment, the solution near the electrode surface was continuously agitated as a result of the formation of hydrogen bubbles. The values of C_{DL}, E_i^0, k_i^0 and α_i were the same as those employed in prior work (Mukouyama et al., 2015; Mukouyama et al., 2017a) and **Eqs 17** and **18** were respectively used for $pH^s \leq 7$ and $pH^s > 7$. The resulting I–U curve (**Figure 6A**) reproduces the essential features of the experimental results (**Figure 1B**, red curve). Specifically, the current is constant in the potential region between −0.5 and −1.6 V and the absolute value of the current increases as U decreases from −1.6 V. Importantly, these calculations provided a valuable insight of how pH^s changes in the potential range studied: pH^s significantly increases, from approximately 2.5 to 12, in the constant-current state and reaches 13 at −1.8 V (**Figure 6C**).

To understand the mechanism responsible for the significant increase in pH^s, the calculated results were examined in detail. In the potential region associated with the large pH increase (i.e., −0.5 to −1.6 V), the reduction current is almost constant and the slope of the current increase was only approximately 1.2 × 10^{-4} mAV^{-1} in the vicinity of pH^s = 7. However, the rate constant for the formation of on-top H, k_2, increases exponentially with decreases in U (**Eq. 7**), and this in turn increases the rate at which H^+ is consumed at the electrode surface. Thus, pH^s rapidly increases as U decreases in this potential region due to the exponential increase in k_2.

To clarify the role of the reaction plane, a simulation is performed without using **Eq. 18** but using the following equation, which is obtained from a simple modification of **Eq. 17**, at various pH^s values.

$$\frac{dC_H^s}{dt} = \frac{2}{\beta\delta}\left[\frac{D_H}{\beta\delta}\left(C_H^b - C_H^s\right) + r_H\right] \qquad (17\text{-}2)$$

Although β is defined at $pH^s > 7$, the thickness of the H^+ diffusion region can be expressed using β (i.e., the thickness = $\beta\delta$) even at $pH^s \leq 7$ (**Supplementary Figure S4**, right), since the β value is practically equal to 1 under these conditions. Thus, the thickness can be expressed as $\beta\delta$ at any value of pH^s, which allows us to utilize **Eq. 17-2** to a wide pH^s range. The parameters used in this simplified simulation are the same as **Figure 6**. As shown in **Supplementary Figure S4**, I–U curve obtained from this calculation can be regarded as essentially identical to that shown in **Figure 6A**: the largest difference is only 0.03 mA at pH^s = about 12.

As shown in **Figure 6** and **Supplementary Figure S4**, the HER current starts to increase when the pH^s value reaches about 12. This effect is attributed to the rapid decrease in β at $pH^s > 12$, as can be seen in **Figure 4C**. As β decreases, the flux of H^+ ions toward the reaction plane increases because it is inversely proportional to $\beta\delta$ (**Eq. 12**), which in turn results in an increase in the HER current. We thus conclude that the increase in the H^+ flux agrees with the experimental observation that water reduction occurs at low potentials.

Further evidence for this effect was obtained by performing the same calculations using **Eq. 17** at various pH^s values, i.e., without using the concept of the reaction plane. As expected, in this case, an increase in the HER current is not seen even at very low potentials despite the pH^s increasing to greater than 12 (**Figure 7**).

Numerical Simulation of the Hydrogen Peroxide Reduction Reaction

One of the advantages of our model is that it can be applied to various reaction systems simply by replacing the reaction term, r_H (**Eq. 16**). Therefore, we subsequently verified the versatility of our newly developed process by simulating the HPRR on a Pt electrode. The HPRR system is much more complex than the HER because H_2O_2 dissociates into HO_2^- in the diffusion layer ($H_2O_2 \rightleftharpoons HO_2^- + H^+$) depending on pH^s. Furthermore, the oxidation reactions of both H_2O_2 and HO_2^- must also be considered. The associated reaction equations are as follows.

$$Pt + H_2O_2 \underset{k_{-19}}{\overset{k_{19}}{\rightleftharpoons}} Pt\text{-}OOH + H^+ + e^- \quad (19)$$

$$Pt + HO_2^- \xrightarrow{k_{20}} Pt\text{-}OOH + e^- \quad (20)$$

$$Pt\text{-}OOH + OH^- \xrightarrow{k_{21}} Pt + O_2 + H_2O + e^- \quad (21)$$

Rate equations for the reduction and oxidation reactions include the surface concentrations of H_2O_2 (C_{HO}^s) and HO_2^- (C_{HOa}^s). Using these variables, ODEs describing the derivatives of the coverages of adsorbed species with respect to time can be derived, as shown below.

$$\begin{aligned} N_0 d\theta_H/dt &= v_1 - v_{-1}, \\ N_0 d\Theta_H/dt &= v_2 - v_{-2} - 2v_3, \\ N_0 d\theta_{OH}/dt &= 2v_5 + 2v_{5a} - v_6, \\ N_0 d\theta_{OOH}/dt &= v_{19} - v_{-19} + v_{20} - v_{21}, \end{aligned}$$

$$\begin{aligned} &v_1 = k_1 C_H^s \theta_{va},\ v_{-1} = k_{-1}\theta_H \\ &v_2 = k_2 C_H^s (1-\Theta_H),\ v_{-2} = k_{-2}\Theta_H,\ v_3 = k_3 \Theta_H^2 \\ &v_5 = k_5 C_{HO}^s \theta_{va}^2,\ v_{5a} = k_{5a} C_{HOa}^s \theta_{va}^2,\ v_6 = k_6 C_H^s \theta_{OH} \\ &v_{19} = k_{19} C_{HO}^s \theta_{va},\ v_{-19} = k_{-19} C_H^s \theta_{OOH} \\ &v_{20} = k_{20} C_{HOa}^s \theta_{va},\ v_{21} = k_{21}\ (K_w/C_H^s)\theta_{OOH} \end{aligned}$$

Here, θ_H is the coverage of upd-H, θ_{OH} that of Pt-OH and θ_{OOH} that of Pt-OOH, while θ_{va} is the area associated with vacant sites (equal to $1 - \theta_H - \theta_{OH} - \theta_{OOH}$) and v_i is the rate of the corresponding reaction. Note that the on-top H will be located at different sites from other adsorbed species, and so the coverage

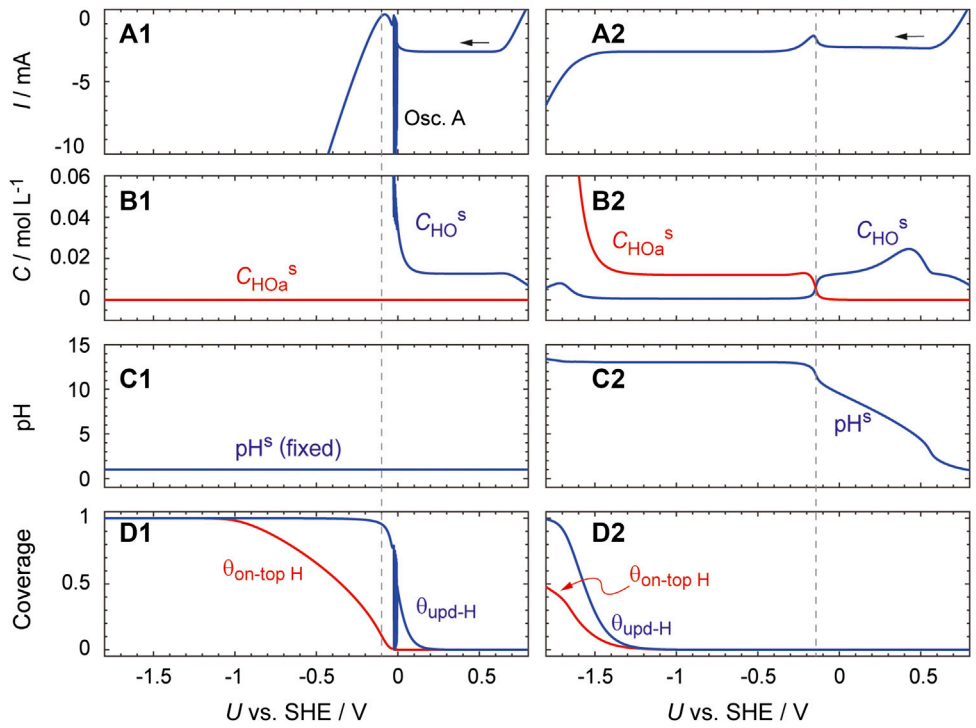

FIGURE 8 | Simulated curves generated with U being scanned at a rate of 0.01 V s^{-1} from 1.0 V. They were obtained **(left)** by performing the calculation with $dC_H^s/dt = 0$ and **(right)** by using **Eqs. 17** and **18** to calculate dC_H^s/dt. Parameter values used were: $C_H^b = 1.0 \times 10^{-4}$ mol cm^{-3}, $C_{HO}^b = 3.1 \times 10^{-4}$ mol cm^{-3}, $A = 0.03$ cm^2, $E_1^0 = E_{-1}^0 = 0.14$ V, $E_6^0 = E_{-19}^0 = 1.13$ V, $E_{19}^0 = 0.84$ V, $E_{20}^0 = E_{21}^0 = 0$ V, $k_1^0 = 1.0 \times 10^{-2}$ cm s^{-1}, $k_{-1}^0 = 1.0 \times 10^{-5}$ mol cm^{-2} s^{-1}, $k_5^0 = k_{5a}^0 = 4.0 \times 10^{-2}$ cm s^{-1}, $k_6^0 = k_{-19}^0 = 1.0 \times 10^{-5}$ cm s^{-1}, $k_{19}^0 = k_{20}^0 = 1.2 \times 10^{-1}$ cm s^{-1}, $k_{21}^0 = 1.2 \times 10^4$ cm s^{-1}, $\alpha_1 = 0.3$, $\alpha_{-1} = 0.7$, $\alpha_6 = 0.72$, $\alpha_i = 0.5$ (i = 19, −19, 20, or 21). The other parameters (namely, δ, T, N_0, R_Ω, C_{DL}, E_2^0, E_{-2}^0, k_2^0, k_{-2}^0, k_3^0, α_2, α_{-2}) were the same as those used for **Figure 6**. The initial values of C_H^s and C^s are set at C_H^b and C_{HO}^b, respectively. To remove errors at an initial stage, the data obtained at $U \leq 0.8$ V are displayed.

of on-top H (Θ_H) is not included in θ_{va}. The reaction term (r_H) can then be expressed as follows.

$$r_H = -v_1 + v_{-1} - v_2 + v_{-2} - v_{5a} - v_6 + v_{19} - v_{-19} + v_{21}$$

For simplicity, it is assumed that H_2O_2 dissociates only at the electrode surface, and hence the diffusion constant of H_2O_2 is the same as that of HO_2^-. Based on this assumption, the derivative of C^s (= $C_{HO}{}^s$ + $C_{HOa}{}^s$) with respect to time can be obtained, as provided below.

$$(\delta/2)\mathrm{d}C^s/\mathrm{d}t = (D_{HO}/\delta)\left(C_{HO}^b - C^s\right) - v_5 - v_{5a} - v_{19} + v_{-19} - v_{20}$$

Here, D_{HO} is the diffusion coefficient of H_2O_2 (1.7×10^{-5} cm^2 s^{-1}). The thickness of the H_2O_2 diffusion layer is assumed to be equal to that of the H^+ diffusion layer (δ) at all pH^s for the following reason. The solution was strongly agitated due to vigorous generation of hydrogen (or oxygen) bubbles, and a bubble detaches from the electrode surface when its diameter reaches about 0.01 cm (Mukouyama et al., 2014). Therefore, in the region of the electrolyte that is more than 0.01 cm away from the electrode, the concentration of the electroactive species is considered to be uniform due to the agitation effect caused by the bubble generation. Thus, it can be assumed that the thickness of the diffusion layer is determined by the size of the bubbles, regardless of the kinds of electroactive species. The surface concentrations of H_2O_2 and HO_2^- ($C_{HO}{}^s$ and $C_{HOa}{}^s$) are subsequently determined based on the law of mass action (that is, $K_a = C_{HOa}{}^s\, C_H{}^s/C_{HO}{}^s$ where K_a is the acid dissociation constant of H_2O_2). Hence, we can write the following.

$$C_{HO}^s = C^s C_H^s/\left(C_H^s + K_a\right)$$
$$C_{HOa}^s = C^s K_a/\left(C_H^s + K_a\right)$$

We obtain $K_a = 1.995 \times 10^{-15}$ mol cm^{-3} (=1.995×10^{-12} mol L^{-1}) from pK_a = 11.7.

Figure 8 shows the results calculated under the above assumptions, together with those calculated by assuming that pH^s does not change from pH^b. This model reproduces the essential features of the experimental observations presented in **Figure 2**. The HPRR current is shown to be constant over the potential region from 0.6 to 0.1 V. In addition, if pH^s is fixed at a constant value (as shown in the left panels in the figure), a current oscillation (oscillation A) appears at ca. −0.05 V and the HER current starts to increase at −0.1 V. Oscillation B, which appeared in the HER region during the actual experiment (**Figure 2B**), is not reproduced. This is because the essential factors to induce oscillation B, namely, an electrode surface inhomogeneity and bubble-induced convection (Mukouyama et al., 2001), are not considered in this simulation.

In the case that a pH^s increase is considered (the right panels), the HPRR current is constant in the potential region below −0.3 V and the HER current increases not at −0.1 V but at −1.45 V. Importantly, the increase in pH^s as U decreases is almost linear and H_2O_2 dissociates into HO_2^- at pH^s values above approximately 11.7 (panels B2 and C2). Oscillation I is absent in contrary to the actual experiment displayed in **Figure 2C**, implying that the simulation of oscillation I requires additional factors. Remarkably, when **Eq. 17** is used to calculate $dC_H{}^s/dt$, the current increase is not reproduced even for $U < -1.45$ V (**Supplementary Figure S5**). These results indicate that the concept of the reaction plane is necessary to capture the essential features of the HPRR.

CONCLUSION

The present work successfully developed an ODE model that can generate simulated pH^s values for various electrochemical reactions. This technique is based on introducing a reaction plane in which the H^+ and OH^- concentrations are balanced under the assumption of a stationary state. Numerical calculations employing this model were able to predict increases in pH^s during the HER at a Pt electrode in H_2SO_4 solutions. This process suitably reproduced the experimental results, including the appearance of a current plateau originating from the limited diffusion of H^+ ions and the occurrence of direct water reduction at low potentials (−1.8 V or lower). Notably, our model has another significant advantage in that it is generally applicable to various reactions simply by replacing the reaction term, r_H (**Eq. 16**). This was demonstrated by simulating both the HER and HPRR, the latter of which exhibits complicated effects of pH. Thus, this work shows that the ODE model permits quantitative estimations of pH^s during various reactions in which H^+ or OH^- are involved, such as the reductions of CO_2 and NO_3^-. Furthermore, with a slight modification, the model can be adopted to the electrochemical oxidations of H_2O and certain organic compounds. We anticipate that this new process will contribute to the future development of various electrocatalysts.

DATA AVAILABILITY STATEMENT

The original contributions presented in the study are included in the article/**Supplementary Material**, further inquiries can be directed to the corresponding author.

AUTHOR CONTRIBUTIONS

All authors listed have made a substantial, direct, and intellectual contribution to the work and approved it for publication.

FUNDING

This work was partially supported by JSPS KAKENHI Grant No. 19K22232.

SUPPLEMENTARY MATERIAL

The Supplementary Material for this article can be found online at: https://www.frontiersin.org/articles/10.3389/fenrg.2020.582284/full#supplementary-material.

REFERENCES

Auinger, M., Katsounaros, I., Meier, J. C., Klemm, S. O., Biedermann, P. U., Topalov, A. A., et al. (2011). Near-surface ion distribution and buffer effects during electrochemical reactions. *Phys. Chem. Chem. Phys.* 13 (36), 16384–16394. doi:10.1039/c1cp21717h

Ayemoba, O., and Cuesta, A. (2017). Spectroscopic evidence of size-dependent buffering of interfacial pH by cation hydrolysis during CO_2 electroreduction. *ACS Appl. Mater. Interfaces* 9 (33), 27377–27382. doi:10.1021/acsami.7b07351

Billy, J. T., and Co, A. C. (2017). Experimental parameters influencing hydrocarbon selectivity during the electrochemical conversion of CO_2. *ACS Catal.* 7 (12), 8467–8479. doi:10.1021/acscatal.7b02373

Carneiro-Neto, E. B., Lopes, M. C., and Pereira, E. C. (2016). Simulation of interfacial pH changes during hydrogen evolution reaction. *J. Electroanal. Chem.* 765, 92–99. doi:10.1016/j.jelechem.2015.09.029

Deligianni, H., and Romankiw, L. T. (1993). In situ surface pH measurement during electrolysis using a rotating pH electrode. *IBM J. Res. Dev.* 37 (2), 85–95. doi:10.1147/rd.372.0085

Dunwell, M., Yang, X., Setzler, B. P., Anibal, J., Yan, Y., and Xu, B. (2018). Examination of near-electrode concentration gradients and kinetic impacts on the electrochemical reduction of CO_2 using surface-enhanced infrared spectroscopy. *ACS Catal.* 8 (5), 3999–4008. doi:10.1021/acscatal.8b01032

Fuladpanjeh-Hojaghan, B., Elsutohy, M. M., Kabanov, V., Heyne, B., Trifkovic, M., and Roberts, E. P. L. (2019). In-operando mapping of pH distribution in electrochemical processes. *Angew Chem. Int. Ed. Engl.* 58 (47), 16815–16819. doi:10.1002/anie.201909238

Grozovski, V., Vesztergom, S., Láng, G. G., and Broekmann, P. (2017). Electrochemical hydrogen evolution: H^+ or H_2O reduction? A rotating disk electrode study. *J. Electrochem. Soc.* 164 (11), E3171–E3178. doi:10.1149/2.0191711jes

Hall, A. S., Yoon, Y., Wuttig, A., and Surendranath, Y. (2015). Mesostructure-induced selectivity in CO_2 reduction catalysis. *J. Am. Chem. Soc.* 137 (47), 14834–14837. doi:10.1021/jacs.5b08259

Ji, J., Cooper, W. C., Dreisinger, D. B., and Peters, E. (1995). Surface pH measurements during nickel electrodeposition. *J. Appl. Electrochem.* 25 (7), 642–650. doi:10.1007/BF00241925

Kas, R., Kortlever, R., Yılmaz, H., Koper, M. T. M., and Mul, G. (2015). Manipulating the hydrocarbon selectivity of copper nanoparticles in CO_2 electroreduction by process conditions. *Chem. Electro. Chem.* 2 (3), 354–358. doi:10.1002/celc.201402373

Katsounaros, I., Meier, J. C., Klemm, S. O., Topalov, A. A., Biedermann, P. U., Auinger, M., et al. (2011). The effective surface pH during reactions at the solid-liquid interface. *Electrochem. Commun.* 13 (6), 634–637. doi:10.1016/j.elecom.2011.03.032

Koper, M. T. M., and Sluyters, J. H. (1991). Electrochemical oscillators: their description through a mathematical model. *J. Electroanal. Chem. Interfacial Electrochem.* 303 (1), 73–94. doi:10.1016/0022-0728(91)85117-8

Lamy-Pitara, E., El Mouahid, S., and Barbier, J. (2000). Effect of anions on catalytic and electrocatalytic hydrogenations and on the electrocatalytic oxidation and evolution of hydrogen on platinum. *Electrochim. Acta.* 45 (25-26), 4299–4308. doi:10.1016/s0013-4686(00)00522-3

Leenheer, A. J., and Atwater, H. A. (2012). Imaging water-splitting electrocatalysts with pH-sensing confocal fluorescence microscopy. *J. Electrochem. Soc.* 159 (9), H752–H757. doi:10.1149/2.022209jes

Ma, M., Trześniewski, B. J., Xie, J., and Smith, W. A. (2016). Selective and efficient reduction of carbon dioxide to carbon monoxide on oxide-derived nanostructured silver electrocatalysts. *Angew. Chem. Int. Ed.* 55 (33), 9748–9752. doi:10.1002/anie.201604654

Mukouyama, Y., Hommura, H., Nakanishi, S., Nishimura, T., Konishi, H., and Nakato, Y. (1999). Mechanism and simulation of electrochemical current oscillations observed in the H_2O_2-reduction reaction on platinum electrodes in acidic solutions. *Bull. Chem. Soc. Jpn.* 72 (6), 1247–1254. doi:10.1246/bcsj.72.1247

Mukouyama, Y., Kawasaki, H., Hara, D., and Nakanishi, S. (2015). Transient chaotic behavior during simultaneous occurrence of two electrochemical oscillations. *J. Solid State Electrochem.* 19 (11), 3253–3263. doi:10.1007/s10008-015-2813-z

Mukouyama, Y., Kawasaki, H., Hara, D., Yamada, Y., and Nakanishi, S. (2017a). Appearance of new oscillation (named oscillation H) induced by Na_2SO_4 and K_2SO_4 in electroreduction of H_2O_2 on platinum. *J. Electrochem. Soc.* 164 (2), H1–H10. doi:10.1149/2.0011702jes

Mukouyama, Y., Kawasaki, H., Hara, D., Yamada, Y., and Nakanishi, S. (2017b). Appearance of new oscillations (named oscillations I and J) during reduction of H_2O_2 on platinum electrode. *J. Electrochem. Soc.* 164 (9), H675–H684. doi:10.1149/2.1561709jes

Mukouyama, Y., Kikuchi, M., and Okamoto, H. (2008). Appearance of new potential oscillation during hydrogen evolution reaction by addition of Na_2SO_4 and K_2SO_4. *J. Electroanal. Chem.* 617 (2), 179–184. doi:10.1016/j.jelechem.2008.02.006

Mukouyama, Y., Nakanishi, S., Konishi, H., Ikeshima, Y., and Nakato, Y. (2001). New-type electrochemical oscillation caused by electrode-surface inhomogeneity and electrical coupling as well as solution stirring through electrochemical gas evolution reaction. *J. Phys. Chem. B* 105 (44), 10905–10911. doi:10.1021/jp012461s

Mukouyama, Y., Nakazato, R., Shiono, T., Nakanishi, S., and Okamoto, H. (2014). Potential oscillation during electrolysis of water in acidic solutions under numerous conditions. *J. Electroanal. Chem.* 713, 39–46. doi:10.1016/j.jelechem.2013.11.002

Ooka, H., Figueiredo, M. C., and Koper, M. T. M. (2017). Competition between hydrogen evolution and carbon dioxide reduction on copper electrodes in mildly acidic media. *Langmuir* 33 (37), 9307–9313. doi:10.1021/acs.langmuir.7b00696

Rudd, N. C., Cannan, S., Bitziou, E., Ciani, I., Whitworth, A. L., and Unwin, P. R. (2005). Fluorescence confocal laser scanning microscopy as a probe of pH gradients in electrode reactions and surface activity. *Anal. Chem.* 77 (19), 6205–6217. doi:10.1021/ac050800y

Ryu, J., Wuttig, A., and Surendranath, Y. (2018). Quantification of interfacial pH variation at molecular length scales using a concurrent non-faradaic reaction. *Angew. Chem. Int. Ed.* 57 (30), 9300–9304. doi:10.1002/anie.201802756

Schmickler, W., and Santos, E. (2010). *Interfacial electrochemistry*. 2nd edn. Berlin, Germany: Springer-Verlag.

Sen, S., Liu, D., and Palmore, G. T. R. (2014). Electrochemical reduction of CO_2 at copper nanofoams. *ACS Catal.* 4 (9), 3091–3095. doi:10.1021/cs500522g

Singh, M. R., Clark, E. L., and Bell, A. T. (2015). Effects of electrolyte, catalyst, and membrane composition and operating conditions on the performance of solar-driven electrochemical reduction of carbon dioxide. *Phys. Chem. Chem. Phys.* 17 (29), 18924–18936. doi:10.1039/c5cp03283k

Singh, M. R., Kwon, Y., Lum, Y., Ager, J. W., and Bell, A. T. (2016). Hydrolysis of electrolyte cations enhances the electrochemical reduction of CO_2 over Ag and Cu. *J. Am. Chem. Soc.* 138 (39), 13006–13012. doi:10.1021/jacs.6b07612

Skúlason, E., Tripkovic, V., Björketun, M. E., Gudmundsdóttir, S., Karlberg, G., Rossmeisl, J., et al. (2010). Modeling the electrochemical hydrogen oxidation and evolution reactions on the basis of density functional theory calculations. *J. Phys. Chem. C* 114 (42), 18182–18197. doi:10.1021/jp1048887

Song, J., Song, H., Kim, B., and Oh, J. (2019). Towards higher rate electrochemical CO_2 conversion: from liquid-phase to gas-phase systems. *Catalysts* 9 (3), 224. doi:10.3390/catal9030224

Suzurikawa, J., Nakao, M., Kanzaki, R., and Takahashi, H. (2010). Microscale pH gradient generation by electrolysis on a light-addressable planar electrode. *Sensor. Actuator. B Chem.* 149 (1), 205–211. doi:10.1016/j.snb.2010.05.058

Varela, A. S., Kroschel, M., Reier, T., and Strasser, P. (2016). Controlling the selectivity of CO_2 electroreduction on copper: the effect of the electrolyte concentration and the importance of the local pH. *Catal. Today* 260, 8–13. doi:10.1016/j.cattod.2015.06.009

Yang, K. D., Ko, W. R., Lee, J. H., Kim, S. J., Lee, H., Lee, M. H., et al. (2017). Morphology-directed selective production of ethylene or ethane from CO_2 on a Cu mesopore electrode. *Angew. Chem. Int. Ed.* 56 (3), 796–800. doi:10.1002/anie.201610432

Yoon, Y., Hall, A. S., and Surendranath, Y. (2016). Tuning of silver catalyst mesostructure promotes selective carbon dioxide conversion into fuels. *Angew. Chem. Int. Ed.* 55 (49), 15282–15286. doi:10.1002/anie.201607942

Zhang, F., and Co, A. C. (2020). Direct evidence of local pH change and the role of alkali cation during CO_2 electroreduction in aqueous media. *Angew. Chem. Int. Ed.* 59 (4), 1674–1681. doi:10.1002/anie.201912637

Conflict of Interest: The authors declare that the research was conducted in the absence of any commercial or financial relationships that could be construed as a potential conflict of interest.

frontiers in Energy Research

REVIEW
published: 27 January 2021
doi: 10.3389/fenrg.2020.613092

Activity and Stability of Oxides During Oxygen Evolution Reaction—From Mechanistic Controversies Toward Relevant Electrocatalytic Descriptors

Aleksandar R. Zeradjanin[1]*, *Justus Masa*[1], *Ioannis Spanos*[1] and *Robert Schlögl*[1,2]

[1]Max Planck Institute for Chemical Energy Conversion, Mülheim an der Ruhr, Germany, [2]Fritz-Haber-Institut der Max-Planck Gesellschaft, Berlin, Germany

Plotting the roadmap of future "renewable energy highway" requires drastic technological advancement of devices like electrolyzers and fuel cells. Technological breakthrough is practically impossible without advanced fundamental understanding of interfacial energy conversion processes, including electrocatalytic water splitting. Particularly challenging is the oxygen evolution reaction which imposes high demands on the long-term activity of electrocatalysts and electrode support materials. To cross the "Rubicon" and in a deterministic manner claim that we developed principles of rational catalyst design, we need first to comprehend the determinants of electrocatalytic activity as well as character of their time evolution. How reliable are reported activity and stability trends, could we interrelate activity and stability, and how meaningful that relation really is are some of the important questions that have to be tackled in building of a more comprehensive view on critically important anodic oxygen evolution.

Keywords: electrocatalysis, oxygen evolution, activity–stability relations, mechanism, catalytic descriptors

OPEN ACCESS

Edited by:
Kai S. Exner,
Sofia University, Bulgaria

Reviewed by:
Michael Bron,
Martin Luther University of Halle-Wittenberg, Germany
Kristina Tschulik,
Ruhr University Bochum, Germany

***Correspondence:**
Aleksandar R. Zeradjanin
aleksandar.zeradjanin@cec.mpg.de

Specialty section:
This article was submitted to Electrochemical Energy Conversion and Storage, a section of the journal Frontiers in Energy Research

Received: *01 October 2020*
Accepted: *23 December 2020*
Published: *27 January 2021*

Citation:
Zeradjanin AR, Masa J, Spanos I and Schlögl R (2021) Activity and Stability of Oxides During Oxygen Evolution Reaction—From Mechanistic Controversies Toward Relevant Electrocatalytic Descriptors. Front. Energy Res. 8:613092. doi: 10.3389/fenrg.2020.613092

INTRODUCTION

Importance of Oxygen Evolution for Sustainable Energy Conversion and Storage

The need for clean and renewable energy sources is one of the most important challenges of modern societies (Lewis and Nocera, 2006). The possibility to store or convert energy from renewable sources (predominantly solar and wind) is of essential importance but conceals a scientific and technical complexity, which up-to-date has eluded definitive comprehension (Greeley and Markovic, 2012). Although considerable human and material resources have been recruited to resolve numerous issues related to renewable energy conversion and storage, the implementation of practical and scalable technologies still appears not to be economically feasible (Gasteiger and Markovic, 2009). One of the central challenges is the intermittent nature of renewable energy sources (Bockris, 2013). Namely, electricity generated by photovoltaics or wind turbines fluctuates with time in an unpredictable manner. A proper response to intermittency would be to store excess electricity in the form of chemical bonds and later, on demand, reconvert the stored chemical energy into electricity (Bockris, 1972). From a conceptual point of view, this necessitates the deployment of devices like electrolyzers and fuel cells that are capable of instantly or quickly responding to the oscillations of the power grid (Katsounaros et al., 2014). The possibility to generate liquid fuels (e.g., methanol) from CO_2,

although very appealing, is still too far from practical efficiencies. A more realistic approach is to convert renewable electricity to hydrogen gas by means of electrolytic water splitting. Water electrolysis is a mature technology, which however is still not efficient enough to be recognized as a state-of-the-art solution for the storage of renewable electricity. In the past, alkaline water electrolysis was favored due to the possibility to use cheap electrode and electrolyte materials in such environments. Nowadays, acidic polymer electrolyte membrane (PEM) electolyzers are more attractive as they allow much higher current densities despite the necessity to use expensive and rare noble metals as components of the electrode materials. The two main reactions occurring in an acidic (pH = 0) electrolyzers are:

$$2H^+ + 2e^- \rightleftharpoons H_2 \quad E^\circ = 0.00\ \text{V vs. SHE}, \tag{1}$$

$$2H_2O \rightleftharpoons O_2 + 4H^+ + 4e^- \quad E^\circ = 1.23\ \text{V vs. SHE}. \tag{2}$$

Similar equations can be written for alkaline (pH = 14) electrolyzers

$$2H_2O + 2e^- \rightleftharpoons H_2 + 2OH^- \quad E^\circ = -0.800\ \text{V vs. SHE}, \tag{3}$$

$$4OH^- \rightleftharpoons O_2 + 2H_2O + 4e^- \quad E^\circ = 0.403\ \text{V vs. SHE}. \tag{4}$$

Potentials are expressed on the SHE (standard hydrogen electrode) scale to clearly indicate the impact of pH value on the absolute potential scale (for an explanatory note of the absolute potential scale (Recommendations, 1986)). From the shown reactions (1–4), it is evident from the thermodynamic view point that it would be best to conduct hydrogen evolution (HER) in acidic media and oxygen evolution reaction (OER) in alkaline media in a system with two electrolytes and with a theoretical voltage of 0.4 V (Zeradjanin et al., 2014b). This system requires a bipolar membrane (Simons and Khanarian, 1978), and unavoidably, a catalyst that will accelerate water ionization (Oener et al., 2020). However, this kind of acido-alkaline system still suffers major instabilities (Zeradjanin et al., 2014b; Oener et al., 2020).

The HER, despite being very complex, is a relatively facile two-electron process involving only one intermediate (Zeradjanin et al., 2016). However, catalysis of the oxygen evolution reaction (OER) that requires the exchange of four electrons and four protons and the formation of at least two (probably three) intermediates (Dau et al., 2010) is even more challenging. Complexity and low intrinsic rate of OER as electrocatalytic process is actually at the very root of why widespread deployment of water electrolysis is still postponed. Therefore, in-depth understanding of electrocatalytic interfaces at relevant dynamic conditions, including the formation and mutual interaction of the intermediates, is one of the essential tasks that have to be fulfilled before we can come up with rational approaches of designing materials with superior electrocatalytic properties.

Reaction Pathway(s)

If we take into consideration the intermediates that participate in the OER, there are two distinct reaction pathways. Both of them are based on the assumption that under conditions of anodic polarization, water behaves as a Brönsted acid. The simplest pathway assumes partial oxidation of water in the first step, which comprises of electron transfer from physiosorbed water molecule to the electrode surface and deprotonation of water resulting in OH_{ad} formation (React. 5). Further, electron transfer and deprotonation of OH_{ad} in the second step and formation of O_{ad} (React. 6) as a prerequisite for chemical recombination of O_{ad} in the third step and formation of O_2 molecule (React. 7).

$$H_2O \rightleftarrows HO_{ad} + H^+ + e^-, \tag{5}$$

$$HO_{ad} \rightleftarrows O_{ad} + H^+ + e^-, \tag{6}$$

$$2O_{ad} \rightleftarrows O_2. \tag{7}$$

This means that steps **Eq. 5** and **Eq.6** should happen at the same site, but it is also necessary to have the two sites next to each other to enable step **Eq.7**. Considering that in the lattice of the most active commercial electrocatalysts used for anodic oxidations (i.e., rutile RuO_2), the Ru–Ru distance in the tetragonal plane is 3.5 Å (McKeown et al., 1999) and that the distance between two oxygen atoms in the oxygen molecule is approximately 1.2 Å, it is necessary that the Ru–O bond involving oxygen adsorbed at coordinatively unsaturated site bends toward a neighboring Ru–O in the tetragonal plane. Both mentioned Ru–O bonds have a length of around 1.95 Å and mutual angle of 90°, implying that the Ru–O bond involving oxygen adsorbed at coordinatively unsaturated site would need to bend for approximately 1.5 Å. Energetically, this should probably not be favored due to existence of nonbonding electron pairs of oxygen as well as due to parallel dipoles of Ru–O which should repel each other. Worth to mention is that under *in operando* conditions where a wide range of potentials is applied including potentials sufficient for OER to commence, stretching of metal–oxygen bonds is almost negligible, fluctuating around 0.05 Å (Nong et al., 2018). DFT-based analysis also indicates skepticism about participance of recombination step **Eq.7** at the RuO_2 surface; however, it cannot be excluded (Ma et al., 2018).

Besides the recombination pathway, a very intuitive pathway is the one usually considered in most computational models. Although discussed initially in the late 1960s (Damjanovic et al., 1966), it lends its popularity today to DFT studies (Rossmeisl et al., 2005, 2007). According to this pathway, the first two steps are like in the case of the recombination step (**React. 5** and **React. 6**). In the third step, O_{ad} reacts with water to form HOO_{ad} together with transfer of a proton and electron (React. 8). Finally, in the fourth step, electron transfer from HOO_{ad} to the electrode surface together with release of a proton into the electrolyte is coupled with oxygen formation (React. 9).

$$O_{ad} + H_2O \rightleftarrows HOO_{ad} + H^+ + e^-, \tag{8}$$

$$HOO_{ad} \rightleftarrows O_2 + H^+ + e^-. \tag{9}$$

In comparison to the mechanism in acidic electrolytes, a distinct feature of the reaction pathway in alkaline electrolytes is that it starts with an elementary step in which only one electron is exchanged (React. 10), in other words, there is no deprotonation. In this step, a hydroxyl ion from the electrolyte

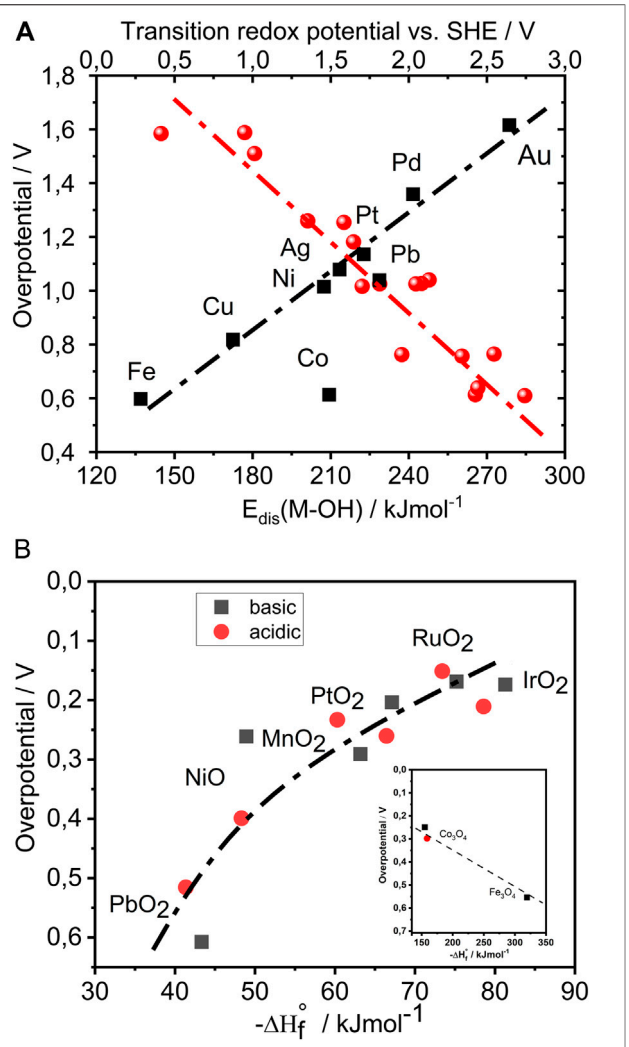

FIGURE 1 | A) Measured OER overpotential for 9 metals in 1M KOH, at 25°C and 1 A/cm^{-2}, as a function of computed heat of M-OH formation (red circles). Replotted using data from Rüetschi and Delahay (1955). Measured overpotential for OER as a function of characteristic redox transitions from lower to higher oxidation state (black rectangular), in 5M KOH at temperature of 25°C and 1 A/cm^{-2}. Replotted using data from Rasiyah (1984). In the original reference, the computed M-OH formation heats were estimated using two or sometimes three methods. This is the reason why in the plot marked with red there is overall more than 9 points. **(B)** Illustration of activity trends for OER in acidic and alkaline media where overpotential is a function of bulk enthalpy of transition from lower to higher oxidation state of oxide. Replotted using data from (Trasatti, 1984). In the inset are shown two spinels removed from the original "volcano" plot.

is getting adsorbed on the metal-center forming HO_{ad} with simultaneous transfer of an electron to the electrode. In the second step (React. 11), OH^- from the electrolyte deprotonates HO_{ad} forming a water molecule and O_{ad} while simultaneously transferring an electron to the electrode. The final step is recombination as proposed for the acidic media (React. 7)

$$OH^- \rightleftharpoons OH_{ad} + e^-, \quad (10)$$

$$HO_{ad} + OH^- \rightleftarrows O_{ad} + H_2O + e^-. \quad (11)$$

If we make the analogy between water electrolysis and gas-phase (de)hydrogenation, we can observe that in the case of OER, water is getting dehydrogenated. The released hydrogen atoms, electrons in the outer circuit and the solvated protons in the electrolyte, are transferred to the cathode to participate in hydrogenation. Concerted proton/electron transfer is possible; however, it is usually considered that electron transfer is much more facile in comparison to proton transfer. This leaves the open possibility, not only for a reaction pathway or mechanism with decoupled proton/electron transfer, especially at higher polarizations (overpotentials), but also for the existence of destabilized intermediates that are not identified by the usual schemes of reaction pathways. To further broaden this knowledge, the reader is directed to interesting discussions on other mechanistic pathways, including the bifunctional and binuclear mechanisms (Busch, 2018).

Origins of Electrocatalytic Performance and Existing Activity Trends

Due to the nature of the reaction, that is, decomposition of the solvent itself including strong acidification of the interfacial region during OER at high anodic potentials, every element from the periodic table used as electrocatalyst will be oxidized with time. Therefore, it is well accepted that metal oxides are the dominant class of chemical compounds that could survive the corrosive conditions of OER on a long term. From the reaction pathways shown above, it is straightforward that bond strengths of intermediates at the oxide surfaces are one of the essential parameters that determine kinetics of OER. Activity trends for OER were already observed in the 50s (Rüetschi and Delahay, 1955). In this important work, the M–OH bond strength was introduced as the first activity descriptor for OER. A linear relationship between the overpotential for OER in alkaline electrolyte and the M–OH bond strength was observed from which the computed M–OH bond strength was directly proportional to drop in the overpotential for OER, leading to the following activity trend for oxidized metals. Co > Fe > Cu > Ni > Pb > Ag > Cd > Pd > Pt > Au (Rüetschi and Delahay, 1955). From a semiquantitative point of view, the relationship in **Figure 1A** suggests that a change in adsorption energy of approximately 100 kJ/mol could change the overpotential by almost 1V, thus revealing great potential in enhancing kinetics of OER by tuning the M–OH adsorption energy. In this work, some important oxides are missing (those having less than seven d-electrons in the metallic state); however, it represents an important initial contribution toward understanding electrocatalysis of the OER. Later in the 1970s, more systematic studies of the OER on oxidized metals in acidic media were made, where the activity trend followed the order: Ir ~ Ru > Pd > Rh > Pt > Au > Nb (Miles, 1976), as well as analysis of thermally prepared oxides in alkaline media with the activity trend following the order: Ru > Ir ~ Pt ~ Rh ~ Pd ~ Ni ~ Os >> Co >> Fe (Miles, 1978). Evidently, the OER activity trends on these two sets of samples were different, although it was not clear whether that was due to the chemistry of the oxides or pH of the electrolyte.

In other words, either adsorption energies of intermediates like HO_{ad} strongly depend on pH or besides adsorption energy of intermediates we have additional governing factors which influence the kinetics of OER. In that context, important to notice is that anodic oxidation of water and/or adsorbed oxygen species originating from water requires previous transition of metal cation from lower to higher oxidation state. Higher oxidation state of cation will be more susceptible for the electron from adsorbed oxygen species. After the electron is transferred from the adsorbed oxygen species to the metal cation, the cation will get reduced and return to the initial oxidation state. In this way, a redox cycle is established for each elementary step. This requires an overlap of energy levels of the d-orbitals of the metal cation and energy levels of the p-orbitals of adsorbed oxygen species at the potential of redox transition. Redox transitions as descriptor were investigated in the 1980s where the dependence of reaction rate on redox transition is shown in **Figure 1A** (Rasiyah, 1984). The dependence predicts that for a drop in redox potential of 500 mV, the overpotential should drop by 250 mV. Considering the linear relation from **Figure 1A**, it seems formally that lower redox transitions relate to stronger OH adsorption; however, all the catalysts shown in these datasets were having seven or more d-electrons, which make the data incomplete. The question is what are in fact the most relevant redox transitions for the OER activity? More precisely, are the relevant redox transitions only those which overlap with OER onset or relevant or also those at much more negative potentials?

Trasatti in the 1980s systematically investigated thermally prepared oxides under acidic and alkaline conditions (Trasatti, 1984). Although the pH effect on kinetics could be clearly noticed, the general activity trends in acidic and alkaline media, interestingly, were very similar. Experiments indicate that RuO_2 is the most active oxide for OER. However, due to the low stability of RuO_2, the material of choice was typically IrO_2, which is less active than RuO_2, but very stable under the harsh oxidizing conditions of OER. It is very important to notice that RuO_2 and IrO_2 are among the very few electrocatalytically active oxides that exhibit metallic-type conductivity. The reason for this is the relatively small electronegativity difference between oxygen and metal (less than 1.3 units) that results in the absence of a band gap (Di Quarto et al., 1997). Illustration of activity trends for OER, based on experimental data gathered by Trasatti, is shown in the form of plot in **Figure 1B**. Overpotential is given as a function of enthalpy of transition from lower to higher oxidation state of the metal oxide, a bulk parameter related to difference in surface adsorption energy of two intermediates as well as related to characteristic redox transitions of oxides. Like in thermal chemistry, the high reaction rate was attributed to optimal bond strengths of one or more intermediates. Optimal bond strength is expressed by a qualitative rule "neither too strong nor too weak," today's widely accepted paradigm of catalysis known as Sabatier principle. If the binding of the intermediates is too strong, then the recombination of the intermediates should be inhibited. At the same time, if binding of the intermediate is too weak, the intermediate will desorb before the product is formed. Despite the importance of the Sabatier principle being recognized in electrocatalysis early on, old works (Rüetschi and Delahay, 1955; Miles, 1976) did not explain activity trends using the concept of the "volcano" plot. On the contrary, Trasatti's model was taken as relevant, probably due to the fact that the descriptor he introduced was a bridge between adsorption energies and redox transitions, two essential parameters influencing OER kinetics. The "volcano" plot shown in the original reference (Trasatti, 1984) was perceived for decades as confirmation that the Sabatier principle also holds in OER electrocatalysis. A similar plot was obtained by computational chemists, several decades later. Namely, works of Rossmeisl and Norskov are showing similar trends with slight differences at the top of the "volcano" (Rossmeisl et al., 2007). Computationally obtained trends predicted Co_3O_4 to be the most active catalyst for OER, which does not correspond to the well-established experimental activity trends. Later, computational chemists revised their conclusions, including the so-called Hubbard correction into the analysis, and taking into consideration electrostatic repulsions coupled to the adsorption process, resulting in a consistency with the experimental trends. Also, besides individual adsorption energies, they used the difference in adsorption energies of two intermediates ($\Delta G_{ad}(O)-\Delta G_{ad}(OH)$) as a descriptor ((Man et al., 2011). In comparison to the individual adsorption energy, the differential descriptor was analogous to the previously mentioned bulk enthalpy of transition from lower to higher oxidation state of oxide. However, the data points in **Figure 1B** were obtained from the OER performances of oxides with two different crystal lattices, namely, the rutile-type and the spinel-type (inset). In particular, the weakly binding branch of Trasatti's "volcano" plot contains rutile oxides, while the strongly adsorbing branch is based on spinel oxides (Co_3O_4 and Fe_3O_4). Therefore, the resulting dependence for the rutiles should be pseudo-linear where increase in the binding strength of the intermediates should be coupled with a drop in the overpotential for OER. In a semiquantitative manner, it seems that for a change in the enthalpy of transition from lower to higher oxidation state of about 50 kJ/mol, the overpotential would change by 500 mV, which is interestingly similar to what was predicted earlier (Rüetschi and Delahay, 1955). Besides the rutile and spinel oxides, perovskites have attracted the interests of researchers; however, their stability in acidic electrolytes is extremely low (Bockris, 1984). As a matter of fact, only rutile structures exhibit high practical stability under the harsh oxidizing conditions of water splitting in acidic media (Martelli et al., 1994). Worth also mentioning is that in the discussed literature (period 1950s–1980s), activity trends were usually analyzed at technically relevant conditions, meaning current density of 1 A cm^{-2}, usually concentrated electrolytes and temperatures of 80°C or higher. This is a probable reason why trends in older literature could deviate from the modern literature where experiments are done at 25°C and current densities of few tens of mA cm^{-2} (McCrory et al., 2013; Frydendal et al., 2014). The free energy relations shown in **Figure 1** are more qualitative than quantitative in nature; however, validity of the trends was widely accepted until today. At the same time, the shown trends were mostly explanatory in nature. The predictive

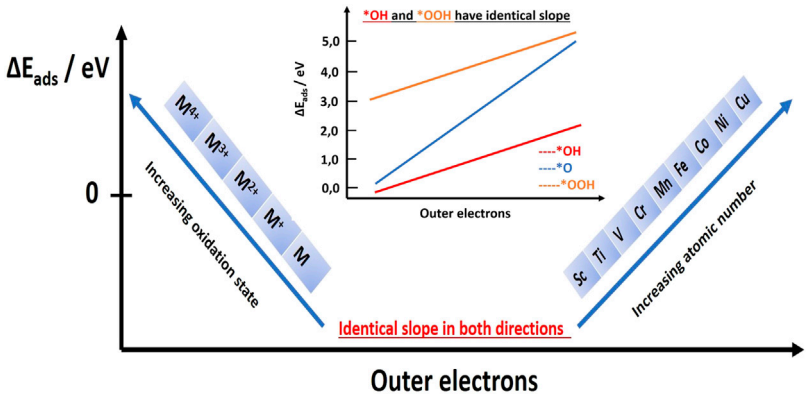

FIGURE 2 | Illustration of how the adsorption energies change with the number of outer electrons for different metals and for various oxidation states of one metal. Replotted using information from Calle-Vallejo et al. (2013). In the inset is the illustration of scaling relations indicating that the change in the adsorption energy of one of the OER intermediates, due to change in electronic configuration (number of outer electrons), alters adsorption energies of the other two OER intermediates in the same manner. Importantly, adsorption energies of *OH and *OOH are also quantitatively changing in the same manner. Replotted using data from Calle-Vallejo et al. (2011).

power based on existing understanding of electrocatalysis was shown to be limited. In other words, there is no electrocatalyst that could really overcome the activity of RuO_2, and there is no known guiding principle of design thus far that could drive us in that direction.

Modern Catalytic Descriptors and Impact of Computational Chemistry

A catalytic descriptor is a relatively easily tunable property of a catalytic material or property of electrode/electrolyte interface that can be brought into direct relation with the reaction rate. A descriptor should have an explanatory role and predictive role. In other words, it has to shed light on activation processes and give a hint how to accelerate the reaction rate. In the last 10–15 years, intensive efforts were undertaken to discover new catalytic descriptors that could shed additional light on the origins of the electrocatalytic activity of OER, further contribute to building the theory of electrocatalysis as well as to advance rational catalyst design. Despite electrochemistry being a primarily experimental science, it is interesting that the most influential and authoritative descriptors and activity trends came from works of computational chemists (Nørskov et al., 2004; Rossmeisl et al., 2005). The school of Norskov and Rossmeisl extended the Anderson–Newns model for metal surfaces from 1960s (Newns, 1969) and computed adsorption energies of intermediates using the density functional theory (DFT). In a qualitative manner, parallel to metal surfaces can be deduced for oxides, where adsorbate bond strengths vary linearly with the relative position of the metal d-band center with respect to the Fermi level of the metal. In the case of oxides, what is relevant is the filling of bonding and antibonding orbitals created by hybridization of d-orbitals of the metal and O_{2p} orbitals of oxygen species in the oxide. After the interaction, d-orbitals are split into t_{2g} and e_g orbitals, whose filling determines the bond strengths of intermediates. For each of the reactions that describe the elementary steps, the corresponding change in free energy can be derived. The most endergonic elementary step (the so-called potential-determining step) defines what intermediate is the most difficult to obtain. Therefore, the introduced computational activity descriptor known as thermodynamic overpotential corresponds to the energy required to overcome the potential-determining step (PDS) per unit charge transfer. Importantly, Rossmeisl and Norskov showed that adsorption energies of typical OER intermediates are linearly related (**Figure 2**), constituting the so-called scaling relations (Man et al., 2011). This means that if we alter the bond strength of one intermediate, we alter the bond strength of the other intermediates, for example, by weakening HO_{ad}, we are also weakening HOO_{ad} and strengthening O_{ad}. In other words, for a reaction pathway based on reactions **Eqs 5**, **6**, **8**, and **9** and the corresponding changes in free energy of the elementary step, it is noticed universally that sum of change in free energies of **Eq. 6** and **Eq. 8** is always constant. Between HO_{ad} and HOO_{ad}, there is a constant energy difference of about 3 eV. Besides the theoretical overpotential originating from the potential-determining step, a more balanced thermodynamic descriptor is the electrochemical-step symmetry index (ESSI) (Govindarajan et al., 2018). Compared to theoretical overpotential, which relies on a single free-energy change, the ESSI takes all endergonic steps into account and practically represents the average/mean value of deviation from the reversible potential. Considering thermodynamic descriptors, today it seems that a rational strategy should be to first optimize catalyst(s) in the framework of scaling relations, then proceed toward catalyst optimization based on breaking of scaling relations. Scaling relations were considered a decisive limitation for rational catalyst design because it is not easy to decouple intermediates and tune their bond strengths individually. It was recently however shown that scaling relations can be overcome on more complex surfaces (Halck et al., 2014); nonetheless, it has been established that breaking the scaling relations is a necessary

yet insufficient condition to attain enhanced electrocatalytic activity (Govindarajan et al., 2018).

The work of Shao-Horn et al. where filling of e_g orbitals was proposed as an activity descriptor for OER attracted significant attention, where the e_g orbital filling practically dictates the bond strength of intermediates (Suntivich et al., 2011). These authors found that for perovskites, the optimal e_g filling correlates with the potential at a predefined current density in the form of a "volcano." This correlation practically means that the OER activity on perovskites relates to the optimal adsorption energy, confirming one more time the Sabatier principle as a universal rule in electrocatalysis. According to the authors, the proposed descriptor is fundamentally different from the number of 3d electrons (both e_g and t_{2g} electrons) proposed in the 1980s (Bockris and Otagawa, 1983), to which we partially agree. However, we could not find such a significant point of distinction from the concept published in 1970s (Matsumoto and Sato, 1979). Namely, in the work of Shao-Horn's group, filling of the surface transition metal antibonding states of the e_g orbital is a more appropriate descriptor for catalysis because through the σ-bonding, the e_g orbital has a stronger overlap with the oxygen-related adsorbate than does the p-bonding with the t_{2g} orbital and can thus more directly promote electron transfer between surface cations and adsorbed reaction intermediates. Matsunoto's work suggests that the degree of the overlap between the e_g orbital of the cation and the p_σ orbital of the oxygen atom in OH^- ion influences σ^* antibonding band formation and consequently its electron filling, which is very similar to the concept described by the group of Shao-Horn.

The problem with the result of the group of Shao-Horn is that the compared oxides have significantly different chemistry despite of the perovskite-type crystal structure. A fair comparison should be made with oxides where only one cation is changing the number of valence electrons like in some previous experimental works on perovskites (Bockris and Otagawa, 1983; Bockris, 1984) or some previous computational analysis (Man et al., 2011). At the same time, from the results of Shao-Horn's group, $LaNiO_3$, $LaMnO_3$, and $LaCoO_3$ have the same e_g orbital occupancy and different activity, which shows that the proposed descriptor conceals some drawback(s). The concept proposed by the group of Shao-Horn is a continuation of earlier work of Arikado dealing with electrocatalysis of a chlorine evolution reaction in the 1970s (Arikado et al., 1978). The chlorine evolution reaction, that is, a two-electron reaction, interestingly, exhibits identical trends on a significant number of oxides investigated for OER, that is, a four-electron reaction (Trasatti, 1984). At the same time, interpretation of the origins of electrocatalytic activity in the work of Arikado is different in some aspects. Namely, oxides with empty e_g and partially filled t_{2g} orbitals (e.g., RuO_2) have lower exchange current and higher Tafel slope than oxides with half or just filled t_{2g} and partially filled e_g orbitals (e.g., $LaNiO_3$). Importantly, the latter ones exhibit superior behavior only very close to equilibrium, while far away from equilibrium their Tafel slopes increase. Meanwhile, the former ones exhibit a constant Tafel slope in a larger range of potential. This highlights a general rule that activity trends are relative phenomena, dependent on overpotential. Very recently, a purely thermodynamic approach to computational electrochemistry was upgraded by using the applied overpotential of a reaction originating in rate-determining step, as indicator of free energy of intermediate formation in the potential-determining step (Exner, 2020a). To the best of our knowledge, this is the first approach that introduces kinetic effects into a framework of computational free-energy relations.

A recent summary on catalytic descriptors showed that the surface d-band center, work function, excess Bader charge on the adsorbates, integrated crystal orbital overlap population, and crystal orbital Hamilton populations are linear functions of the number of outer electrons (Su et al., 2016). Some of these quantities require complex computation; however, it is not trivial to notice that the number of outer electrons, that is, here an essential quantity, can be read directly from the periodic table (even if we do not know the exact electronic configuration of the valence level). Important to mention is that the number of outer electrons can be linearly related to the adsorption energies of characteristic OER intermediates on oxide surfaces as well as to various oxidation states of oxide, as shown in **Figure 2** (Calle-Vallejo et al., 2013). Interestingly, the slope of graph of the number of outer electrons vs. adsorption energy is identical to the slope of graph of number of outer electrons vs. oxidation state of oxide but with opposite sign. This means that if we compare oxides whose cations have different atomic numbers, then higher the number of outer electrons, the more endergonic the adsorption process will be. At the same time, if we compare oxides whose cation has identical atomic number (i.e., originating from the same metal), then higher the oxidation state of the metal cation in the oxide is, the more endergonic the adsorption process will be. It seems that if the number of outer electrons in the metal oxide increases by one, the adsorption energy will become approximately 50 kJ/mol more endergonic, and the oxidation number of the corresponding metal in the oxide will be approximately one integer more negative. Important to note is the following: if we apply a sufficiently high anodic overpotential so that the oxidation state of the cation becomes more positive, then according to **Figure 2**, we should weaken the binding of the adsorbed oxygen species. This can be the case only if we remove an electron from the bonding orbital. This is a bit contradictory to the assumption that only filling of antibonding orbitals is relevant for understanding the activity of oxides.

The fact is that all the aforementioned descriptors broaden our view on electrocatalysis; however, they remain inside the conventional paradigm, that is, a conquest for optimal adsorption energies. All proposed descriptors correlated to outer electrons have a direct link to the adsorption energies of intermediates, routinely resulting in the "volcano"-type dependence, where the optimal value of the descriptor corresponds to the maximal reaction rate given at the top of "volcano." What remains as a relevant question is how much further adsorption energies can be tuned to correspond to the very top of the "volcano" plot (or even above it) and whether there is any other way to enhance the intrinsic activity except by tuning adsorption energies of intermediates. It was predicted for ORR (oxygen reduction reaction) that the surface functional groups that could reversibly exchange protons with the electrolyte at

redox potentials similar to the potential at which ORR proceeds could be an interesting solution to promote reactions (Busch et al., 2016). Similar reasoning could be adopted for OER. The question is how stable the functional groups under conditions of OER can be and how to control with synthesis the redox potential of the introduced functional group. Further, it is possible to introduce adsorbates (e.g., boron) which alter not only the slope of scaling relations but also exhibits negative scaling (Su et al., 2016), meaning that for the example of boron adsorbed on d-metals, the metal-boron bond strength drops as the number of outer electrons drops, completely opposite to oxygen-containing adsorbates. It is therefore evident that high covalency of the metal-adsorbate bond is important for breaking of scaling relations. Unfortunately, high covalency of metal-adsorbate bonds with the tendency to break scaling relations can be easily counterbalanced with the effect of solvation, especially if the solvent has a high dielectric constant (Calle-Vallejo et al., 2017). Further, a reasonable strategy to modify the OER activity of catalysts and avoid scaling relations is doping with cations that can activate proton donor–acceptor functionality on the conventionally inactive bridge surface sites (Halck et al., 2014). Probably the most popular approach today to tune catalyst activity is to introduce strain in the oxide lattice using a component(s) that can be easily leached out (Yao et al., 2019) or by interaction with the support (Zhou et al., 2019). Importantly, lattice strain has as a consequence a geometric effect in the form of lattice distortion and chemical effect in the form of change in oxygen nonstoichiometry (Wang et al., 2019). Therefore, for lattice distortions, an important descriptor could be the distance between metal centers in the lattice (Pittkowski et al., 2018), while oxygen nonstoichiometry can be analyzed in light of the relative position of the O_{2p} band center with respect to the Fermi level, an important descriptor that will be discussed in the section on electrocatalyst stability. Having all this in mind, it is important to distinguish catalyst optimization through the concept of tuning of adsorption energies (with the goal of approaching the top of the volcano) in the framework of scaling relations from scaling-free catalyst optimization (Govindarajan et al., 2019). Besides adsorption energies of intermediates and characteristic redox transitions, other descriptors (band structure, crystal/ligand field stabilization energy, effective Bohr magneton, etc. . .) relevant for electron transfer, surface restructuring, formation of radicals as well as magnetic properties of electrocatalytic materials were summarized in the past, offering much broader interpretation of activity (Matsumoto and Sato, 1986), than the descriptors introduced by contemporary leading groups. It seems that of essential importance on that road to designing new complex oxides is to dissect the rate law for OER by attributing, if possible, to every term in the equation for the rate law suitable properties of electrocatalyst materials or property of the property of electrocatalytic interface. In other words, parameters that define reaction rate, besides material descriptors, should be correlated with the structure and properties of the interface that are a result of the interaction of the electrocatalyst with the electrolyte, known as interfacial descriptors. Example of the interfacial descriptor is change of the work function of the metal upon the adsorption of the gas molecule through the water layer (Zeradjanin et al., 2017).

Some Controversial Issues Considering Activity Trends

DFT based OER activity trends on oxides (Man et al., 2011) seem to be very similar to the experimental trends (Bockris, 1984). This should be a straightforward example how theory and experiment complement each other. However, when comparing the abovementioned references, it is worth to observe the following: 1) the computational model analyzed well-defined single-crystal surfaces, while the experimental study was based on analysis of defect-rich polycrystalline materials where atom surroundings including coordination number vary in an unpredictable manner; 2) the descriptor used in the computational model was difference in surface adsorption energy of two intermediates, while the descriptor in the case of the experimental trends was bulk number of d-electrons easily readable from the periodic table; and 3) the values obtained by the computational model are estimated at equilibrium conditions, while results of the experimental model are measured at a specific current density. Having in mind that various crystal facets could exhibit different Tafel slopes (e.g., Tafel slope of poly-RuO_2 is lower than for any single-crystal constituent), and that the Tafel slope can change with overpotential at a point that it is difficult to predict, and that the surface is generally expected to have different features from those of the bulk, it is in fact very strange that the trends obtained on single crystal surfaces, at equilibrium conditions, using a surface catalytic descriptor, are almost identical to the trends obtained on polycrystalline materials, at far from equilibrium conditions using a bulk descriptor. This could be explained eventually by some unknown link between bulk and surface properties. An attempt to conceptualize that point of view was establishment of the intimate relationship between bulk thermochemistry and surface adsorption through outer electrons (Calle-Vallejo et al., 2015). However, oxides with different degrees of structural disorder caused by thermal treatment were shown to exhibit very similar catalytic properties, which indicated a negligible effect of the bulk phase on OER electrocatalysis (Gunkel et al., 2017). Perhaps, such similarity between experimental trends and computational trends for drastically different surfaces and applied conditions will be explained in the future by more realistic computational frameworks, like those reported recently that include experimental kinetic effects into a computational model (Exner, 2019; 2020b).

Stability Trends

Systematic studies on stability trends were initiated relatively recently. For example, in 2012 the Max-Planck-Institut für Eisenforschung (MPIE) reported an automated experimental setup dedicated for stability studies comprising a miniaturized electrochemical scanning flow cell coupled to a highly sensitive inductively coupled plasma mass spectrometer (SFC-ICPMS) (Topalov et al., 2012a). This setup allowed the recording of time-resolved potential-dependent catalyst dissolution profiles.

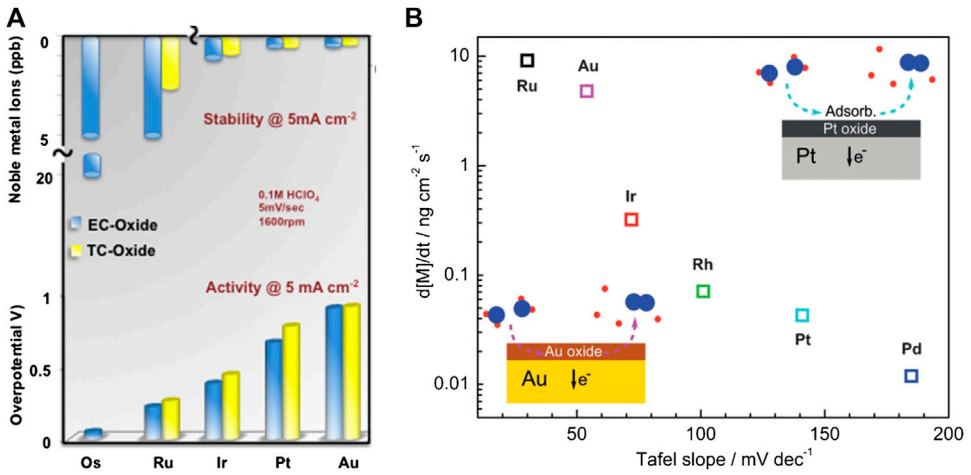

FIGURE 3 | (A) Activity–stability relation for five oxidized noble metals and four thermally prepared oxides in 0.1 M $HClO_4$ used as electrolyte, at 1600 rotations per minute (rpm), at scan rate of 5 mV/sec at galvanostatic regime of 5 mA cm^{-2}. Overpotential is given in relation to the amount of dissolved metal ions. Reprinted from Ref. Danilovic et al. (2014), with permission from the American Chemical Society. **(B)** Dissolution rate as a function of the Tafel slope for OER, for six oxidized noble metals, in 0.1 M H_2SO_4 measured at galvanostatic regime of 5 mA cm^{-2}. Reprinted from Ref. Cherevko et al. (2014c), with permission from Wiley.

For all analyzed metal oxides, dissolution was observed during both anodic and cathodic polarization. Despite the latter dominating, the former is more typical for conditions of OER. At the same time, dissolution can be continuous or transient, where transient dissolution is usually more intense for a short period of time, despite originating from the surface that has the tendency to passivate (Topalov et al., 2014). Some insights into stability/corrosion of electrocatalytic materials could be obtained from thermodynamic data given in Pourbaix diagrams; however, SFC-ICPMS allows measuring the dissolution rates at conditions far from equilibrium. Experimental results on catalyst stability from different groups are sometimes controversial. Importantly, the fundamental question about the existence and nature of a correlation between activity and stability remains open (Cherevko et al., 2014c). The first systematic quantitative activity–stability dataset appeared in 2014 (Danilovic et al., 2014), as shown in **Figure 3A**. In this work, it was found that the most active oxidized metals (Au ≪ Pt < Ir < Ru ≪ Os) are, in fact, the least stable (Au ≫ Pt > Ir > Ru ≫ Os). The relationship between activity and stability, according to Danilovic, is governed by the nature of metal cations as well as by the density of surface defects. The potential transformation of a stable metal cation with a valence state of n = +4 was assumed to end up with unstable metal cation with n > +4. The result of Danilovic was supported by thermodynamic analysis (Binninger et al., 2015), where OER universally proceeds partially *via* lattice oxygen. Importantly, kinetic reasoning is not included in the model of Binninger et al. Also, the appearance of metal cations in a higher oxidation state does not necessarily mean that these higher-valent cations are the active species for OER. Important to note is that for different groups that used ICP-MS, the electrochemical cells (including the mass transport conditions) were different. This could explain some differences in the reported data; however, the trends should generally be the same, which was not the case. A drastic difference between the group of Markovic and the group of Mayrhofer was the behavior of gold during water oxidation. Whereas for Markovic's group, the gold anode was shown to be the most stable precursor for OER in perchloric acid (Danilovic et al., 2014); the group of Mayrhofer (Cherevko et al., 2014c) found that gold was among the most unstable precursors for OER in sulfuric acid. Although, the difference could be attributed to anions, the impact of anions was not further investigated in detail. The group of Mayrhofer could not find the inverse relation between activity (Ru > Ir > Rh > Pd > Pt > Au) and stability (Ru < Au < Ir < Rh < Pt < Pd) at stationary conditions; however, a clear correlation between technically relevant anodic dissolution rate and the Tafel slope in OER was found, as shown in **Figure 3B**. The trends differ at different current densities as stationary and nonstationary conditions also exhibit differences (Cherevko et al., 2014c), while trends at acidic pH in comparison to alkaline pH are surprisingly almost identical (Schalenbach et al., 2018).

The Tafel slope is a kinetic parameter that indicates reaction pathway and sensitivity of the reaction barrier with respect to electrode potential. The lower the Tafel slope, the higher is the dissolution rate, and presumably, higher participation of lattice oxygen in the OER pathway. The relation given in **Figure 3B** is essentially different from the relation that could be derived from the Stern–Geary equation used in corrosion research. In the Stern–Geary equation, the corrosion current is increasing as the Tafel slope of the dissolution process increases, while in **Figure 3B**, corrosion current (rate of side anodic reaction) is dropping as the Tafel slope of OER (indicator of barrier of main anodic reaction) is increasing. It is important to stress that anodic dissolution during electrolytic OER cannot be observed as a classical corrosion process. Classical corrosion is a spontaneous process where chemical energy is transformed into electric energy, in which a case due to proximity of local anode and local cathode, electricity cannot be utilized through the external circuit. At a corroding surface, there is simultaneous

coexistence of an anode where corrosion proceeds and cathode where oxygen reduction or hydrogen evolution (or some other reductive process) proceeds with electrons from the anode. As dissolution current and OER current cannot be combined into a direct relationship, there is hope for designing electrocatalytically highly active materials which could simultaneously survive for a long time in harsh environments. From existing literature data, there is no clear reason why activity and stability should be inversely related, as assumed by many. However, the relation between stability and Tafel slope for OER shown in **Figure 3B** seems more acceptable. A link between the dissolution rate and the Tafel slope for OER is the reaction pathway in which oxygen-containing species from the water and oxygen species from the crystal lattice compete for participance in formation of oxygen molecule. It was expected that oxides with high Tafel slope (Pt and Pd) will have low dissolution rate and negligible participance of lattice oxygen in generation of the oxygen molecule. The opposite to these should be oxides with low Tafel slope (Ru and Au) having high dissolution rate and significant participance of lattice oxygen in the generation of the oxygen molecule. The third group (Rh and Ir) is the case where the intermediate Tafel slope corresponds to intermediate dissolution rates and oxygen generated partially from the lattice. Taking into consideration **Figure 3B** and the relation between electronic configuration of the pure metal (i.e., number of unpaired d-electrons (Rao et al., 1963) or overall number of unpaired valence electrons) and coverage with adsorbed oxygen at equilibrium potential, one could conclude the following: 1) the larger the number of unpaired valence electrons, the larger will be equilibrium coverage with OH_{ad} and O_{ad} species; 2) the larger the equilibrium coverage with oxygen-containing species, the higher will be the probability to have more place exchange between surface Pt atoms and oxygen species per geometric unit of the surface, if anodic potential is applied; 3) more place exchange between surface Pt atoms and oxygen species per geometric unit of the surface at high anodic potentials will cause more intensive distortion of the crystal lattice of the oxide formed; 4) more defective oxide structure due to intensive place exchange will be more prone to dissolution under anodic polarizations or under conditions of oxide reduction; 5) more defective oxide will contain numerous defects which improve electronic conductivity and exhibit lower apparent Tafel slope, despite the OER pathway on all the analyzed oxides being the same. While electrochemical data are straightforward, lattice oxygen participation in OER kinetics was analyzed by various groups using differential electrochemical mass spectrometry (DEMS) or online electrochemical mass spectrometry (OLEMS), using isotope labeled experiments. In isotope labeled experiments, the oxide was built using source of O^{18}, and then water electrolysis is performed together with analysis of mass fragments that could correspond to oxygen evolved from the lattice like $O_2{}^{18}$. It was shown that oxygen originates significantly from the lattice on RuO_x (Wohlfahrt-Mehrens and Heitbaum, 1987) and Au_xO_y (Diaz-Morales et al., 2013), to a minor extent from IrO_y (Fierro et al., 2007) and practically no lattice oxygen evolved from PtO_x (Willsau et al., 1985), as predicted in **Figure 3B**. There are datasets that indicate that on RuO_2, no oxygen is evolved from the lattice (Stoerzinger et al., 2017), however, knowing that even in the case of IrO_x that is much more stable than RuO_x oxygen originates to a small extent from the lattice (Fierro et al., 2007), we believe that the absence of oxygen from the lattice in the case of RuO_x is not likely. Until now, no data on isotope-labeled experiments during OER on RhOx and PdO_x were found; nevertheless, existing data on other noble metals confirmed the perspective illustrated in **Figure 3B**. A widespread perception is that *in situ* or *operando* spectroscopic techniques will bring important clarifications regarding OER mechanism or at least supply new important information. If we focus on IrO_x as the most relevant OER catalyst in acidic media, ambient pressure X-ray photoelectron spectroscopy (APXPS) indicates that under OER conditions, iridium undergoes a transformation in oxidation state from Ir^{4+} to Ir^{5+} (Sanchez Casalongue et al., 2014), which is unexpected from the Pourbaix diagram. Higher oxidation states are more prone to solvation; so the possibility of existence of higher oxidation state Ir^{4+} suggests possible degradation mechanism. Results from OLEMS, besides oxidation state Ir^{5+}, suggest formation of oxidation state of Ir^{6+} in the form of unstable IrO_3 that up to now has never been reported to have been isolated (Kasian et al., 2018). Recently, the formation of the Ir^{5+} oxidation state as an intermediate species was confirmed using *in situ* X-ray absorption (XAS), while Ir^{6+} was predicted by modeling to enable fast water nucleophilic attack as prerequisite for generation of oxygen molecule (Lebedev et al., 2020). Nevertheless, the point of view that IrO_2 goes to higher oxidation states during OER cannot explain the high stability of IrO_2 in acidic media in comparison to other oxides.

Crystalline vs. Amorphous Oxides

Rutile-type IrO_2 is used as a state-of-the-art OER catalyst in acidic water electrolysis due to its stability, although the reaction onset on this type of catalyst is around 1.6 V vs. SHE, suggesting that the practical reaction overpotential during electrolysis is at least 400 mV (Martelli et al., 1994). Amorphous IrO_x (additionally hydrated to different extents) exhibits at least 100 mV lower overpotential (Cherevko et al., 2016). Until now, no clear explanation has been given for this phenomenon. Amorphous oxides, due to the defective structure, could exhibit higher active surface area, but the intrinsic reasons why amorphous oxides are more active are still unknown. Interestingly, the stability of amorphous oxides was believed to be inferior in electrochemical environments in comparison to crystalline oxides. However, quantitative studies, which employed *in situ* dissolution diagnostics, showed that this issue is controversial. First, lower stability of amorphous hydrous oxide using SFC-ICPMS was reported (Geiger et al., 2016). By using a combination of SFC-ICPMS, TEM (transmission electron microscopy), and XAS (X-ray absorption spectroscopy), Jovanovič et al. observed quite the opposite (Jovanovič et al., 2017). This result suggested the existence of different types of amorphous IrO_x, some of which could maintain long-term high activity. Amorphous hydrated oxides are usually obtained electrochemically. Considering the significant number of stationary and nonstationary electrochemical procedures which can be used to generate

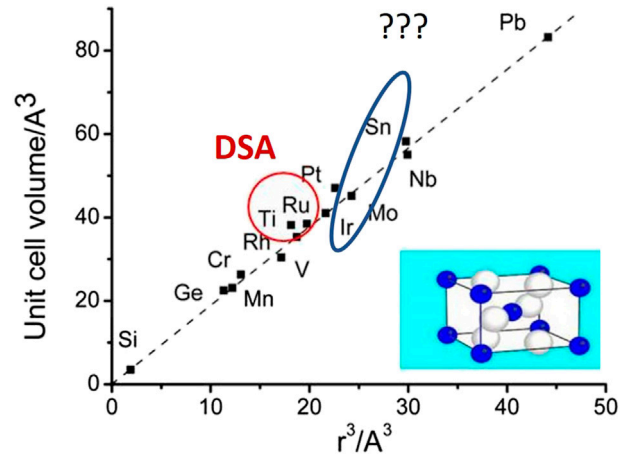

FIGURE 4 | Unit cell volume as a function of effective ionic volume for several metal oxides with rutile structure, with indicated two distinct examples of mixed oxides intensively studied in literature (i.e. TiRu mixed oxide used as commercial dimensionally stable anode (DSA) and unstable SnIr mixed oxide). Replotted using data from Shannon (1968).

amorphous hydrated IrO_x, the electrochemical synthesis and investigation of various types of amorphous hydrated IrO_x can be a reasonable platform for obtaining a multitude of different surfaces with different electrocatalytic properties. OLEMS data suggest that more probable generation of oxygen from the lattice is expected in the case of hydrated IrO_x, while rutile IrO_2 exhibits significantly more stable catalytic performance during OER (Kasian et al., 2019; Schweinar et al., 2020). The reasons for this were not really clarified. A widely spread perception is that anodic dissolution of oxides is linked with instability of their higher oxidation states. At the same time, one of the characteristics of amorphous hydrated oxides is lower average oxidation state and higher concentration of oxygen vacancies in comparison to the rutile structure. If higher oxidation states of oxides (e.g., IrO_3 or RuO_4) would be responsible for dissolution, then amorphous hydrated oxides, despite having initially lower average oxidation number of cations, could be more easily transformed to higher oxidation state (requiring lower overpotential). Increase in oxidation state generally is coupled with drop in radius of cation. Both phenomena enhance cation solvation. However, as shown previously, while oxidation state higher than 4+ is expected for Ru, it is not so probable for Ir.

Mixed (Ternary) Oxides

Besides the in-depth investigation of amorphous oxides including their electrocatalytic properties, an alternative strategy in obtaining more active, more stable, and less expensive OER catalysts is the design of mixed oxides (Trasatti, 1991). A realistic approach would be first to conduct comprehensive investigation of various ternary systems, where one of the components is known to be catalytically active (RuO_x or IrO_x). In the previous few decades, a lot of effort was devoted to building electrocatalytically active substitutional solid solutions. The following guiding principles were used: a) atomic radius of solvent and solute should not differ by more than 15%; b) crystal structures of solvent and solute should be similar; c) solvent and solute should have same valence or alternatively solute should have higher valence than solvent but not vice versa; and finally, d) solute and solvent should have similar electronegativity to avoid formation of intermetallic compounds. One illustrative example of a crystal lattice match/mismatch for various rutile-type of oxides is given in **Figure 4** (Shannon, 1968).

From **Figure 4**, it can be understood why, for example, commercially available dimensionally stable anodes (DSAs), often used in various industrial electrolytic processes, are actually mixed oxides (or more precisely substitutional solid solution) of Ru and Ti (Trasatti, 2000). Clearly, their crystal lattice parameters match to a large extent. Mixed TiRu oxide is also an excellent catalyst for OER, however, not sufficiently stable due to leaching of both Ti and Ru, which is one more example of the challenge of long-term catalyst stability in the case of OER. A very stable mixed oxide with solid electrocatalytic activity for OER is $Ta_2O_5 + IrO_2$ (Martelli et al., 1994). Very interesting is the behavior of the complex oxide $RuO_x + IrO_x$ (Kötz and Stucki, 1986). Parameters of the crystal lattice of isolated oxides are very similar, as shown in **Figure 4A**. There was evidence for change in the characteristic redox transitions shown with cyclic voltammetry as well as chemical shift of the t_{2g} valence level (around 1 eV) revealed by XPS, suggesting d–d interactions. The Tafel slope of the catalyst is however mostly influenced by IrO_2. Despite of the charge transfer from Ir toward the Ru cation that probably reduces the oxidation state of RuO_2, the mixed oxide has lower activity than that of RuO_2, although even with a small percent of IrO_2 in the mixture, stability increases drastically. In other words, despite the change in stability being significant, the change in activity was minor. This behavior was unexpected, but at the same time, it showed yet another example that there is no direct correlation between activity and stability.

Nowadays, attempts to build electrocatalytically active interstitial solid solutions are relatively rare. In interstitial solid solutions, the solvent and the solute should also have similar electronegativity and valence; however, the atomic radius of the solute should be smaller than the interstitial sites in the solvent lattice. A highly active and stable interstitial solid solution, to our knowledge, was never reported in the literature, although it could be a very interesting direction of future research.

It seems that in the case of mixed oxides, changing the chemical composition results in various complex modifications like: change in the ratio between the oxidation states of the respective cations, formation of oxygen vacancies, inducing lattice strain *via* cation of particular radius or charge, enhancing d–d interaction or p–d hybridization, etc. All these modifications contribute in optimizing of frontier orbital filling/occupancy and tuning of characteristic redox transitions. A natural question to ask at this point is what else is relevant for intrinsic activity of OER?

Some Elements of Diagnostics of Reaction Mechanism

While the reaction pathway gives us the first information about reaction intermediates and number of elementary steps from

reaction mechanism by using discriminatory criteria of electrode kinetics (partial orders of reaction, transfer coefficient, and stoichiometric number) and by using spectroscopic techniques, we learn much more including: what is the rate-determining step, does the generation of one molecule of the product require one or more active sites, the existence of coupled or decoupled electron and proton transfer, the coverage with intermediates, lateral interaction of intermediates, the formation and stabilization of radicals, etc. One of the key points relevant for understanding of the mechanism is the rate-determining step (RDS) that can only be investigated experimentally. This is a significant point of distinction between experimental and computational chemistry. Computational chemistry operates with potential-determining step (koper, 2013) (explained previously in the text) that is not accessible to experimentalists. Considering that the potential-determining step does not have to overlap with the rate-determining step, we accept the notion that experimental electrochemistry has definite priority in establishing activity trends and in building a picture of reaction mechanism. A desirable approach should be combined with computational/experimental studies like kinetic scaling relations where RDS is obtained from the free energy diagram as a function of the applied electrode potential (Exner and Over, 2019). In this approach, the free energy diagram was constructed from experimental Tafel plots and ab initio Pourbaix diagrams

One interesting experimental result is that the activation energy for OER on oxidized polycrystalline gold is around 55 kJ/mol, almost identical to the activation energy of oxidized gold dissolution (Cherevko et al., 2014b). Knowing that the reaction rate of OER on gold is much higher in comparison to the dissolution rate, equality of the activation energies of OER and gold dissolution processes suggests that dissolution happens with a very low frequency factor or in other words on very few active centers. This suggests that defects that are usually massively present on polycrystalline oxidized metal surfaces cannot be the explanation for the origins of dissolution/instability, contrary to what was usually assumed (Danilovic et al., 2014).

What we skipped intentionally in the above discussion on activity and stability descriptors is the relative position of O_{2p} orbitals with respect to d-orbitals and with respect to the Fermi level (Hong et al., 2015; Grimaud et al., 2017). This descriptor could shed more light on the mechanism and interrelation between activity and stability. Namely, when the O_2/H_2O redox potential aligns with the Fermi level of the oxide, OER can be triggered. Further, anodic polarization causes an average increase in oxidation state of cations which returns to the previous oxidation state by receiving the electron from oxygen-containing species from water. This is the catalytic cycle in which the metal cation evidently plays a major role by changing oxidation states and concomitantly the bond strengths of the intermediates accordingly. However, it is possible that electron(s) from lattice oxygen species is/are transferred to the cation, resulting in release of molecular oxygen, formation of oxygen vacancies, and possibly transition of the cation to a lower oxidation state. The reason for the oxidation of the lattice oxygen can be a shift of the Fermi level into the O_{2p} band of a highly covalent oxide at which the difference between the O_{2p} center and the d-band center is minimized. In that case, from electronic states that are substantially O_{2p} in character (**Figure 5**), the generation of oxygen from oxygen sites is probable. Evidently, this kind of mechanism does not imply *a priori* some destructive effects on the crystal lattice, despite of the general perception that the appearance of oxygen vacancies is linked to lattice instability under OER conditions (Hao et al., 2020). It is rather desirable because it "protects" the cation from higher oxidation states that are more prone to solvation/dissolution. From all that has been discussed until now, it would be essential to quantify isotope labeling measurements using DEMS or OLEMS and analyze the obtained data to conclude what is the actual ratio between species in higher oxidation states produced probably through disproportionation (e.g., RuO_4) and oxygen molecules originating from lattice fragments (e.g., O_2[36]) and then correlate the data with *in situ* dissolution data (e.g., from ICP-MS). The issue here is that it is very questionable how sensitive and reliable DEMS or OLEMS setups are for quantitative analysis, as pointed out earlier (Grote et al., 2014).

An in-depth discussion on role of lattice oxygen in the OER reaction mechanism slightly shifts focus from the classical view that the metal cation is essential and/or the exclusive active site. Using a combination of synchrotron-based X-ray photoemission and absorption spectroscopies, ab initio calculations, and microcalorimetry suggests that holes in the O_{2p} states of IrO_x favor the formation of weakly bound oxygen that is extremely susceptible to nucleophilic attack of water (Pfeifer et al., 2016). Formation of an electrophilic oxygen species, O^{I-}, as a key OER intermediate, proceeds in the electrochemical step followed by a chemical step of molecular oxygen formation. This mechanism is occurring on both, amorphous and rutile Ir oxides, where the reaction rate is higher on former due to better flexibility of its surface (Saveleva et al., 2018).

Dynamic Character of Water Electrolysis

Industrial electrolytic processes, including water splitting, are conducted galvanostatically due to technical preferences which allow relatively straightforward current control, opposite to potential control. At the same time, the imposed current intensity is directly proportional to the mass of the product. It is a widely accepted point of view that water electrolysis is operated *via* stationary polarization; however, interfacial processes are rather complex and definitely time dependent. One of the important phenomena which influence the overall efficiency of water electrolysis is the formation of gas bubbles at industrially relevant current densities (Zeradjanin et al., 2014c). During the OER, the interfacial region is oversaturated with dissolved oxygen. When the oversaturation overcomes the barrier for the nucleation of a new phase, a gas bubble is formed. Gas bubbles periodically nucleate, grow, and finally detach from the surface. So the overall pseudo-stationary oxygen evolution process, occurring during galvanostatic polarization, is the sum of several time-dependent processes, where at different times the current passes through different fractions of the available/accessible active surface area (Zeradjanin et al., 2012b). Gas evolution kinetics strongly

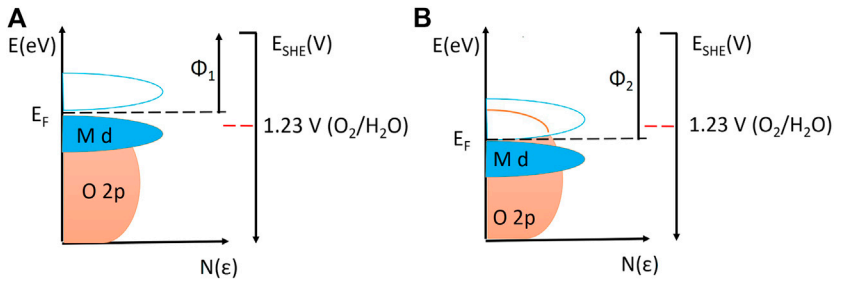

FIGURE 5 | Density of states and relative positions of d band, O2p band, Fermi level, and work functions on the vacuum scale, in relation to OER reversible potential on the standard hydrogen redox potential scale. **(A)** Oxide with low work function and Fermi level positioned above OER reversible redox potential. **(B)** Oxide with high work function and Fermi level positioned below OER reversible redox potential and inside O2p band, allowing OER from the lattice. Replotted using information from (Hong et al., 2015).

depend on: the hydrophilicity of the electrode surface (Chen et al., 2012), the morphological pattern (Zeradjanin et al., 2012a), as well as the spatial distribution of the morphological pattern (Zeradjanin et al., 2014a, 2018). It was shown that catalytic layers with specially designed morphology could achieve very facile gas evolution if the process of gas-bubble growth is limited at initial moments after nucleation (Zeradjanin et al., 2014c). The abovementioned available/accessible surface area is the one that is at the defined instance not covered by gas bubbles, and consequently, it is between the geometric surface area and "total/real" surface area. It is known as effective surface area and represents an essential quantity if one is to accurately estimate kinetic parameters (Calderon et al., 2009; Zeradjanin, 2018a). In the galvanostatic regime, if gas-bubble coverage is very high, the entire current passes through a small portion of the surface, causing locally high current densities as well as high local overpotentials that can damage the catalyst structure. Therefore, facile gas evolution is extremely important for catalyst stability (Zeradjanin et al., 2014c). Notably there are interesting attempts to accelerate gas evolution with external forces like centrifugal field, ultrasonic field, or magneto-hydrodynamic field (Taqieddin et al., 2017); however, they require additional components in the electrolyzer, which is at the moment not a desirable approach. Besides gas evolution phenomena, galvanostatic electrolysis is coupled with constant charging of the double layer. Double-layer charging is also a time-dependent process. The exact influence of double-layer charging on reaction kinetics, besides being perceived as a parasitic process, was never really understood. Finally, it is worth to stress that electricity originating from renewable sources will fluctuate, so to understand the behavior of electrocatalysts in a realistic manner; it is essential to conduct electrolysis at nonstationary conditions (e.g., galvanostatic pulses).

Challenges in Benchmarking Activity and Stability

One of the controversial aspects of electrocatalysis research is benchmarking the activity and stability of OER. The most accepted approach, probably due to simplicity, is where overpotential required to reach a current density of 10 $mAcm^{-2}$ is taken as figure of merit (McCrory et al., 2013). The approach proposed in this work to normalize surface area using cyclic voltammetry is oversimplification of a well-known method based on scan rate-dependent potential-controlled reversible exchange of protons between the electrolyte and oxide surface (Ardizzone et al., 1990). Despite there was some criticism related to absorption of protons in the oxide subsurface layers (Vogt, 1994), still no better method was proposed to date (Baronetto et al., 1994), especially having in mind that subsurface regions can actively participate in the reaction mechanism (Grimaud et al., 2017). Despite some fresh efforts to estimate the surface area (Watzele and Bandarenka, 2016; Watzele et al., 2019), still not much advancement was made since the IUPAC recommendation in 1991 (Trasatti and Petrii, 1991). A more relevant experimental protocol that includes data on catalyst stability was reported recently (Spanos et al., 2017). It is important to note that at technical conditions, the regime of current density and temperature is much more severe than in contemporary laboratory research. At the same time, it is extremely difficult to distinguish at technical conditions where energy losses are coming from (intrinsic kinetics, ohmic drops, diffusion limitations, gas-bubble effect, proton conductivity of the membrane, etc.), like it was done in the case of chlor-alkali electrolysis (Trasatti, 2000). In laboratory experiments, it is much easier to make a "dissection" of the energy losses. For obtaining of accurate kinetic data, besides ohmic drop correction (routinely using impedance spectroscopy at high frequencies), it is necessary to utilize a measurement cell with well-defined mass transport. The rotating disc electrode (RDE) is still the best tool to extract kinetic data, simply due to well-defined conditions of convective diffusion including well-defined value of diffusion-limited current. The validity of RDE implies a laminar flow that is assured only at flat surfaces or with very thin films << 100 $\mu g\,cm^{-2}$ (Gasteiger et al., 2005). Besides the classical measurement pitfalls (thick catalytic layers, using of the Ag/AgCl reference electrode, and glass-made electrochemical cell with alkaline electrolytes, etc.), one issue is still very problematic and that is the gas-bubble coverage and its influence on effective surface area (Zeradjanin, 2018a). An important aspect to add is that theoretical validity of the mathematical model of RDE (laminar flow) is up to 100,000 rotations/minute; however, due

to roughness and inclinations of flat surface, it is considered that 10,000 rotation/minute is a more realistic upper limit. At that rotation rate, the size of the diffusion layer in aqueous electrolytes is around 5 μm, which suggests that nanobubbles or microbubbles with a diameter smaller than 5 μm will not be influenced by convection. In fact, gas bubbles inside the diffusion layer will block the active sites to an extent that it is difficult to estimate and that depends on the kinetics of the OER on a given material as well as on the hydrophilicity of the surface. Therefore, the challenge of reliably determining the effective surface area remains unsolved despite some commendable attempts to quantify the fraction of the surface accessible for reaction under dynamic conditions (Zeradjanin, 2018a). From the discussion above, one can conclude that extracting of overpotential at a predefined current density is prone to significant errors, especially due to issues with effective surface area, but also due to ohmic drop correction that can be problematic for gas evolving electrodes. In the past, it was more common to extract the Tafel slope as an intensive catalytic property (independent of surface area) (Trasatti, 1991); however, considering the existing challenges to ohmic drop correction as well as challenges related to effective surface area that are both overpotential dependent, one can say that extracting Tafel slopes as a kinetic parameter can conceal almost similar drawbacks. It remains a difficult task to search for specific reactions that can be used to reliably determine the number of active sites of a particular catalytic material. Active sites should be determined in relevant surroundings because the properties of the surroundings itself (coordination number, presence of defects in the lattice, etc.) are essential for the intrinsic activity. In other words, estimation of the activity of fragmented systems like the approaches used in single-entity electrochemistry can be used to understand the interplay of an individual entity and the assembly; however, the obtained results cannot be directly relevant for interpreting the behavior of an assembly of the entities (Baker, 2018).

Besides numerous recommendations for activity benchmarking in the last couple of years, catalyst stability benchmarking is becoming more spread and recognized as relevant. For stability benchmarking, it is necessary to have a setup that can measure *in situ* dissolution of metal species from metal oxide, for example, by means of SFC-ICPMS as previously mentioned (Topalov et al., 2014). Despite the fact that ICPMS works well in acidic electrolytes and with a low detection limit of 10 ppt (parts per trillion) (Topalov et al., 2012b) in alkaline media, it is difficult to calibrate the setup, especially if concentrations of alkaline electrolyte are above 0.05 mol/dm^3 (Cherevko et al., 2014a). In that case, it is better to use ICPOES (inductively coupled plasma optical emission spectrometry), which has an order of magnitude lower detection limit than ICPMS; nonetheless, it can operate in more concentrated alkaline electrolytes with concentrations of up to 1 mol/dm^3. Proper stability benchmarking requires, independent from the utilized electrochemical technique, that the dissolved amount of metal originating from the catalyst is normalized with the current corresponding to generated oxygen. The usefulness of this approach was first implicitly shown in a comparison of two RuO_x-based catalysts with almost identical chemistry but different morphology. Namely, the catalyst with a "cracked" morphology in comparison to a "crack-free" morphology showed two times higher current intensity and two times lower dissolution rate, indicating four times more effective surface of the "cracked" sample (Zeradjanin et al., 2014c). Later, similar logic was applied in the group of Markovic from Argonne National Laboratory, where the ratio between the amount of produced oxygen and the amount of dissolved metal species at a given overpotential named as activity–stability factor, was proposed as a unified activity–stability descriptor (Kim et al., 2017).

Instead of Conclusions (Remaining Fundamental Questions and Future Research Directions)

After decades of research on the electrocatalysis of OER, various aspects on the origins of activity and stability have been significantly clarified. However, as shown in this review, despite the progress of computational chemistry and spectroscopy, many aspects of the reaction mechanism remain elusive for comprehension. Therefore, we should be prudent with conclusions. To generate a more vivid picture about the complex interfacial transformations that result in the generation of the oxygen molecule, in the future more detailed work should be done in following areas:

1) Theory of charge transfer at interface oxide/electrolyte. Besides electron transfer, focus should be on proton transfer as well as on cation transfer during the dissolution process. Analysis should be done on conductive oxides as well as on semiconductors.
2) Complex compounds (i.e., intermetallics and/or alloys as precursors for surface mixed oxides. . .) based on the interaction of modestly active d-metals with metals out of d-block which have very low electronegativity, like recently reported Al_2Pt (Antonyshyn et al., 2020) that can give drastic enhancement in OER activity and stability. Similar is with metal–metalloid alloys (e.g., NiB) as precursors, where the metalloid influences the kinetics of water deprotonation and causes a shift in characteristic redox transitions of the catalytically active metal oxide (Masa et al., 2019), while a more intensive oxidation of the materials causes complex anion formation that remains in the double layer and could induce a self-healing effect on the catalyst surface (Masa and Schuhmann, 2019).
3) Role of external fields like electric field (Ghaani et al., 2020) or magnetic field (Garcés-Pineda et al., 2019) that can significantly enhance gas evolution, conductivity, or interfacial charge transfer.
4) Dynamic structural features of interfacial water layer should be investigated with various techniques (Zeradjanin et al., 2020) including sophisticated Terahertz spectroscopies as well as dynamic properties of the electrocatalyst surface layer should be probed with vibrational spectroscopies.

5) Role of impurities in the electrolyte like in the case of Fe cations from alkaline electrolytes interacting with Ni-based oxide or Co-based oxide (Spanos et al., 2019), assuring significant enhancement of the OER activity.
6) The compensation effect on various classes of oxides (e.g., rutiles) as is well known in heterogenous catalysis (Cremer, 1955; Bond et al., 2000; Bligaard et al., 2003) is practically uninvestigated in electrochemistry. It would be of major importance to experimentally determine adsorption energies and compare with computational models, investigate the quantitative relationship between activation energy and preexponential (frequency) factor, and enlarge the understanding of what are the contributors to the activation energy (Zeradjanin et al., 2021) and preexponential factor (proton tunneling, lattice vibrations, etc. . .) (Zeradjanin, 2018b).
7) Electrocatalysis of OER related to electron spin should be studied systematically (Bockris, 1984). Transition of the spin state from the spin singlet of OH^-/H_2O reactant to the spin triplet O_2 molecule product imposes additional complexity on OER kinetics (Li et al., 2020). The rate of the chemical reaction will be extremely slow if the spin of the electronic wave function of the products differs from that of the reactants (Sun et al., 2020). Worth to mention is that the spin-related properties are: crystal field stabilization energy, coordination number, oxidation state, bonding, frontier orbital filling, conductivity, and magnetism.
8) A self-evident way to protect oxides from degradation is to reduce OER overpotential at working conditions. Consequently, the way to enhance stability is to improve the intrinsic OER activity of the catalyst. Therefore, we could say that finding new ways to improve the catalyst activity for OER, inside or outside the paradigm of the Sabatier principle, could be essential strategy to generally enhance catalyst performance.

AUTHOR CONTRIBUTIONS

AZ concealed concept and wrote draft of the review. JM, IS, and RS helped shaping and writing of review.

ACKNOWLEDGMENTS

Authors acknowledge Max Planck Society for granting open access of this work.

REFERENCES

Antonyshyn, I., Barrios Jiménez, A. M., Sichevych, O., Burkhardt, U., Veremchuk, I., Schmidt, M., et al. (2020). Al 2 Pt for oxygen evolution in water splitting: a strategy for creating multifunctionality in electrocatalysis. *Angew. Chem. Int. Ed. Engl.*, 59, 16770–16776, doi:10.1002/anie.202005445

Ardizzone, S., Fregonara, G., and Trasatti, S. (1990). "Inner" and "outer" active surface of RuO_2 electrodes. *Electrochim. Acta* 35, 263–267. doi:10.1016/0013-4686(90)85068-X

Arikado, T., Iwakura, C., and Tamura, H. (1978). Some oxide catalysts for the anodic evolution of chlorine: reaction mechanism and catalytic activity. *Electrochim. Acta* 23, 9–15. doi:10.1016/0013-4686(78)87026-1

Baker, L. A. (2018). Perspective and prospectus on single-entity electrochemistry. *J. Am. Chem. Soc.* 140, 15549–15559. doi:10.1021/jacs.8b09747

Baronetto, D., Krstajić, N., and Trasatti, S. (1994). Reply to "note on a method to interrelate inner and outer electrode areas" by H. Vogt. *Electrochim. Acta* 39, 2359–2362. doi:10.1016/0013-4686(94)E0158-K

Binninger, T., Mohamed, R., Waltar, K., Fabbri, E., Levecque, P., Kötz, R., et al. (2015). Thermodynamic explanation of the universal correlation between oxygen evolution activity and corrosion of oxide catalysts. *Sci. Rep.* 5, 12167. doi:10.1038/srep12167

Schmidt, T., Honkala, K., Logadottir, A., Nørskov, J. K., Dahl, S., and Jacobsen, C. J. H. (2003). On the compensation effect in heterogeneous catalysis. *J. Phys. Chem. B* 107, 9325–9331. doi:10.1021/jp034447g

Bockris, J. O., and Otagawa, T. (1983). Mechanism of oxygen evolution on perovskites. *J. Phys. Chem.* 87, 2960–2971. doi:10.1021/j100238a048

Bockris, J. O. (1972). A hydrogen economy. *Science* 176, 1323. doi:10.1126/science.176.4041.1323

Bockris, J. O. (1984). The electrocatalysis of oxygen evolution on perovskites. *J. Electrochem. Soc.* 131, 290. doi:10.1149/1.2115565

Bockris, J. O. M. (2013). The hydrogen economy: its history. *Int J Hydrogen Energ.*, 38, 2579–2588. doi:10.1016/j.ijhydene.2012.12.026

Bond, G. C., Keane, M. A., Kral, H., and Lercher, J. A. (2000). Compensation phenomena in heterogeneous catalysis: general principles and a possible explanation. *Catal. Rev.* 42, 323–383. doi:10.1081/CR-100100264

Busch, M., Halck, N. B., Kramm, U. I., Siahrostami, S., Krtil, P., and Rossmeisl, J. (2016). Beyond the top of the volcano?–a unified approach to electrocatalytic oxygen reduction and oxygen evolution. *Nanomater. Energy* 29, 126–135. doi:10.1016/j.nanoen.2016.04.011

Busch, M. (2018). Water oxidation: from mechanisms to limitations. *Current Opinion in Electrochemistry* 9, 278–284. doi:10.1016/j.coelec.2018.06.007

Calderon, E. H., Wüthrich, R., Mandin, P., Fóti, G., and Comninellis, C. (2009). Estimation of the effectiveness factor of an outer-sphere redox couple (Fe^{3+}/Fe^{2+}) using rotating disk Ti/IrO_2 electrodes of different loading. *J. Appl. Electrochem.* 39, 1379–1384. doi:10.1007/s10800-009-9813-6

Calle-Vallejo, F., Martínez, J. I., and Rossmeisl, J. (2011). Density functional studies of functionalized graphitic materials with late transition metals for oxygen reduction reactions. *Phys. Chem. Chem. Phys.* 13, 15639. doi:10.1039/c1cp21228a

Calle-Vallejo, F., Inoglu, N. G., Su, H.-Y., Martínez, J. I., Man, I. C., Koper, M. T. M., et al. (2013). Number of outer electrons as descriptor for adsorption processes on transition metals and their oxides. *Chem. Sci.* 4, 1245. doi:10.1039/c2sc21601a

Calle-Vallejo, F., Díaz-Morales, O. A., Kolb, M. J., and Koper, M. T. M. (2015). Why is bulk thermochemistry a good descriptor for the electrocatalytic activity of transition metal oxides?. *ACS Catal.* 5, 869–873. doi:10.1021/cs5016657

Calle-Vallejo, F., Krabbe, A., and García-Lastra, J. M. (2017). How covalence breaks adsorption-energy scaling relations and solvation restores them. *Chem. Sci.* 8, 124–130. doi:10.1039/C6SC02123A

Chen, R., Trieu, V., Zeradjanin, A. R., Natter, H., Teschner, D., Kintrup, J., et al. (2012). Microstructural impact of anodic coatings on the electrochemical chlorine evolution reaction. *Phys. Chem. Chem. Phys.* 14, 7392. doi:10.1039/c2cp41163f

Hempelmann, S., Zeradjanin, A. R., Keeley, G. P., and Mayrhofer, K. J. J. (2014a). A comparative study on gold and platinum dissolution in acidic and alkaline media. *J. Electrochem. Soc.* 161, H822–H830. doi:10.1149/2.0881412jes

Cherevko, S., Zeradjanin, A. R., Topalov, A. A., Keeley, G. P., and Mayrhofer, K. J. J. (2014b). Effect of temperature on gold dissolution in acidic media. *J. Electrochem. Soc.* 161, H501–H507. doi:10.1149/2.0551409jes

Cherevko, S., Zeradjanin, A. R., Topalov, A. A., Kulyk, N., Katsounaros, I., and Mayrhofer, K. J. J. (2014c). Dissolution of noble metals during oxygen evolution in acidic media. *ChemCatChem* 6, 2219–2223. doi:10.1002/cctc.201402194

Cherevko, S., Geiger, S., Kasian, O., Kulyk, N., Grote, J.-P., Savan, A., et al. (2016). Oxygen and hydrogen evolution reactions on Ru, RuO 2 , Ir, and IrO 2 thin film electrodes in acidic and alkaline electrolytes: a comparative study on activity and stability. *Catal. Today* 262, 170–180. doi:10.1016/j.cattod.2015.08.014

Cremer, E. (1955). "The compensation effect in heterogeneous catalysis," in *Advances in Catalysis*. Amsterdam, Netherlands: Elsevier, 75–91. doi:10.1016/S0360-0564(08)60525-8

Damjanovic, A., Dey, A., and Bockris, J. O. (1966). Kinetics of oxygen evolution and dissolution on platinum electrodes. *Electrochim. Acta* 11, 791–814. doi:10.1016/0013-4686(66)87056-1

Danilovic, N., Subbaraman, R., Chang, K. C., Chang, S. H., Kang, Y. J., Snyder, J., et al. (2014). Activity–stability trends for the oxygen evolution reaction on monometallic oxides in acidic environments. *J. Phys. Chem. Lett.* 5, 2474–2478. doi:10.1021/jz501061n

Markovic, H., Limberg, C., Reier, T., Risch, M., Roggan, S., and Strasser, P. (2010). The mechanism of water oxidation: from electrolysis via homogeneous to biological catalysis. *ChemCatChem* 2, 724–761. doi:10.1002/cctc.201000126

Di Quarto, F., Sunseri, C., Piazza, S., and Romano, M. C. (1997). Semiempirical correlation between optical band gap values of oxides and the difference of electronegativity of the elements. Its importance for a quantitative use of photocurrent spectroscopy in corrosion studies. *J. Phys. Chem. B* 101, 2519–2525. doi:10.1021/jp970046n

Diaz-Morales, O., Calle-Vallejo, F., De Munck, C., and Koper, M. T. M. (2013). Electrochemical water splitting by gold: evidence for an oxide decomposition mechanism. *Chem. Sci.* 4, 2334. doi:10.1039/c3sc50301a

Exner, K. S., and Over, H. (2019). Beyond the rate-determining step in the oxygen evolution reaction over a single-crystalline IrO 2 (110) model electrode: kinetic scaling relations. *ACS Catal.* 9, 6755–6765. doi:10.1021/acscatal.9b01564

Exner, K. S. (2019). Design criteria for oxygen evolution electrocatalysts from first principles: introduction of a unifying material-screening approach. *ACS Appl. Energy Mater.* 2, 7991–8001. doi:10.1021/acsaem.9b01480

Exner, K. S. (2020a). A universal descriptor for the screening of electrode materials for multiple-electron processes: beyond the thermodynamic overpotential. *ACS Catal.* 10, 12607–12617. doi:10.1021/acscatal.0c03865

Exner, K. S. (2020b). Recent progress in the development of screening methods to identify electrode materials for the oxygen evolution reaction. *Adv. Funct. Mater.* 30, 2005060. doi:10.1002/adfm.202005060

Fierro, S., Nagel, T., Baltruschat, H., and Comninellis, C. (2007). Investigation of the oxygen evolution reaction on Ti/IrO_2 electrodes using isotope labelling and on-line mass spectrometry. *Electrochem. Commun.* 9, 1969–1974. doi:10.1016/j.elecom.2007.05.008

Frydendal, R., Paoli, E. A., Knudsen, B. P., Wickman, B., Malacrida, P., Stephens, I. E. L., et al. (2014). Benchmarking the stability of oxygen evolution reaction catalysts: the importance of monitoring mass losses. *ChemElectroChem* 1, 2075. doi:10.1002/celc.201402262

Garcés-Pineda, F. A., Blasco-Ahicart, M., Nieto-Castro, D., López, N., and Galán-Mascarós, J. R. (2019). Direct magnetic enhancement of electrocatalytic water oxidation in alkaline media. *Nat Energy* 4, 519–525. doi:10.1038/s41560-019-0404-4

Gasteiger, H. A., and Marković, N. M. (2009). Chemistry. just a dream—Or future reality? *Science* 324, 48–49. doi:10.1126/science.1172083

Gasteiger, H. A., Kocha, S. S., Sompalli, B., and Wagner, F. T. (2005). Activity benchmarks and requirements for Pt, Pt-alloy, and non-Pt oxygen reduction catalysts for PEMFCs. *Appl. Catal. B Environ.* 56, 9–35. doi:10.1016/j.apcatb.2004.06.021

Geiger, S., Kasian, O., Shrestha, B. R., Mingers, A. M., Mayrhofer, K. J. J., and Cherevko, S. (2016). Activity and stability of electrochemically and thermally treated iridium for the oxygen evolution reaction. *J. Electrochem. Soc.* 163, F3132–F3138. doi:10.1149/2.0181611jes

Ghaani, M. R., Kusalik, P. G., and English, N. J. (2020). Massive generation of metastable bulk nanobubbles in water by external electric fields. *Sci. Adv.* 6, eaaz0094. doi:10.1126/sciadv.aaz0094

Govindarajan, N., García-Lastra, J. M., Meijer, E. J., and Calle-Vallejo, F. (2018). Does the breaking of adsorption-energy scaling relations guarantee enhanced electrocatalysis?. *Current Opinion in Electrochemistry* 8, 110–117. doi:10.1016/j.coelec.2018.03.025

Govindarajan, N., Koper, M. T. M., Meijer, E. J., and Calle-Vallejo, F. (2019). Outlining the scaling-based and scaling-free optimization of electrocatalysts. *ACS Catal.* 9, 4218–4225. doi:10.1021/acscatal.9b00532

Greeley, J., and Markovic, N. M. (2012). The road from animal electricity to green energy: combining experiment and theory in electrocatalysis. *Energy Environ. Sci.* 5, 9246. doi:10.1039/c2ee21754f

Grimaud, A., Diaz-Morales, O., Han, B., Hong, W. T., Lee, Y. L., Giordano, L., et al. (2017). Activating lattice oxygen redox reactions in metal oxides to catalyse oxygen evolution. *Nat. Chem.* 9, 457–465. doi:10.1038/nchem.2695

Shao-Horn, J. P., Zeradjanin, A. R., Cherevko, S., and Mayrhofer, K. J. (2014). Coupling of a scanning flow cell with online electrochemical mass spectrometry for screening of reaction selectivity. *Rev. Sci. Instrum.* 85, 104101. doi:10.1063/1.4896755

Gunkel, F., Jin, L., Mueller, D. N., Hausner, C., Bick, D. S., Jia, C.-L., et al. (2017). Ordering and phase control in epitaxial double-perovskite catalysts for the oxygen evolution reaction. *ACS Catal.* 7, 7029–7037. doi:10.1021/acscatal.7b02036

Halck, N. B., Petrykin, V., Krtil, P., and Rossmeisl, J. (2014). Beyond the volcano limitations in electrocatalysis--oxygen evolution reaction. *Phys. Chem. Chem. Phys.* 16, 13682–13688. doi:10.1039/C4CP00571F

Hao, S., Liu, M., Pan, J., Liu, X., Tan, X., Xu, N., et al. (2020). Dopants fixation of ruthenium for boosting acidic oxygen evolution stability and activity. *Nat. Commun.* 11, 5368. doi:10.1038/s41467-020-19212-y

Hong, W. T., Risch, M., Stoerzinger, K. A., Grimaud, A., Suntivich, J., and Shao-Horn, Y. (2015). Toward the rational design of non-precious transition metal oxides for oxygen electrocatalysis. *Energy Environ. Sci.* 8, 1404–1427. doi:10.1039/C4EE03869J

Zhang, P., Hodnik, N., Ruiz-Zepeda, F., Arčon, I., Jozinović, B., Zorko, M., et al. (2017). Electrochemical dissolution of iridium and iridium oxide particles in acidic media: transmission electron microscopy, electrochemical flow cell coupled to inductively coupled plasma mass spectrometry, and X-ray absorption spectroscopy study. *J. Am. Chem. Soc.* 139, 12837–12846. doi:10.1021/jacs.7b08071

Gaberšček, O., Grote, J. P., Geiger, S., Cherevko, S., and Mayrhofer, K. J. J. (2018). The common intermediates of oxygen evolution and dissolution reactions during water electrolysis on iridium. *Angew Chem. Int. Ed. Engl.* 57, 2488–2491. doi:10.1002/anie.201709652

Kasian, O., Geiger, S., Li, T., Grote, J.-P., Schweinar, K., Zhang, S., et al. (2019). Degradation of iridium oxides via oxygen evolution from the lattice: correlating atomic scale structure with reaction mechanisms. *Energy Environ. Sci.* 12, 3548–3555. doi:10.1039/C9EE01872G

Katsounaros, I., Cherevko, S., Zeradjanin, A. R., and Mayrhofer, K. J. (2014). Oxygen electrochemistry as a cornerstone for sustainable energy conversion. *Angew Chem. Int. Ed. Engl.* 53, 102–121. doi:10.1002/anie.201306588

Kim, Y. T., Lopes, P. P., Park, S. A., Lee, A. Y., Lim, J., Lee, H., et al. (2017). Balancing activity, stability and conductivity of nanoporous core-shell iridium/iridium oxide oxygen evolution catalysts. *Nat. Commun.* 8, 1449. doi:10.1038/s41467-017-01734-7

Kötz, R., and Stucki, S. (1986). Stabilization of RuO_2 by IrO_2 for anodic oxygen evolution in acid media. *Electrochim. Acta* 31, 1311–1316. doi:10.1016/0013-4686(86)80153-0

Markovic, M. T. M. (2013). Analysis of electrocatalytic reaction schemes: distinction between rate-determining and potential-determining steps. *J. Solid State Electrochem.* 17, 339–344. doi:10.1007/s10008-012-1918-x

Lebedev, D., Ezhov, R., Heras-Domingo, J., Comas-Vives, A., Kaeffer, N., Willinger, M., et al. (2020). Atomically dispersed iridium on indium tin oxide efficiently catalyzes water oxidation. *ACS Cent. Sci.*,6, 1189–1198. doi:10.1021/acscentsci.0c00604

Lewis, N. S., and Nocera, D. G. (2006). Powering the planet: chemical challenges in solar energy utilization. *Proc. Natl. Acad. Sci. USA.* 103, 15729–15735. doi:10.1073/pnas.0603395103

Li, X., Cheng, Z., and Wang, X. (2020). Understanding the mechanism of oxygen evolution reaction (OER) with the consideration of spin. Available at: http://arxiv.org/abs/2004.05326

Ma, Z., Zhang, Y., Liu, S., Xu, W., Wu, L., Hsieh, Y.-C., et al. (2018). Reaction mechanism for oxygen evolution on RuO_2, IrO_2, and RuO_2@IrO_2 core-shell nanocatalysts. *J. Electroanal. Chem.* 819, 296–305. doi:10.1016/j.jelechem.2017.10.062

Man, I. C., Su, H.-Y., Calle-Vallejo, F., Hansen, H. A., Martínez, J. I., Inoglu, N. G., et al. (2011). Universality in oxygen evolution electrocatalysis on oxide surfaces. *ChemCatChem* 3, 1159–1165. doi:10.1002/cctc.201000397

Martelli, G. N., Ornelas, R., and Faita, G. (1994). Deactivation mechanisms of oxygen evolving anodes at high current densities. *Electrochim. Acta* 39, 1551–1558. doi:10.1016/0013-4686(94)85134-4

Masa, J., and Schuhmann, W. (2019). The role of non-metallic and metalloid elements on the electrocatalytic activity of cobalt and nickel catalysts for the oxygen evolution reaction. *ChemCatChem* 11, 5842–5854. doi:10.1002/cctc.201901151

Masa, J., Piontek, S., Wilde, P., Antoni, H., Eckhard, T., Chen, Y., et al. (2019). Ni-metalloid (B, Si, P, as, and Te) alloys as water oxidation electrocatalysts. *Adv. Energy Mater.* 9, 33–39. doi:10.1002/aenm.201900796

Matsumoto, Y., and Sato, E. (1979). Oxygen evolution on La1−xSrxMnO$_3$ electrodes in alkaline solutions. *Electrochim. Acta* 24, 421–423. doi:10.1016/0013-4686(79)87030-9

Matsumoto, Y., and Sato, E. (1986). Electrocatalytic properties of transition metal oxides for oxygen evolution reaction. *Mater. Chem. Phys.* 14, 397–426. doi:10.1016/0254-0584(86)90045-3

McCrory, C. C., Jung, S., Peters, J. C., and Jaramillo, T. F. (2013). Benchmarking heterogeneous electrocatalysts for the oxygen evolution reaction. *J. Am. Chem. Soc.* 135, 16977–16987. doi:10.1021/ja407115p

McKeown, D. A., Hagans, P. L., Carette, L. P. L., Russell, A. E., Swider, K. E., and Rolison, D. R. (1999). Structure of hydrous ruthenium oxides: implications for charge storage. *J. Phys. Chem. B* 103, 4825–4832. doi:10.1021/jp990096n

Miles, M. H. (1976). Periodic variations of overvoltages for water electrolysis in acid solutions from cyclic voltammetric studies. *J. Electrochem. Soc.* 123, 1459. doi:10.1149/1.2132619

Miles, M. H. (1978). The oxygen electrode reaction in alkaline solutions on oxide electrodes prepared by the thermal decomposition method. *J. Electrochem. Soc.* 125, 1931. doi:10.1149/1.2131330

Newns, D. M. (1969). Self-consistent model of hydrogen chemisorption. *Phys. Rev.* 178, 1123–1135. doi:10.1103/PhysRev.178.1123

Nørskov, J. K., Rossmeisl, J., Logadottir, A., Lindqvist, L., Kitchin, J. R., Bligaard, T., et al. (2004). Origin of the overpotential for oxygen reduction at a fuel-cell cathode. *J. Phys. Chem. B* 108, 17886–17892. doi:10.1021/jp047349j

Nong, H. N., Reier, T., Oh, H.-S., Gliech, M., Paciok, P., Vu, T. H. T., et al. (2018). A unique oxygen ligand environment facilitates water oxidation in hole-doped IrNiOx core–shell electrocatalysts. *Nat Catal* 1, 841–851. doi:10.1038/s41929-018-0153-y

Oener, S. Z., Foster, M. J., and Boettcher, S. W. (2020). Accelerating water dissociation in bipolar membranes and for electrocatalysis. *Science* 369, 1099–1103. doi:10.1126/science.aaz1487

Pfeifer, V., Jones, T. E., Wrabetz, S., Massué, C., Velasco Vélez, J. J., Arrigo, R., et al. (2016). Reactive oxygen species in iridium-based OER catalysts. *Chem. Sci.* 7, 6791–6795. doi:10.1039/C6SC01860B

Schlögl, R., Krtil, P., and Rossmeisl, J. (2018). Rationality in the new oxygen evolution catalyst development. *Curr Opin Electrochem.* 12, 218–224. doi:10.1016/j.coelec.2018.11.014

Rao, M. L. B., Damjanovic, A., and Bockris, J. O. (1963). Oxygen adsorption related to the unpaired d-electrons in transition metals. *J. Phys. Chem.* 67, 2508–2509. doi:10.1021/j100805a520

Rasiyah, P. (1984). The role of the lower metal oxide/higher metal oxide couple in oxygen evolution reactions. *J. Electrochem. Soc.* 131, 803. doi:10.1149/1.2115703

Recommendations (1986). The absolute electrode potential: an explanatory note (Recommendations 1986). *J. Electroanal. Chem. Interfacial Electrochem.* 209, 417–428. doi:10.1016/0022-0728(86)80570-8

Rossmeisl, J., Logadottir, A., and Nørskov, J. K. (2005). Electrolysis of water on (oxidized) metal surfaces. *Chem. Phys.* 319, 178–184. doi:10.1016/j.chemphys.2005.05.038

Rossmeisl, J., Qu, Z.-W., Zhu, H., Kroes, G.-J., and Nørskov, J. K. (2007). Electrolysis of water on oxide surfaces. *J. Electroanal. Chem.* 607, 83–89. doi:10.1016/j.jelechem.2006.11.008

Rüetschi, P., and Delahay, P. (1955). Influence of electrode material on oxygen overvoltage: a theoretical analysis. *J. Chem. Phys.* 23, 556–560. doi:10.1063/1.1742029

Sanchez Casalongue, H. G., Ng, M. L., Kaya, S., Friebel, D., Ogasawara, H., and Nilsson, A. (2014). In Situ observation of surface species on iridium oxide nanoparticles during the oxygen evolution reaction. *Angew Chem. Int. Ed. Engl.* 53, 7169–7172. doi:10.1002/anie.201402311

Saveleva, V. A., Wang, L., Teschner, D., Jones, T., Gago, A. S., Friedrich, K. A., et al. (2018). Operando evidence for a universal oxygen evolution mechanism on thermal and electrochemical iridium oxides. *J. Phys. Chem. Lett.* 9, 3154–3160. doi:10.1021/acs.jpclett.8b00810

Savinova, M., Kasian, O., Ledendecker, M., Speck, F. D., Mingers, A. M., Mayrhofer, K. J. J., et al. (2018). The electrochemical dissolution of noble metals in alkaline media. *Electrocatalysis* 9, 153–161. doi:10.1007/s12678-017-0438-y

Schweinar, K., Gault, B., Mouton, I., and Kasian, O. (2020). Lattice oxygen exchange in rutile IrO. *J. Phys. Chem. Lett.* 11, 5008–5014. doi:10.1021/acs.jpclett.0c01258

Shannon, R. D. (1968). Synthesis and properties of two new members of the rutile family RhO_2 and PtO_2. *Solid State Commun.* 6, 139–143. doi:10.1016/0038-1098(68)90019-7

Simons, R., and Khanarian, G. (1978). Water dissociation in bipolar membranes: experiments and theory. *J. Membr. Biol.* 38, 11–30. doi:10.1007/BF01875160

Spanos, I., Auer, A. A., Neugebauer, S., Deng, X., Tüysüz, H., and Schlögl, R. (2017). Standardized benchmarking of water splitting catalysts in a combined electrochemical flow cell/inductively coupled plasma–optical emission spectrometry (ICP-oes) setup. *ACS Catal* 7, 3768–3778. doi:10.1021/acscatal.7b00632

Spanos, I., Tesch, M. F., Yu, M., Tüysüz, H., Zhang, J., Feng, X., et al. (2019). Facile protocol for alkaline electrolyte purification and its influence on a Ni–Co oxide catalyst for the oxygen evolution reaction. *ACS Catal* 9, 8165–8170. doi:10.1021/acscatal.9b01940

Stoerzinger, K. A., Diaz-Morales, O., Kolb, M., Rao, R. R., Frydendal, R., Qiao, L., et al. (2017). Orientation-dependent oxygen evolution on RuO 2 without lattice exchange. *ACS Energy Lett.* 2, 876–881. doi:10.1021/acsenergylett.7b00135

Su, H.-Y., Sun, K., Wang, W.-Q., Zeng, Z., Calle-Vallejo, F., and Li, W.-X. (2016). Establishing and understanding adsorption–energy scaling relations with negative slopes. *J. Phys. Chem. Lett.* 7, 5302–5306. doi:10.1021/acs.jpclett.6b02430

Sun, Y., Sun, S., Yang, H., Xi, S., Gracia, J., and Xu, Z. J. (2020). Spin-related electron transfer and orbital interactions in oxygen electrocatalysis. *Adv. Mater.* 32. doi:10.1002/adma.202003297

Suntivich, J., May, K. J., Gasteiger, H. A., Goodenough, J. B., and Shao-Horn, Y. (2011). A perovskite oxide optimized for oxygen evolution catalysis from molecular orbital principles. *Science* 334, 1383–1385. doi:10.1126/science.1212858

Taqieddin, A., Nazari, R., Rajic, L., and Alshawabkeh, A. (2017). Review—physicochemical hydrodynamics of gas bubbles in two phase electrochemical systems. *J. Electrochem. Soc.* 164, E448–E459. doi:10.1149/2.1161713jes

Topalov, A. A., Katsounaros, I., Auinger, M., Cherevko, S., Meier, J. C., Klemm, S. O., et al. (2012a). Dissolution of platinum: limits for the deployment of electrochemical energy conversion?. *Angew. Chem. Int. Ed.* 51, 12613–12615. doi:10.1002/anie.201207256

Topalov, A. A., Katsounaros, I., Auinger, M., Cherevko, S., Meier, J. C., Klemm, S. O., et al. (2012b). Dissolution of platinum: limits for the deployment of electrochemical energy conversion?. *Angew. Chem. Int. Ed.* 51, 12613–12615. doi:10.1002/anie.201207256

Topalov, A. A., Cherevko, S., Zeradjanin, A. R., Meier, J. C., Katsounaros, I., and Mayrhofer, K. J. J. (2014). Towards a comprehensive understanding of platinum dissolution in acidic media. *Chem. Sci.* 5, 631–638. doi:10.1039/C3SC52411F

Trasatti, S., and Petrii, O. A. (1991). Real surface area measurements in electrochemistry. *Pure Appl. Chem.* 63, 711–734. doi:10.1351/pac199163050711

Trasatti, S. (1984). Electrocatalysis in the anodic evolution of oxygen and chlorine. *Electrochim. Acta* 29, 1503–1512. doi:10.1016/0013-4686(84)85004-5

Trasatti, S. (1991). Physical electrochemistry of ceramic oxides. *Electrochim. Acta* 36, 225–241. doi:10.1016/0013-4686(91)85244-2

Trasatti, S. (2000a). Electrocatalysis: understanding the success of DSA®. *Electrochim. Acta* 45, 2377–2385. doi:10.1016/S0013-4686(00)00338-8

Vogt, H. (1994). Note on a method to interrelate inner and outer electrode areas. *Electrochim. Acta* 39, 1981–1983. doi:10.1016/0013-4686(94)85077-1

Wang, L., Stoerzinger, K. A., Chang, L., Yin, X., Li, Y., Tang, C. S., et al. (2019). Strain effect on oxygen evolution reaction activity of epitaxial NdNiO 3 thin films. *ACS Appl. Mater. Interfaces* 11, 12941–12947. doi:10.1021/acsami.8b21301

Watzele, S., and Bandarenka, A. S. (2016). Quick determination of electroactive surface area of some oxide electrode materials. *Electroanalysis* 28, 2394–2399. doi:10.1002/elan.201600178

Watzele, S., Hauenstein, P., Liang, Y., Xue, S., Fichtner, J., Garlyyev, B., et al. (2019). Determination of electroactive surface area of Ni-, Co-, Fe-, and Ir-based oxide electrocatalysts. *ACS Catal* 9, 9222–9230. doi:10.1021/acscatal.9b02006

Willsau, J., Wolter, O., and Heitbaum, J. (1985). Does the oxide layer take part in the oxygen evolution reaction on platinum?. *J. Electroanal. Chem. Interfacial Electrochem.* 195, 299–306. doi:10.1016/0022-0728(85)80050-4

Wohlfahrt-Mehrens, M., and Heitbaum, J. (1987). Oxygen evolution on Ru and RuO_2 electrodes studied using isotope labelling and on-line mass spectrometry. *J. Electroanal. Chem. Interfacial Electrochem.* 237, 251–260. doi:10.1016/0022-0728(87)85237-3

Yao, Y., Hu, S., Chen, W., Huang, Z.-Q., Wei, W., Yao, T., et al. (2019). Engineering the electronic structure of single atom Ru sites via compressive strain boosts acidic water oxidation electrocatalysis. *Nat Catal* 2, 304–313. doi:10.1038/s41929-019-0246-2

Zeradjanin, A. R., La Mantia, F., Masa, J., and Schuhmann, W. (2012a). Utilization of the catalyst layer of dimensionally stable anodes—interplay of morphology and active surface area. *Electrochim. Acta* 82, 408–414. doi:10.1016/j.electacta.2012.04.101

Zeradjanin, A. R., Ventosa, E., Bondarenko, A. S., and Schuhmann, W. (2012b). Evaluation of the catalytic performance of gas-evolving electrodes using local electrochemical noise measurements. *ChemSusChem* 5, 1905–1911. doi:10.1002/cssc.201200262

Zeradjanin, A. R., Menzel, N., Schuhmann, W., and Strasser, P. (2014a). On the faradaic selectivity and the role of surface inhomogeneity during the chlorine evolution reaction on ternary Ti–Ru–Ir mixed metal oxide electrocatalysts. *Phys. Chem. Chem. Phys.* 16, 13741–13747. doi:10.1039/C4CP00896K

Zeradjanin, A. R., Topalov, A. A., Cherevko, S., and Keeley, G. P. (2014b). Sustainable generation of hydrogen using chemicals with regional oversupply – feasibility of the electrolysis in acido-alkaline reactor. *Int. J. Hydrogen Energy* 39, 16275–16281. doi:10.1016/j.ijhydene.2014.08.026

Zeradjanin, A. R., Topalov, A. A., Van Overmeere, Q., Cherevko, S., Chen, X., Ventosa, E., et al. (2014c). Rational design of the electrode morphology for oxygen evolution – enhancing the performance for catalytic water oxidation. *RSC Adv.* 4, 9579. doi:10.1039/c3ra45998e

Zeradjanin, A. R., Grote, J.-P., Polymeros, G., and Mayrhofer, K. J. J. (2016). A critical review on hydrogen evolution electrocatalysis: re-exploring the volcano-relationship. *Electroanalysis* 28, 2256–2269. doi:10.1002/elan.201600270

Zeradjanin, A. R., Vimalanandan, A., Polymeros, G., Topalov, A. A., Mayrhofer, K. J. J., and Rohwerder, M. (2017). Balanced work function as a driver for facile hydrogen evolution reaction–comprehension and experimental assessment of interfacial catalytic descriptor. *Phys. Chem. Chem. Phys.* 19, 17019–17027. doi:10.1039/C7CP03081A

Zeradjanin, A. R., Ventosa, E., Masa, J., and Schuhmann, W. (2018). Utilization of the catalyst layer of dimensionally stable anodes. Part 2: impact of spatial current distribution on electrocatalytic performance. *J. Electroanal. Chem.* 828, 63–70. doi:10.1016/j.jelechem.2018.09.034

Zeradjanin, A. R., Polymeros, G., Toparli, C., Ledendecker, M., Hodnik, N., Erbe, A., et al. (2020). What is the trigger for the hydrogen evolution reaction?–towards electrocatalysis beyond the sabatier principle. *Phys. Chem. Chem. Phys.* 22, 8768–8780. doi:10.1039/D0CP01108H

Zeradjanin, A. R., Spanos, I., Masa, J., Rohwerder, M., and Schlögl, R. (2021). Perspective on experimental evaluation of adsorption energies at solid/liquid interfaces. *J. Solid State Electrochem.* 25, 33–42. doi:10.1007/s10008-020-04815-8

Zeradjanin, A. R. (2018a). Frequent pitfalls in the characterization of electrodes designed for electrochemical energy conversion and storage. *ChemSusChem* 11, 1278–1284. doi:10.1002/cssc.201702287

Zeradjanin, A. R. (2018b). Is a major breakthrough in the oxygen electrocatalysis possible?. *Current Opinion in Electrochemistry* 9, 214–223. doi:10.1016/j.coelec.2018.04.006

Zhou, Z., Zaman, W. Q., Sun, W., Zhang, H., Tariq, M., Cao, L., et al. (2019). Effective strain engineering of IrO 2 toward improved oxygen evolution catalysis through a catalyst-support system. *ChemElectroChem* 6, 4586–4594. doi:10.1002/celc.201901037

Conflict of Interest: The authors declare that the research was conducted in the absence of any commercial or financial relationships that could be construed as a potential conflict of interest.

frontiers in Energy Research

ORIGINAL RESEARCH
published: 02 February 2021
doi: 10.3389/fenrg.2020.606742

Computational Screening of Doped Graphene Electrodes for Alkaline CO_2 Reduction

Anand M. Verma, Karoliina Honkala and Marko M. Melander**

Department of Chemistry, Nanoscience Center, University of Jyväskylä, Jyväskylä, Finland

The electrocatalytic CO_2 reduction reaction (CO_2RR) is considered as one of the most promising approaches to synthesizing carbonaceous fuels and chemicals without utilizing fossil resources. However, current technologies are still in the early phase focusing primarily on identifying optimal electrode materials and reaction conditions. Doped graphene-based materials are among the best CO_2RR electrocatalysts and in the present work we have performed a computational screening study to identify suitable graphene catalysts for CO_2RR to CO under alkaline conditions. Several types of modified-graphene frameworks doped with metallic and non-metallic elements were considered. After establishing thermodynamically stable electrodes, the electrochemical CO_2RR to CO is studied in the alkaline media. Both concerted proton-coupled electron transfer (PCET) and decoupled proton and electron transfer (ETPT) mechanisms were considered by developing and using a generalization of the computational hydrogen electrode approach. It is established that the CO_2 electrosorption and associated charge transfer along the ETPT pathway are of utmost importance and significantly impact the electrochemical thermodynamics of CO_2RR. Our study suggests an exceptional performance of metal-doped nitrogen-coordinated graphene electrodes, especially 3N-coordinated graphene electrodes.

Keywords: electrocatalysis, graphene, electrosorption, proton-coupled electron transfer, density functional theory

OPEN ACCESS

Edited by:
Kai S. Exner,
Sofia University, Bulgaria

Reviewed by:
Axel Gross,
University of Ulm, Germany
Michael Busch,
Aalto University, Finland

****Correspondence:***
Karoliina Honkala
karoliina.honkala@jyu.fi
Marko M. Melander
marko.m.melander@jyu.fi

Specialty section:
This article was submitted to Electrochemical Energy Conversion and Storage, a section of the journal Frontiers in Energy Research

Received: *15 September 2020*
Accepted: *11 December 2020*
Published: *02 February 2021*

Citation:
Verma AM, Honkala K and Melander MM (2021) Computational Screening of Doped Graphene Electrodes for Alkaline CO_2 Reduction. Front. Energy Res. 8:606742. doi: 10.3389/fenrg.2020.606742

1 INTRODUCTION

The extensive use of fossil resources has escalated the emission of green house gases, particularly CO_2, and disrupted the atmospheric carbon balance. An appealing approach for maintaining this balance is to utilize renewable energy resources but their intermittent nature presents a serious obstacle in the energy conversion and storage applications (Vasileff et al., 2017; Jia C. et al., 2019). In this regard, converting renewable electrical energy into chemical energy through the electrochemical CO_2 reduction reaction (CO_2RR) has been identified as an efficient solution (Tian et al., 2018; Jia C. et al., 2019). Recently, an integrated electrocatalytic CO_2RR process has drawn appreciable attention due to its extra-ordinary features in enabling atmospheric sequestration of CO_2 followed by ambient CO_2RR to synthesize chemicals or fuels (MacDowell et al., 2010; Vasileff et al., 2017; Jia C. et al., 2019). Further flexibility is obtained by using the electrode potential and reaction conditions (pH, electrolyte) to control reaction thermodynamics and kinetics as well as activity and selectivity.

However, achieving efficient CO_2RR is a challenging task and requires optimization of the electrode material as well as the reaction conditions. There are multiple reasons for this. Firstly, CO_2 is a highly stable molecule as reflected by its high negative reduction potential (−1.90 V *vs.* SHE)

required to drive the first-electron transfer process. To circumvent this, active electrocatalysts need to be developed, where CO_2 can be converted to several different products through sequences of complex, multistep proton-coupled electron transfer (PCET) steps. In addition, as many CO_2 derived products have similar thermodynamic stability, the developed electrocatalyst has to be selective. Controlling selectivity while retaining high activity is the primary goal in CO_2RR electrocatalysis and requires exquisite control over the complex PCET chemistry, which depends sensitively on the electrode material, electrode potential, pH, and electrolyte. Therefore, optimizing the electrocatalytic performance presents a serious challenge to CO_2RR-based applications (Schneider et al., 2012; Jia C. et al., 2019).

In the search for ideal CO_2RR catalysts, numerous metallic electrodes have been thoroughly explored experimentally and computationally (Back et al., 2015a; Back et al., 2015b; Mistry et al., 2014; Peterson et al., 2010; Peterson and Nørskov, 2012; Shi et al., 2014; Zhu et al., 2014; Hori, 2008; DeWulf et al., 1989; Kim et al., 1988; Hori et al., 1986; Hori et al., 1989; Lu et al., 2014; Chen et al., 2012; Gattrell et al., 2006; Akhade et al., 2014; Bagger et al., 2019). However, most of them suffer from one or several of the following shortcomings: low faradic efficiency and selectivity, high overpotential, CO poisoning, high cost, and/or low abundance. The extended metal surfaces are also subject to the d-band center theory and intrinsic thermodynamic scaling relationships between the reaction energies of CO_2RR intermediates. These features together with the Sabatier principle set constraints on the achievable electrocatalytic performance of metallic CO_2RR catalysts and hampers the search for efficient electrode materials (Peterson and Nørskov, 2012; Hansen et al., 2013; Back et al., 2015b; Li et al., 2015).

To circumvent these inherent limitations of current CO_2RR electrocatalysts, several unorthodox or innovative CO_2RR electrocatalysts have been suggested recently (Qu et al., 2010; Wang et al., 2015; Lu and Jiao, 2016; Sun et al., 2017; Kibria et al., 2019; Nitopi et al., 2019). Carbon-based electrocatalysts and in particular doped graphene sheets, are among the most promising materials and have been widely investigated as potential CO_2RR electrodes. Graphene electrocatalysts have several attractive physical properties such as high surface area, high electron mobility, high thermal conductivity, high Young's modulus etc. Furthermore, their geometrical flexibility and electronic structure have been suggested to enable escaping the scaling relationships (Kim et al., 2014; Li et al., 2015). While pure graphene can facilitate *outer-sphere* electron transfer reactions, edges or other defects are usually required for appreciable electrocatalytic activity (Brownson et al., 2012). Even higher activity and selectivity can be achieved by doping pristine or defected graphene with metal or non-metallic elements (Varela et al., 2018; Jia M. et al., 2019; Wu et al., 2019).

Given the promising CO_2RR performance of such graphene-based materials (Varela et al., 2018; Jia M. et al., 2019; Wu et al., 2019), several experimental and computational investigations have explored the origin of their electrocatalytic behavior and to search for new electrocatalysts. Most computational studies have focused on identifying the optimal reaction energies of the *electrochemical PCET steps* but the piling evidence (Ringe et al., 2019; Lee et al., 2020; Vijay et al., 2020) indicates that the non-PCET CO_2 adsorption step is limiting CO_2RR. The reason for calculations focusing on electrochemical PCET steps is that the computational hydrogen electrode (CHE) model (Nørskov et al., 2004), in its original form can only account for PCET steps. The importance of non-PCET steps, such as CO_2 adsorption, can be highlighted by comparing two recent CO_2RR studies (Li et al., 2019; Guo et al., 2020). Considering only the PCET steps, led to the conclusion that CO_2RR on a Fe_4N is thermodynamically facile and a potential as small as ~0.1 V *vs.* RHE is sufficient to produce COOH (Guo et al., 2020). However, accounting for non-PCET steps led to a very different conclusion as the CO_2 adsorption itself is the potential limiting step that has a high thermodynamic barrier of ~0.9 eV (Li et al., 2019).

In addition to considering the electrode material, it should be recognized that the electrocatalytic CO_2RR activity and selectivity are inherent properties of electrochemical interfaces. As the interfacial properties depend sensitively on the electrode material, the electrolyte, pH, and electrode potential (Lu and Jiao, 2016; Nitopi et al., 2019), they can be used for controlling the reaction environment and the electrocatalytic CO_2RR performance (Pérez-Gallent et al., 2017; Aljabour et al., 2018; Gao et al., 2018; Guo et al., 2018; Ringe et al., 2019). Recent studies have demonstrated that the CO_2 adsorption step is sensitive to these properties and it also determines the CO_2RR activity and selectivity (Ringe et al., 2019; Lee et al., 2020; Vijay et al., 2020). Furthermore, the faradaic efficiency of CO_2RR is higher in alkaline conditions where the competing hydrogen evolution reaction (HER) is suppressed. Utilizing highly alkaline conditions facilitates obtaining high current densities at lower overpotentials (Gabardo et al., 2018) and the issue of carbonate formation can be circumvented using gas diffusion electrodes (Malkhandi and Yeo, 2019). However, one has to consider both bulk and local pH which may differ as H^+/OH^- are consumed or formed at the interface resulting in a pH gradient between the electrolyte and electrode interface (Bohra et al., 2019; Varela, 2020). Furthermore, these local pH changes are found to be sensitive to the used electrode potential and current density (Lu et al., 2020).

Given the advantages of pH control and highly alkaline conditions, it is surprising that previous computational CO_2RR studies have solely focused on the acidic CO_2RR. A crucial difference between acidic and alkaline CO_2RR is the proton donor: in acidic conditions, the proton is donated by the hydronium ion or some other acid, whereas, under alkaline conditions, the solvent (water) is more likely the hydrogen donor. This difference can introduce changes to the reaction mechanism: A fully coupled PCET mechanism is preferred in acidic conditions, whereas, under alkaline conditions, a decoupled transfer of an electron and a proton may become the dominant mechanism (Koper, 2013a). In order to understand alkaline CO_2RR, one has to examine the possibility of decoupled electron transfer/proton transfer (ETPT) steps but this requires going beyond the original CHE (Nørskov et al., 2004) model, which is applicable to coupled PCET reactions only. This limitation can be circumvented using more general approaches

such as general grand canonical DFT methods (Mermin, 1965; Melander et al., 2019; Melander, 2020) and the decoupled CHE (Lindgren et al., 2020). While these methods are applicable to ETPT pathways as well, they are currently computationally too demanding for large scale computational screening studies and more tractable methods need to be developed.

In this study, we address the CO_2RR-to-CO on several graphene electrodes in alkaline conditions and account for both PCET and ETPT pathways. To enable this, the commonly applied computational hydrogen electrode method is extended to study the decoupled ETPT reactions. In particular, we consider the effect of partial ET and the potential-dependency of CO_2 adsorption. On this basis a computational screening approach is developed and applied to identify promising doped graphene electrocatalysts for alkaline CO_2RR. A four-level selection criteria is introduced to rank and select catalysts according to their thermodynamic stability, ability to bind and activate CO_2, electrosorption properties, and theoretical limiting and overpotentials. These principles allow us to identify thermodynamically stable doped graphene electrodes with low limiting and overpotentials in alkaline environments. Our study outlines that highly exergonic CO_2 adsorption associated with high degree of electron transfer is detrimental for catalytic performance. We find that N-coordinated Pt and Ru-doped electrodes are promising candidates as pH universal CO_2RR electrodes.

2 METHODS

2.1 Modeling of Graphene Sheets

Pristine graphene is modeled using a simplified non-periodic structure with 42 carbon atoms forming a honeycomb structure with 14 benzene rings. The dangling carbon atoms at the edges of the sheet are terminated with hydrogen atoms (Verma et al., 2018). The flake-based graphene models have been previously shown to be perform well compared to their respective periodic models (Lazar et al., 2013; Verma et al., 2018; Shang et al., 2020). This is attributed to the accounts of non-clustering of carbon atoms and negligible edge effects due to hydrogen-terminations, which make the graphene-flake models trustworthy. In addition, terminating the dangling edge carbon atoms with hydrogen lead to uniform and delocalized distribution of charge and orbitals all over the catalyst surface (Tachikawa and Kawabata, 2011), which prevents any possible artificial localization effects. The graphene-flake models are computationally less expensive compared than extended models while providing a faithful description of graphene. Finally, the graphene-flake model allows us to carry out the large-scale screening studies at the hybrid functional DFT-level (see below for details), which is required to accurately capture the adsorption energies of the CO_2RR intermediates on doped graphene catalysts (Vijay et al., 2020).

Pristine graphene sheets are chemically inert, but their reactivity can be tuned with dopants and defects. The single vacancy is arguably the simplest point defect in graphene; however, larger point defects such as di- and tri-vacancies are also observed in experiments (Warner et al., 2012; He et al., 2014) forming after the coalescence of two or three neighboring mono-vacancies (Trevethan et al., 2014). Different vacancy and doping structures can be experimentally realized using, e.g., selective bombardment followed by ion deposition (Wang et al., 2012), or more refined chemical synthesis (Varela et al., 2018). These vacancies or defects can host a variety of dopants (Wang et al., 2012; He et al., 2014), which we modeled by introducing foreign atom(s) into the created vacancy. These atoms include platinum group metals (Rh, Pd, Pt, and Ru), coinage metals (Ag, Au, and Cu), base metals (Al, Fe, Ni, Mo, Co, Mn, Zn, and Cr), and non-metals (B and N). Structural information for all the studied systems is provided as a **Supplementary Material** set.

We consider three different vacancy structures: single-vacancy (SV), di-vacancy (DV), and tri-vacancy (TV), by removing one, two, and three central carbon atoms, respectively. Three SV systems are investigated namely, M_SV, M_2_SV, and MPt_SV (see **Figures 1A–C**). The M_SV structure results from the deposition of a single metal on a single-vacant structure and presents the simplest doped structure. In the case of M_2_SV and MPt_SV structures, homo- and heteroatom dimers are placed on SV as models for nucleated reaction centers (Ferrante et al., 2016). We also investigated an experimentally inspired M_2_2SV structure (He et al., 2014), where two neighboring single vacancies are both filled with identical atomic dopants, see **Figure 1D**. The M_DV structure, shown in **Figure 1F** has a single dopant in a di-vacancy. The trapping of dopant pairs over tri-vacant surface is energetically more favourable than a single metal dopant and have been observed experimentally (He et al., 2014), and for this reason the M_2_TV structure is considered as well (**Figure 1H**).

The N-coordinated, heteroatom-doped carbon frameworks are the most experimentally (Li et al., 2017; Cheng et al., 2019; Wang et al., 2019; Zhang et al., 2019; Koshy et al., 2020) and computationally (Tripkovic et al., 2013; Li et al., 2015; Ju et al., 2017; Pan et al., 2018; Varela et al., 2019) studied doped graphene electrodes for oxygen reduction reaction (ORR) and CO_2RR. In these N-coordinated structure, the reaction-center is modified by replacing the coordinating carbon atoms with nitrogens. Such modifications of the M_SV and M_DV structures lead to the M_3N and M_4N electrodes having either three or 4 N atoms (**Figures 1E,G**), respectively.

2.2 Density Functional Theory Methods

All density functional theory (DFT) (Hohenberg and Kohn, 1964; Kohn and Sham, 1965) calculations were carried out using Gaussian 09 (RB.01) (Frisch et al., 2009) package with the help of the Gauss View 5 (Dennington et al., 2009) visualizer. Exchange-correlation effects were described using the B3PW91 (Perdew et al., 1991) functional with Grimme's D3 (Grimme et al., 2010) dispersion corrections. The metallic atoms were treated within the effective core potential (ECP) formalism and the LANL2DZ (Hay and Wadt, 1985a; Hay and Wadt, 1985b; Wadt and Hay, 1985) basis set, while for all the other atoms (C, H, O, N, and B) the 6-31 + g (d,p) (Petersson et al., 1988; Petersson and Al-Laham, 1991) basis set was used. The atomic structures were relaxed until the maximum residual force reached below 0.02 eV $Å^{-1}$. The satisfactory performance of the adopted computational approach has been demonstrated previously for graphene (Verma et al., 2018) and metallic clusters (Verma and Kishore, 2017; Verma and Kishore, 2018; Verma and Kishore, 2019).

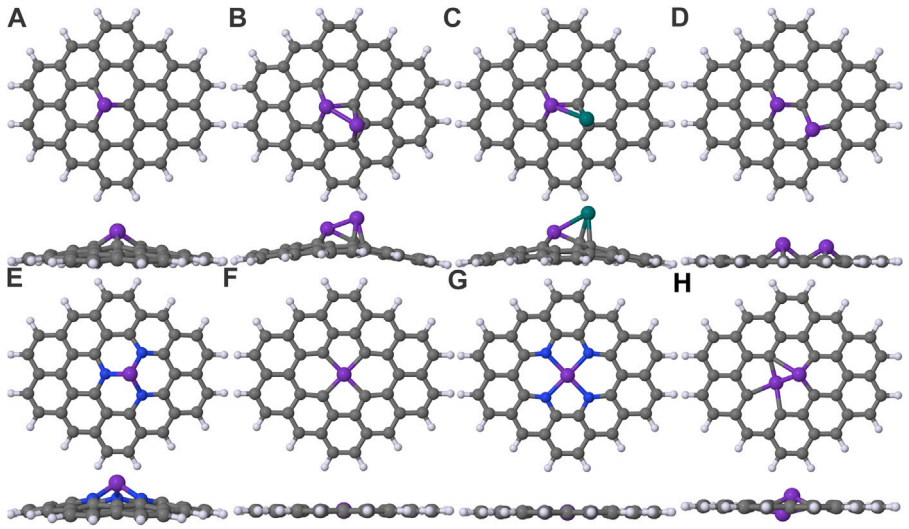

FIGURE 1 | Various models of heteroatom doped graphene electrodes: **(A)** M_SV, **(B)** M_2_SV, **(C)** MPt_SV, **(D)** M_2_2SV, **(E)** M_3N, **(F)** M_DV, **(G)** M_4N, and **(H)** M_2_TV. The elements carbon, nitrogen and hydrogen are in gray, blue and lavender colors, respectively. The dopant atom is a model atom in purple color. The anchoring Pt atom in M_2_SV model is presented in teal color.

Both implicit and explicit solvent effects were mostly excluded from the present study. Considering explicit solvation would have been computationally intractable and the implicit solvent models do not markedly affect the adsorption properties of CO_2RR intermediates in constant charge calculations as, e.g., explicit hydrogen bonding cannot be captured with such models (Heenen et al., 2020). The exclusion of solvation effects from modeling the electrocatalytic reactions is a common approximation that has been shown to successfully describe a variety of electrocatalytic systems (Frydendal et al., 2015; Busch et al., 2016; Calle-Vallejo et al., 2017; Valter et al., 2018). However, we have checked the effect of implicit solvation for some of the consider structures. In particular, we addressed implicit solvent effects using the polarizable continuum model (PCM) (Scalmani and Frisch, 2010) for the best performing electrodes identified from the vacuum calculations. For this, we computed the overpotentials using **Equation 6** with and without implicit solvent for the best performing catalysts, and the differences are at largest 0.16 V *vs.* RHE corresponding to 0.16 eV difference in reaction energies as shown in **Table 1**.

Metal-modified graphene structures are subject to spin-inversion and, therefore, spin-unrestricted DFT was used and a careful investigation of spin multiplicities was necessary to locate the lowest energy spin states. To ensure the correct spin-multiplicity, single point energies at different spin multiplicities were calculated followed by re-optimizations of the atomic structures at the correct spin-multiplicity. The Mulliken charge (q^M), magnetic moment (m), and the most stable spin multiplicity for each dopant in the considered graphene frameworks can be found in **Supplementary Table S1**. Note that all the formation and binding free energy calculations were performed using the most stable spin state structures and their energetics.

Vibrational frequency calculations were performed for all the optimized structures to confirm that they are true minima. The vibrational frequencies were computed to determine the vibrational entropy and zero-point energy contributions in the thermodynamics of CO_2RR. The thermodynamic parameters were calculated at 298.15 K temperature and 1 atm pressure. In the **Supplementary Material**, we present the methodology utilized to compute the thermodynamic entropy, enthalpy, and free energy. The charge analysis was based on the Mulliken scheme (Mulliken, 1955), which is assumed to be accurate enough for the comparison of similar models and similar basis sets.

2.3 Computation of Catalyst Stability

Electrode stability is a prerequisite for maintaining catalytic activity for extended operation time(Krasheninnikov et al., 2009; Wang et al., 2013; Back et al., 2017). In doped graphene electrodes, the deactivation is thought to take place through dopant dissolution (Shao et al., 2019). The dissolution will result in the formation of a graphene vacancy, while the dissolved atoms will likely form metallic nanoparticles or other stable products. Hence, the thermodynamic stability of the studied catalysts was evaluated against pristine graphene and the most stable (bulk) phase of the dopant. The catalyst stability was first referenced against gas-phase metal ions and subsequently against the dopant's most stable bulk phase by utilizing experimental cohesive energies (Kittel, 2004). This way the formation energy is compared against the most stable bulk phase of a given dopant. Finally, the formation free energy (G_{FE}) is computed as:

$$G_{FE} = 1/N\left[G_{MGr} - \left(N \times G_M + N \times G_{vacant\,Gr}\right) + N \times G_{coh}\right] \quad (1)$$

where N is the number of dopant atoms, G_{MGr} is the free energy of the doped graphene electrode, G_M is the free energy of the metal atom in the gas-phase, $G_{vacant\,Gr}$ is the free energy of the vacant graphene, and G_{coh} is the cohesive energy of the dopant(s) (Kittel, 2004).

2.4 Computation of Reaction Free Energies

The CO_2 adsorption free energy (G_{Ads}) over the doped graphene electrodes was calculated using:

$$G_{Ads} = \left[G_{MGr+CO_2} - \left(G_{MGr} + G_{CO_2}\right)\right] \quad (2)$$

where G_{MGr+CO_2} is the free energy of CO_2 adsorbed over modified-graphene, G_{MGr} is the free energy of the bare modified-graphene, and G_{CO_2} is the free energy of gas-phase CO_2.

To model alkaline conditions, we consider water as the hydrogen donor as commonly assumed for alkaline CO_2RR (Yin et al., 2019). In general, the reaction may take place either *via* a sequential ETPT or a concerted PCET mechanism (Dunwell et al., 2018). In the ETPT pathway, the first ET denotes partial charge transfer taking place during CO_2 adsorption on the graphene catalyst, which is followed by further partial ET and PT. For both the sequential and concerted pathways, the elementary steps for CO_2RR to CO are:

$$CO_2(aq) + \delta e^- + Gr \rightleftharpoons CO_2(*)^{\delta e-} \quad (3a)$$

$$CO_2(*)^{\delta e-} + (1-\delta)e^- + H_2O(aq) \rightleftharpoons COOH(*) + OH^-(aq) \quad (3b)$$

$$COOH(*) + e^- \rightleftharpoons CO(*) + OH^-(aq) \quad (3c)$$

$$CO(*) + \rightleftharpoons CO(aq) + Gr \quad (3d)$$

where Gr (also referred as "*") is the graphene catalyst and δ denotes the partial charge. When **Equations 3a,b**, are separated, the mechanism is sequential (ETPT) whereas if they are summed the PCET mechanism is followed.

To compute the electrochemical CO_2RR thermodynamics along both the ETPT and PCET pathways in alkaline conditions, the CHE method was extended to include partial charge transfer and ETPT steps. Note that we are interested in ET taking place during adsorption, i.e., electrosorption, not outer-sphere ET to a dissolved CO_2 forming CO_2^-(aq). The crucial difference is that the solution phase ET to CO_2 can be considered as an *outer-sphere* ET reaction the thermodynamics of which are not affected by the electrode material. In that case, the tabulated (Bratsch, 1989) reduction potentials can simply be used for computing the thermodynamics of this *outer-sphere* ET reaction. For such *outer-sphere* reactions, the thermodynamics can also be accurately computed using standard approaches (Marenich et al., 2014). Here, we instead consider an *inner-sphere* ET taking place during adsorption, and in this case, the electrode cannot be neglected due to the strong interactions and hybridization between the electronic states of electrode and CO_2. For such reactions, the potential-dependent thermodynamics require going beyond standard approaches and methods such as grand canonical DFT are required (Hörmann et al., 2020). Grand canonical DFT as implemented presently is, however, too costly for large-scale screening studies and we propose a computationally feasible extension to CHE to enable addressing (partial) ET. The extension is motivated by the recent decoupled hydrogen electrode method (Lindgren et al., 2020), which combines the CHE with grand canonical DFT. We utilize a computationally more feasible approximation based on the electrosorption valency (Schmickler and Guidelli, 2014) to model the partial ET taking place during CO_2 adsorption to capture the potential-dependency of this step. By combining the electrosorption valency and CHE, the reaction thermodynamics for each elementary step can be calculated using:

$$\Delta G_1(RHE) = G\left(CO_2^{\delta e-}(*)\right) - G(Gr) - G\left(CO_2(aq)\right) + \gamma U(RHE) \quad (4a)$$

$$\Delta G_2(RHE) = \Delta G_w + (1-\gamma)U(RHE) + G(COOH(*)) - \frac{1}{2}G\left(H_2(aq)\right) - G\left(CO_2^{\delta e-}(*)\right) \quad (4b)$$

$$\Delta G_3(RHE) = \Delta G_w + U(RHE) + G(CO(*)) + G\left(H_2O(aq)\right) - \frac{1}{2}G\left(H_2(aq)\right) - G(COOH(*)) \quad (4c)$$

$$\Delta G_4 = G\left(CO(aq)\right) + G(Gr) - G(CO(*)) \quad (4d)$$

A complete derivation of **Equation 4** is presented in the **Supplementary Material**. Here $\Delta G_w = \tilde{\mu}_{H^+} + \tilde{\mu}_{OH^-} - \mu_{H_2O}$ is the water dissociation free energy (0.83 eV at pH = 14) (Bratsch, 1989) **Equations 4a,b** are written for the ETPT pathway and when added together, the reaction free energy for the concerted PCET step is obtained, i.e., $\Delta G_{1+2}(RHE) = \Delta G_1(RHE) + \Delta G_2(RHE)$. $\gamma = (\partial \Delta G^{ads}(U)/\partial U)$ is the electrosorption valency (Schmickler and Guidelli, 2014), which changes the adsorption energy as $\Delta\Delta G^{ads}(U) = \gamma \Delta U$. Note that $\gamma \leq \delta$ and the partial charge transfer upon adsorption do not directly change the Gibbs free energy. As discussed in the SM, γ is a potential-dependent quantity and could be obtained from experiments or using potential-dependent grand canonical DFT, (Melander et al., 2019; Hörmann et al., 2020) but such data is not available for the catalysts studied here. Therefore, we assume that the electrosorption valency is independent of the potential ($\gamma(U) \approx \gamma$), which is a good approximation at potentials close to the reference potential but breaks down as $|U| \gg |U_{ref}|$. This is seen as unphysically large equilibrium potential values for CO_2 adsorption steps–the true upper bound for the $CO_2 \rightarrow CO_2^-$ should be close to its thermodynamic reduction potential of −1.9 V *vs.* SHE (Bratsch, 1989). Here, we approximate the electrosorption valency using the fitting approach (Schmickler and Guidelli, 2014), which gives:

$$\gamma \approx \delta\left[0.84 + 0.16 \times \exp\left(-3\left(\chi^{Gr} - \chi^{CO_2}\right)^2\right)\right] \quad (5)$$

where χs are Pauling electronegativities. $\chi^{Gr} \approx 2.5$ for all metal-doped graphene electrodes. $\chi^{CO_2} \approx 1.5$ is computed using the experimental (NIST database, 2020) CO_2 electron affinity and ionization energies for computing its Mulliken electronegativity (Mulliken, 1934). The Mulliken electronegativity is then converted to the Pauling scale using the linear correlation (Herrick, 2005) between the two scales.

To compare and analyze the electrochemical thermodynamics, we also define the thermodynamic equilibrium potential (U_{eq}), the thermodynamic limiting potential (U_L), and overpotential (η) (Durand et al., 2011) as further discussed in the SM. However, our definition will take into account the ETPT steps with partial charge transfer in terms of the electrosorption valency.

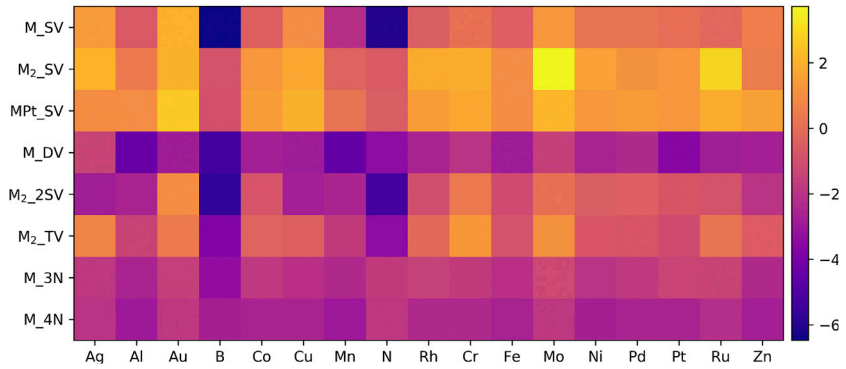

FIGURE 2 | Formation free energies (eV) of various heteroatom doped graphene models. Increasing negative energetics denote stronger formation stability of dopant(s) to the vacant site(s).

$$U_{Eq}(RHE) = \left[\sum_i \Delta G_i(U = 0\ vs.\ RHE)\right] \Big/ n_{e,tot} \quad (6a)$$

$$U_L(ETPT) = -\max\{\Delta G_1(U = 0)/\gamma,\ \Delta G_2(U = 0)/(1-\gamma),\ \Delta G_3(U = 0)\} \quad (6b)$$

$$U_L(PCET) = -\max\{\Delta G_{1+2}(U = 0),\ \Delta G_3(U = 0)\} \quad (6c)$$

$$\eta_{PCET/ETPT} = |U_{eq} - U_L(PCET/ETPT)| \quad (6d)$$

where $n_{e,tot} = 2$ is the total number of electrons transferred in the CO_2RR to CO.

3 RESULTS

3.1 Structures and Stabilities

Thermodynamic stability against dissolution is a key material property mandatory for maintaining electrocatalytic activity and, therefore, we first addressed the stability of our graphene model electrodes against pristine graphene and the thermodynamically most stable (bulk) phase of the dopant. **Figure 2** summarizes the Gibbs free energies for formation, computed according to **Equation 1**. Additional data on formation thermodynamics with numerical values, zero-point energy corrections, and formation enthalpies are reported in the **Supplementary Tables S2–S5**. We found that majority of the studied dimers (M_2_SV and MPt_SV) in single vacancies are thermodynamically unstable and these results are therefore presented and discussed solely in the SM. For other systems, the findings of **Figure 2** are discussed in more detail below.

3.1.1 Single and Two Mono-Vacant Graphene

The M_SV graphenes are the simplest doped graphene structures (see **Figure 1A**). Calculations showed that all metal atoms exhibit slight protrusion out of the graphene plane upon bonding with the dangling carbon atoms, and the vertical distance between a metal atom and graphene plane varies from 0.73 Å to 1.19 Å in good agreement with previous computational studies (Li et al., 2015; Verma et al., 2018; Zhao et al., 2019). About half of the M_SV systems are thermodynamically stable as can be seen from **Figure 2**. The free energy of formation ranges from −0.19 to −6.47 eV; however, doping with coinage metals and a few of base and platinum group metals is thermodynamically unfavorable (see **Supplementary Table S5**). The formation free energies of B- and N-doped graphene are above −6 eV, which demonstrates their extremely strong interaction with the graphene single vacancy.

In the case of M_2_2SV, the metal dopants are also elevated out of the graphene plane similar to M_SV. Almost all M_2_2SV systems are symmetric with the dopants occupying two vacancies. The formation free energy of stable M_2_2SV electrodes ranges from −0.42 eV to −5.70 eV. Doping by non-metallic B and N atoms is extremely exergonic (~−5.5 eV). We found that, upon structural optimization, the Ag, Al, and Cu dopants spontaneously drift away from the vacancy to form dimers, therefore, they are excluded from electrochemical thermodynamics studies.

3.1.2 Di- and Tri-vacant Graphene

In the M_DV graphene, dopant atoms are bound to four nearest undercoordinated C atoms and remain in the basal plane due to the large size of the double vacancy compared to the dopant's atomic radius. The considered non-metallic elements B and N feature benzene-like hexagons with two out of the four undercoordinated carbon atoms. According to the formation free energy analysis, all M_DV graphene structures are highly stable with formation energies ranging from −1.43 eV to −5.28 eV.

The tri-vacancy of M_2_TV models can accommodate the dopant pair in two different orientations: 1) both dopant atoms above the tri-vacancy (**Supplementary Figure S4A**) and 2) one atom above and one below the tri-vacancy (**Supplementary Figure S4B**). We found that the latter geometry is more stable (see **Supplementary Figure S4C**) and was selected for further studies. In the M_2_TV structure, the dopant atoms are bound to the three nearest undercoordinated carbon atoms. Non-metallic B and N dimers break down during structural optimization to form benzene-like structures, and the resulting structures mimic mono-vacant graphenes. The computed formation free energies show that non-metallic dopants in the M_2_TV structure are highly stable, while

metallic M_2_TV electrodes are at best modestly stable, and Ag-, Au-, Cr-, Mo-, and Ru-doped graphenes are unstable.

3.1.3 N-Coordinated Graphene

All the optimized M_3N and M_4N structures are highly symmetric and show no buckling behavior. We find that the average M-N bond distances along with other geometrical features of both N-coordinated structures are similar to their carbon coordinated counterparts (M_SV and M_DV) (Zhao et al., 2019; Kattel et al., 2012). Our calculations suggest that the incorporation of three nitrogen atoms enhances the dopant's stability as can be inferred from the formation free energies ranging from −1.22 eV to −3.28 eV, which are more exergonic than their M_SV counterparts. The formation free energies of M_4N structures vary from −1.84 eV to −2.99 eV and are comparable to the values computed for M_DV models. However, it is evident that the non-metallic dopants prefer 4C-coordination as their formation free energies (see **Figure 2**) are much more exergonic than in the 4N-coordination environment. Therefore, the 4N-coordination environment does not enhance the stability of metallic dopants compared to 4C-coordination in agreement with previous computational results (Zhao et al., 2019).

In general, the geometric and energetic stabilities of modified-graphene sheets depend strongly on the dopant and vacancy but some overall trends are observed. The Ag-, Au-, Cr-, and Mo-doped carbon-coordinated graphene structures are always unstable irrespective of the type of vacancy whereas all the considered dopants in 3N- and 4N-environments are highly stable, which is in line with previous studies (Tripkovic et al., 2013; Li et al., 2015; Ju et al., 2017; Pan et al., 2018; Varela et al., 2019; Wang et al., 2019; Zhang et al., 2019; Koshy et al., 2020).

3.2 CO_2 Adsorption

As discussed in the Introduction, CO_2 adsorption and activation are crucial steps for CO_2RR in alkaline conditions as the adsorption is often thermodynamically unfavorable and limits CO_2RR activity (Jones et al., 2014; Gauthier et al., 2019; Yu et al., 2019; Vijay et al., 2020). Furthermore (partial) charge transfer during CO_2 adsorption may take place and this process is sensitive to the electrode potential but formally independent of solution pH. CO_2 may also be activated upon adsorption, which is seen as the deviation of the O–C–O angle from 180^o. Under alkaline conditions, where only weak proton donors (water) are present, the CO_2 adsorption and an accompanied ET step are important contrary to pure PCET steps. Therefore, we closely monitor the CO_2 adsorption geometry and energy over all of the considered electrodes, regardless of electrode stability. **Figure 3** displays CO_2 binding geometries on the stable M_SV, M_2_2SV, M_3N, M_DV, and M_4N electrodes whereas binding geometries on stable M_2_SV, MPt_SV, and M_2_TV structures are illustrated in **Supplementary Figure S5**. Electronic structure information such as magnetic moments and stable spin multiplicities are supplied in **Supplementary Table S6** for each system, and numerical values for adsorption energies, enthalpies, and free energies are provided in the **Supplementary Tables S7–S10**.

Among the M_SV electrodes, CO_2 adsorption is exergonic only on Fe_SV (−0.12 eV). In this case, CO_2 remains linear upon adsorption (see **Figure 3A**) and the oxygen atom interacts weakly with the metal site having Fe–O distance 2.16 Å and small electron transfer from CO_2 (0.22 e). A similar pattern is observed for the M_DV electrodes as well. The CO_2 adsorption is exergonic only on Fe_DV (see **Figure 3D**) with similar binding configuration and free energy as observed for Fe_SV; however, the charge transfer (0.47 e) from CO_2 is rather high compared to Fe_SV. On the B- and N-doped SV sheets, CO_2 merely physisorbs as seen from the long B-C and N-C distances, which are over 3.1 Å. This is similar to the CO_2 adsorption on the pristine graphene (Rad and Foukolaei, 2015). The activation of CO_2, i.e., non-linear CO_2 structure, occurs only on Mn_SV and Cr- and Mo-based SV and DV structures but the CO_2 adsorption is thermodynamically unfavorable. Note that the formation of Cr- and Mo-doped SV electrodes are thermodynamically unstable as well.

Figure 3B illustrates the adsorption geometry of CO_2 on Mn_2_2SV. The adsorption geometry is similar on all the CO_2-activating M_2_2SV structures. CO_2 adsorption is exergonic on B-, Co-, Mn-, and N-based 2SV structures with adsorption free energies varying from −0.18 eV to −0.68 eV. However, only Co_2_2SV and Mn_2_2SV are able to activate CO_2 and facilitate modest electron transfer to the molecule. While Fe_2_2SV and Ru_2_2SV structures can also activate CO_2, they exhibit thermoneutral adsorption. On the other hand, upon structural optimization, the coinage and a few base metal (Al, Ni, and Zn) dopants stem out of the vacancies and form CO_2-dimer complex above graphene structure, and hence these systems were excluded from further studies.

Apart from Ag- and Cu-doped M_3N models, the majority of M_3N structures exhibit promising CO_2 adsorption characteristics as CO_2 both adsorbs and becomes activated with the O–C–O angle varying between 127.9^o to 150.4^o. The molecule interacts with the metal dopant *via* the carbon atom and one oxygen in a bidentate conformation shown in **Figure 3C** for the Mo_3N structure. In the case of non-metallic dopants, CO_2 favors a monodentate adsorption configuration. The free energies of adsorption range from −0.24 eV to −0.74 eV being comparable to the values found for the M_2_2SV structures. CO_2 adsorption on 4N-coordinated electrodes is surprisingly unfavorable: roughly half of the M_4N structures can activate CO_2 but only Mo_4N (see **Figure 3E**) exhibits exergonic adsorption free energy (−0.89 eV) with exceptionally large charge transfer (−0.67 e). Similar to M_3N graphenes, CO_2 favors a bidentate adsorption geometry on Mo_4N with O–C–O angle of 130.7^o. Given the experimentally proven performance of 4N catalysts, it is unexpected to observe rather high endergonic adsorption energies on these electrodes. Possible reasons for the observed weak adsorption include, e.g., the neglected axial ligands and dipolar interactions as further elucidated in the Discussion section, or the deformation of the electrode structure upon adsorption. To test the latter, we computed the deformation energy for Fe_4N in the same way as in ref (Nykänen and Honkala, 2011). but the contribution from structural deformation is very small and therefore unfavourable

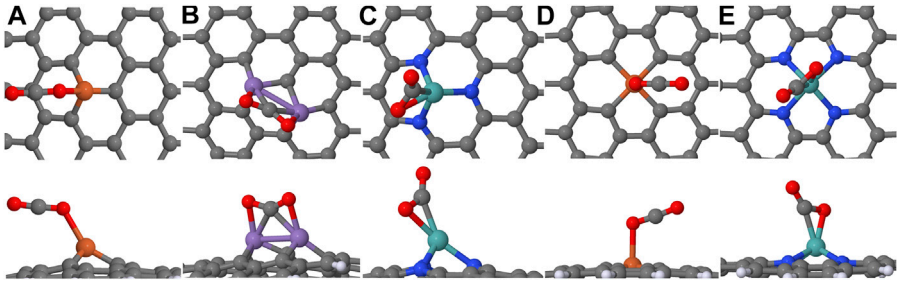

FIGURE 3 | The optimized binding geometries of CO_2 over considered electrodes: **(A)** Fe_SV, **(B)** Mn_2_2SV, **(C)** Mo_3N, **(D)** Fe_DV, and **(E)** Mo_4N. The elements carbon, oxygen, and nitrogen are in gray, red, and blue colors, respectively.

adsorption energies cannot be attributed to structural deformations.

3.3 Selection Criteria

After analyzing the electrode stabilities and CO_2 adsorption, we develop the selection criteria for identifying the most promising modified graphene CO_2RR electrocatalysts from a large pool of materials. For instance, the doping of heteroatom to the graphene electrode should be highly stable to avoid any possible dissolution. The binding of CO_2 to the electrode material should be strong enough to avoid being the limiting step at industrially relevant current densities/potentials. Furthermore, at high pH conditions, Tafel slopes approach 120 mV/dec (Gabardo et al., 2018), which is indicative of electron-transfer (ET) step being the limiting step (Dunwell et al., 2018). Therefore, CO_2 should be activated upon adsorption, become negatively charged, and bind strongly: these features are ranked based on O-C-O angle, negative charge transfer, and negative G_{Ads} values.

To rank and identify prospective CO_2RR electrocatalysts, we introduce a four-level selection criteria (see the flow chart in **Supplementary Figure S6**). First, we screen all bare electrodes and select the ones with negative formation free energy but disregard the systems with geometric instability. The electrodes fulfilling the first criterion are subjected to CO_2 adsorption energy screening. Catalysts, over which the adsorption free energy is below or equal to 0.15 eV (i.e., more adsorbing) are selected. Third, after passing the screening of binding free energies, the next step is CO_2 activation for which we set the threshold value of 150^o for O–C–O angle. Fourth, after previous three criteria, we consider the net charge transfer due to the binding of CO_2 to the electrode as another criteria. In this section, the systems demonstrating net charge transfer below or equal to 0.15 are selected. The upper range of 0.15 eV in the binding free energies of CO_2 and in the net charge transfer is considered to account for any possible number sensitivity due to the DFT methods (Gauthier et al., 2020). This is an acceptable condition considering the fact that the electronic structure results often deviate by 0.1 eV due to different DFT functionals or basis sets.

A combined plot of three key selection parameters, i.e., adsorption free energy (G_{Ads}), O–C–O angle, and charge transfer (q) for each of the electrode categories, namely, M_SV, M_DV, M_2_2SV, M_2_TV, M_3N, and M_4N, is supplied in **Supplementary Figure S7**. Based on the selection criteria, the qualified systems to study the electrochemical thermodynamics are: M_2_2SV (Co, Mn, Rh, Fe, and Ru), M_2_TV (Al, Cu, and Zn), M_3N (Al, N, Rh, Cr, Fe, Mo, Pd, Pt, and Ru), and M_4N (Mo and Ru). Thus, a total of 19 electrodes are selected for further study. Note that none of M_SV and M_DV electrodes qualify the present selection criteria.

3.4 COOH and CO Binding: Scaling Relations

CO and COOH adsorption energies typically exhibit scaling relations and are therefore often taken as CO_2RR activity and selectivity descriptors (Peterson and Nørskov, 2012; Koper, 2013a; Kuhl et al., 2014; Nitopi et al., 2019). However, there are indications (Kim et al., 2014; Li et al., 2015; Back et al., 2017) that the CO/COOH scaling relations and descriptors are not valid for graphene-based electrodes. To study whether scaling relations can be established among the materials studied here, we attempt to find correlations between the CO_2, COOH, and CO adsorption free energies. This analysis is carried out for the M_3N and M_2_2SV electrodes only as M_4N and M_2_TV electrodes contain too few data points. The binding energies are presented in the **Supplementary Table S11** and are utilized in the next section to study the electrochemical thermodynamics.

From **Supplementary Figures S8, S9**, it is evident that a poor correlation exists between the binding free energies of COOH and CO_2 over M_3N (R^2 = 0.07) and M_2_2SV (R^2 = 0.24) electrodes. Similar results are observed for COOH/CO scaling relationships on M_3N (R^2 = 0.29) and M_2_2SV (R^2 = 0.08) electrodes as well. These poor scaling relations are in agreement with previous studies on graphene-based electrodes (Li et al., 2015; Back et al., 2017; Li et al., 2019; Guo et al., 2020), which indicates that graphene electrodes may break scaling relationships making these materials an interesting class of CO_2RR electrocatalysts. However, it needs to be recognized that the number of materials subjected to the scaling relation studies is small and too far-reaching conclusions on breaking scaling should be avoided. Yet, it has been shown that even slight modifications to N-doped graphene electrodes lead to different scaling relations (Guo et al., 2020).

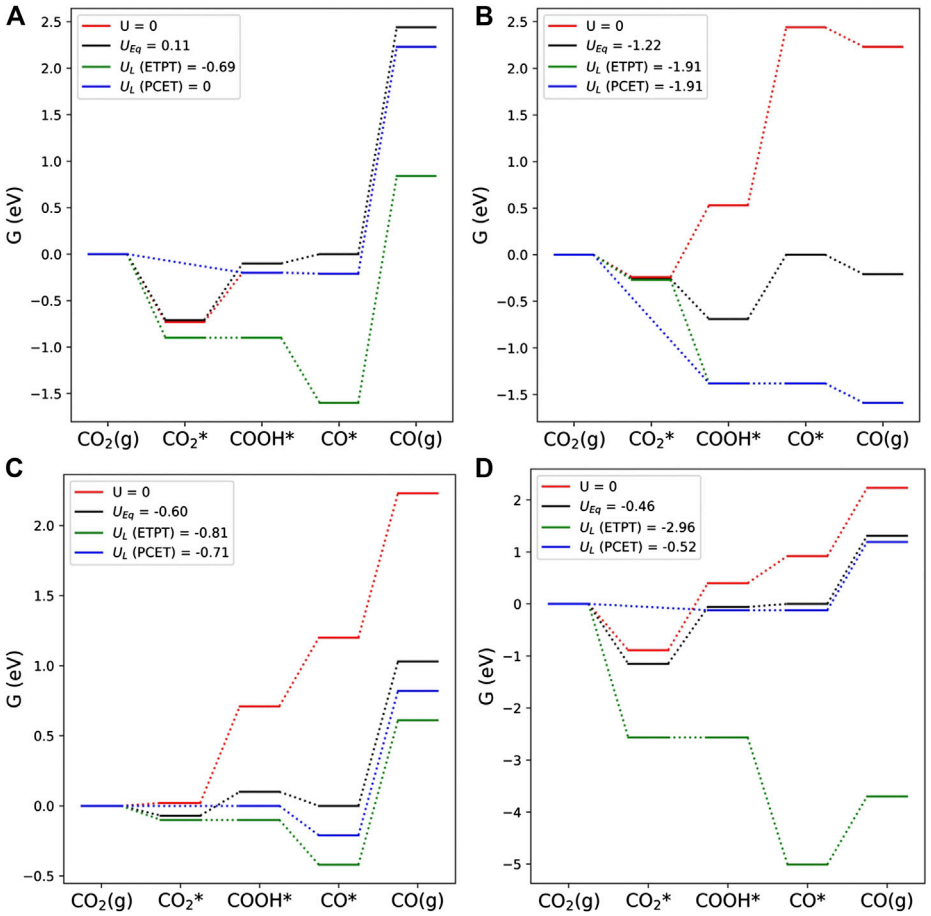

FIGURE 4 | Electrochemical thermodynamics of CO_2 reduction reaction using PCET and ETPT mechanisms over four selected electrodes: **(A)** Pt_3N, **(B)** Al_3N, **(C)** Ru_2_2SV, and **(D)** Mo_4N.

3.5 Electrochemical Thermodynamics

To address the electrochemical performance of the qualified electrodes, electrochemical thermodynamics for CO_2 reduction to CO were computed using **Equations 4**, **6**. While **Figure 4** displays the thermodynamic profiles for selected materials with varying behavior along the PCET and ETPT pathways, the limiting potentials and overpotentials are illustrated in **Figure 5**. For other materials, not shown here, the potential energy surfaces are displayed in **Supplementary Figure S10** and the explicit potential values are collected in **Supplementary Table S12**.

As displayed in **Figure 4A**, a large potential difference (0.69 V) between the ETPT and PCET pathways is observed for the Pt_3N catalyst. We attribute this difference to the inclusion of the CO_2 binding in the former mechanism. The CO_2 adsorption step itself is rather exergonic and associated with a modest charge transfer (~−0.3 e) from the electrode. Along the PCET pathway, COOH and CO formation steps are mildly exergonic at zero potential resulting in *positive* equilibrium potential. This observation suggests that PCET pathway on Pt_3N is nearly thermodynamically ideal and requires zero limiting potential (blue PES). On the other hand, the ETPT mechanism is far from ideal and a large negative limiting potential is required due to the highly endergonic CO_2→COOH step and the significant partial charge transfer (~0.7 e) in this step.

CO_2RR thermodynamics on the Al_3N catalysts, shown in **Figure 4B**, provides an example where both the ETPT and PCET pathways attain same limiting potential. Herein, CO_2 adsorption energy is modestly exergonic and features insignificant charge transfer. Furthermore, CO formation is highly unfavourable compared to COOH and is therefore identified as the potential-determining step. As the reaction free energy for CO formation (see **Equation 4c**) is same for both PCET and ETPT pathways, the resulting thermodynamic potentials are also equal.

In **Figure 4C**, the Ru_2_2SV electrode is considered. CO_2 adsorption is almost thermoneutral at zero potential (red line) associated with a small charge transfer (~−0.2 e) from the electrode. The formation of COOH is identified as the limiting step owing to its high endergonicity. Altogether these factors make ETPT and PCET limiting potentials rather similar, which in turn implies that this material is a promising candidate for both ETPT and PCET pathways, i.e., for both alkaline and acid conditions. However, the CO adsorption free energy (~−1 eV)

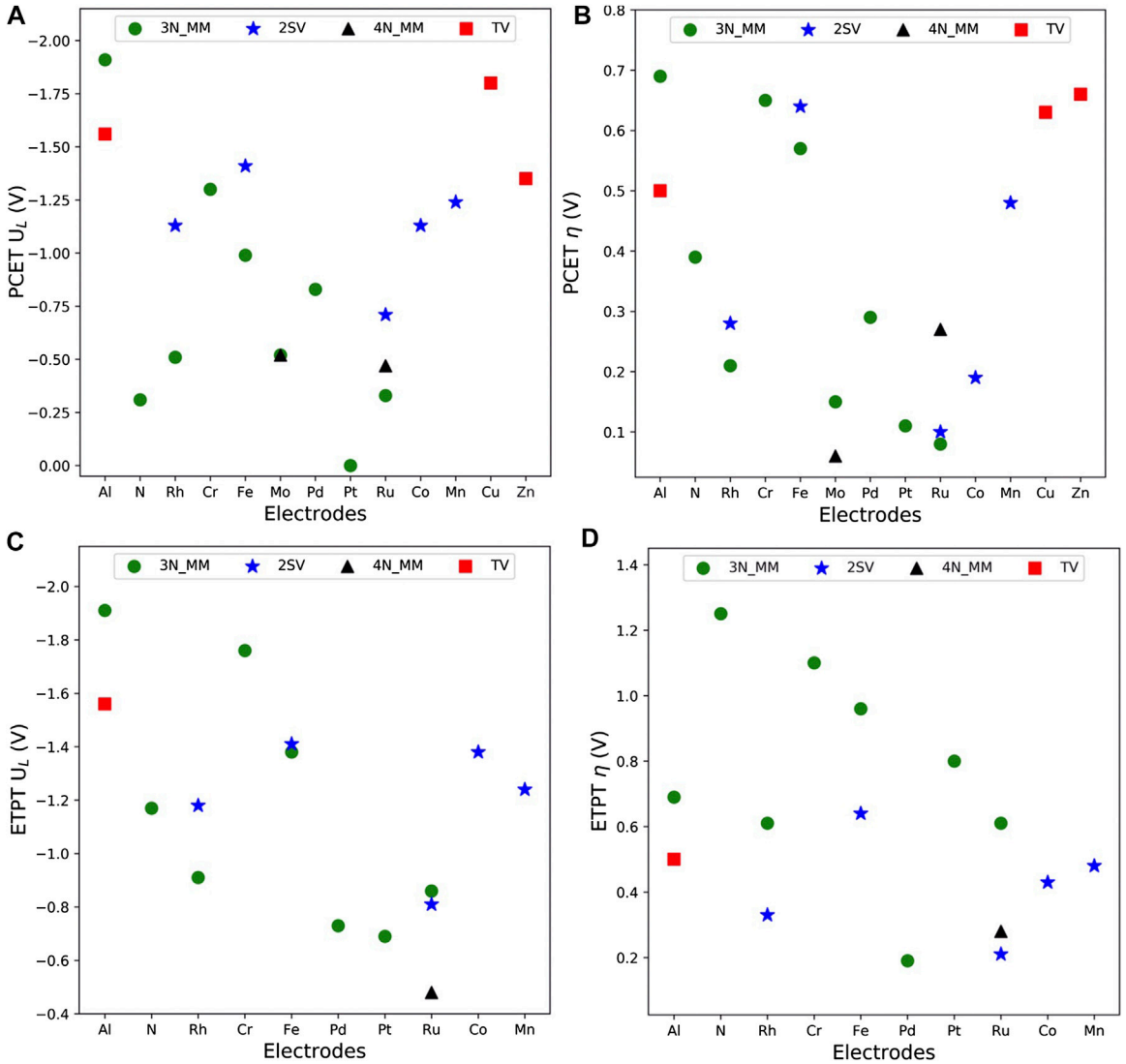

FIGURE 5 | Calculated theoretical limiting (**(A,C)**, 0 to −2.0 V *vs.* RHE) and overpotential (**(B,D)**,0–1.5 V *vs.* RHE) of electrocatalytic CO_2RR process *via* PCET **(A,B)** and ETPT **(C,D)** mechanisms.

on the electrode is too strong, which makes it susceptible to catalyzing further reduction or poisoning.

The last example, given in **Figure 4D**, features very different limiting potentials for the ETPT and PCET pathways on the Mo_4N electrode. In this case, CO_2 adsorbs strongly, significant charge transfer (~−0.7 e) to the molecule takes place, and the COOH formation is quite endergonic at zero potential (red line). Together these factors result in a large negative limiting potential along the ETPT pathway, while the PCET exhibits a fairly modest overpotential. Similar behavior is seen for the Mo_3N electrode as well and we conclude that the N-Mo-modified graphene catalysts are unsuitable for a ETPT mechanism but could work for the PCET pathway.

Comparison of the ETPT potential energy profiles given in **Figure 4** shows that CO_2 adsorption and associated charge transfer are pivotal for this mechanism to be operational, but they are absent from PCET due to the assumption of simultaneous electron and proton transfer. Overall, these differences modify the reaction thermodynamics, and we observed that the charge transfer during adsorption has a profound effect on the electrocatalytic thermodynamics as

TABLE 1 | Thermodynamic overpotentials in the presence of implicit solvation (η^{aq}) (V *vs.* RHE) for the three promising ETPT and PCET electrocatalysts. Also, the magnitude of deviation ($\Delta\eta$) from the vacuum phase (η^{vac}) is indicated.

Electrode	η^{aq}		$\Delta\eta = = \eta^{vac} - \eta^{aq}$	
	ETPT	PCET	ETPT	PCET
Pt_3N	0.75	0.15	0.05	−0.04
Ru_3N	0.63	0.04	−0.02	0.05
Ru_4N	0.28	0.11	0.00	0.16

manifested by the limiting potentials shown in **Figures 4**, **5**. We found that the slightly exergnonic CO_2 adsorption is beneficial as it enables the formation of a stable CO_2-catalyst complex and prevents excessively endergonic COOH formation. Furthermore, charge transfer associated with CO_2 adsorption should be as low as possible: if the COOH formation requires only a very small degree of charge transfer, a very high reductive potential is needed to make this step thermodynamically favorable as shown in, e.g., **Figure 4D**. In a case where no charge transfer takes place during $CO_2^- + H^+ \rightarrow COOH$, the COOH formation step is fully chemical and cannot be controlled by the electrode potential. The very large limiting potentials along the ETPT pathways are likely an artifact of the simple charge transfer and electrosorption model adopted herein, but we believe that the present model enables qualitatively correct comparison of thermodynamics between ETPT and PCET processes.

The thermodynamic potentials are extensively used for ranking or comparing the expected performance of different catalysts, and limiting potentials and overpotentials should be close to zero for the best performing catalysts. **Figure 5** presents both potentials for the PCET and ETPT pathways. For all the qualified electrodes, the overpotentials are within 0.7 V (*vs.* RHE) for PCET pathways. The best-performing electrodes include Ru, Rh, and Mo-doped 3N graphene and Ru and Mo-doped 4N graphene for which the limiting potentials vary from 0 to −0.52 V *vs.* RHE and overpotentials range from 0.06 to 0.21 V *vs.* RHE. For the ETPT mechanism, the best-performing electrodes contain Pd_3N, Ru_3N, Pt_3N, Ru_2_2SV, and Ru_4N with limiting potentials between −0.48 and −0.86 V *vs.* RHE and overpotentials varying from 0.28 to 0.8 V *vs.* RHE. The limiting potentials found for the studied structures are either comparable or even smaller than those previously computed for 4N and 3N catalysts (Guo et al., 2020; Pan et al., 2020), non-metallic defected graphene (Siahrostami et al., 2017), and single-atom doped metal catalysts (Lim et al., 2014). Overall, the ETPT mechanism leads to higher overpotentials and limiting potentials than the PCET pathway, which we take to indicate that pure ET steps are detrimental for the reaction thermodynamics as commonly suggested (Koper, 2013b). Interestingly, we find that three of the studied materials–Ru_3N, Pt_3N, and Ru_4N–exhibit very promising electrochemical thermodynamics along both the ETPT and PCET pathways making these materials promising candidates for CO_2RR under both acidic (PCET) and alkaline (ETPT) conditions.

Next, we simulated the three promising ETPT and PCET electrocatalysts (Ru_3N, Pt_3N, and Ru_4N) using the PCM model (Scalmani and Frisch, 2010) for water to check the solvation effects on the overpotentials, and their deviations from the vacuum phase thermodynamics. The adsorption free energies of CO_2 in the aqueous medium are lower ($G_{Ads(aq)}^{Pt\_3N}$ = −0.49 eV; $G_{Ads(aq)}^{Ru\_3N}$ = −0.08 eV; and $G_{Ads(aq)}^{Ru\_4N}$ = 0.02 eV) than those of computed for the vacuum phase, but charge transfer from electrodes to the CO_2 in the solution phase is significantly higher (−0.5 e to −0.6 e). The aqueous phase PCET and ETPT limiting potentials of Pt_3N and Ru_3N are slightly lower compared to vacuum phase, whereas, slightly higher limiting potentials are observed for Ru_4N. As shown in **Table 1**, including solvation introduces only small changes to overpotentials. The largest change is observed for Ru_4N ($\Delta\eta$ = 0.16 V), which is still relatively small given typical DFT inaccuracies. We ascribe the observed difference to slightly more stable adsorption of COOH* in the solution phase compared to vacuum phase. Finally, it can be concluded that the implicit solvation framework does not significantly change the thermodynamics computed in gas-phase, and thus the conclusions remain largely unaffected by the implicit solvation.

4 DISCUSSION

Our computational predictions show that the CO_2RR activity and selectivity on a given graphene-based electrode depend on the mechanism, i.e., whether the PCET or ETPT pathway is followed. For conditions favoring the PCET mechanism, the N-coordinated graphene electrodes demonstrate the best performance among the studied models. The aforementioned holds true also when ETPT is operational but this typically leads to larger limiting potentials. Pd_3N is an exception to this rule and is the only electrode for which a lower overpotential along the ETPT than the PCET pathway is observed. This anomaly is caused by the slightly positive CO_2 binding energy and minor charge transfer. In general, we find that the coupled PCET is thermodynamically more favorable but for kinetic reasons the ETPT pathway may be preferred (Koper, 2013b).

The obtained results show that the ETPT pathway is highly sensitive to the CO_2 electrosorption energy and charge transfer. Ignoring these important features from mechanistic consideration and focusing solely on the PCET mechanism, often leads to a different potential-determining step, and underestimation of thermodynamic potentials. For example, the current and previous computational studies (Li et al., 2019; Vijay et al., 2020) on Fe_4N show that the CO_2 binding itself introduces a thermodynamic barrier of ~0.9 eV, whereas, the PCET pathway (Guo et al., 2020) presents a quite small (~0.1 eV) thermodynamic barrier for producing COOH. These results demonstrate that CO_2 adsorption directly affects the CO_2RR elementary thermodynamics and should therefore be considered. The adsorption process and its potential-dependency are particularly important under alkaline conditions where the coupled PCET becomes less likely, and at high current densities where mass transfer and adsorption are the limiting processes. We identified that slightly exergonic CO_2 adsorption associated with minor charge transfer is a desirable feature for promising catalysts. The conclusions from a large number of studies (see Introduction) neglecting the adsorption step and focusing only on PCET steps are limited to acidic conditions or to the electrodes that cannot catalyze the ETPT pathway.

The importance of the adsorption step can be further illustrated by the widely studied Fe_4N electrode. Our results suggest that the Fe_4N electrode (Zhang et al., 2018; Li et al., 2019; Vijay et al., 2020) does not belong to the best performing CO_2RR materials. We attribute this to the thermodynamically unfavorable CO_2 adsorption step, which agrees with the recent finding that the adsorption step on Fe_4N is thermodynamically uphill even under high electrode potentials and field strengths (Vijay et al., 2020). Therefore, CO_2RR on Fe_4N is limited by CO_2

adsorption and mass transfer at industrially relevant current densities (Vijay et al., 2020). Even though our decoupled pathway and CO_2RR analyses are based on a relatively simple and ideal electrosorption valency concept, the identification of CO_2 adsorption as a crucial step is expected to be rather general. In particular, our approach provides a fast approach to identify a catalyst, where ET during adsorption is an important feature.

In addition to accounting for ETPT and electrosorption, future studies should also consider the role of "innocent" ligands introduced by the pH or the supporting electrolyte. A recent joint experimental and computational work (Li et al., 2019) has shown that axial ligands are important in determining the CO_2RR to CO performance on M_4N-type materials. While the experimental results exhibit a high current density and Faradaic efficiency toward CO at applied potentials of −0.5 and −0.6 V *vs.* RHE, the calculations predict a significant thermodynamic barrier of ~0.9 eV for CO_2 adsorption in agreement with our results. As the initial computational results were not in line with the experimental findings, the effect of axial adsorption of H_2O and OH was considered. While the adsorption energy was found to be further destabilized with axial OH adsorption, the axially adsorbed H_2O stabilized CO_2 adsorption on Fe_4N by ~0.3 eV. Including the axial H_2O ligand in the computational Fe_4N model resulted in a better agreement with experiments as the CO_2 adsorption posed only a small thermodynamic barrier (0.06 eV) at −0.6 V *vs.* RHE. Furthermore, the simulated Pourbaix diagrams (Li et al., 2019) confirmed that Fe_4N electrode may bind axial ligands on both sides. While the kinetic role of the axial ligands was not considered for CO_2RR, the oxygen reduction reaction kinetics were shown to be very sensitive to the presence of "innocent" axial ligands (Rebarchik et al., 2020).

Previous studies (Peterson and Nørskov, 2012; Kuhl et al., 2014; Nitopi et al., 2019) suggested that CO binding strength is a descriptor that determines the CO_2RR product distribution. Materials with strong CO adsorption are either poisoned or produce C_1- or C_2-species or form hydrogen *via* the competing HER. On the contrary, electrodes binding CO weakly yield CO as the major product due to favourable CO desorption kinetics. Apart from Al-, Cr-, and Pd-dopants, the majority of 3N-coordinated electrodes bind CO quite strongly suggesting that they might be poisoned by CO. The CO adsorption on Al_3N ($\eta_{ETPT/PCET}$ = 0.69 V) is weak and leads to facile CO desorption. Intermediate CO adsorption energies on Cr_3N and Pd_3N suggest that these two materials are promising electrocatalysts for producing C_1- or C_2-molecules; however, the former suffers from rather high limiting potential making Pd_3N the only 3N-graphene electrode suitable for further CO reduction. With the exception of Ru_2_2SV, all the other 2SV electrodes exhibit CO binding strength within ~−0.7 eV indicating that they will primarily produce CO. The M_2_2SV electrodes show low overpotentials but feature high negative limiting potentials (above −1V) except for Ru_2_2SV, which is identified as the most promising M_2_2SV structure. Both M_4N and M_2_TV electrodes suffer from either strong CO binding or high limiting potentials, and are therefore unsuitable for CO production.

5 CONCLUSION

In this work, we identified promising modified graphene electrodes for CO_2RR to CO under alkaline conditions. Robust selection criteria based on thermodynamic stability, CO_2 adsorption thermodynamics, and potential-dependent reaction free energies were devised and applied. The computational hydrogen electrode concept was extended to treat decoupled PCET steps at electrode surfaces to account for the possible decoupled ETPT mechanism in alkaline conditions. We utilized this development to evaluate the effect of pure charge transfer during adsorption, i.e., electrosorption, and found that a high degree of partial charge transfer during CO_2 is detrimental to electrocatalyst performance and that moderately strong CO_2 adsorption energy without charge transfer leads to promising electrode materials. We identified metal sites coordinated to three nitrogen atoms (M_3N) and two single vacancy metal (M_2_2SV) electrodes as highly promising materials for CO_2RR following either the coupled or decoupled pathways. N-coordinated Ru and Pt electrodes exhibit promising characteristics for both coupled and decoupled pathways making these materials interesting candidates as pH-universal CO_2RR electrodes and call for further experimental and computational studies.

DATA AVAILABILITY STATEMENT

The datasets presented in this study can be accessed at https://gitlab.com/ 1341 compcatjyu/co2rr-on-graphene-electrodes.

AUTHOR CONTRIBUTIONS

AV performed the calculations and analysed the data. MM developed the thermodynamic model and oversaw the analysis. KH oversaw the calculations and analysis. All authors contributed to conceptualising the work and writing the manuscript.

FUNDING

MM was supported by the Academy of Finland grants 307853 and 317739. AV and KH were supported by the Academy of Finland grant 317739.

ACKNOWLEDGMENTS

The computational resources were provided by the CSC–IT Center for Science, Espoo, Finland (https://www.csc.fi/en/) and the FGCI–Finnish Grid and Cloud Infrastructure.

SUPPLEMENTARY MATERIAL

The Supplementary Material for this article can be found online at: https://www.frontiersin.org/articles/10.3389/fenrg.2020.606742/full#supplementary-material.

REFERENCES

Akhade, S. A., Luo, W., Nie, X., Bernstein, N. J., Asthagiri, A., and Janik, M. J. (2014). Poisoning effect of adsorbed CO during CO electroreduction on late transition metals. *Phys. Chem. Chem. Phys.* 16, 20429–20435. doi:10.1039/C4CP03340J

Aljabour, A., Coskun, H., Apaydin, D. H., Ozel, F., Hassel, A. W., Stadler, P., et al. (2018). Nanofibrous cobalt oxide for electrocatalysis of CO reduction to carbon monoxide and formate in an acetonitrile-water electrolyte solution. *Appl. Catal. B.* 229, 163–170. doi:10.1016/j.apcatb.2018.02.017

Back, S., Kim, H., and Jung, Y. (2015a). Selective heterogeneous CO electroreduction to methanol. *ACS Catal.* 5, 965–971. doi:10.1021/cs501600x

Back, S., Yeom, M. S., and Jung, Y. (2015b). Active sites of Au and Ag nanoparticle catalysts for CO electroreduction to CO. *ACS Catal.* 5, 5089–5096. doi:10.1021/acscatal.5b00462

Back, S., Lim, J., Kim, N.-Y., Kim, Y.-H., and Jung, Y. (2017). Single-atom catalysts for CO electroreduction with significant activity and selectivity improvements. *Chem. Sci.* 8, 1090–1096. doi:10.1039/C6SC03911A

Bagger, A., Ju, W., Varela, A. S., Strasser, P., and Rossmeisl, J. (2019). Electrochemical CO reduction: classifying Cu facets. *ACS Catal.* 9, 7894–7899. doi:10.1021/acscatal.9b01899

Bohra, D., Chaudhry, J. H., Burdyny, T., Pidko, E. A., and Smith, W. A. (2019). Modeling the electrical double layer to understand the reaction environment in a CO electrocatalytic system. *Energy Environ. Sci.* 12, 3380–3389. doi:10.1039/C9EE02485A

Bratsch, S. G. (1989). Standard electrode potentials and temperature coefficients in water at 298.15 K. *J. Phys. Chem. Ref. Data* 18, 1–21. doi:10.1063/1.555839

Brownson, D. A. C., Kampouris, D. K., and Banks, C. E. (2012). Graphene electrochemistry: fundamental concepts through to prominent applications. *Chem. Soc. Rev.* 41, 6944–6976. doi:10.1039/C2CS35105F

Busch, M., Halck, N. B., Kramm, U. I., Siahrostami, S., Krtil, P., and Rossmeisl, J. (2016). Beyond the top of the volcano? – a unified approach to electrocatalytic oxygen reduction and oxygen evolution. *Nano. Energy* 29, 126–135. doi:10.1016/j.nanoen.2016.04.011

Calle-Vallejo, F., Krabbe, A., and García-Lastra, J. M. (2017). How covalence breaks adsorption-energy scaling relations and solvation restores them. *Chem. Sci.* 8, 124–130. doi:10.1039/C6SC02123A

Chen, Y., Li, C. W., and Kanan, M. W. (2012). Aqueous CO reduction at very low overpotential on oxide-derived Au nanoparticles. *J. Am. Chem. Soc.* 134, 19969–19972. doi:10.1021/ja309317u

Cheng, Y., Yang, S., Jiang, S. P., and Wang, S. (2019). Supported single atoms as new class of catalysts for electrochemical reduction of carbon dioxide. *Small Methods* 3, 1800440. doi:10.1002/smtd.201800440

Dennington, R., Keith, T. A., and Millam, J. M. (2009). *Gaussview Version 5.* Semichem Inc. Shawnee Mission KS.

DeWulf, D. W., Jin, T., and Bard, A. J. (1989). Electrochemical and surface studies of carbon dioxide reduction to methane and ethylene at copper electrodes in aqueous solutions. *J. Electrochem. Soc.* 136, 1686. doi:10.1149/1.2096993

Dunwell, M., Luc, W., Yan, Y., Jiao, F., and Xu, B. (2018). Understanding surface-mediated electrochemical reactions: CO reduction and beyond. *ACS Catal.* 8, 8121–8129. doi:10.1021/acscatal.8b02181

Durand, W. J., Peterson, A. A., Studt, F., Abild-Pedersen, F., and Nørskov, J. K. (2011). Structure effects on the energetics of the electrochemical reduction of CO by copper surfaces. *Surf. Sci.* 605, 1354–1359. doi:10.1016/j.susc.2011.04.028

Ferrante, F., Prestianni, A., Cortese, R., Schimmenti, R., and Duca, D. (2016). Density functional theory investigation on the nucleation of homo-and heteronuclear metal clusters on defective graphene. *J. Phys. Chem. C.* 120, 12022–12031. doi:10.1021/acs.jpcc.6b02833

Frisch, M. J., Trucks, G. W., Schlegel, H. B., Scuseria, G. E., Robb, M. A., Cheeseman, J. R., et al. (2009). *GaussianËœ09 revision B.01.* Wallingford CT: Gaussian Inc.

Frydendal, R., Busch, M., Halck, N. B., Paoli, E. A., Krtil, P., Chorkendorff, I., et al. (2015). Enhancing activity for the oxygen evolution reaction: the beneficial interaction of gold with manganese and cobalt oxides. *ChemCatChem.* 7, 149–154. doi:10.1002/cctc.201402756

Gabardo, C. M., Seifitokaldani, A., Edwards, J. P., Dinh, C.-T., Burdyny, T., Kibria, M. G., et al. (2018). Combined high alkalinity and pressurization enable efficient CO electroreduction to CO. *Energy Environ. Sci.* 11, 2531–2539. doi:10.1039/C8EE01684D

Gao, D., McCrum, I. T., Deo, S., Choi, Y.-W., Scholten, F., Wan, W., et al. (2018). Activity and selectivity control in CO electroreduction to multicarbon products over CuO_x catalysts via electrolyte design. *ACS Catal.* 8, 10012–10020. doi:10.1021/acscatal.8b0258

Gattrell, M., Gupta, N., and Co, A. (2006). A review of the aqueous electrochemical reduction of CO to hydrocarbons at copper. *J. Electroanal. Chem.* 594, 1–19. doi:10.1016/j.jelechem.2006.05.013

Gauthier, J. A., Chen, L. D., Bajdich, M., and Chan, K. (2020). Implications of the fractional charge of hydroxide at the electrochemical interface. *Phys. Chem. Chem. Phys.* 22, 6964–6969. doi:10.1039/C9CP05952K

Gauthier, J. A., Fields, M., Bajdich, M., Chen, L. D., Sandberg, R. B., Chan, K., et al. (2019). Facile electron transfer to CO during adsorption at the metal— solution interface. *J. Phys. Chem. C.* 123, 29278–29283. doi:10.1021/acs.jpcc.9b10205

Grimme, S., Antony, J., Ehrlich, S., and Krieg, H. (2010). A consistent and accurate ab initio parametrization of density functional dispersion correction (DFT-D) for the 94 elements H-Pu. *J. Chem. Phys.* 132, 154104. doi:10.1063/1.3382344

Guo, C., Zhang, T., Liang, X., Deng, X., Guo, W., Wang, Z., et al. (2020). Single transition metal atoms on nitrogen-doped carbon for CO electrocatalytic reduction: CO production or further CO reduction? *Appl. Surf. Sci.* 533, 147466. doi:10.1016/j.apsusc.2020.147466

Guo, S.-X., Li, F., Chen, L., MacFarlane, D. R., and Zhang, J. (2018). Polyoxometalate-promoted electrocatalytic CO reduction at nanostructured silver in dimethylformamide. *ACS Appl. Mater. Interfaces* 10, 12690–12697. doi:10.1021/acsami.8b01042

Hansen, H. A., Varley, J. B., Peterson, A. A., and Nørskov, J. K. (2013). Understanding trends in the electrocatalytic activity of metals and enzymes for CO reduction to CO. *J. Phys. Chem. Lett.* 4, 388–392. doi:10.1021/jz3021155

Hay, P. J., and Wadt, W. R. (1985a). Ab initio effective core potentials for molecular calculations. potentials for K to Au including the outermost core orbitals. *J. Chem. Phys.* 82, 299–310. doi:10.1063/1.448975

Hay, P. J., and Wadt, W. R. (1985b). Ab initio effective core potentials for molecular calculations. potentials for the transition metal atoms Sc to Hg. *J. Chem. Phys.* 82, 270–283. doi:10.1063/1.448799

He, Z., He, K., Robertson, A. W., Kirkland, A. I., Kim, D., Ihm, J., et al. (2014). Atomic structure and dynamics of metal dopant pairs in graphene. *Nano Lett.* 14, 3766–3772. doi:10.1021/nl500682j

Heenen, H. H., Gauthier, J. A., Kristoffersen, H. H., Ludwig, T., and Chan, K. (2020). Solvation at metal/water interfaces: an ab initio molecular dynamics benchmark of common computational approaches. *J. Chem. Phys.* 152, 144703. doi:10.1063/1.5144912

Herrick, D. R. (2005). Connecting pauling and mulliken electronegativities. *J. Chem. Theor. Comput.* 1, 255–260. doi:10.1021/ct049942a

Hohenberg, P., and Kohn, W. (1964). Inhomogeneous electron gas. *Phys. Rev.* 136, B864. doi:10.1103/PhysRev.136.B864

Hori, Y. i. (2008). "Electrochemical CO reduction on metal electrodes," in *Modern aspects of electrochemistry* (New York, NY: Springer), 89–189.

Hori, Y., Kikuchi, K., Murata, A., and Suzuki, S. (1986). Production of methane and ethylene in electrochemical reduction of carbon dioxide at copper electrode in aqueous hydrogencarbonate solution. *Chem. Lett.* 15, 897–898. doi:10.1246/cl.1986.897

Hori, Y., Murata, A., and Takahashi, R. (1989). Formation of hydrocarbons in the electrochemical reduction of carbon dioxide at a copper electrode in aqueous solution. *J. Chem. Soc. Faraday Trans.* 1 85, 2309–2326. doi:10.1039/F19898502309

Hörmann, N. G., Marzari, N., and Reuter, K. (2020). Electrosorption at metal surfaces from first principles. *Npj Comput. Mater.* 6, 136. doi:10.1038/s41524-020-00394-4

Jia, C., Dastafkan, K., Ren, W., Yang, W., and Zhao, C. (2019). Carbon-based catalysts for electrochemical CO reduction. *Sust. Energy Fuels* 3, 2890–2906. doi:10.1039/C9SE00527G

Jia, M., Fan, Q., Liu, S., Qiu, J., and Sun, Z. (2019). Single-atom catalysis for electrochemical CO reduction. *Curr. Opin. Green Sustain. Chem.* 16, 1–6. doi:10.1016/j.cogsc.2018.11.002

Jones, J.-P., Prakash, G. S., and Olah, G. A. (2014). Electrochemical CO reduction: recent advances and current trends. *Isr. J. Chem.* 54, 1451–1466. doi:10.1002/ijch.201400081

Ju, W., Bagger, A., Hao, G.-P., Varela, A. S., Sinev, I., Bon, V., et al. (2017). Understanding activity and selectivity of metal-nitrogen-doped carbon catalysts for electrochemical reduction of CO. *Nat. Commun.* 8, 1–9. doi:10.1038/s41467-017-01035-z

Kattel, S., Atanassov, P., and Kiefer, B. (2012). Stability, electronic and magnetic properties of in-plane defects in graphene: a first-principles study. *J. Phys. Chem. C.* 116, 8161–8166. doi:10.1021/jp2121609

Kibria, M. G., Edwards, J. P., Gabardo, C. M., Dinh, C.-T., Seifitokaldani, A., Sinton, D., et al. (2019). Electrochemical CO reduction into chemical feedstocks: from mechanistic electrocatalysis models to system design. *Adv. Mater.* 31, 1807166. doi:10.1002/adma.201807166

Kim, D., Resasco, J., Yu, Y., Asiri, A. M., and Yang, P. (2014). Synergistic geometric and electronic effects for electrochemical reduction of carbon dioxide using gold–copper bimetallic nanoparticles. *Nat. Commun.* 5, 1–8. doi:10.1038/ncomms5948

Kim, J., Summers, D., and Frese, K., Jr (1988). Reduction of CO and CO to methane on Cu foil electrodes. *J. Electroanal. Chem. Interfacial Electrochem.* 245, 223–244. doi:10.1016/0022-0728(88)80071-8

Kittel, C. (2004). *Introduction to solid state physics*. New York, NY: Wiley.

Kohn, W., and Sham, L. J. (1965). Self-consistent equations including exchange and correlation effects. *Phys. Rev.* 140, A1133. doi:10.1103/PhysRev.140.A1133

Koper, M. T. M. (2013a). Theory of multiple proton-electron transfer reactions and its implications for electrocatalysis. *Chem. Sci.* 4, 2710–2723. doi:10.1039/C3SC50205H

Koper, M. T. M. (2013b). Theory of the transition from sequential to concerted electrochemical proton–electron transfer. *Phys. Chem. Chem. Phys.* 15, 1399–1407. doi:10.1039/C2CP42369C

Koshy, D. M., Chen, S., Lee, D. U., Stevens, M. B., Abdellah, A. M., Dull, S. M., et al. (2020). Understanding the origin of highly selective CO electroreduction to CO on Ni, N-doped carbon catalysts. *Angew. Chem. Int. Ed.* 132, 4072–4079. doi:10.1002/anie.201912857

Krasheninnikov, A., Lehtinen, P., Foster, A. S., Pyykkö, P., and Nieminen, R. M. (2009). Embedding transition-metal atoms in graphene: structure, bonding, and magnetism. *Phys. Rev. Lett.* 102, 126807. doi:10.1103/physrevlett.102.126807

Kuhl, K. P., Hatsukade, T., Cave, E. R., Abram, D. N., Kibsgaard, J., and Jaramillo, T. F. (2014). Electrocatalytic conversion of carbon dioxide to methane and methanol on transition metal surfaces. *J. Am. Chem. Soc.* 136, 14107–14113. doi:10.1021/ja505791r

Lazar, P., Karlický, F., Jurečka, P., Kocman, M., Otyepková, E., Šafářová, K., et al. (2013). Adsorption of small organic molecules on graphene. *J. Am. Chem. Soc.* 135, 6372–6377. doi:10.1021/ja403162r

Lee, M.-Y., Ringe, S., Kim, H., Kang, S., and Kwon, Y. (2020). Electric field mediated selectivity switching of electrochemical CO reduction from formate to CO on carbon supported Sn. *ACS Energy Lett.* 5, 2987–2994. doi:10.1021/acsenergylett.0c01387

Li, J., Pršlja, P., Shinagawa, T., Martín Fernández, A. J., Krumeich, F., Artyushkova, K., et al. (2019). Volcano trend in electrocatalytic CO reduction activity over atomically dispersed metal sites on nitrogen-doped carbon. *ACS Catal.* 9, 10426–10439. doi:10.1021/acscatal.9b02594

Li, X., Bi, W., Chen, M., Sun, Y., Ju, H., Yan, W., et al. (2017). Exclusive Ni–N sites realize near-unity CO selectivity for electrochemical CO reduction. *J. Am. Chem. Soc.* 139, 14889–14892. doi:10.1021/jacs.7b09074

Li, Y., Su, H., Chan, S. H., and Sun, Q. (2015). CO electroreduction performance of transition metal dimers supported on graphene: a theoretical study. *ACS Catal.* 5, 6658–6664. doi:10.1021/acscatal.5b01165

Lim, H.-K., Shin, H., Goddard, W. A., Hwang, Y. J., Min, B. K., and Kim, H. (2014). Embedding covalency into metal catalysts for efficient electrochemical conversion of CO. *J. Am. Chem. Soc.* 136, 11355–11361. doi:10.1021/ja503782w

Lindgren, P., Kastlunger, G., and Peterson, A. A. (2020). A challenge to the G 0 interpretation of hydrogen evolution. *ACS Catal.* 10, 121–128. doi:10.1021/acscatal.9b02799

Lu, Q., and Jiao, F. (2016). Electrochemical CO reduction: electrocatalyst, reaction mechanism, and process engineering. *Nano. Energy* 29, 439–456. doi:10.1016/j.nanoen.2016.04.009

Lu, Q., Rosen, J., Zhou, Y., Hutchings, G. S., Kimmel, Y. C., Chen, J. G., et al. (2014). A selective and efficient electrocatalyst for carbon dioxide reduction. *Nat. Commun.* 5, 1–6. doi:10.1038/ncomms4242

Lu, X., Zhu, C., Wu, Z., Xuan, J., Francisco, J. S., and Wang, H. (2020). *In situ* observation of the pH gradient near the gas diffusion electrode of CO reduction in alkaline electrolyte. *J. Am. Chem. Soc.* 142, 15438–15444. doi:10.1021/jacs.0c06779

MacDowell, N., Florin, N., Buchard, A., Hallett, J., Galindo, A., Jackson, G., et al. (2010). An overview of CO capture technologies. *Energy Environ. Sci.* 3, 1645–1669. doi:10.1039/C004106H

Malkhandi, S., and Yeo, B. S. (2019). Electrochemical conversion of carbon dioxide to high value chemicals using gas-diffusion electrodes. *Curr. Opin. Chem. Eng.* 26, 112–121. doi:10.1016/j.coche.2019.09.008

Marenich, A. V., Ho, J., Coote, M. L., Cramer, C. J., and Truhlar, D. G. (2014). Computational electrochemistry: prediction of liquid-phase reduction potentials. *Phys. Chem. Chem. Phys.* 16, 15068–15106. doi:10.1039/C4CP01572J

Melander, M. M. (2020). Grand canonical rate theory for electrochemical and electrocatalytic systems I: general formulation and proton-coupled electron transfer reactions. *J. Electrochem. Soc.* 167, 116518. doi:10.1149/1945-7111/aba54b

Melander, M. M., Kuisma, M. J., Christensen, T. E. K., and Honkala, K. (2019). Grand-canonical approach to density functional theory of electrocatalytic systems: thermodynamics of solid-liquid interfaces at constant ion and electrode potentials. *J. Chem. Phys.* 150, 041706. doi:10.1063/1.5047829

Mermin, N. D. (1965). Thermal properties of the inhomogeneous electron gas. *Phys. Rev.* 137, A1441–A1443. doi:10.1103/PhysRev.137.A1441

Mistry, H., Reske, R., Zeng, Z., Zhao, Z.-J., Greeley, J., Strasser, P., et al. (2014). Exceptional size-dependent activity enhancement in the electroreduction of CO over Au nanoparticles. *J. Am. Chem. Soc.* 136, 16473–16476. doi:10.1021/ja309317u

Mulliken, R. S. (1934). A new electroaffinity scale; Together with data on valence states and on valence ionization potentials and electron affinities. *J. Chem. Phys.* 2, 782–793. doi:10.1063/1.1749394

Mulliken, R. S. (1955). Electronic population analysis on LCAO-MO molecular wave functions. *I. J. Chem. Phys.* 23, 1833–1840. doi:10.1063/1.1740588

NIST database (2020). Nist webbook. Available at: https://webbook.nist.gov/cgi/cbook.cgi?ID=C124389.

Nitopi, S., Bertheussen, E., Scott, S. B., Liu, X., Engstfeld, A. K., Horch, S., et al. (2019). Progress and perspectives of electrochemical CO reduction on copper in aqueous electrolyte. *Chem. Rev.* 119, 7610–7672. doi:10.1021/acs.chemrev.8b00705

Nørskov, J. K., Rossmeisl, J., Logadottir, A., Lindqvist, L., Kitchin, J. R., Bligaard, T., et al. (2004). Origin of the overpotential for oxygen reduction at a fuel-cell cathode. *J. Phys. Chem. B.* 108, 17886–17892. doi:10.1021/jp047349j

Nykänen, L., and Honkala, K. (2011). Density functional theory study on propane and propene adsorption on Pt(111) and PtSn alloy surfaces. *J. Phys. Chem. C.* 115, 9578–9586. doi:10.1021/jp1121799

Pan, F., Li, B., Sarnello, E., Fei, Y., Feng, X., Gang, Y., et al. (2020). Pore-edge tailoring of single atomic iron-nitrogen sites on graphene for enhanced CO reduction. *ACS Catal.* 10, 10803–10811. doi:10.1021/acscatal.0c02499

Pan, F., Zhang, H., Liu, K., Cullen, D., More, K., Wang, M., et al. (2018). Unveiling active sites of CO reduction on nitrogen-coordinated and atomically dispersed iron and cobalt catalysts. *ACS Catal.* 8, 3116–3122. doi:10.1021/acscatal.8b00398

Perdew, J. P., Ziesche, P., and Eschrig, H. (1991). *Electronic structure of solids'91*. Berlin: Akademie Verlag.

Pérez-Gallent, E., Marcandalli, G., Figueiredo, M. C., Calle-Vallejo, F., and Koper, M. T. (2017). Structure-and potential-dependent cation effects on CO reduction at copper single-crystal electrodes. *J. Am. Chem. Soc.* 139, 16412–16419. doi:10.1021/jacs.7b10142

Peterson, A. A., Abild-Pedersen, F., Studt, F., Rossmeisl, J., and Nørskov, J. K. (2010). How copper catalyzes the electroreduction of carbon dioxide into hydrocarbon fuels. *Energy Environ. Sci.* 3, 1311–1315. doi:10.1039/C0EE00071J

Peterson, A. A., and Nørskov, J. K. (2012). Activity descriptors for CO electroreduction to methane on transition-metal catalysts. *J. Phys. Chem. Lett.* 3, 251–258. doi:10.1021/jz201461p

Petersson, a., Bennett, A., Tensfeldt, T. G., Al-Laham, M. A., Shirley, W. A., and Mantzaris, J. (1988). A complete basis set model chemistry. I. the total energies of closed-shell atoms and hydrides of the first-row elements. *J. Chem. Phys.* 89, 2193–2218. doi:10.1063/1.455064

Petersson, G., and Al-Laham, M. A. (1991). A complete basis set model chemistry. II. open-shell systems and the total energies of the first-row atoms. *J. Chem. Phys.* 94, 6081–6090. doi:10.1063/1.460447

Qu, L., Liu, Y., Baek, J.-B., and Dai, L. (2010). Nitrogen-doped graphene as efficient metal-free electrocatalyst for oxygen reduction in fuel cells. *ACS Nano.* 4, 1321–1326. doi:10.1021/nn901850u. PMID: 20155972

Rad, A. S., and Foukolaei, V. P. (2015). Density functional study of Al-doped graphene nanostructure towards adsorption of CO, CO and HO. *Synth. Met.* 210, 171–178. doi:10.1016/j.synthmet.2015.09.026

Rebarchik, M., Bhandari, S., Kropp, T., and Mavrikakis, M. (2020). How noninnocent spectator species improve the oxygen reduction activity of single-atom catalysts: microkinetic models from first-principles calculations. *ACS Catal.* 10, 9129–9135. doi:10.1021/acscatal.0c01642

Ringe, S., Clark, E. L., Resasco, J., Walton, A., Seger, B., Bell, A. T., et al. (2019). Understanding cation effects in electrochemical CO reduction. *Energy Environ. Sci.* 12, 3001–3014. doi:10.1039/C9EE01341E

Scalmani, G., and Frisch, M. J. (2010). Continuous surface charge polarizable continuum models of solvation. i. general formalism. *J. Chem. Phys.* 132, 114110. doi:10.1063/1.3359469

Schmickler, W., and Guidelli, R. (2014). The partial charge transfer. *Electrochim. Acta.* 127, 489–505. doi:10.1016/j.electacta.2014.02.057

Schneider, J., Jia, H., Muckerman, J. T., and Fujita, E. (2012). Thermodynamics and kinetics of CO, CO, and H binding to the metal centre of CO reduction catalysts. *Chem. Soc. Rev.* 41, 2036–2051. doi:10.1039/C1CS15278E

Shang, R., Steinmann, S. N., Xu, B.-Q., and Sautet, P. (2020). Mononuclear Fe in N-doped carbon: computational elucidation of active sites for electrochemical oxygen reduction and oxygen evolution reactions. *Cat. Sci. Tech.* 10, 1006–1014. doi:10.1039/C9CY01935A

Shao, Y., Dodelet, J.-P., Wu, G., and Zelenay, P. (2019). PGM-free cathode catalysts for PEM fuel cells: a mini-review on stability challenges. *Adv. Mater.* 31, 1807615. doi:10.1002/adma.201807615

Shi, C., Hansen, H. A., Lausche, A. C., and Nørskov, J. K. (2014). Trends in electrochemical CO reduction activity for open and close-packed metal surfaces. *Phys. Chem. Chem. Phys.* 16, 4720–4727. doi:10.1039/C3CP54822H

Siahrostami, S., Jiang, K., Karamad, M., Chan, K., Wang, H., and Nørskov, J. (2017). Theoretical investigations into defected graphene for electrochemical reduction of CO. *ACS Sustain. Chem. Eng.* 5, 11080–11085. doi:10.1021/acssuschemeng.7b03031

Sun, Z., Ma, T., Tao, H., Fan, Q., and Han, B. (2017). Fundamentals and challenges of electrochemical CO reduction using two-dimensional materials. *Inside Chem.* 3, 560–587. doi:10.1016/j.chempr.2017.09.009

Tachikawa, H., and Kawabata, H. (2011). Ground and low-lying excited electronic states of graphene flakes: a density functional theory study. *J. Phys. B Atom. Mol. Opt. Phys.* 44, 205105. doi:10.1088/0953-4075/44/20/205105

Tian, Z., Priest, C., and Chen, L. (2018). Recent progress in the theoretical investigation of electrocatalytic reduction of CO. *Adv. Theory Simul.* 1, 1800004. doi:10.1002/adts.201800004

Trevethan, T., Latham, C. D., Heggie, M. I., Briddon, P. R., and Rayson, M. J. (2014). Vacancy diffusion and coalescence in graphene directed by defect strain fields. *Nanoscale* 6, 2978–2986. doi:10.1039/c3nr06222h

Tripkovic, V., Vanin, M., Karamad, M., Björketun, M. E., Jacobsen, K. W., Thygesen, K. S., et al. (2013). Electrochemical CO and CO reduction on metal-functionalized porphyrin-like graphene. *J. Phys. Chem. C.* 117, 9187–9195. doi:10.1021/jp306172k

Valter, M., Busch, M., Wickman, B., Grönbeck, H., Baltrusaitis, J., and Hellman, A. (2018). Electrooxidation of glycerol on gold in acidic medium: a combined experimental and DFT study. *J. Phys. Chem. C.* 122, 10489–10494. doi:10.1021/acs.jpcc.8b02685

Varela, A. S., Ju, W., and Strasser, P. (2018). Molecular nitrogen-carbon catalysts, solid metal organic framework catalysts, and solid metal/nitrogen-doped carbon (MNC) catalysts for the electrochemical CO reduction. *Adv. Energy Mater.* 8, 1703614. doi:10.1002/aenm.201703614

Varela, A. S., Ju, W., Bagger, A., Franco, P., Rossmeisl, J., and Strasser, P. (2019). Electrochemical reduction of CO on metal-nitrogen-doped carbon catalysts. *ACS Catal.* 9, 7270–7284. doi:10.1021/acscatal.9b01405

Varela, A. S. (2020). The importance of pH in controlling the selectivity of the electrochemical CO reduction. *Curr. Opin. Green Sustain. Chem.* 26, 100371. doi:10.1016/j.cogsc.2020.100371

Vasileff, A., Zheng, Y., and Qiao, S. Z. (2017). Carbon solving carbon's problems: recent progress of nanostructured carbon-based catalysts for the electrochemical reduction of CO. *Adv. Energy Mater.* 7, 1700759. doi:10.1002/aenm.201700759

Verma, A. M., Agrawal, K., and Kishore, N. (2018). Binding of phenolic model compounds with noble metal doped graphene sheets. *Comp. Theo. Chem.* 1134, 37–46. doi:10.1016/j.comptc.2018.05.001

Verma, A. M., and Kishore, N. (2019). First-principles study on the gas-phase decomposition of bio-oil oxygenated compounds over the palladium catalyst surface. *Phys. Chem. Chem. Phys.* 21, 22320–22330. doi:10.1039/C9CP04858H

Verma, A. M., and Kishore, N. (2018). Molecular modeling approach to elucidate gas phase hydrodeoxygenation of guaiacol over a Pd (111) catalyst within DFT framework. *J. Mol. Model* 24, 254. doi:10.1007/s00894-018-3803-8

Verma, A. M., and Kishore, N. (2017). Molecular simulations of palladium catalysed hydrodeoxygenation of 2-hydroxybenzaldehyde using density functional theory. *Phys. Chem. Chem. Phys.* 19, 25582–25597. doi:10.1039/C7CP05113A

Vijay, S., Gauthier, J. A., Heenen, H. H., Bukas, V. J., Kristoffersen, H. H., and Chan, K. (2020). Dipole-field interactions determine the CO reduction activity of 2D Fe-N-C single-atom catalysts. *ACS Catal.* 10, 7826–7835. doi:10.1021/acscatal.0c01375

Wadt, W. R., and Hay, P. J. (1985). Ab initio effective core potentials for molecular calculations. potentials for main group elements Na to Bi. *J. Chem. Phys.* 82, 284–298. doi:10.1063/1.448800

Wang, H., Wang, Q., Cheng, Y., Li, K., Yao, Y., Zhang, Q., et al. (2012). Doping monolayer graphene with single atom substitutions. *Nano Lett.* 12, 141–144. doi:10.1021/nl2031629

Wang, H., Feng, Q., Cheng, Y., Yao, Y., Wang, Q., Li, K., et al. (2013). Atomic bonding between metal and graphene. *J. Phys. Chem. C.* 117, 4632–4638. doi:10.1021/jp311658m

Wang, W.-H., Himeda, Y., Muckerman, J. T., Manbeck, G. F., and Fujita, E. (2015). CO hydrogenation to formate and methanol as an alternative to photo-and electrochemical CO reduction. *Chem. Rev.* 115, 12936–12973. doi:10.1021/acs.chemrev.5b00197

Wang, X., Zhao, Q., Yang, B., Li, Z., Bo, Z., Lam, K. H., et al. (2019). Emerging nanostructured carbon-based non-precious metal electrocatalysts for selective electrochemical CO reduction to CO. *J. Math. Chem. A.* 7, 25191–25202. doi:10.1039/C9TA09681G

Warner, J. H., Margine, E. R., Mukai, M., Robertson, A. W., Giustino, F., and Kirkland, A. I. (2012). Dislocation-driven deformations in graphene. *Science* 337, 209–212. doi:10.1126/science.1217529

Wu, J., Sharifi, T., Gao, Y., Zhang, T., and Ajayan, P. M. (2019). Emerging carbon-based heterogeneous catalysts for electrochemical reduction of carbon dioxide into value-added chemicals. *Adv. Mater.* 31, 1804257. doi:10.1002/adma.201804257

Yin, Z., Peng, H., Wei, X., Zhou, H., Gong, J., Huai, M., et al. (2019). An alkaline polymer electrolyte CO electrolyzer operated with pure water. *Energy Environ. Sci.* 12, 2455–2462. doi:10.1039/C9EE01204D

Yu, F., Wei, P., Yang, Y., Chen, Y., Guo, L., and Peng, Z. (2019). Material design at nano and atomic scale for electrocatalytic CO reduction. *Nano Mater. Sci.* 1, 60–69. doi:10.1016/j.nanoms.2019.03.006

Zhang, B., Zhang, J., Shi, J., Tan, D., Liu, L., Zhang, F., et al. (2019). Manganese acting as a high-performance heterogeneous electrocatalyst in carbon dioxide reduction. *Nat. Commun.* 10, 1–8. doi:10.1038/s41467-019-10854-1

Zhang, C., Yang, S., Wu, J., Liu, M., Yazdi, S., Ren, M., et al. (2018). Electrochemical CO reduction with atomic iron-dispersed on nitrogen-doped graphene. *Adv. Energy Mater.* 8, 1703487. doi:10.1002/aenm.201703487

Zhao, T., Tian, Y., Wang, Y., Yan, L., and Su, Z. (2019). Mechanistic insight into electroreduction of carbon dioxide on FeN_x (x= 0–4) embedded graphene. *Phys. Chem. Chem. Phys.* 21, 23638–23644. doi:10.1039/C9CP03370J

Zhu, W., Zhang, Y.-J., Zhang, H., Lv, H., Li, Q., Michalsky, R., et al. (2014). Active and selective conversion of CO to CO on ultrathin Au nanowires. *J. Am. Chem. Soc.* 136, 16132–16135. doi:10.1021/ja5095099

Conflict of Interest: The authors declare that the research was conducted in the absence of any commercial or financial relationships that could be construed as a potential conflict of interest.

frontiers in Energy Research

ORIGINAL RESEARCH
published: 11 February 2021
doi: 10.3389/fenrg.2021.606313

First-Principles Design of Rutile Oxide Heterostructures for Oxygen Evolution Reactions

Hyeong Yong Lim, Sung O Park, Su Hwan Kim, Gwan Yeong Jung and Sang Kyu Kwak**

School of Energy and Chemical Engineering, Ulsan National Institute of Science and Technology (UNIST), Ulsan, South Korea

The oxygen evolution reaction (OER) plays a key role in the determination of overall water-splitting rate. Lowering the high overpotential of the OER of transition metal oxides (TMOs), which are used as conventional OER electrocatalysts, has been the focus of many studies. The OER activity of TMOs can be tuned via the strategic formation of a heterostructure with another TMO substrate. We screened 11 rutile-type TMOs (i.e., MO_2; M = V, Cr, Mn, Nb, Ru, Rh, Sn, Ta, Os, Ir, and Pt) on a rutile (110) substrate using density functional theory calculations to determine their OER activities. The conventional volcano approach based on simple binding energies of reaction intermediates was implemented; in addition, the electrochemical-step symmetry index was employed to screen heterostructures for use as electrode materials. The results show that RuO_2 and IrO_2 are the most promising catalysts among all candidates. The scaling results provide insights into the intrinsic properties of the heterostructure as well as materials that can be used to lower the overpotential of the OER.

Keywords: density functional theory, oxygen evolution reaction, rutile-type oxide, heterostructure, scaling relation

OPEN ACCESS

Edited by:
Kai S. Exner,
Sofia University, Bulgaria

Reviewed by:
Marko Melander,
University of Jyväskylä, Finland
Herbert Over,
University of Giessen, Germany

****Correspondence:***
Gwan Yeong Jung
gyjung@unist.ac.kr
Sang Kyu Kwak
skkwak@unist.ac.kr

Specialty section:
This article was submitted to Electrochemical Energy Conversion and Storage, a section of the journal Frontiers in Energy Research

Received: *14 September 2020*
Accepted: *05 January 2021*
Published: *11 February 2021*

Citation:
Lim HY, Park SO, Kim SH, Jung GY and Kwak SK (2021) First-Principles Design of Rutile Oxide Heterostructures for Oxygen Evolution Reactions. Front. Energy Res. 9:606313. doi: 10.3389/fenrg.2021.606313

INTRODUCTION

Green hydrogen production remains a challenge that must be overcome to achieve a hydrogen economy (Turner, 2004). Water electrolysis is one of the approaches toward hydrogen eco-friendliness. It is based on the hydrogen evolution reaction (HER) and oxygen evolution reaction (OER) as cathodic and anodic reactions, respectively. However, the slow kinetics of the OER limit the commercialization of this approach. Oxide systems based on Ir or Ru (i.e., IrO_x or RuO_x) are known to have the best OER performances (Lee et al., 2012; Frydendal et al., 2014; Suen et al., 2017). However, these materials are expensive. Therefore, many studies have been conducted to identify a cost-effective alternative oxide material with high activity. For example, transition-metal substitution (García-Mota et al., 2011) and the introduction of oxygen vacancies (Xiao et al., 2020) have been studied as means to control the compositions of expensive materials. However, transition-metal substitution and oxygen vacancies only locally affect the active sites.

To activate the metal oxide, support materials are mixed with the oxide to enhance the electrical conductivity and activity of the electrocatalytic reaction (Kumar et al., 2016; Qingxiang et al., 2018; Bu et al., 2019; Lu et al., 2019). In addition, research on heterostructures is conducted with the goal of activating the material on the substrate. Modifications are mainly based on the strain effect and charge transfer due to the formation of an interface between the support material and catalyst. For instance, the heterostructure of $La_{0.5}Sr_{0.5}CoO_{3-\delta}$ and $MoSe_2$ induces the phase transition of $MoSe_2$ from the 2H to the 1T phase (Oh et al., 2019). In addition, the charge transfer from the Co ion to Mo ion improves the electrochemical activity. The results of another study showed that the heterostructure of IrO_x and $SrIrO_3$ outperforms iridium or ruthenium oxide systems (Seitz et al.,

2016). Based on density functional theory (DFT) calculations, IrO_3 or anatase IrO_2 motifs are formed during strontium leaching in the outermost surface layers of $SrIrO_3$ and contribute to the high activity. Another strength of the heterostructure is that it can possibly contribute to reducing the use of precious metals by replacing them into low-cost metals while maintaining similar intrinsic activity of each active site (Esposito et al., 2010; Zhou et al., 2014; Wang et al., 2015; Jin et al., 2016). Rutile (TiO_2) is a well-known substrate material for metal oxide systems because of its high structural stability and simple structure (Hanaor et al., 2012). It is suitable for the growth of oxide films, facilitating the fabrication of heterostructures with various metal oxides. In addition, rutile affects the catalytic activity of metal oxides and has a high cost effectiveness (Seitsonen and Over, 2010; Stacchiola et al., 2013; Wei et al., 2015; Sun et al., 2016; Li et al., 2017). However, the effect of the rutile support on the activity remains unclear due to difficulties with respect to the characterization of the heterostructure during experiments (Stacchiola et al., 2013).

In this study, we performed DFT calculations to theoretically investigate the effect of the TiO_2 substrate on the heterostructure and thus on the OER. We screened the OERs of heterostructures consisting of various rutile-type metal oxides (i.e., VO_2, CrO_2, MnO_2, NbO_2, RuO_2, RhO_2, SnO_2, TaO_2, OsO_2, IrO_2, and PtO_2) and a TiO_2 substrate. The results show that these rutile heterostructures follow the universal scaling relations of metals and oxides; however, the binding strengths of the O* intermediates increase due to the TiO_2 substrate. The volcano plot and electrochemical-step symmetry index (ESSI) show that the RuO_2 and IrO_2 are the closest to an ideal catalyst. The results of our computational screening provide insights into the effects of support materials on electrocatalytic reactions.

METHODS

Spin-polarized DFT calculations were performed with the projector-augmented wave (PAW) method (Blochl, 1994) and Vienna Ab initio Simulation Package (VASP) (Kresse and Furthmiiller, 1996). The electron exchange–correlation energy was treated within the generalized gradient approximation (GGA) and the Perdew–Burke–Ernzerhof functional (Perdew et al., 1997). To determine the trend of the OER activity, the DFT + U method within Liechtenstein's approach (Anisimovdag et al., 1997) was used and the following correction parameters were employed: U = 4.95 eV for Ti, 2 eV for V, 7.15 eV for Cr, 6.63 eV for Mn, 3.32 eV for Nb, 6.73 eV for Ru, 5.97 eV for Rh, 5.91 eV for Ir, and 6.25 eV for Pt (Xu et al., 2015). The energy cutoff for the plane wave basis set was set at 520 eV. The geometry was optimized using the residual minimization method and the direct inversion in the iterative subspace method (RMM–DIIS) algorithm until the net force on each atom was below 0.02 eV·Å^{-1}, and the total energy was 10^{-6} eV per atom. Dipole slab corrections were also applied to all slab model calculations. The *k*-point sampling of the Brillouin zone was done with a 4 × 4 × 1 for bulk calculations and 6 × 6 × 8 for slab calculations.

RESULTS AND DISCUSSION

To theoretically investigate the OER activities of rutile-type heterostructures, we considered the heterostructures of 11 rutile-type oxides (i.e., MO_2, where M = V, Cr, Mn, Nb, Ru, Rh, Sn, Ta, Os, Ir, and Pt) with a TiO_2 substrate. To accurately illustrate the OER activity, the following magnetic structures were used for all calculations according to Xu et al.'s work: nonmagnetic (NM) for TiO_2, NbO_2, RuO_2, RhO_2, IrO_2, and PtO_2, and ferromagnetic (FM) for CrO_2 and MnO_2 (Xu et al., 2015). Furthermore, the ground state magnetic configurations of the other candidate models were identified as FM for VO_2 and NM for SnO_2, TaO_2, and OsO_2, respectively (**Supplementary Figure S1**). Surface models, that is, six-layer stoichiometric slabs, were built by using the 2 × 1 supercell of the optimized unit cell. The vacuum of ~15 Å was applied in the (110) direction, which is the most stable facet of rutile-type oxides (**Figure 1A**; Kung, 1989). Note that a tri-layer consisting of oxygen–metal–oxygen (O–M–O) atomic layers was considered to be a single layer in our slab models. The top four layers of the slab models were allowed to fully relax. The two layers at the bottom were fixed to represent the bulk state. For heterostructures, the top three layers of the TiO_2 slab model were replaced with MO_2 layers while maintaining the cell dimensions of the TiO_2 substrate. The coordinatively unsaturated sites (CUS) of the metal atoms at the top surface were considered to be the adsorption sites for each intermediate (i.e., OH*, O*, and OOH*) for the OER. To examine the oxygen coverage effect on the OER activity, the pristine and fully O* covered surfaces were representatively compared (i.e., denoted as $2O_b$ and $2O_b$ $2O_c$, where the subscripts "b" and "c" represent the bridge sites and CUS, respectively).

The overall OER process consists of four elementary steps involving proton-coupled electron transfer (PCET; **Figure 1B**) (Hammes-Schiffer, 2015; Costentin and Savéant, 2017). In this study, we followed the conventional four-electron pathways with respect to the OER of rutile heterostructures, which can be described as follows:

$$H_2O_{(l)} + M \rightarrow MOH^* + (H^+ + e^-) \quad (1)$$

$$MOH^* \rightarrow MO^* + (H^+ + e^-) \quad (2)$$

$$MO^* + H_2O_{(l)} \rightarrow MOOH^* + (H^+ + e^-) \quad (3)$$

$$MOOH^* \rightarrow M + O_{2(g)} + (H^+ + e^-). \quad (4)$$

The adsorption free energy was calculated using the following equation:

$$\Delta G = \Delta E + \Delta ZPE - T\Delta S - eU + k_B T \ln a_{H^+}, \quad (5)$$

where ΔE is the binding energy of each reaction intermediate; ΔZPE is the zero-point vibrational enthalpy; $-T\Delta S$ is the entropic correction at room temperature, $-eU$ is the energy shift by the electrode potential, where U is the electrode applied potential relative to the standard hydrogen electrode (SHE) and e is the elementary charge transferred; and $k_B T \ln a_{H^+}$ is used as correction for the free energy of H^+ ions, where a_{H^+} is the activity of the proton. In this study, we considered the standard conditions for Gibbs free energy calculations

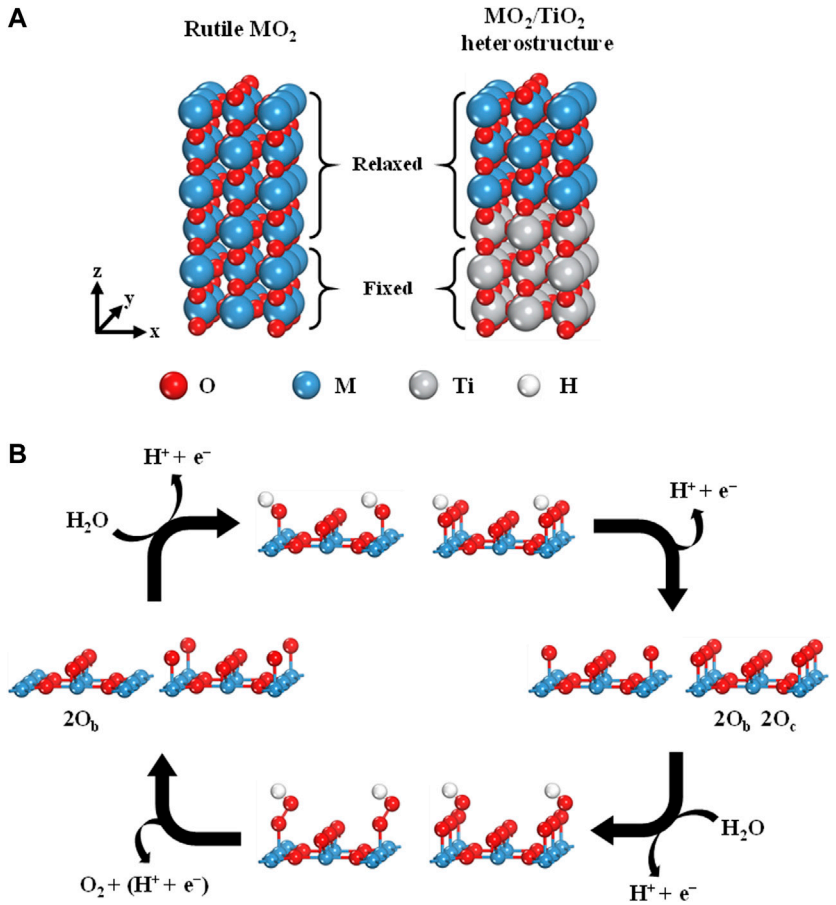

FIGURE 1 | (A) Six-layered (110) surface of rutile-type MO_2 **(left)** and MO_2/TiO_2 heterostructure **(right)**. **(B)** OER scheme of four elementary reaction steps on the rutile-type (110) surface with $2O_b$ and $2O_b$ $2O_c$.

(i.e., T = 298 K and pH = 0). Free energy correction values were taken from Valdes et al.'s work (Valdes et al., 2008). The binding energy for each reaction intermediate (i.e., ΔE_{OH^*}, ΔE_{O^*}, and ΔE_{OOH^*}) was calculated as follows:

$$\Delta E_{OH^*} = E(OH^*) - E(*) - [E(H_2O) - 0.5E(H_2)] \quad (6)$$

$$\Delta E_{O^*} = E(O^*) - E(*) - [E(H_2O) - E(H_2)] \quad (7)$$

$$\Delta E_{OOH^*} = E(OOH^*) - E(*) - [2E(H_2O) - 1.5E(H_2)], \quad (8)$$

where $E(OH^*)$, $E(O^*)$, and $E(OOH^*)$ represent the total energies of the slab models for each adsorbate, $E(*)$ is the total energy of the bare slab, and $E(H_2O)$ and $E(H_2)$ represent the total energies of an isolated water molecule and hydrogen gas, respectively. The differences in the Gibbs free energy (ΔG) of each step were calculated as follows:

$$\Delta G_1 = \Delta G_{OH^*} \quad (9)$$

$$\Delta G_2 = \Delta G_{O^*} - \Delta G_{OH^*} \quad (10)$$

$$\Delta G_3 = \Delta G_{OOH^*} - \Delta G_{O^*} \quad (11)$$

$$\Delta G_4 = 4.92 - \Delta G_{OOH^*} \quad (12)$$

.

Finally, the theoretical overpotential of the OER (η_{OER}) can be calculated as follows:

$$\eta_{OER} = \max([\Delta G_1, \Delta G_2, \Delta G_3, \Delta G_4]/e) - U_{eq}, \quad (13)$$

where U_{eq} indicates the equilibrium potential of the OER (i.e., 1.23 V vs. reversible hydrogen electrode). **Eqs 1–13** assume that thermodynamics of the reaction steps is a valid descriptor for reaction kinetics based on the Brønsted–Evans–Polanyi (BEP) relations (Vojvodic et al., 2011), which refer to that a free-energy change in the transition states (kinetics) follows a change in the reaction heat (thermodynamics). Note that the connection between thermodynamics and kinetics is not always established (Kuo et al., 2017; Kuo et al., 2018), which requires further kinetic experiments or microkinetic modeling based on the activation barrier calculations for all plausible transition states.

We examined the scaling relations between the adsorption free energies of the reaction intermediates (i.e., OH*, O*, and OOH*; **Supplementary Table S2**) for all rutile-type catalysts of interest (**Figure 2A**). The binding energies of OOH* and OH* are linearly correlated, with an offset of 3.20 eV. Note that our scaling trend is

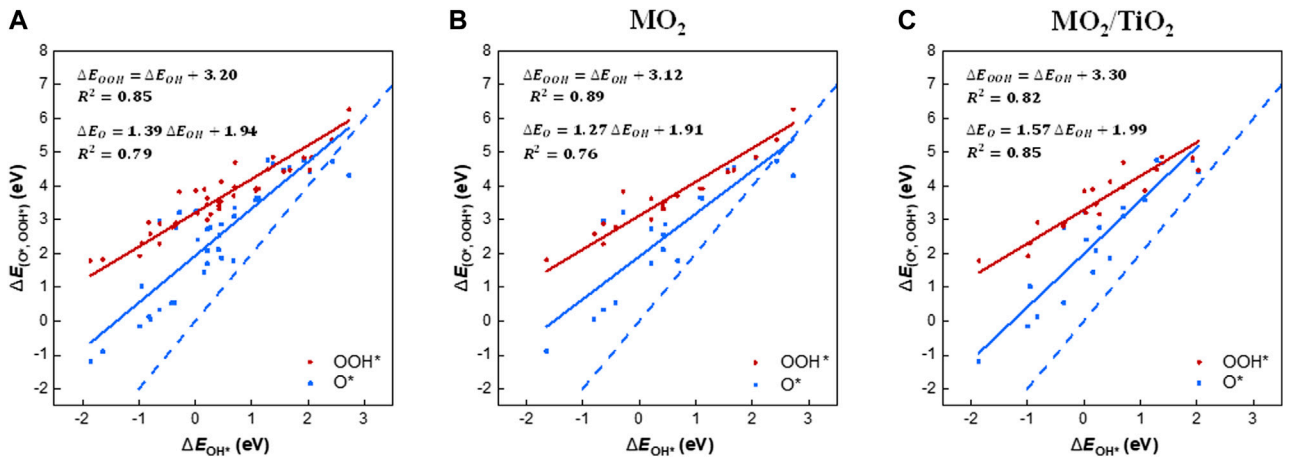

FIGURE 2 | Scaling relations of the binding energies of the OER intermediates (i.e., OH*, O*, and OOH*) with the binding energy of OH*, which is the first intermediate for the OER. The diagrams contain the binding energies on the (110) surface of **(A)** all rutile-type oxides in this study, **(B)** MO_2, and **(C)** MO_2/TiO_2 heterostructures, respectively. The solid lines are the linear trends of the binding energies of OOH* (red) and O* (blue) with respect to the binding energy of OH*. The blue dashed line in all diagrams is the guideline of the O* intermediate, which indicates the double bonding nature on the surface, with a slope of 2.

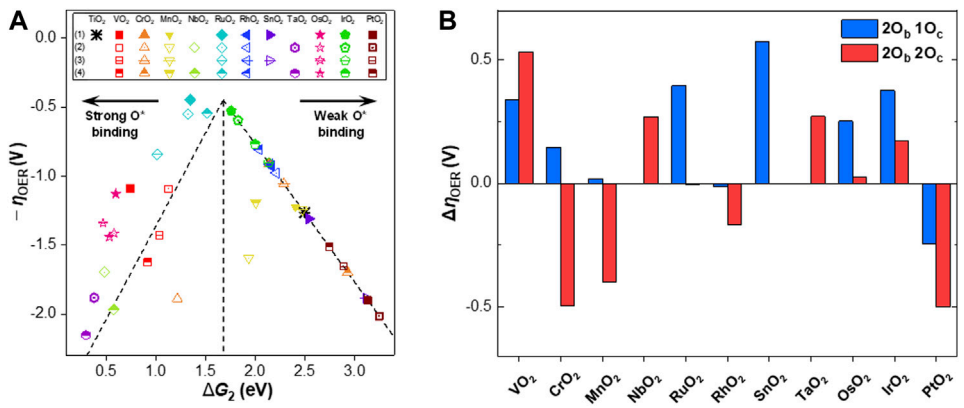

FIGURE 3 | (A) Volcano plot for the negative overpotential of the OER ($-\eta_{OER}$) as a function of ΔG_2. The numbers in the inset indicate each surface: 1) $2O_b$ of MO_2, 2) $2O_b$ $2O_c$ of MO_2, 3) $2O_b$ of MO_2/TiO_2, and 4) $2O_b$ $2O_c$ of MO_2/TiO_2. (cf. **Supplementary Table S2**). **(B)** Difference between the overpotentials of MO_2 and MO_2/TiO_2 [$\Delta\eta_{OER} = \eta_{OER}(MO_2/TiO_2) - \eta_{OER}(MO_2)$]. A positive value of $\Delta\eta_{OER}$ indicates the decrease in the OER activity and a negative $\Delta\eta_{OER}$ reflects an enhancement.

similar to the "universal" scaling relation reported by Man et al. [i.e., $\Delta E_{OOH^*} = \Delta E_{OH^*} + 3.20$ (±0.20 eV)] (Man et al., 2011), implying that all rutile-type systems, including heterostructures, follow the conventional scaling relations for metals and oxide surfaces. Based on the best fit, 68% of the points are within ±0.35 eV (1σ) and 95% are within ±0.70 eV (2σ). The scaling relationship between ΔE_{O^*} and ΔE_{OH^*} exhibits a slope of 1.39 (blue solid line), that is, it is much less steep than the slope of two (blue dashed line), which is the indicator line of the double bonding nature of O* (Rossmeisl et al., 2007).

To analyze the substrate effect of TiO_2 on the heterostructures, we divided the scaling relations into two groups, that is, (110) surfaces of MO_2 and MO_2/TiO_2 heterostructures (**Figure 2B,C**). Notably, the binding energies of OOH* and O* on the MO_2/TiO_2 (110) surface are more concentrated than those of MO_2. The scaling relation between OOH* and OH* of MO_2/TiO_2 (red solid line) shows an increased intercept by 0.18 compared with the corresponding scaling relation of MO_2, implying slightly weakened interactions between OOH* and the surface. Note that the scaling relations between the binding strengths of O* and OH* species on MO_2 and MO_2/TiO_2 (blue solid lines) apparently differ. The slopes of MO_2/TiO_2 (110) heterostructures are closer to 2 (i.e., double bonding nature of O*) than those of MO_2 (110) surfaces (Rossmeisl et al., 2007). This is due to the intensified binding strengths of O* intermediates in heterostructures compared with MO_2 surfaces (Divanis et al., 2020). This indicates that the TiO_2 substrate generally stabilizes the O* intermediates, which might lead to a decrease in η_{OER} of rutile oxides involving weakly bound O* intermediates.

Based on the scaling relations between the binding energies of the reaction intermediates, a volcano plot was constructed, as

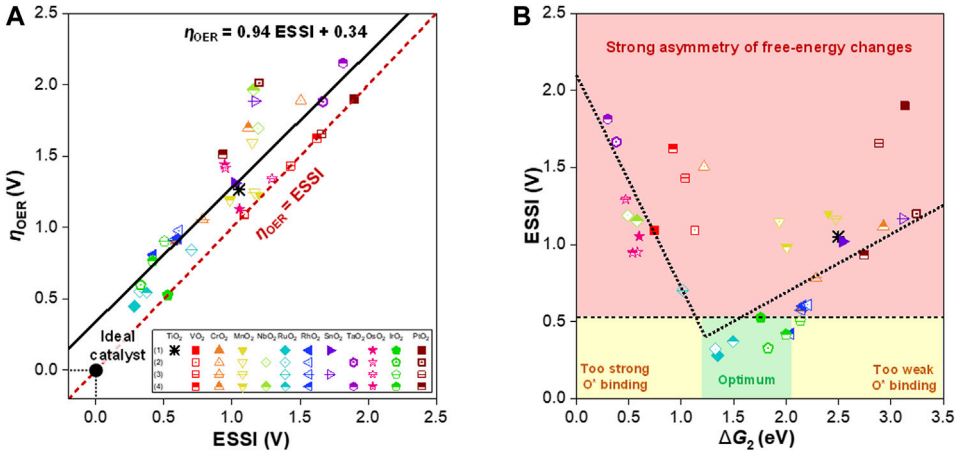

FIGURE 4 | (A) η_{OER} as a function of the ESSI. Black solid line indicates the linear relation between η_{OER} and ESSI. Red dotted line indicates the guideline of η_{OER} = ESSI. **(B)** ESSI-ΔG_2 activity map. Three regions are classified depending on the OER activity—green area of 1.2 eV < ΔG_2 < 2.06 eV with ESSI < 0.53 V; yellow area of ΔG_2 < 1.2 eV or ΔG_2 > 2.06 eV with ESSI < 0. 53 V; and red area of ESSI > 0.53 V.

shown in **Figure 3A**. We chose $\Delta G_{O^*} - \Delta G_{OH^*}$ (denoted as ΔG_2) as a descriptor, which is commonly used to predict the OER activity of the 4 e^- reaction (Man et al., 2011; Krishnamurthy et al., 2018). The plot shows that the O* bonds of PtO_2, OsO_2, TaO_2, and RhO_2 on the TiO_2 substrate are stronger than those without the TiO_2 substrate, and the activities change along the volcano curve. In the cases of both oxygen coverages of PtO_2/TiO_2 and RhO_2/TiO_2, ΔG_2, which is the potential-determining step for each system, was reduced, exhibiting the improved OER activities (i.e., smaller $|\eta_{OER}|$) compared to those of PtO_2 and RhO_2, respectively. In the cases of OsO_2, TaO_2, and NbO_2, the bonds of the O* intermediates are too strong in the presence of the TiO_2 substrate, resulting in a decreased OER activity.

Similar to the previous studies (Rossmeisl et al., 2007; Man et al., 2011), RuO_2 and IrO_2 were both identified as the active OER catalysts among the MO_2 candidates (i.e., η_{OER} < ~0.5 V, **Figure 3A**). In the case of $2O_b$ $2O_c$ of RuO_2, the OER activity maintains similarity in the presence of TiO_2 substrate, which is located near the top of the volcano. In general, the TiO_2 substrate stabilizes the adsorbates (i.e., OOH*, O*, and OH*) on $2O_b$ $2O_c$ of RuO_2, which appears as stronger adsorption free energies by 0.54–0.70 eV (**Supplementary Table S1**). Nevertheless, η_{OER} is almost unchanged (i.e., $\Delta\eta_{OER}$ = −0.01 V) because the free energy change in the potential determining step (i.e., $\Delta G_{OOH^*} - \Delta G_{O^*}$) remains similar (**Supplementary Table S2**). In addition, it is also noteworthy that η_{OER} for $2O_b$ $2O_c$ of IrO_2 is relatively similar, still exhibiting higher activity than other candidates except RuO_2.

The changes in η_{OER} induced by the TiO_2 substrate are summarized in **Figure 3B**. As the value becomes more negative, the activity of MO_2/TiO_2 improves compared with that of MO_2. Notably, $2O_b$ $2O_c$ of CrO_2, MnO_2, RuO_2, RhO_2, and PtO_2 shows an enhanced activity. In addition, $2O_b$ of RhO_2 and PtO_2 also shows an improved activity on the TiO_2 substrate. However, regardless of the coverage, the TiO_2 substrate decreases the OER activity of VO_2, OsO_2, and IrO_2. In particular, $2O_b$ $2O_c$ of VO_2 and $2O_b$ of SnO_2 exhibit significantly increased overpotentials ($\Delta\eta_{OER}$ of 0.53 and 0.57 V, respectively).

To determine the promising free-energy regime for the OER, we further analyzed the free energies of the steps in terms of the ESSI, as suggested by Calle-Vallejo and coworkers (Govindarajan et al., 2018). The ESSI is an energetic descriptor that indicates the degree of similarity with an ideal catalyst, where all OER steps are perfectly symmetric at 1.23 eV. The ESSI is defined by the following equation and is only applied to steps with $\Delta G_i\,(i = 1, 2, 3, 4) \geq 1.23$ eV (denoted as ΔG_i^*):

$$\mathrm{ESSI} = \frac{1}{n}\sum_{i}^{n}\left(\Delta G_i^* - 1.23\right). \tag{14}$$

Figure 4A shows η_{OER} of each model as a function of the ESSI, representing a good linear correlation. $2O_b$ of RuO_2 is the closest model to the ideal catalyst, followed by $2O_b$ $2O_c$ of RuO_2 and RuO_2/TiO_2. The $2O_b$ of PtO_2 appears on the η_{OER} = ESSI (red dashed line) and has a null bar with respect to the ESSI, which means that only a single step is greater than 1.23 V (i.e., ΔG_2 = 3.13 eV). In the presence of the TiO_2 substrate, ΔG_2 for $2O_b$ of PtO_2 is reduced, leading to a decrease of the ESSI and η_{OER}. Meanwhile, $2O_b$ $2O_c$ of PtO_2 lies relatively far from the line of η_{OER} = ESSI, which has a wide bar with respect to the ESSI, and thus corresponds to a good candidate for optimization (Govindarajan et al., 2018). In practice, the TiO_2 substrate on $2O_b$ $2O_c$ of PtO_2 works for enhancing the OER activity with a decrease in both η_{OER} and ESSI.

Based on the scaling relation between the ESSIs and η_{OER}'s, we determined a promising group of OER catalysts using the ESSI-ΔG_2 activity map introduced by Exner (Exner, 2019; **Figure 4B**). The activity map is used to identify OER candidates by adjusting the ESSI threshold. The ESSI threshold (< 0.53 V) was determined from **Supplementary Figure S2** by applying η_{OER} of IrO_2, which is the conventional OER catalyst. The free-energy regime was set to 1.20 eV < ΔG_2 < 2.06 eV by

applying the standard deviation of ± 0.43 eV of the scaling relationship between ΔG_2 and ΔG_3 (**Supplementary Figure S3**) on 1.63 eV. The median value of 1.63 eV in the free-energy regime is determined by assuming the threshold electrode potential as the point where the experimental Tafel slope exceeds 59 mV/dec (i.e., η_{OER} > 0.4 V), accounting for kinetics (Exner and Over, 2019). The green-colored area includes $2O_b$ of RuO_2, $2O_b$ $2O_c$ of RuO_2, $2O_b$ $2O_c$ of RuO_2/TiO_2, $2O_b$ of IrO_2, $2O_b$ $2O_c$ of IrO_2, $2O_b$ $2O_c$ of IrO_2/TiO_2, and $2O_b$ $2O_c$ of RhO_2, which are the most promising candidates. Particularly, a portion of promising candidates for the OER (i.e., RuO_2, RuO_2/TiO_2, IrO_2, IrO_2/TiO_2, and RhO_2/TiO_2) are more evidently classified on the ESSI-ΔG_2 map (**Figure 4B**), while they are somewhat deviated from the apex in the volcano plot (**Figure 3A**). This implies that conventional volcano analysis does not guarantee to predict the most active OER catalyst, whereas the ESSI-ΔG_2 activity map, which is based on the kinetic scaling relations, is a more robust descriptor for the OER (Exner, 2019; Exner and Over, 2019). The $2O_b$ $2O_c$ surface of IrO_2 exhibits high symmetry of the reaction steps comparable to RuO_2. On the $2O_b$ and $2O_b$ $2O_c$ surfaces of RhO_2/TiO_2, the values of ΔG_2 decrease compared to those of RhO_2. Accordingly, the free-energy differences of the other steps are adjusted to compensate for the decrease in ΔG_2, while maintaining ΔG_2 as a potential-determining step with reduced η_{OER} (cf. **Supplementary Table S2**). Next, $2O_b$ of IrO_2/TiO_2 belongs to the yellow-colored region, which needs to be reconsidered for activity optimization (Govindarajan et al., 2019). The candidates in the region of ESSI > 0.53 V (i.e., red-highlighted region in **Figure 4B**) are classified as an inferior group, showing poor OER activities over all ranges of ΔG_2 due to the highly asymmetric free-energy changes of the OER intermediates (Exner, 2019).

CONCLUSION

We screened a variety of rutile oxide heterostructures based on a TiO_2 substrate using scaling relations and relevant descriptors to identify a promising OER catalyst. The scaling relations between the reaction intermediates demonstrate that the rutile-type MO_2 heterostructures follow the universal scaling relationship of metal oxides. In addition, the TiO_2 substrate stabilizes the O* bond on the (110) metal oxide surface. Based on the conventional volcano plot, RuO_2 and IrO_2 are found to be highly active OER catalysts as previously reported. Based on the ESSI descriptor, the superior activity of the RuO_2 can be attributed to the high symmetry of the reaction steps. Furthermore, based on the ESSI-ΔG_2 activity map, the candidates can be classified into an optimum group, a second promising group of OER catalysts with potential for optimization, and an inferior group that does not require particular attention.

The results of our computational screening using the scaling relations of rutile-type heterostructures provide valuable insights into the effect of the support material on the overpotential and thus guidelines for the design of a promising OER catalyst.

DATA AVAILABILITY STATEMENT

The original contributions presented in the study are included in the article/**Supplementary Material**, further inquiries can be directed to the corresponding authors.

AUTHOR CONTRIBUTIONS

All calculations and data analyses were performed by HYL. All authors contributed to the discussion of the results and wrote and revised the manuscript. SKK and GYJ supervised the project.

FUNDING

This work was supported by the National Research Foundation of Korea (NRF) grant funded by the Korea government (Ministry of Science and ICT) (NRF-2019M1A2A2065614) and the Global PhD Fellowship Program (NRF-2019H1A2A1076827 and NRF-2016H1A2A1908137). SKK acknowledges the UNIST grant (2.200487.01) for the support of the publication. Computational resources were provided by UNIST High Performance Computing (HPC) systems and Korea Institute of Science and Technology Information (KISTI) (KSC-2019-CRE-0255).

SUPPLEMENTARY MATERIAL

The Supplementary Material for this article can be found online at: https://www.frontiersin.org/articles/10.3389/fenrg.2021.606313/full#supplementary-material.

REFERENCES

Anisimovdag, V. I., Aryasetiawan, F., and Lichtenstein, A. I. (1997). First-principles calculations of the electronic structure and spectra of strongly correlated systems: the LDA + U method. *J. Phys. Condens. Matter* 9, 767–808. doi:10.1088/0953-8984/9/4/002

Blochl, P. E. (1994). Projector augmented-wave method. *Phys. Rev. B* 50, 17953. doi:10.1103/PhysRevB.50.17953

Bu, Y., Jang, H., Gwon, O., Kim, S. H., Joo, S. H., Nam, G., et al. (2019). Synergistic interaction of perovskite oxides and N-doped graphene in versatile electrocatalyst. *J. Mater. Chem. A* 7 (5), 2048–2054. doi:10.1039/c8ta09919g

Costentin, C., and Savéant, J.-M. (2017). Theoretical and mechanistic aspects of proton-coupled electron transfer in electrochemistry. *Curr. Opin. Electrochem.* 1, 104–109. doi:10.1016/j.coelec.2016.11.001

Divanis, S., Kutlusoy, T., Boye, I. M. I., Man, I. C., and Rossmeisl, J. (2020). Oxygen evolution reaction: a perspective on a decade of atomic scale simulations. *Chem. Sci.* 11, 2943. doi:10.1039/c9sc05897d

Esposito, D. V., Hunt, S. T., Stottlemyer, A. L., Dobson, K. D., McCandless, B. E., Birkmire, R. W., et al. (2010). Low-cost hydrogen-evolution catalysts based on monolayer platinum on tungsten monocarbide substrates. *Angew. Chem. Int. Ed.* 49, 9859–9862. doi:10.1002/anie.201004718

Exner, K. S. (2019). Design criteria for oxygen evolution electrocatalysts from first principles: introduction of a unifying material-screening approach. *ACS Appl. Energy Mater.* 2, 11. doi:10.1021/acsaem.9b01480

Exner, K. S., and Over, H. (2019). Beyond the rate-determining step in the oxygen evolution reaction over a single-crystalline IrO_2 (110) model electrode: kinetic scaling relations. *ACS Catal.* 9, 6755–6765. doi:10.1021/acscatal.9b01564

Frydendal, R., Paoli, E. A., Knudsen, B. P., Wickman, B., Malacrida, P., Stephens, I. E. L., et al. (2014). Benchmarking the stability of oxygen evolution reaction catalysts: the importance of monitoring mass losses. *ChemElectroChem.* 1, 2075–2081. doi:10.1002/celc.201402262

García-Mota, M., Vojvodic, A., Metiu, H., Man, I. C., Su, H.-Y., Rossmeisl, J., et al. (2011). Tailoring the activity for oxygen evolution electrocatalysis on rutile TiO_2(110) by transition-metal substitution. *ChemCatChem.* 3, 1607–1611. doi:10.1002/cctc.201100160

Govindarajan, N., Garcia-Lastra, J. M., Meijer, E. A., and Calle-Vallejo, F. (2018). Does the breaking of adsorption-energy scaling relations guarantee enhanced electrocatalysis? *Curr. Opin. Electrochem.* 8, 110–117. doi:10.1016/j.coelec.2018.03.025

Govindarajan, N., Koper, M. T. M., Meijer, E. J., and Calle-Vallejo, F. (2019). Outlining the scaling-based and scaling-free optimization of electrocatalysts. *ACS Catal.* 9, 4218–4225. doi:10.1021/acscatal.9b00532

Hammes-Schiffer, S. (2015). Proton-coupled electron transfer: moving together and charging forward. *J. Am. Chem. Soc.* 137, 8860–8871. doi:10.1021/jacs.5b04087

Hanaor, D. A. H., Xu, W., Ferry, M., and Sorrell, C. C. (2012). Abnormal grain growth of rutile TiO_2 induced by $ZrSiO_4$. *J. Cryst. Growth* 359, 83–91. doi:10.1016/j.jcrysgro.2012.08.015

Jin, B., Zhou, X., Huang, L., Lickleder, M., Yang, M., and Schmuki, P. (2016). Aligned MoO_x/MoS_2 core–shell nanotubular structures with a high density of reactive sites based on self-ordered anodic molybdenum oxide nanotubes. *Angew. Chem., Int. Ed. Engl.* 55, 12252. doi:10.1002/anie.201605551

Kresse, G., and Furthmiiller, J. (1996). Efficiency of ab-initio total energy calculations for metals and semiconductors using a plane-wave basis set. *Comput. Mater. Sci.* 6, 15–50. doi:10.1016/0927-0256(96)00008-0

Krishnamurthy, D., Sumaria, V., and Viswanathan, V. (2018). Maximal predictability approach for identifying the right descriptors for electrocatalytic reactions. *J. Phys. Chem. Lett.* 9, 588–595. doi:10.1021/acs.jpclett.7b02895

Kumar, K., Canaff, C., Rousseau, J., Arrii-Clacens, S., Napporn, T. W., Habrioux, A., et al. (2016). Effect of the oxide–carbon heterointerface on the Activity of Co_3O_4/NRGO nanocomposites toward ORR and OER. *J. Phys. Chem. C* 120 (15), 7949–7958. doi:10.1021/acs.jpcc.6b00313

Kung, H. H. (1989). *Transition metal oxides: surface chemistry and catalysis*. Amsterdam: Elsevier Science.

Kuo, D. Y., Kawasaki, J. K., Nelson, J. N., Kloppenburg, J., Hautier, G., Shen, K. M., et al. (2017). Influence of surface adsorption on the oxygen evolution reaction on IrO_2(110). *J. Am. Chem. Soc.* 139, 3473–3479. doi:10.1021/jacs.6b11932

Kuo, D. Y., Paik, H., Kloppenburg, J., Faeth, B., Shen, K. M., Schlom, D. G., et al. (2018). Measurements of oxygen electroadsorption energies and oxygen evolution reaction on RuO_2(110): a discussion of the sabatier principle and its role in electrocatalysis. *J. Am. Chem. Soc.* 140, 17597–17605. doi:10.1021/jacs.8b09657

Lee, Y., Suntivich, J., May, K. J., Perry, E. E., and Shao-Horn, Y. (2012). Synthesis and activities of rutile IrO_2 and RuO_2 nanoparticles for oxygen evolution in acid and alkaline solutions. *J. Phys. Chem. Lett.* 3 (3), 399–404. doi:10.1021/jz2016507

Li, X., Sun, X., Xu, X., Liu, W., Peng, H., Fang, X., et al. (2017). CO oxidation on PdO catalysts with perfect and defective rutile-TiO_2 as supports: elucidating the role of oxygen vacancy in support by DFT calculations. *Appl. Surf. Sci.* 401, 49–56. doi:10.1016/j.apsusc.2016.12.210

Lu, X. F., Chen, Y., Wang, S. B., Gao, S. Y., and Lou, X. W. (2019). Interfacing manganese oxide and cobalt in porous graphitic carbon polyhedrons boosts oxygen electrocatalysis for Zn–Air batteries. *Adv. Mater.* 31 (39), 1902339. doi:10.1002/adma.201902339

Man, I. C., Su, H.-Y., Calle-Vallejo, F., Hansen, H. A., Martínez, J. I., Inoglu, N. G., et al. (2011). Universality in oxygen evolution electrocatalysis on oxide surfaces. *ChemCatChem.* 3, 1159–1165. doi:10.1002/cctc.201000397

Oh, N. K., Kim, C., Lee, J., Kwon, O., Choi, Y., Jung, G. Y., et al. (2019). *In-situ* local phase-transitioned $MoSe_2$ in $La_{0.5}Sr_{0.5}CoO_{3-\delta}$ heterostructure and stable overall water electrolysis over 1000 hours. *Nat. Commun.* 10, 1723. doi:10.1038/s41467-019-09339-y

Perdew, J. P., Burke, K., and Ernzerhof, M. (1997). Generalized gradient approximation made simple. *Phys. Rev. Lett.* 77, 3865. doi:10.1103/PhysRevLett.77.3865

Qingxiang, W., Dastafkan, K., and Chuan, Z. (2018). Design strategies for non-precious metal oxide electrocatalysts for oxygen evolution reactions. *Curr. Opin. Electrochem.* 10, 16–23. doi:10.1016/j.coelec.2018.03.015

Rossmeisl, J., Qu, Z.-W., Zhu, H., Kroes, G.-J., and Nørskov, J. K. (2007). Electrolysis of water on oxide surfaces. *Electroanal. Chem.* 607, 83. doi:10.1016/j.jelechem.2006.11.008

Seitsonen, A. P., and Over, H. (2010). Oxidation of HCl over TiO_2-supported RuO_2: a density functional theory study. *J. Phys. Chem. C* 114, 22624–22629. doi:10.1021/jp108603a

Seitz, L. C., Dickens, C. F., Nishio, K., Hikita, Y., Montoya, J., Doyle, A., et al. (2016). A highly active and stable $IrO_x/SrIrO_3$ catalyst for the oxygen evolution reaction. *Science* 353 (6303), 1011–1014. doi:10.1126/science.aaf5050

Stacchiola, D. J., Senanayake, S. D., Liu, P., and Rodriguez, J. A. (2013). Fundamental studies of well-defined surfaces of mixed-metal oxides: special properties of MO_x/TiO_2(110) {M = V, Ru, Ce, or W}. *Chem. Rev.* 113, 4373–4390. doi:10.1021/cr300316v

Suen, N.-T., Hung, S.-F., Quan, Q., Zhang, N., Xu, Y.-J., and Chen, H. M. (2017). Electrocatalysis for the oxygen evolution reaction: recent development and future perspectives. *Chem. Soc. Rev.* 46 (337), 337–365. doi:10.1039/c6cs00328a

Sun, X., Peng, X., Xu, X., Jin, H., Wang, H., and Wang, X. (2016). H_2 adsorption and dissociation on PdO(101) films supported on rutile TiO_2(110) facet: elucidating the support effect by DFT calculations. *J. Mol. Model.* 22, 204. doi:10.1007/s00894-016-3072-3

Turner, J. A. (2004). Sustainable hydrogen production. *Science* 305, 972–974. doi:10.1126/science.1103197

Valdes, A., Qu, Z.-W., Kroes, G.-J., Rossmeisl, J., and Norskov, J. K. (2008). Oxidation and photo-oxidation of water on TiO_2 surface. *J. Phys. Chem. C* 2, 9872–9879. doi:10.1021/jp711929d

Vojvodic, A., Calle-Vallejo, F., Guo, W., Wang, S., Toftelund, A., Studt, F., et al. (2011). On the behavior of Brønsted-Evans-Polanyi relations for transition metal oxides. *J. Chem. Phys.* 134, 244509. doi:10.1063/1.3602323

Wang, D. Y., Gong, M., Chou, H. L., Pan, C. J., Chen, H. A., Wu, Y., et al. (2015). Highly active and stable hybrid catalyst of cobalt-doped FeS_2 nanosheets–carbon nanotubes for hydrogen evolution reaction. *J. Am. Chem. Soc.* 137, 1587. doi:10.1021/jacs.5b07788

Wei, W., Dai, Y., Huang, B., Li, X., Nagele, F., Over, H., et al. (2015). Density functional characterization of the electronic structures and band bending of rutile RuO_2/TiO_2(110) heterostructures. *J. Phys. Chem. C* 119, 12394–12399. doi:10.1021/acs.jpcc.5b01884

Xiao, Z., Huang, Y.-C., Dong, C.-L., Xie, C., Liu, Z., Du, S., et al. (2020). Operando identification of the dynamic behavior of oxygen vacancy-rich Co_3O_4 for oxygen evolution reaction. *J. Am. Chem. Soc.* 142, 12087. doi:10.1021/jacs.0c00257

Xu, Z., Rossmeisl, J., and Kitchin, J. R. (2015). A linear response DFT+U study of trends in the oxygen evolution activity of transition metal rutile dioxides. *J. Phys. Chem. C* 119, 4827–4833. doi:10.1021/jp511426q

Zhou, W., Hou, D., Sang, Y., Yao, S., Zhou, J., Li, G., et al. (2014). MoO_2 nanobelts@nitrogen self-doped MoS_2 nanosheets as effective electrocatalysts for hydrogen evolution reaction. *J. Mater. Chem. A* 2, 11358. doi:10.1039/c4ta01898b

Conflict of Interest: The authors declare that the research was conducted in the absence of any commercial or financial relationships that could be construed as a potential conflict of interest.

frontiers in Energy Research

ORIGINAL RESEARCH
published: 30 March 2021
doi: 10.3389/fenrg.2021.653542

Electrode and Electrolyte Materials From Atomistic Simulations: Properties of Li_xFePO_4 Electrode and Zircon-Based Ionic Conductors

Piotr M. Kowalski[1,2]*, *Zhengda He*[1,2] *and Oskar Cheong*[1,2,3]

[1] *Forschungszentrum Jülich GmbH, Institute of Energy and Climate Research - IEK-13: Theory and Computation of Energy Materials, Jülich, Germany,* [2] *Jülich Aachen Research Alliance, JARA Energy & Center for Simulation and Data Science (CSD), Jülich, Germany,* [3] *Chair of Theory and Computation of Energy Materials, Faculty of Georesources and Materials Engineering, RWTH Aachen University, Aachen, Germany*

Li_xFePO_4 orthophosphates and fluorite- and pyrochlore-type zirconate materials are widely considered as functional compounds in energy storage devices, either as electrode or solid state electrolyte. These ceramic materials show enhanced cation exchange and anion conductivity properties that makes them attractive for various energy applications. In this contribution we discuss thermodynamic properties of Li_xFePO_4 and yttria-stabilized zirconia compounds, including formation enthalpies, stability, and solubility limits. We found that at ambient conditions Li_xFePO_4 has a large miscibility gap, which is consistent with existing experimental evidence. We show that cubic zirconia becomes stabilized with Y content of ∼8%, which is in line with experimental observations. The computed activation energy of 0.92 eV and ionic conductivity for oxygen diffusion in yttria-stabilized zirconia are also in line with the measured data, which shows that atomistic modeling can be applied for accurate prediction of key materials properties. We discuss these results with the existing simulation-based data on these materials produced by our group over the last decade. Last, but not least, we discuss similarities of the considered compounds in considering them as materials for energy storage and radiation damage resistant matrices for immobilization of radionuclides.

Keywords: orthophosphates, atomistic simulations (*ab-initio* calculations), energy storage materials, ceramics, thermodynamics, solid solution, solid-state electrolyte

OPEN ACCESS

Edited by:
Jun Huang,
Central South University, China

Reviewed by:
Peng Li,
Wuhan University, China
Junxiang Chen,
Chinese Academy of Sciences, China

***Correspondence:**
Piotr M. Kowalski
p.kowalski@fz-juelich.de

Specialty section:
This article was submitted to Electrochemical Energy Conversion and Storage, a section of the journal Frontiers in Energy Research

Received: *14 January 2021*
Accepted: *05 March 2021*
Published: *30 March 2021*

Citation:
Kowalski PM, He Z and Cheong O (2021) Electrode and Electrolyte Materials From Atomistic Simulations: Properties of Li_xFePO_4 Electrode and Zircon-Based Ionic Conductors. Front. Energy Res. 9:653542. doi: 10.3389/fenrg.2021.653542

1. INTRODUCTION

MPO_4 orthophosphates, with M cations being transition metals, rare-earth elements or actinides, are ceramic materials of interest in various research fields, including geochronology (Williams et al., 2007), geothermometry (Andrehs and Heinrich, 1998; Mogilevsky, 2007), energy storage (Iyer et al., 2006; Yamada et al., 2006; Dunn et al., 2015; Dong et al., 2017; Cerdas et al., 2018; Li et al., 2018; Phan et al., 2019), and nuclear waste management (Ewing and Wang, 2002; Neumeier et al., 2017a; Schlenz et al., 2018), to name but a few. Most of the potential applications come from high durability (e.g., radiation damage resistance) of these materials (Neumeier et al., 2017a; Phan et al., 2019). There exist large varieties of phosphate-based ceramics of different crystalline structures (e.g., cheralite, apatites, olivine, kosnarite, see Iyer et al., 2006; Neumeier et al., 2017a; Phan et al., 2019). The orthophosphates of interest for energy storage, $FePO_4$ and $LiFePO_4$, have olivine-type

structure of orthorombic space group symmetry of *Pnma* in which Fe exists in an octahedral environment (Iyer et al., 2006; Maxisch and Ceder, 2006, see **Figure 1** for visualization of the structures). It consists of eight-fold coordinated Fe^{3+} cations, which become reduced to Fe^{2+} upon incorporation of Li. Besides, there exist less stable $FePO_4$ monoclinic, orthorombic, and trigonal phases with Fe in tetrahedraly coordinated crystallographic positions (Iyer et al., 2006; Yamada et al., 2006; Dong et al., 2017). $LiFePO_4$ materials are one of the best known candidates for energy storage electrodes (Dunn et al., 2015; Cerdas et al., 2018). These exhibit high theoretical energy density of 170 mAh/g and voltage of 3.5 V (Phan et al., 2019). Because of this, these materials are considered for large scale energy storage devices, including batteries for hybrid and electric automobiles (Prosini et al., 2002; Dunn et al., 2015; Cerdas et al., 2018). Intercalation of Li ions into $FePO_4$ results in formation of a solid solution between Li cations and vacant sites (Phan et al., 2019). Depending on the sizes of mixing species, a solid solution compounds could form a thermodynamically stable solid solution or a compound with a mixture of two phases, each rich in one of the cations (Kowalski and Li, 2016; Ji et al., 2019a). The second case indicates formation of a temperature dependent miscibility gap. The two endmember phases may be of the same type, like in the case of Li_xFePO_4, or different phases, like in the monazite-xenotime system (Mogilevsky, 2007; Ji et al., 2019a). The formation of miscibility gap is correlated with the maximum solubility (Ji et al., 2019a). Such a temperature-dependent maximum solubility offers opportunity to use such a system as geothermometer (Andrehs and Heinrich, 1998; Mogilevsky, 2007). It is known from experiment that Li_xFePO_4 solid solution posses a wide miscibility gap at ambient temperature (Yamada et al., 2006; Meethong et al., 2007; Li et al., 2018; Phan et al., 2019). In particular, studies of Yamada et al. (2006) indicate relatively low Li solubility limits in Li_xFePO_4 system at $x = 0.05$ and 0.89. The thermodynamics of such a system, however, although has been modeled by CALPHAD method (Phan et al., 2019), has not been modeled in details using *ab initio* atomistic modeling methods and the results of various studies differ substantially (Phan et al., 2019).

Zirconium-based ceramics have been shown to posses interesting ion-conduction characteristics (Diazguillen et al., 2008; Mandal et al., 2008; Xia et al., 2010; Anithakumari et al., 2016; Li and Kowalski, 2018), with yttria stabilized zirconia being one of the fastest ionic conductors (Kilo et al., 2003; Krishnamurthy et al., 2005b). It is thus used as solid electrolyte in various energy storage devices (Zakaria et al., 2020). The fast oxygen conduction properties are associated with formation and distribution of vacant sites (in fluorite and pyrochlore, Bukaemskiy et al., 2021) and interesting short- and long-range ordering phenomena (Wuensch, 2000; Yamamura, 2003; Anithakumari et al., 2016; Drey et al., 2020; Kowalski, 2020; Bukaemskiy et al., 2021). For instance, certain pyrochlore compounds exhibit high ionic conductivity (e.g., $Eu_2Zr_2O_7$, Yamamura, 2003) and form a stable, cation-disordered solid phase (defect fluorite, Li et al., 2015). Such phases show interesting short- and long-range ordering (Shamblin et al., 2016; Drey et al., 2020; Kowalski, 2020; Bukaemskiy et al., 2021), with distribution of vacancies determining the amplitude of pre-exponential factor and efficiency of ionic conduction (Bukaemskiy et al., 2021). For instance, Bukaemskiy et al. (2021) demonstrated that the maximum of ionic conductivity in $YO_{1.5} - ZrO_2$ system occurs at $x = 0.146$ due to vacancy avoidance phenomenon and related vacancy jump probability. This correlates well with the existing ionic conductivity data (Bukaemskiy et al., 2021). Cubic phase of zirconia (ZrO_2) becomes stabilized upon doping with tri-valent elements, e.g., Y

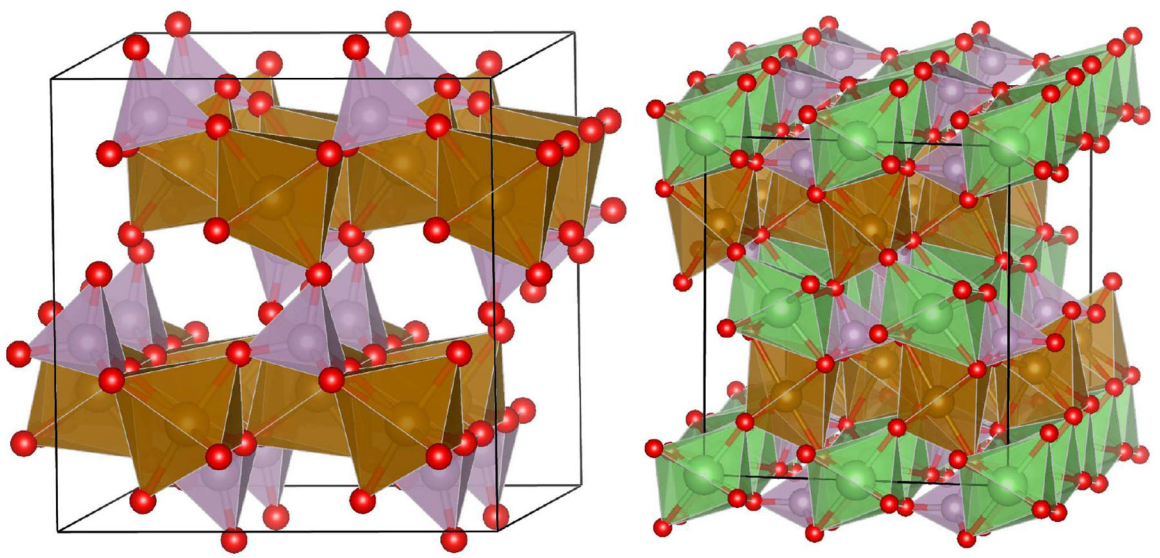

FIGURE 1 | Structures of $FePO_4$ **(left)** and $LiFePO_4$ **(right)**.

(Li et al., 1994; Kilo et al., 2003; Krishnamurthy et al., 2005b) at about 8% content of dopant. The formed solid solution shows very high ionic conductivity that increases significantly with dopant amount (Ioffe et al., 1978; Bukaemskiy et al., 2021). These compounds are thus considered as solid electrolyte for energy storage devices (Zakaria et al., 2020).

In the last two decades, atomistic modeling became a widely used research technique in various research fields, including energy materials (Chroneos et al., 2013; Jahn and Kowalski, 2014; Wu et al., 2019). We used it intensively over the past decade for computation of, for instance, various physical and chemical properties of orthophosphate- and zircon-based ceramics (e.g., Kowalski et al., 2015; Ji et al., 2019a). This is because steady advancements in high performance computing and computational software, especially in *ab initio* methods-based codes, allows nowadays for computation of complex systems containing hundreds of atoms from first principles (Jahn and Kowalski, 2014). Regarding ceramic compounds considered here, computational studies have been used to deliver information on: the structural (Rustad, 2012; Feng et al., 2013; Blanca-Romero et al., 2014; Beridze et al., 2016; Huittinen et al., 2017), the electronic structure (Tang and Holzwarth, 2003; Blanca-Romero et al., 2014; Kowalski et al., 2017a; Lee et al., 2017), the elastic (Wang et al., 2005; Feng et al., 2013; Ali et al., 2016; Kowalski and Li, 2016; Ji et al., 2017a; Kowalski et al., 2017b), the thermodynamic (Mogilevsky, 2007; Feng et al., 2013; Li et al., 2014; Kowalski et al., 2015, 2016; Ji et al., 2017b; Neumeier et al., 2017b; Eremin et al., 2019), the thermochemical (Rustad, 2012; Beridze et al., 2016; Kowalski, 2020), the electrochemical (Krishnamurthy et al., 2005b; Lee et al., 2017), and the radiation damage resistance (Kowalski et al., 2016; Li et al., 2016; Ji et al., 2017c; Jolley et al., 2017) parameters as well as materials at high-pressure (López-Solano et al., 2010; Stavrou et al., 2012; Ali et al., 2016; Shein and Shalaeva, 2016; Gomis et al., 2017). The relevant research activity increases steadily worldwide, with most of the papers published just recently. One important aspect is the correct calculations of compounds with *d*- and *f*- elements that contain strongly correlated electrons [e.g., Fe, Ni, lanthanides (*Ln*), actinides (*An*)]. In a series of papers we have shown that standard DFT approach often fails for such cases and these compounds must be carefully computed, including proper accounting for the correlation effects (Beridze and Kowalski, 2014; Blanca-Romero et al., 2014; Kowalski et al., 2015; Li and Kowalski, 2018). These simulations must be performed with methods beyond the standard DFT+*U* approach and include derivation of the Hubbard *U* parameter and careful choice of projectors for estimation of occupancy of *d*− and *f*− levels within the DFT+*U* scheme (Maxisch and Ceder, 2006; Kvashnina et al., 2018; Kick et al., 2019). In particular, we apply the linear response method (Cococcioni and de Gironcoli, 2005) with Wannier orbitals as representation of *d* or *f* states (Kvashnina et al., 2018) and here we will demonstrate impact of these procedures on the estimation of formation enthalpies and solubility limits of Li_xFePO_4 compound.

In this contribution we provide an overview of the recent atomistic modeling activities on the orthophosphates and zirconates, focusing on the information that have been delivered by atomistic modeling activities at Forschungszentrum Jülich and that allowed on many occasions for better characterization of these materials, including long-term thermodynamic stability, thermochemical parameters, and thermal conductivity. Besides such overview, we present results of computation of thermochemical and thermodynamic parameters of Li_xFePO_4 solid solution, with focus on the formation of miscibility gap in this system, as well as simulation of yttria-stabilized zirconia with focus on prediction the phase stability and ionic conductivity in this class of materials. We especially highlight a cross-linking, interdisciplinary character of our research, from which the general science community could highly benefit.

2. COMPUTATIONAL APPROACH

In all *ab initio*[1] calculations discussed here we used a density functional theory (DFT)-based quantum chemistry approach and calculations were performed with Quantum-ESPRESSO simulation package (Giannozzi et al., 2009). We applied the PBEsol exchange-correlation functional (Perdew et al., 2008), the ultrasoft pseudopotentials to represent the core electrons of the atoms (Vanderbilt, 1990) and the plane-wave energy cutoff of 50 Ryd. The PBEsol functional is specifically selected because it correctly reproduces slowly varying electron density limit and results in good structural parameters of solids (Perdew et al., 2008). This is important for consideration of, for instance, thermodynamics of solid solutions (Li et al., 2014; Kowalski and Li, 2016; Ji et al., 2019a). Following our broad experience on computation of lanthanide orthophosphates and zirconates (e.g., Blanca-Romero et al., 2014; Li et al., 2015; Beridze et al., 2016) we applied the self-consistent DFT+*U* approach. The DFT+*U* calculations were performed with the Hubbard *U* parameter values computed from first principles using the linear response method of Cococcioni and de Gironcoli (2005). In order to apply realistic projectors for occupations of *d* orbitals of Fe we used Poor Man Wannier scheme implemented in Quantum-ESPRESSO. This computational setup was extensively tested by us in several studies and, among others, proved to give very good results for orthophosphates and zirconates (Blanca-Romero et al., 2014; Beridze et al., 2016; Finkeldei et al., 2017). The activation barriers were computed using Nudged Elastic Band (NEB) method implemented in Quantum-ESPRESSO, with 10 images and climbing image procedure to compute the transition state. The exponential pre-factors were computed with the aid of transition state theory (Moynihan et al., 1982) and probability of vacancy migration derived by Bukaemskiy et al. (2021), so that the ionic conductivity, σ, is estimated using the modified here formula of Moynihan et al. (1982):

$$\sigma = [15.354x(1-2x)\left(\frac{1-3x}{1-2x}\right)^2]n(Ze)^2/(6k_bT)\nu_0 d^2 \; exp(-E_a/(k_bTN_a)), \quad (1)$$

[1] In this contribution we call DFT methods an *ab initio* approach as the exchange-correlation functionals utilized in our studies were designed based on pure-theoretical considerations.

TABLE 1 | The computed Hubbard *U* parameters for Fe in Fe_2O_3, $FePO_4$ and $LiFePO_4$ compounds.

Compound	Redox state of Fe	Hubbard *U* parameter
Fe_2O_3	Fe(III)	3.9
$FePO_4$	Fe(III)	3.8
$LiFePO_4$	Fe(II)	3.3

Values are reported in eV.

where Ze is the charge of the carrier, k_b is the Boltzmann constant, N_a is Avogadro number, d is the distance of the jump, E_a is the activation barrier, T is the temperature and ν_0 is the attempt frequency. The first part in the square bracket reflects the vacancy migration probability contribution to the pre-exponential factor derived by Bukaemskiy et al. (2021). The attempt frequency ν_0 was estimated from the computation of phonon spectra of the initial (IS) and transition states (TS), as

$$\nu_0 = \frac{\prod_i^{3N-3} \nu_{i,IS}}{\prod_i^{3N-4} \nu_{i,TS}}. \quad (2)$$

The computation of Li_xFePO_4 phases were performed with 2*x*2*x*1 supercells (96 atoms for $FePO_4$ and 112 atoms for $LiFePO_4$ phases) using the 2*x*2*x*2 *k*-point grid. The oxides were computed as: Fe_2O_3 (*Pnmm* symmetry, with supercell containing 30 atoms and 4*x*6*x*2 *k*-point grid), hexagonal P_2O_5 as is in Blanca-Romero et al. (2014) and Y_2O_3 as cubic oxide. The magnetic arrangements in iron phases were computed using the models of Whittingham et al. (2005) and Lee et al. (2017).

The Hubbard *U* parameters computed with the linear response method are listed in **Table 1**. As in our previous studies (Beridze and Kowalski, 2014; Beridze et al., 2016; Kvashnina et al., 2018; Sun et al., 2020) we see strong dependence on the Fe redox state, with the *U* parameter for Fe(III) being ∼0.5 eV larger than for Fe(II). This is well-consistent with previous studies of $FePO_4$ and $LiFePO_4$ phases by Maxisch and Ceder (2006), who obtained 4.9 and 3.7 eV for both phases (taken as effective value, $U_{\text{eff}} = U - J$), respectively.

3. RESULTS AND DISCUSSION

3.1. Structural Data

The first test of a computational method is its ability to reproduce the measured lattice parameters of the computed crystalline solid. The lattice parameters of considered materials were measured by different studies and are well-known. These are collected in **Table 2** and compared to the computed data.

Our previous studies showed that the structural parameters of lanthanide-orthophosphates are very sensitive to the applied computational method, especially to the exchange-correlation functional (Blanca-Romero et al., 2014). A correct treatment of strongly correlated 4*f* electrons also plays an important role in those cases. Here, with our computational setup we got much better fit to the measured data than Maxisch and Ceder (2006), who applied the PBE exchange-correlation functional that tends to overestimate lattice parameters and volumes, which is also evident in the data collected in **Table 2**. Blanca-Romero et al. (2014) performed extensive tests of the capability of different DFT-based approaches to reproduce the measured lattice parameters and bond-distances of monazite-type lanthanide-orthophosphates. In that paper, we found that the standard DFT method with explicitly computed 4*f* electrons overestimates the lattice parameters and bond-lengths by up to 3%, which is consistent with previous studies (Wang et al., 2005; Rustad, 2012). A very good match to the experimental values of structural parameters was achieved applying the parameter free DFT+*U* method, with the PBEsol exchange-correlation functional (Perdew et al., 2008) and the Hubbard *U* parameters derived *ab initio*. An improved description of structures by the PBEsol exchange-correlation functional is an important property of that functional. It recovers the known solution for slowly varying electron densities and with that it improves the description of structural parameters over widely used GGA functionals such as PBE (see discussion by Perdew et al., 2008). It is evident also for zirconate-based materials. In our past studies of $Nd_{2-x}Zr_{2+x}O_{7+x/2}$ compound, with the PBEsol exchange-correlation functional we got perfect match to the lattice parameter in case of the pyrochlore phase (Finkeldei et al., 2017).

TABLE 2 | The computed and measured lattice parameters of Fe_2O_3, $FePO_4$, $LiFePO_4$ and cubic zirconia compounds.

Compound	a	b	c	Vol.	Meth.	References
Fe_2O_3	5.06	5.06	13.79	305.66	DFT+*U*	This study
Fe_2O_3	4.95	4.95	13.69	291.35	DFT	This study
Fe_2O_3	5.03	5.03	13.74	301.76	Exp.	Finger and Hazen, 1980
$FePO_4$	9.92	5.82	4.83	278.91	DFT+*U*	This study
$FePO_4$	9.90	5.84	4.83	279.66	DFT	This study
$FePO_4$	9.94	5.93	4.88	288.06	DFT	Maxisch and Ceder, 2006
$FePO_4$	9.96	5.88	4.86	297.05	DFT+*U*	Maxisch and Ceder, 2006
$FePO_4$	9.78	5.56	4.68	254.63	DFT	Jin et al., 2013
$FePO_4$	9.81	5.79	4.78	271.70	Exp.	Zhu et al., 2014
$FePO_4$	9.82	5.79	4.79	272.36	Exp.	Padhi et al., 1997
$LiFePO_4$	10.34	6.02	4.71	292.75	DFT+*U*	This study
$LiFePO_4$	10.24	5.98	4.68	287.11	DFT	This study
$LiFePO_4$	10.39	6.04	4.73	297.05	DFT	Maxisch and Ceder, 2006
$LiFePO_4$	10.45	6.05	4.74	299.54	DFT	Maxisch and Ceder, 2006
$LiFePO_4$	10.06	5.84	4.71	276.43	DFT	Jin et al., 2013
$LiFePO_4$	10.33	6.00	4.69	291.02	Exp.	Zhu et al., 2014
$LiFePO_4$	10.23	6.00	4.69	288.12	Exp.	García-Moreno et al., 2001
ZrO_2	5.07			130.32	DFT	This study
ZrO_2	5.04			128.02	DFT	Zhao and Vanderbilt, 2002
ZrO_2	5.11			133.43	DFT	Krishnamurthy et al., 2005b
ZrO_2	5.13			135.36	Exp.	Ploc, 1981
ZrO_2	5.09			131.87	Exp.	Zhao and Vanderbilt, 2002
$Y-ZrO_2$ (8%)	5.18			138.99	DFT	This study
$Y-ZrO_2$ (8%)	5.14			135.96	Exp.	Krogstad et al., 2011
$Y-ZrO_2$ (8%)	5.14			135.80	Exp.	Pomfret et al., 2005

TABLE 3 | The computed projected total number of *d* electrons per Fe atom in Fe_2O_3, $FePO_4$ and $LiFePO_4$ compounds using the DFT+*U* approach with atomic orbitals and Wannier functions as projectors.

Compound	Redox state	DFT+*U*	DFT+*U*+Wannier	Expected
Fe_2O_3	Fe(III)	6.29	5.00	5.0
$FePO_4$	Fe(III)	6.16	5.00	5.0
$LiFePO_4$	Fe(II)	6.48	5.99	6.0

TABLE 4 | The computed here with different methods and measured (Iyer et al., 2006) formation enthalpies from oxides of $FePO_4$ and $LiFePO_4$ compounds.

Compound	DFT	DFT+*U*	DFT+*U* (Wannier projectors)	Exp
$FePO_4$	−80	−104	−123	−113
$LiFePO_4$	−52	−177	−153	−152

The energies are reported in kJ/mol.

In the most recent contribution we computed the MUO_4 compounds with $M = \mathrm{Ni, Fe, Co, Cd}$, and found that only by using the correct projectors for estimation of occupation of *d* orbitals, e.g., Wannier functions, we could reproduce experimentally seen structural distortions (Murphy et al., 2021). The problem arises from the fact that with the standard DFT+*U* approach, when using atomic orbitals as projectors, the total occupancy of the *d* or *f* states of interest is much higher than the actual one (Kick et al., 2019; Murphy et al., 2021). As illustrated in **Table 3**, in our case it gives ∼1.3 excess electrons for Fe(III) and ∼0.5 for Fe(II). This is cured when using Wannier orbitals as projectors. Unfortunately, the forces and cell optimizations with this scheme are not yet implemented in Quantum-ESPRESSO or any equivalent codes, so we could not perform geometry optimization with such a more realistic approach.

3.2. Formation Enthalpies

The formation enthalpies from oxides for series of lanthanide orthophosphates have been measured by Ushakov et al. (2001) and of $FePO_4$ and $LiFePO_4$ by Iyer et al. (2006). Rustad (2012) noticed that there is a systematic offset between the computed and measured values for $LnPO_4$ of ∼40 kJ/mol, with the computed enthalpies being less exothermic. Blanca-Romero et al. (2014) have shown that this offset is present also in the DFT+*U* calculations and is to a large extent *Ln*-cation independent, which rules out the 4*f* electrons correlations as a contributing factor. They attributed this to the overestimation of P-O bond lengths, and thus volumes, of the $LnPO_4$ and P_2O_5 compounds. Beridze et al. (2016) have found an identical offset for xenotime phase. When a constant shift of ∼30 kJ/mol is applied to the computed formation enthalpies, the measured values are nicely reproduced. The computed formation enthalpies for $FePO_4$ and $LiFePO_4$ compounds are reported in **Table 4**. It is evident that DFT heavily underestimates the values (taking absolute values) by 40–100 kJ/mol. This is significantly improved with the DFT+*U* approach with an error of 20 kJ/mol. Best result, however, is obtained with the DFT+*U* method when Wanner functions are used as projectors of Fe *d* states occupations. In this scheme, the computed formation enthalpies are within 10 kJ/mol. Accurate prediction of formation enthalpies are crucial for correct estimate of thermodynamic parameters of solid solution, including solubilities (section 3.4).

The most stable phase of ZrO_2 is monoclinic. However, upon doping with tri-valent elements it undergoes phase transition to cubic phase, with possible triclinic phase as an intermediate. The experimental evidence shows transition to that phase at ∼8% of $YO_{1.5}$ (Lee et al., 2003; Götsch et al., 2016; Ahamer et al., 2017). In **Figure 2**, we show the results of computation of formation enthalpies for the three phases of ZrO_2 (monoclinic, tetragonal, and cubic). The results are plotted together with the experimental data of Lee et al. (2003). The computed values show clearly that at ∼ 8% content of Y the enthalpy of cubic phase becomes the lowest and that phase most stable, which is well consistent with the aforementioned experimental data. Moreover, the computed formation enthalpy as a function of Y content is well consistent with the measured values. Also the computed enthalpy difference between monoclinic and cubic phases of ∼14 kJ/mol is well consistent with the previous measurements and estimates (ranging from 6 to 22 kJ/mol, with the best measured value of 10 kJ/mol, Lee et al., 2003).

3.3. Elastic, Thermodynamic, and Thermal Conductivity Parameters

Besides formation enthalpies, our previous studies show good ability of atomistic modeling to predict the elastic, thermodynamic, and thermal parameters of considered systems. Li et al. (2014), Kowalski and Li (2016), and Kowalski et al. (2017b) computed the elastic parameters of series of lanthanide orthophosphates and obtained good agreements with the available experimental data. With these computed data they provided good estimates of parameters that are key for modeling of solid solutions within these compounds. Maxisch and Ceder (2006) computed elastic parameters of $FePO_4$ and $LiFePO_4$ compounds, which we will use for estimates of thermodynamic parameters of solid solutions in Li_xFePO_4 system (section 3.4). In the follow-up studies of lanthanide phosphate we computed heat capacities for series of these compounds and explained the quasirandom-like behavior of heat capacity along lanthanide series by the lanthanide cation-dependent contribution from thermal excitation of 4*f* electrons (Schottky effect, Kowalski et al., 2015, 2017b; Ji et al., 2017a). Ji et al. (2019b) computed thermal conductivity for series of lanthanide phosphates and were able to derive accurate information on phonon mean free path in these systems. These studies demonstrate that with appropriate computational setup, accurate information on various physical parameters can be delivered by atomistic simulations and materials effectively screened for desired physical characteristics. This has been used by us to deliver crucial information on orthophosphate-based ceramics for immobilization of actinides (Huittinen et al., 2017, 2018; Ji et al., 2019a).

Besides computing orthophosphate-type ceramics, we derived various parameters for fluorite- and pyrochlore-type compounds. Among those, with atomistic modeling we computed defect

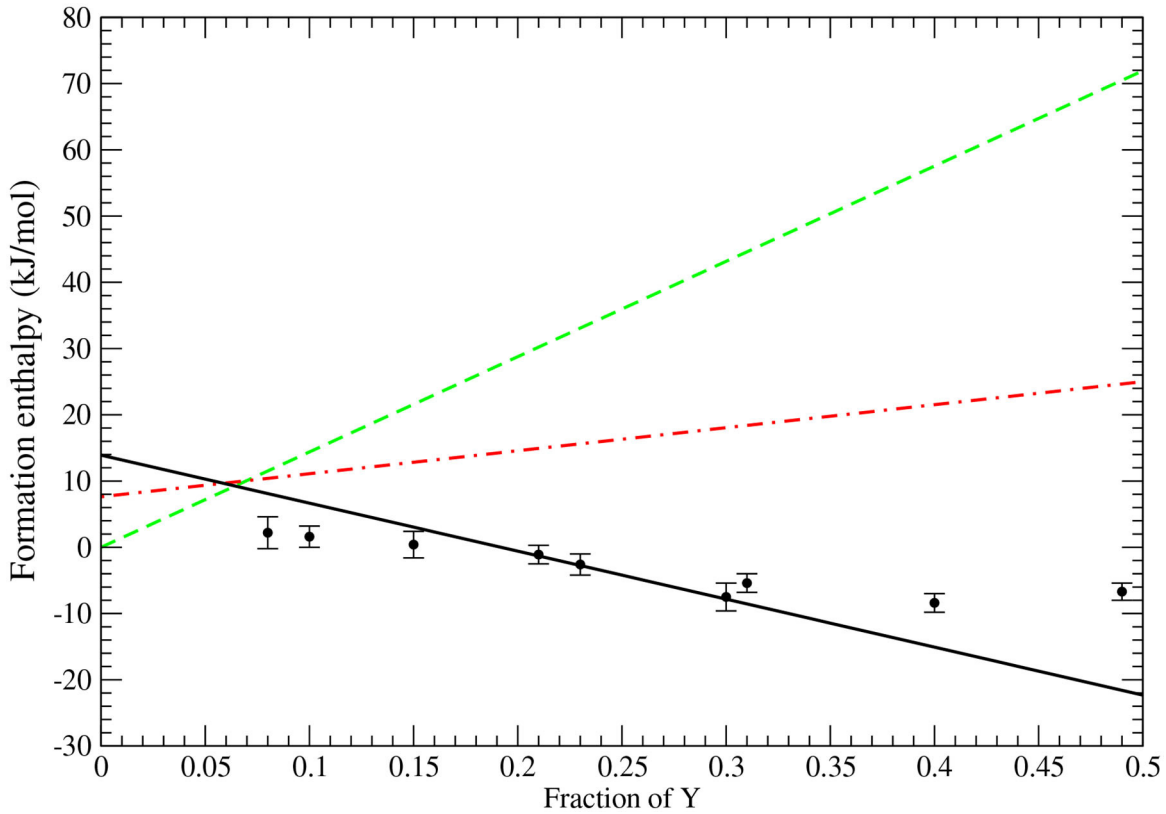

FIGURE 2 | The computed formation enthalpies of $YO_{1.5} - ZrO_2$ system. The lines represent results for monoclinic (dashed green), trigonal (dot-dashed red), and cubic (solid black) phases. The data comes from Lee et al. (2003).

formation energies (Li et al., 2015; Li and Kowalski, 2018), barriers for oxygen diffusion (Li and Kowalski, 2018; Bukaemskiy et al., 2021), structural parameters (Finkeldei et al., 2017, 2020; Bukaemskiy et al., 2021), formation enthalpies (Finkeldei et al., 2017; Kowalski, 2020), and properties of doped systems (Finkeldei et al., 2017, 2020). Interestingly, we found that ability of a material to effectively conduct oxygen is also responsible for enhanced radiation damage resistance of selective pyrochlore compounds and stability of defect pyrochlore (defect fluorite) phase (Li et al., 2015; Li and Kowalski, 2018). In addition, Li and Kowalski (2018) have shown that the formation of split vacancy state for pyrochlore lanthanide-zirconates with lanthanide cations after Eu is responsible for the maximum ionic conductivity of $Eu_2Zr_2O_7$ pyrochlore (Yamamura, 2003).

3.4. Solid Solutions and Solubility

Formation and thermodynamic stability of solid solutions is a topic of studies in various research fields, including battery research (Meethong et al., 2007; Li et al., 2018; Phan et al., 2019). In the past we published a series of studies on lanthanide phosphate ceramic-type solid solutions in the context of geothermometry and nuclear waste management (Li et al., 2014; Kowalski and Li, 2016; Hirsch et al., 2017; Kowalski et al., 2017b; Neumeier et al., 2017b; Ji et al., 2019a). This is because the information gained allows for the assessment of long term stability of ceramic nuclear waste forms against phase separation. It was shown experimentally (Popa et al., 2007; Li et al., 2018; Phan et al., 2019) and by *ab initio* simulations (Li et al., 2014; Kowalski and Li, 2016) that single phase orthophosphate-based solid solutions are highly regular. The excess enthalpy of mixing, H^E, of a $A_{1-x}B_xPO_4$ mixed cation compound could be described by a simple equation (Popa et al., 2007):

$$H^E = Wx(1-x), \tag{3}$$

where W is a Margules interaction parameters (Prieto, 2009). A solid solution is stable against formation of a miscibility gap if $W < 2RT$, where R is the gas constant. It has been demonstrated experimentally (Yamada et al., 2006; Li et al., 2018; Phan et al., 2019) that Li_xFePO_4 solid solution has a wide miscibility gap, for x between 0.05 and 0.89 at room temperature. However, there is a problem with derivation of consistent model for thermodynamic parameters of mixing for this system, including mixing enthalpy or Margules interaction parameters (Phan et al., 2019). It is thus of great interest to characterize W parameter for Li_xFePO_4 system using the computational methods that were proven by us for lanthanide phosphates (Kowalski and Li, 2016; Ji et al., 2019a).

The first systematic *ab initio* calculations of W parameters for monazite-type, orthophosphate solid solutions were performed by Li et al. (2014). In follow-up studies (Kowalski and Li, 2016),

we explained the quadratic dependence of W parameter on the difference in molar volumes of endmembers (ΔV) by a strain energy-based model, in which

$$W = \frac{E}{6V}(\Delta V)^2, \tag{4}$$

where E is the Young's modulus and V is the volume. These studies show that ΔV is an important parameter that determines the value of W parameter. Considering the elastic properties of both endmember phases, this equation can be also written as (Kowalski and Li, 2016):

$$W = \frac{2G_A B_B}{(3B_B + 4G_A)V}(\Delta V)^2, \tag{5}$$

where G_A is the shear modulus of the doped phase and B_B is the bulk modulus of the dopant phase. The Young's, shear and bulk moduli of $FePO_4$ and $LiFePO_4$ phases as computed by Maxisch and Ceder (2006) are given in **Table 5**. The values of Margules interaction parameter computed with the Equations (4) and (5) are also reported. These values are too low and would result in thermodynamically stable solid solution at all Li content (such forms at room temperature for $W < 5$ kJ/mol, Li et al., 2014), which is inconsistent with experimental data of Yamada et al. (2006).

For lanthanide orthophosphates, Neumeier et al. (2017b) compared the derived *ab initio* W parameters with the calorimetric measurements of $La_{1-x}Ln_xPO_4$ (Ln = Eu, Gd) solid solutions. The measured values are smaller than the computed ones. The reason for this discrepancy is the difference in the value of measured and computed ΔV. When Neumeier et al. (2017b) used the measured ΔV values and rescaled the *ab initio* computed values according to Equation (4) as:

$$W = \left(\frac{\Delta V_{exp}}{\Delta V_{comp.}}\right)^2 W_{computed}, \tag{6}$$

they obtained a good match to the measured values. However, in our estimate we used the experimental volumes (**Table 2**) and any such a correction would require significant error in one of the reported volumes. In order to obtain the Margules interaction parameters that are consistent with the measured solubilities (Yamada et al., 2006, see below), instead of the reported $\Delta V = 20$ Å^3 between the two endmember phases it should be $\Delta V = 26$ Å^3. Our computed volumes, however, give even smaller difference of $\Delta V = 14$ Å^3 (**Table 2**).

The experimental maximum solubilities of Yamada et al. (2006) show slightly asymmetric solid solution with maximum solubility of Li in $FePO_4$ of $x_1 = 0.05$ and content/depletion of Li in $LiFePO_4$ of $x_2 = 0.89$. Such an offset between both solubilities is consistent with the prediction of Equation (5). With these measured solubilities, the Margules interaction parameters can be derived. The maximum solubilities x_1 and x_2 at the two ends of slightly asymmetric solid solution or the relevant Margules interaction parameters W_1 and W_2 can be derived by solving self-consistently two equations (Mogilevsky, 2007; Ji et al., 2019a):

$$W_1(1-x_1)^2 + RT\ln(x_1/(1-x_2)) = W_2 x_2^2, \tag{7}$$
$$W_2(1-x_2)^2 + RT\ln(x_2/(1-x_1)) = W_1 x_1^2. \tag{8}$$

These equations realize chemical equilibrium between Li (equilibrium concentration of x_1 in $FePO_4$) and Li-vacancy (equilibrium concentration of x_2 in $LiFePO_4$) in $FePO_4$ (first equation) and Li_xFePO_4 (second equation) phases, respectively, and are derived by equality of the respected chemical potentials (Mogilevsky, 2007). The self-consistent solution of Equations (7) and (8) can be easily done in a numerical way. The resulted Margules interaction parameters for Li_xFePO_4 solid solution obtained taking the measured solubilities as an input (Yamada et al., 2006) and assuming room temperature are given in **Table 5**. The derived $W_1 = 8.0$ kJ/mol and $W_2 = 6.4$ kJ/mol would result in an excess mixing enthalpy, H^E of 1.7 kJ/mol at $x = 0.6$ [computed as $H^E = (W_1(1-x) + W_2 x)x(1-x)$, Li et al., 2014], which is in perfect agreement with the experimental measurements (~2.5±1.0 kJ/mol, Stevens et al., 2006; Phan et al., 2019). Interestingly, the same values can be derived from Equation (5) and elastic moduli reported in **Table 5**, assuming $\Delta V = 26$ Å^3. We note that such an offset is plausible because we consider a solid solution between Li cation and a vacant site, while the considered models were designed strictly for mixing of two cation species. We also attempted direct computation of Margules interaction parameter by *ab initio* methods. We obtained values between 13 and 28 kJ/mol, depending on the computational approach. However, we notice that such a small value of energy (enthalpy) is very sensitive to the computational setup, and can not be derived here precisely because of the inability of computing forces with the Wannier projectors scheme (see section 3.2). Other studies also result in large spread of predicted values (Figure 2 in Phan et al., 2019) and indicate sensitivity of this parameter to other effects, including the electronic entropy of Fe in different redox state in the Li_xFePO_4 solid solution (Zhou et al., 2006).

In **Figure 3**, we plot the free energy of mixing at room temperature, using the Margules interaction parameters extracted form the maximum solubilities measurements of Yamada et al. (2006). With the horizontal line we indicate the widths of wide miscibility and spinodal gaps. This information is important for understanding of charging relationships in the Li_xFePO_4 system (Phan et al., 2019).

TABLE 5 | The computed by Maxisch and Ceder (2006) with the DFT+*U* method Young's (*E*), shear (*G*) and bulk moduli (*B*) for $FePO_4$ and $LiFePO_4$ compounds. The values are given in GPa.

Compound	*E*	*G*	*B*	$W^{(4)}$	$W^{(5)}_{1,2}$	$W^{s}_{1,2}$
$FePO_4$	125.0	51.4	73.6	4.6	4.4	8.0
$LiFePO_4$	123.9	48.4	93.9	4.6	3.8	6.4

$W^{(4)}$, $W^{(5)}_{1,2}$, and $W^{s}_{1,2}$ are the Margules interaction parameters estimated from Equations (4), (5), and solubility data of Yamada et al. (2006) (with Equations 7 and 8), respectively.

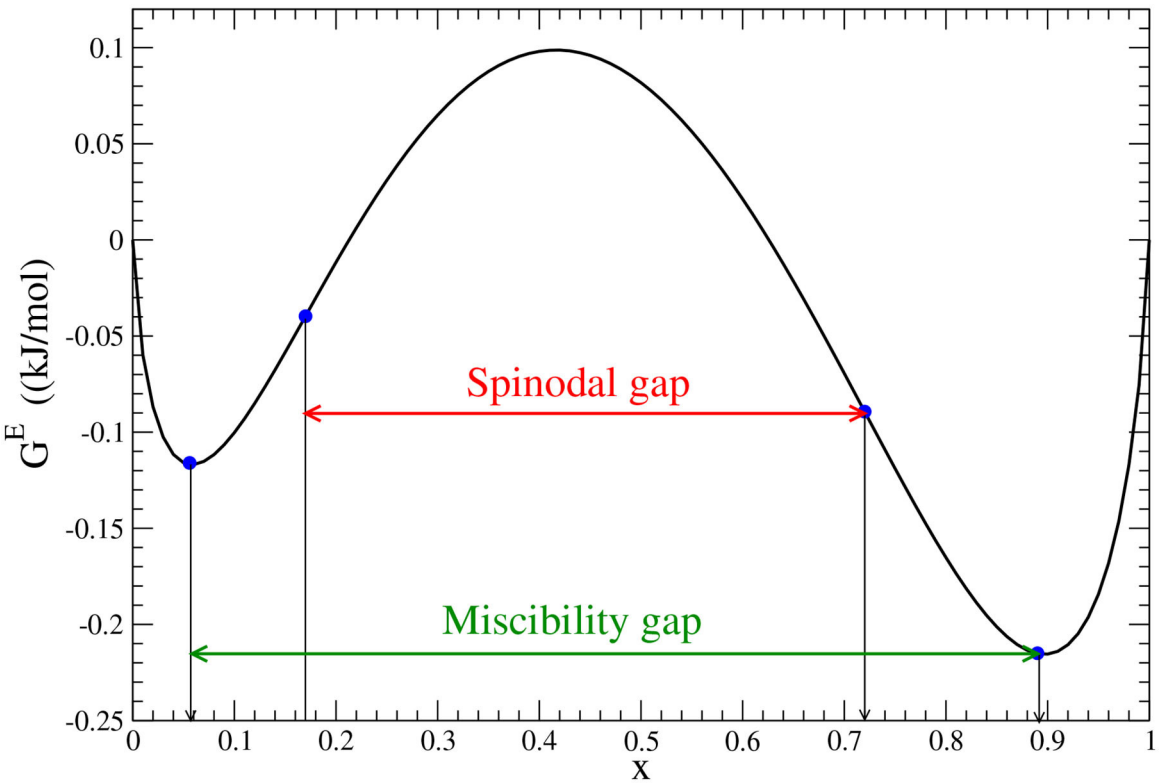

FIGURE 3 | The mixing free energy for Li_xFePO_4 solid solution computed at room temperature, T, as $G^E = [W_1(1-x) + W_2x]x(1-x) + RT[x\ln x + (1-x)\ln(1-x)]$ (Li et al., 2014), assuming configurational entropy of ideal mixing and neglecting other entropy contributions. R is the gas constant. W_1 and W_2 Margules interaction parameters are these from last column of **Table 5**. The miscibility and spinodal gaps are indicated by minima and inflection points marked with blue circles.

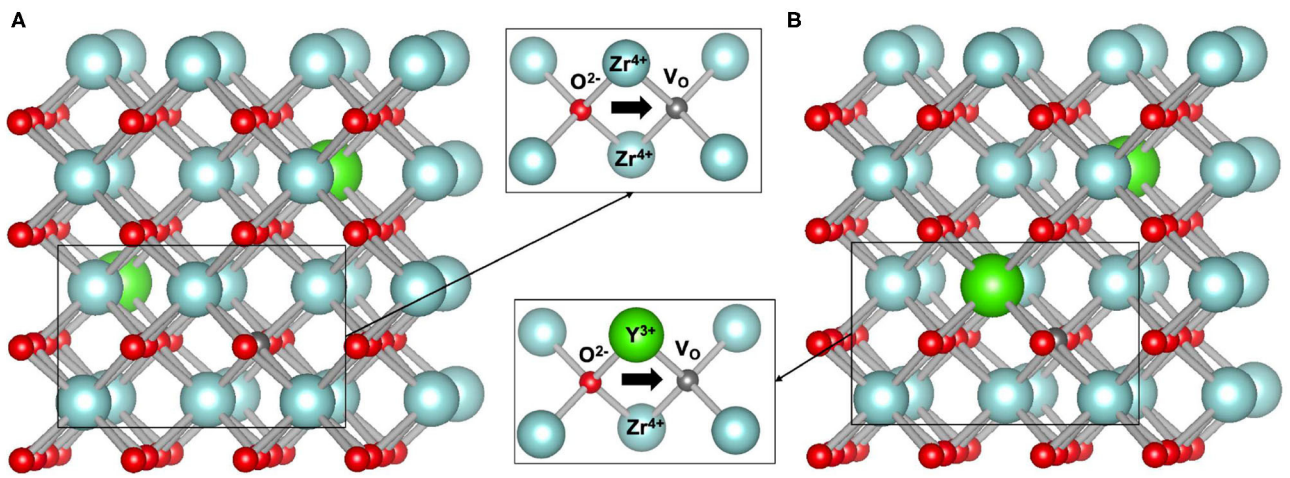

FIGURE 4 | The structure of yttria-stabilized zirconia ($YO_{1.5} - ZrO_2$ system) with indication of the oxygen diffusion mechanism along possible Zr-Zr **(A)** and Y-Zr **(B)** edges.

3.5. Ionic Conductivity

Because of high ionic conductivity, yttria-stabilized zirconia (see **Figure 4** for the structure) is commonly used as solid state electrolyte. Its ionic conduction properties have been investigated in many studies, including experimental (Strickler and Carlson, 1964, 1965; Ioffe et al., 1978; Li et al., 1994; Lee et al., 2001, 2003; Kilo et al., 2003; Zhang et al., 2007) as well as theoretical and atomistic modeling approaches (Kilo et al., 2003; Krishnamurthy

et al., 2005b; Sizov et al., 2014; Bukaemskiy et al., 2021). The conductivity is usually described using Arrhenius-type equation (Ioffe et al., 1978; Ahamer et al., 2017) and the ionic conductivity can be written in the following simple form:

$$\sigma T = \sigma_0 \exp\left(\frac{-E_a}{k_b T}\right) \quad (9)$$

TABLE 6 | The computed here and previously published data on E_a for ionic conductivity in Y-stabilized zirconia.

Compound	E_a (eV)	References
comp. Zr-Y edge	0.92	This study
comp. Zr-Zr edge	0.43	This study
comp. Zr-Y edge	1.29	Krishnamurthy et al., 2005b
comp. Zr-Zr edge	0.58	Krishnamurthy et al., 2005b
exp	0.99–1.02	Kilo et al., 2003
exp, two barriers	0.6; 1.1–1.2	Ahamer et al., 2017
exp	0.91–1.19	Gong et al., 2002
exp	0.89–1.09	Ikeda et al., 1985
exp	0.9–1.0	Lee et al., 2001
exp	0.93–1.15	Liu et al., 2016
exp	0.8–1.3	Strickler and Carlson, 1964
exp	0.85–1.14	Zhang et al., 2007

where σ_0 is the pre-exponential factor and E_a is the activation energy. In **Table 6**, we report the available experimental and computed data on E_a together with the results of our simulations. We note that molecular dynamics simulations could be also used for simulation of ionic diffusion, but for systems with activation barriers close to ∼1 eV such a method requires long simulation times (e.g., 10 ns as applied by Sizov et al., 2014). Such simulation times are beyond the capability of *ab initio* molecular dynamics methods (capable of simulations at ps time scales) and could be performed only with less accurate description of interatomic interactions by simple interatomic potentials, like in studies of Sizov et al. (2014).

The computed activation energy of 0.92 eV is well-consistent with the measured values as well as with some previous theoretical predictions. Here, following the studies of Ahamer et al. (2017) and Guan et al. (2020) we assume diffusion along Y-Zr edge as a diffusion rate determining step. Interestingly, the activation barrier for transition along Zr-Zr edge is twice smaller as the one for transition along Y-Zr edge, which is in line with previous findings (Krishnamurthy et al., 2005b). The diffusion paths along these two edges are depicted in **Figure 4**. In the performed simulations with Eu as dopant, the activation barrier is comparable (0.97 eV). This is consistent with previous studies showing similar effects of other trivalent cations on stabilization of cubic zirconia and its ionic

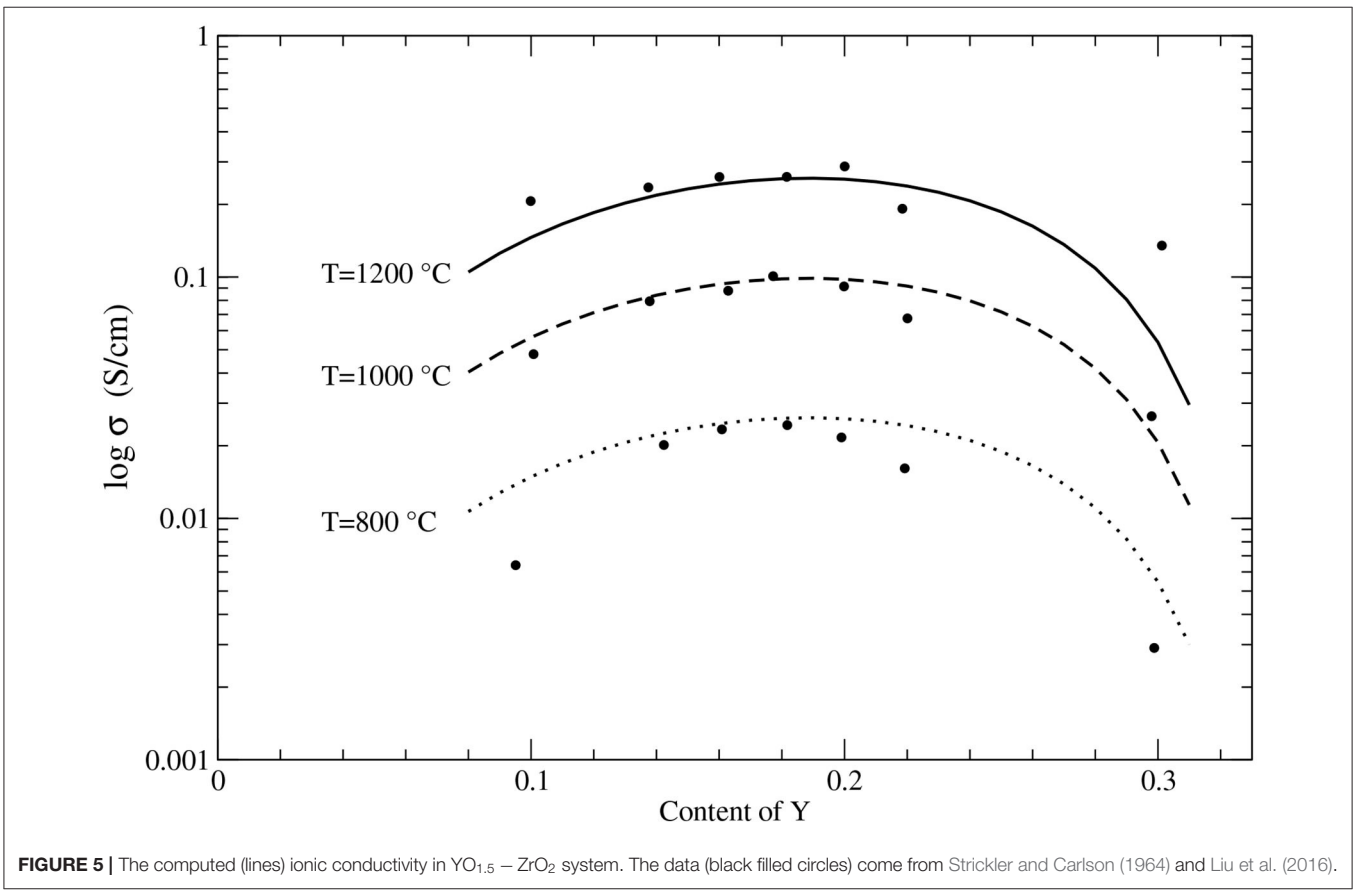

FIGURE 5 | The computed (lines) ionic conductivity in $YO_{1.5} - ZrO_2$ system. The data (black filled circles) come from Strickler and Carlson (1964) and Liu et al. (2016).

conductivity (Krishnamurthy et al., 2005a). With the derived activation barrier we also computed the attempt frequency, ν_0, using the transition state theory (Equation 2). We obtained value of $2.37 \cdot 10^{12}\ s^{-1}$. With the computed activation energy and the attempt frequency, using Equation (1) we derived temperature and Y-content dependent ionic conductivity. The results are plotted in **Figure 5** against the experimental data. Our model matches the measured values reasonably well, including temperature and Y content dependence. This is in great part due to inclusion of vacancy migration probability as estimated by Bukaemskiy et al. (2021) (see Equation 1). This shows that atomistic modeling and appropriate theoretical consideration can deliver accurate prediction for ionic conductivity in solid state electrolyte candidate materials. Nevertheless, as discussed by Ahamer et al. (2017) and Guan et al. (2020), the oxygen diffusion in yttria-stabilized zirconia is a complex process, which details, however, could be revealed by combination of computed and measured data.

4. CONCLUSIONS

In this contribution we presented an overview of our decade-long atomistic modeling contribution to the research on orthophosphates and zirconates type ceramics. We discussed the atomistic modeling derivation of structural, thermodynamic, and diffusion properties that are of importance for application of these materials as compounds in energy storage devices. In particular, we discussed the importance of the application of parameter free DFT+*U* approach and selection of realistic projector functions for counting the occupations of strongly correlated *d* and *f* orbitals for the Hubbard model-based DFT+*U* scheme. Only with this approach we were able to correctly reproduce the measured formation enthalpies of $FePO_4$ and $LiFePO_4$ phases. The consideration of the thermodynamic properties of Li_xFePO_4 solid solutions indicates a system with a wide miscibility gap, which values and slight asymmetry are qualitatively consistent with the existing experimental data. Based on the measured solubility data we derived set of Margules interaction parameters that describe this solid solution. The resulting excess free energy of mixing shows wide miscibility and spinodal gaps at room temperature. We also discussed our studies of zirconium-based ceramics. In particular, we derived the stability diagram of yttrium-doped zirconia, showing that it stabilizes in cubic phase at Y content of ∼8%, well in line with the experimental measurements. The computed formation enthalpies along $YO_{1.5} - ZrO_2$ solid solution are also well consistent with the measured data. With the computation of transition state and application of vacancy distribution model we were able to derive activation energies and temperature-dependent ionic conductivities for oxygen diffusion in this material, that are well-consistent with the measured data. This shows the power of carefully set up atomistic modeling for computation of various properties of ceramic materials as compounds for energy storage devices.

We discussed various successfully studies of application of atomistic modeling to prediction of a set of physical and chemical properties of orthophosphates and zirconates. In most cases, the best results have been obtained by a joint computational and experimental approach, or at least by extensive testing and comparison to the available experimental data. Application of a reliable, state-of-the-art *ab initio* approach is also a crucial factor contributing to this success. With the steady increase in the availability of computational power we expect that atomistic modeling research will be applied to tackle even more complex problems, such as kinetically driven dissolution or corrosion processes, and for effective screening of materials for energy applications.

DATA AVAILABILITY STATEMENT

The original contributions presented in the study are included in the article/supplementary material, further inquiries can be directed to the corresponding author/s.

AUTHOR CONTRIBUTIONS

PK, ZH, and OC contributed equally to computing the data. PK performed collective analysis of the data and editing of the manuscript. All authors contributed to the article and approved the submitted version.

ACKNOWLEDGMENTS

The authors gratefully acknowledge the computing time granted by the JARA Vergabegremium and provided on the JARA Partition part of the supercomputers JURECA at Forschungszentrum Jülich and CLAIX at RWTH Aachen University.

REFERENCES

Ahamer, C., Opitz, A. K., Rupp, G. M., and Fleig, J. (2017). Revisiting the temperature dependent ionic conductivity of yttria stabilized zirconia (YSZ). *J. Electrochem. Soc.* 164, F790–F803. doi: 10.1149/2.0641707jes

Ali, K., Arya, A., Ghosh, P. S., and Dey, G. K. (2016). A first principle study of the pressure dependent elastic properties of monazite $LaPO_4$. *AIP Conf. Proc.* 1728:020090. doi: 10.1063/1.4946141

Andrehs, G., and Heinrich, W. (1998). Experimental determination of REE distributions between monazite and xenotime: potential for temperature-calibrated geochronology. *Chem. Geol.* 149, 83–96. doi: 10.1016/S0009-2541(98)00039-4

Anithakumari, P., Grover, V., Nandi, C., Bhattacharyya, K., and Tyagi, A. K. (2016). Utilizing non-stoichiometry in $Nd_2Zr_2O_7$ pyrochlore: exploring superior ionic conductors. *RSC Adv.* 6, 97566–97579. doi: 10.1039/C6RA08722A

Beridze, G., Birnie, A., Koniski, S., Ji, Y., and Kowalski, P. M. (2016). DFT+U as a reliable method for efficient ab initio calculations of nuclear materials. *Prog. Nucl. Energ.* 92, 142–146. doi: 10.1016/j.pnucene.2016.07.012

Beridze, G., and Kowalski, P. M. (2014). Benchmarking the DFT+U method for thermochemical calculations of uranium molecular compounds and solids. *J. Phys. Chem. A* 118, 11797–11810. doi: 10.1021/jp5101126

Blanca-Romero, A., Kowalski, P. M., Beridze, G., Schlenz, H., and Bosbach, D. (2014). Performance of DFT+U method for prediction of structural and

thermodynamic parameters of monazite-type ceramics. *J. Comput. Chem*. 35, 1339–1346. doi: 10.1002/jcc.23618

Bukaemskiy, A. A., Vinograd, V. L., and Kowalski, P. M. (2021). Ion distribution models for defect fluorite ZrO_2-$AO_1.5$ (A=Ln, Y) solid solutions: I. Relationship between lattice parameter and composition. *Acta Mater*. 202, 99–111. doi: 10.1016/j.actamat.2020.10.045

Cerdas, F., Titscher, P., Bognar, N., Schmuch, R., Winter, M., Kwade, A., et al. (2018). Exploring the effect of increased energy density on the environmental impacts of traction aatteries: a comparison of energy optimized lithium-ion and lithium-sulfur batteries for mobility applications. *Energies* 11:150. doi: 10.3390/en11010150

Chroneos, A., Rushton, M., Jiang, C., and Tsoukalas, L. (2013). Nuclear wasteform materials: atomistic simulation case studies. *J. Nucl. Mater*. 441, 29–39. doi: 10.1016/j.jnucmat.2013.05.012

Cococcioni, M., and de Gironcoli, S. (2005). Linear response approach to the calculation of the effective interaction parameters in the LDA+U method. *Phys. Rev. B* 71:035105. doi: 10.1103/PhysRevB.71.035105

Diazguillen, J., Diazguillen, M., Padmasree, K., Fuentes, A., Santamaria, J., and Leon, C. (2008). High ionic conductivity in the pyrochlore-type $Gd_2 - yLa_yZr_2O_7$ solid solution ($0 \leq y \leq 1$). *Solid State Ion*. 179, 2160–2164. doi: 10.1016/j.ssi.2008.07.015

Dong, H., Guo, H., He, Y., Gao, J., Han, W., Lu, X., et al. (2017). Structural stability and Li-ion transport property of $LiFePO_4$ under high-pressure. *Solid State Ion*. 301, 133–137. doi: 10.1016/j.ssi.2017.01.026

Drey, D. L., O'Quinn, E. C., Subramani, T., Lilova, K., Baldinozzi, G., Gussev, I. M., et al. (2020). Disorder in $Ho_2Ti_{2-x}Zr_xO_7$: pyrochlore to defect fluorite solid solution series. *RSC Adv*. 10, 34632–34650. doi: 10.1039/D0RA07118H

Dunn, J. B., Gaines, L., Kelly, J. C., James, C., and Gallagher, K. G. (2015). The significance of li-ion batteries in electric vehicle life-cycle energy and emissions and recycling's role in its reduction. *Energy Environ. Sci*. 8, 158–168. doi: 10.1039/C4EE03029J

Eremin, N. N., Marchenko, E. I., Petrov, V. G., Mitrofanov, A. A., and Ulanova, A. S. (2019). Solid solutions of monazites and xenotimes of lanthanides and plutonium: atomistic model of crystal structures, point defects and mixing properties. *Comput. Mater. Sci*. 157, 43–50. doi: 10.1016/j.commatsci.2018.10.025

Ewing, R., and Wang, L. (2002). Phosphates as nuclear waste forms. *Rev. Mineral. Geochem*. 48, 673–699. doi: 10.2138/rmg.2002.48.18

Feng, J., Xiao, B., Zhou, R., and Pan, W. (2013). Anisotropy in elasticity and thermal conductivity of monazite-type $REPO_4$ (RE=La, Ce, Nd, Sm, Eu and Gd) from first-principles calculations. *Acta Mater*. 61, 7364–7383. doi: 10.1016/j.actamat.2013.08.043

Finger, L. W., and Hazen, R. M. (1980). Crystal structure and isothermal compression of Fe_2O_3, Cr_2O_3, and V_2O_3 to 50 kbars. *J. Appl. Phys*. 51, 5362–5367. doi: 10.1063/1.327451

Finkeldei, S., Kegler, P., Kowalski, P., Schreinemachers, C., Brandt, F., Bukaemskiy, A., et al. (2017). Composition dependent order-disorder transition in $Nd_xZr_1 - xO_2 - 0.5x$ pyrochlores: a combined structural, calorimetric and *ab initio* modeling study. *Acta Mater*. 125, 166–176. doi: 10.1016/j.actamat.2016.11.059

Finkeldei, S., Stennett, M. C., Kowalski, P. M., Ji, Y., de Visser-Týnová, E., Hyatt, N. C., et al. (2020). Insights into the fabrication and structure of plutonium pyrochlores. *J. Mater. Chem. A* 8, 2387–2403. doi: 10.1039/C9TA05795A

García-Moreno, O., Alvarez-Vega, M., García-Jaca, J., Gallardo-Amores, J. M., Sanjuán, M. L., and Amador, U. Influence of the structure on the electrochemical performance of lithium transition metal phosphates as cathodic materials in rechargeable lithium batteries: A new high-pressure form of $LiMPO_4$ (M = Fe and Ni). *Chem. Mater*. (2001) 13, 1570–1576. doi: 10.1021/cm000596p

Giannozzi, P., Baroni, S., Bonini, N., Calandra, M., Car, R., Cavazzoni, C., et al. (2009). Quantum espresso: a modular and open-source software project for quantum simulations of materials. *J. Phys*. 21:395502. doi: 10.1088/0953-8984/21/39/395502

Gomis, O., Lavina, B., Rodríguez-Hernández, P., Muñoz, A., Errandonea, R., Errandonea, D., et al. (2017). High-pressure structural, elastic, and thermodynamic properties of zircon-type $HoPO_4$ and $TmPO_4$. *J. Phys*. 29:095401. doi: 10.1088/1361-648X/aa516a

Gong, J., Li, Y., Tang, Z., Xie, Y., and Zhang, Z. (2002). Temperature-dependence of the lattice conductivity of mixed calcia/Yttria-stabilized zirconia. *Mater. Chem. Phys*. 76, 212–216. doi: 10.1016/S0254-0584(01)00522-3

Götsch, T., Wallisch, W., Stöger-Pollach, M., Klötzer, B., and Penner, S. (2016). From zirconia to Yttria: sampling the YSZ phase diagram using sputter-deposited thin films. *AIP Adv*. 6:025119. doi: 10.1063/1.4942818

Guan, S.-H., Zhang, K.-X., Shang, C., and Liu, Z.-P. (2020). Stability and anion diffusion kinetics of Yttria-stabilized zirconia resolved from machine learning global potential energy surface exploration. *J. Chem. Phys*. 152:094703. doi: 10.1063/1.5142591

Hirsch, A., Kegler, P., Alencar, I., Ruiz-Fuertes, J., Shelyug, A., Peters, L., et al. (2017). Structural, vibrational, and thermochemical properties of the monazite-type solid solution $La_1 - xPr_xO_4$. *J. Solid State Chem*. 245, 82–88. doi: 10.1016/j.jssc.2016.09.032

Huittinen, N., Arinicheva, Y., Kowalski, P., Vinograd, V., Neumeier, S., and Bosbach, D. (2017). Probing structural homogeneity of $La_1 - xGd_xPO_4$ monazite-type solid solutions by combined spectroscopic and computational studies. *J. Nucl. Mater*. 486, 148–157. doi: 10.1016/j.jnucmat.2017.01.024

Huittinen, N., Scheinost, A. C., Ji, Y., Kowalski, P. M., Arinicheva, Y., Wilden, A., et al. (2018). A spectroscopic and computational study of Cm^3+ Incorporation in lanthanide phosphate rhabdophane ($LnPO_4 \cdot 0.67H_2O$) and monazite ($LnPO_4$). *Inorg. Chem*. 57, 6252–6265. doi: 10.1021/acs.inorgchem.8b00095

Ikeda, S., Sakurai, O., Uematsu, K., Mizutani, N., and Kato, M. (1985). Electrical-conductivity of yttria-stabilized zirconia single-crystals. *J. Mater. Sci*. 20, 4593–4600. doi: 10.1007/BF00559349

Ioffe, A., Rutman, D., and Karpachov, S. (1978). On the nature of the conductivity maximum in zirconia-based solid electrolytes. *Electrochim. Acta* 23, 141–142. doi: 10.1016/0013-4686(78)80110-8

Iyer, R. G., Delacourt, C., Masquelier, C., Tarascon, J.-M., and Navrotsky, A. (2006). Energetics of $LiFePO_4$ and polymorphs of its delithiated form, $FePO_4$. *Electrochem. Solid-State Lett*. 9, A46–A48. doi: 10.1149/1.2140496

Jahn, S., and Kowalski, P. M. (2014). Theoretical approaches to structure and spectroscopy of earth materials. *Rev. Mineral. Geochem*. 78:691. doi: 10.2138/rmg.2014.78.17

Ji, Y., Beridze, G., Bosbach, D., and Kowalski, P. M. (2017a). Heat capacities of xenotime-type ceramics: an accurate *ab initio* prediction. *J. Nucl. Mater*. 494, 172–181. doi: 10.1016/j.jnucmat.2017.07.026

Ji, Y., Beridze, G., Li, Y., and Kowalski, P. M. (2017b). Large scale simulation of nuclear waste materials. *Energy Proc*. 127, 416–424. doi: 10.1016/j.egypro.2017.08.108

Ji, Y., Kowalski, P. M., Kegler, P., Huittinen, N., Marks, N. A., Vinograd, V. L., et al. (2019a). Rare-earth orthophosphates from atomistic simulations. *Front. Chem*. 7:197. doi: 10.3389/fchem.2019.00197

Ji, Y., Kowalski, P. M., Neumeier, S., Deissmann, G., Kulriya, P. K., and Gale, J. D. (2017c). Atomistic modeling and experimental studies of radiation damage in monazite-type $LaPO_4$ ceramics. *Nucl. Instrum. Methods Phys. Res. Sect. B* 393, 54–58. doi: 10.1016/j.nimb.2016.09.031

Ji, Y., Marks, N. A., Bosbach, D., and Kowalski, P. M. (2019b). Elastic and thermal parameters of lanthanide-orthophosphate ($LnPO_4$) ceramics from atomistic simulations. *J. Eur. Ceram*. 39, 4264–4274. doi: 10.1016/j.jeurceramsoc.2019.05.038

Jin, B., Qin Zhang, R., and Jiang, Q. (2013). Electronic and atomic structures of $LiMPO_4$ (M= Fe, $Fe_1/4Mn_1/4Co_1/4Ni_1/4$): a DFT study. *Adv. Electrochem*. 1, 22–26. doi: 10.1166/adel.2013.1005

Jolley, K., Asuvathraman, R., and Smith, R. (2017). Inter-atomic potentials for radiation damage studies in $CePO_4$ monazite. *Nucl. Instrum. Methods Phys. Res. B* 393, 93–96. doi: 10.1016/j.nimb.2016.10.016

Kick, M., Reuter, K., and Oberhofer, H. (2019). Intricacies of DFT+U, not only in a numeric atom centered orbital framework. *J. Chem. Theory Comput*. 15, 1705–1718. doi: 10.1021/acs.jctc.8b01211

Kilo, M., Argirusis, C., Borchardt, G., and Jackson, R. A. (2003). Oxygen diffusion in yttria stabilised zirconia-experimental results and molecular dynamics calculations. *Phys. Chem. Chem. Phys*. 5, 2219–2224. doi: 10.1039/B300151M

Kowalski, P. M. (2020). Formation enthalpy of $Ln_2B_2O_7$-type (B=Ti,Sn,Hf,Zr) compounds. *Scr. Mater*. 189, 7–10. doi: 10.1016/j.scriptamat.2020.07.048

Kowalski, P. M., Beridze, G., Ji, Y., and Li, Y. (2017a). Towards reliable modeling of challenging f electrons bearing materials: experience from modeling of nuclear materials. *MRS Adv*. 2, 491–497. doi: 10.1557/adv.2017.46

Kowalski, P. M., Beridze, G., Li, Y., Ji, Y., Friedrich, C., Sasioglu, E., et al. (2016). Feasible and reliable *ab initio* approach to computation of materials relevant for nuclear waste management. *Ceram. Trans.* 258, 205–217. doi: 10.1002/9781119236016.ch21

Kowalski, P. M., Beridze, G., Vinograd, V. L., and Bosbach, D. (2015). Heat capacities of lanthanide and actinide monazite-type ceramics. *J. Nucl. Mater.* 464, 147–154. doi: 10.1016/j.jnucmat.2015.04.032

Kowalski, P. M., Ji, Y., Li, Y., Arinicheva, Y., Beridze, G., Neumeier, S., et al. (2017b). Simulation of ceramic materials relevant for nuclear waste management: case of $La_1 - xEu_xPO_4$ solid solution. *Nucl. Instrum. Methods Phys. Res. Sect. B* 393, 68–72. doi: 10.1016/j.nimb.2016.09.029

Kowalski, P. M., and Li, Y. (2016). Relationship between the thermodynamic excess properties of mixing and the elastic moduli in the monazite-type ceramics. *J. Eur. Ceram. Soc.* 36, 2093–2096. doi: 10.1016/j.jeurceramsoc.2016.01.051

Krishnamurthy, R., Srolovitz, D. J., Kudin, K. N., and Car, R. (2005a). Effects of lanthanide dopants on oxygen diffusion in Yttria-stabilized zirconia. *J. Am. Ceram.* 88, 2143–2151. doi: 10.1111/j.1551-2916.2005.00353.x

Krishnamurthy, R., Yoon, Y.-G., Srolovitz, D. J., and Car, R. (2005b). Oxygen diffusion in yttria-stabilized zirconia: a new simulation model. *J. Am. Ceram.* 87, 1821–1830. doi: 10.1111/j.1151-2916.2004.tb06325.x

Krogstad, J. A., Lepple, M., Gao, Y., Lipkin, D. M., and Levi, C. G. (2011). Effect of yttria content on the zirconia unit cell parameters. *J. Am. Ceram.* 94, 4548–4555. doi: 10.1111/j.1551-2916.2011.04862.x

Kvashnina, K. O., Kowalski, P. M., Butorin, S. M., Leinders, G., Pakarinen, J., Bès, R., et al. (2018). Trends in the valence band electronic structures of mixed uranium oxides. *Chem. Commun.* 54, 9757–9760. doi: 10.1039/C8CC05464A

Lee, J.-H., Yoon, S., Kim, B.-K., Kim, J., Lee, H.-W., and Song, H.-S. (2001). Electrical conductivity and defect structure of yttria-doped ceria-stabilized zirconia. *Solid State Ion.* 144, 175–184. doi: 10.1016/S0167-2738(01)00903-1

Lee, K., Youn, Y., and Han, S. (2017). Identification of ground-state spin ordering in antiferromagnetic transition metal oxides using the Ising model and a genetic algorithm. *Sci. Technol. Adv. Mater* 18, 246–252. doi: 10.1080/14686996.2017.1300046

Lee, T. A., Navrotsky, A., and Molodetsky, I. (2003). Enthalpy of formation of cubic yttria-stabilized zirconia. *J. Mater. Res.* 18, 908–918. doi: 10.1557/JMR.2003.0125

Li, P., Chen, I.-W., and Penner-Hahn, J. E. (1994). Effect of dopants on zirconia stabilization - an x-ray absorption study: I, trivalent dopants. *J. Am. Ceram.* 77, 118–128. doi: 10.1111/j.1151-2916.1994.tb06964.x

Li, Y., and Kowalski, P. M. (2018). Energetics of defects formation and oxygen migration in pyrochlore compounds from first principles calculations. *J. Nucl. Mater.* 505, 255–261. doi: 10.1016/j.jnucmat.2017.11.005

Li, Y., Kowalski, P. M., Beridze, G., Birnie, A. R., Finkeldei, S., and Bosbach, D. (2015). Defect formation energies in $A_2B_2O_7$ pyrochlores. *Scr. Mater.* 107, 18–21. doi: 10.1016/j.scriptamat.2015.05.010

Li, Y., Kowalski, P. M., Beridze, G., Blanca-Romero, A., Ji, Y., Vinograd, V. L., et al. (2016). Atomistic simulations of ceramic materials relevant for nuclear waste management: cases of monazite and pyrochlore. *Ceram. Trans.* 255:165. doi: 10.1002/9781119234531.ch15

Li, Y., Kowalski, P. M., Blanca-Romero, A., Vinograd, V., and Bosbach, D. (2014). Ab initio calculation of excess properties of solid solutions. *J. Solid State Chem.* 220, 137–141. doi: 10.1016/j.jssc.2014.08.005

Li, Z., Yang, J., Li, C., Wang, S., Zhang, L., Zhu, K., et al. (2018). Orientation-dependent lithium miscibility gap in $LiFePO_4$. *Chem. Mater.* 30, 874–878. doi: 10.1021/acs.chemmater.7b04463

Liu, T., Zhang, X., Wang, X., Yu, J., and Li, L. (2016). A review of zirconia-based solid electrolytes. *Ionics* 22, 2249–2262. doi: 10.1007/s11581-016-1880-1

López-Solano, J., Rodríguez-Hernández, P., Munoz, A., Gomis, O., Santamaría-Perez, D., Errandonea, D., et al. (2010). Theoretical and experimental study of the structural stability of $TbPO_4$ at high pressures. *Phys. Rev. B* 81:144126. doi: 10.1103/PhysRevB.81.144126

Mandal, B., Deshpande, S., and Tyagi, A. (2008). Ionic conductivity enhancement in $Gd_2Zr_2O_7$ pyrochlore by Nd doping. *J. Mater. Res.* 23, 911–916. doi: 10.1557/jmr.2008.0112

Maxisch, T., and Ceder, G. (2006). Elastic properties of olivine Li_xFePO_4 from first principles. *Phys. Rev. B* 73:174112. doi: 10.1103/PhysRevB.73.174112

Meethong, N., Huang, H.-Y. S., Carter, W. C., and Chiang, Y.-M. (2007). Size-dependent lithium miscibility gap in nanoscale $Li_1 - xFePO_4$. *Electrochem. Solid-State Lett.* 10:A134. doi: 10.1149/1.2710960

Mogilevsky, P. (2007). On the miscibility gap in monazite-xenotime systems. *Phys. Chem. Miner.* 34, 201–214. doi: 10.1007/s00269-006-0139-1

Moynihan, C. T., Gavin, D. L., and Syed, R. (1982). Pre-exponential term in the arrhenius equation for electrical conductivity of glass. *J. Phys. Colloq.* 43, C9-395–C9-398. doi: 10.1051/jphyscol:1982975

Murphy, G. L., Zhang, Z., Tesch, R., Kowalski, P. M., Avdeev, M., Kuo, E. Y., et al. (2021). Tilting and distortion in rutile-related mixed metal ternary uranium oxides: a structural, spectroscopic, and theoretical investigation. *Inorgan. Chem.* 60, 2246–2260. doi: 10.1021/acs.inorgchem.0c03077

Neumeier, S., Arinicheva, Y., Ji, Y., Heuser, J. M., Kowalski, P. M., Kegler, P., et al. (2017a). New insights into phosphate based materials for the immobilisation of actinides. *Radiochim. Acta* 105, 961–984. doi: 10.1515/ract-2017-2819

Neumeier, S., Kegler, P., Arinicheva, Y., Shelyug, A., Kowalski, P. M., Schreinemachers, C., et al. (2017b). Thermochemistry of $La_1 - xLn_xPO_4$ monazites (Ln=Gd, Eu). *J. Chem. Thermodyn.* 105, 396–403. doi: 10.1016/j.jct.2016.11.003

Padhi, A. K., Nanjundaswamy, K. S., and Goodenough, J. B. (1997). Phospho-olivines as positive-electrode materials for rechargeable lithium batteries. *J. Electrochem. Soc.* 144:1188. Available online at: https://iopscience.iop.org/article/10.1149/1.1837571

Perdew, J. P., Ruzsinszky, A., Csonka, G. I., Vydrov, O. A., Scuseria, G. E., Constantin, L. A., et al. (2008). Restoring the density-gradient expansion for exchange in solids and surfaces. *Phys. Rev. Lett.* 100:136406. doi: 10.1103/PhysRevLett.100.136406

Phan, A. T., Gheribi, A. E., and Chartrand, P. (2019). Modelling of phase equilibria of LiFePO4 − $FePO_4$ olivine join for cathode material. *Can. J. Chem.* 97, 2224–2233. doi: 10.1002/cjce.23416

Ploc, R. A. (1981). The lattice parameter of cubic ZrO_2 formed on zirconium. *J. Nucl. Mater.* 99, 124–128. doi: 10.1016/0022-3115(81)90146-X

Pomfret, M. B., Stoltz, C., Varughese, B., and Walker, R. A. (2005). Structural and compositional characterization of yttria-stabilized zirconia: evidence of surface-stabilized, low-valence metal species. *Anal. Chem.* 77, 1791–1795. doi: 10.1021/ac048600u

Popa, K., Konings, R. J. M., and Geisler, T. (2007). High-temperature calorimetry of $(La_1 - xLn_x)PO_4$ solid solutions. *J. Chem. Thermodyn.* 39, 236–239. doi: 10.1016/j.jct.2006.07.010

Prieto, M. (2009). Thermodynamics of solid solution-aqueous solution systems. *Rev. Mineral. Geochem.* 70, 47–85. doi: 10.2138/rmg.2009.70.2

Prosini, P. P., Lisi, M., Zane, D., and Pasquali, M. (2002). Determination of the chemical diffusion coefficient of lithium in $LiFePO_4$. *Solid State Ion.* 148, 45–51. doi: 10.1016/S0167-2738(02)00134-0

Rustad, J. R. (2012). Density functional calculations of the enthalpies of formation of rare-earth orthophosphates. *Am. Mineral.* 97:791. doi: 10.2138/am.2012.3948

Schlenz, H., Peters, L., Roth, G., Hirsch, A., and Neumeier, S. (2018). *9. Phosphates as Safe Containers for Radionuclides.* Technical report, Nukleare Entsorgung und Reaktorsicherheit.

Shamblin, J., Feygenson, M., Neuefeind, J., Tracy, C., Zhang, F., Finkeldei, S., et al. (2016). Probing disorder in isometric pyrochlore and related complex oxides. *Nat. Mater.* 15, 507–511. doi: 10.1038/nmat4581

Shein, I. R., and Shalaeva, E. V. (2016). Pressure-induced zircon to monazite phase transition in $Y_1 - xLa_xPO_4$: first-principles calculations. *J. Struct. Chem.* 57, 1513–1518. doi: 10.1134/S0022476616080047

Sizov, V. V., Lampinen, M. J., and Laaksonen, A. (2014). Molecular dynamics simulation of oxygen diffusion in cubic yttria-stabilized zirconia: effects of temperature and composition. *Solid State Ionics* 266, 29–35. doi: 10.1016/j.ssi.2014.08.003

Stavrou, E., Tatsi, A., Raptis, C., Efthimiopoulos, I., Syassen, K., Mu noz, A., et al. (2012). Effects of pressure on the structure and lattice dynamics of $TmPO_4$: experiments and calculations. *Phys. Rev. B* 85:024117. doi: 10.1103/PhysRevB.85.024117

Stevens, R., Dodd, J. L., Kresch, M. G., Yazami, R., Fultz, B., Ellis, B., et al. (2006). Phonons and thermodynamics of unmixed and disordered Li0.6FePO4. *J. Phys. Chem. B* 110, 22732–22735. doi: 10.1021/jp063831l

Strickler, D. W., and Carlson, W. G. (1964). Ionic conductivity of cubic solid solutions in the system $CaO|Y_2O_3|ZrO_2$. *J. Am. Ceram.* 47, 122–127. doi: 10.1111/j.1151-2916.1964.tb14368.x

Strickler, D. W., and Carlson, W. G. (1965). Electrical conductivity in the ZrO_2-rich region of several $M_2O_3 - ZrO_2$ Systems. *J. Am. Ceram.* 48, 286–289. doi: 10.1111/j.1151-2916.1965.tb14742.x

Sun, M., Stackhouse, J., and Kowalski, P. (2020). The +2 oxidation state of cr incorporated into the crystal lattice of UO_2. *Commun. Mater.* 1:13. doi: 10.1038/s43246-020-0014-5

Tang, P., and Holzwarth, N. (2003). Electronic structure of $FePO_4$, $LiFePO_4$, and related materials. *Phys. Rev. B* 68:165107. doi: 10.1103/PhysRevB.68.165107

Ushakov, S., Helean, K., and Navrotsky, A. (2001). Thermochemistry of rare-earth orthophosphates. *J. Mater. Res.* 16:2623. doi: 10.1557/JMR.2001.0361

Vanderbilt, D. (1990). Soft self-consistent pseudopotentials in a generalized eigenvalue formalism. *Phys. Rev. B* 41:7892. doi: 10.1103/PhysRevB.41.7892

Wang, J., Zhou, Y., and Lin, Z. (2005). First-principles elastic stiffness of $LaPO_4$ monazite. *Appl. Phys. Lett.* 87:051902. doi: 10.1063/1.2005392

Whittingham, M. S., Song, Y., Lutta, S., Zavalij, P. Y., and Chernova, N. A. (2005). Some transition metal (oxy) phosphates and vanadium oxides for lithium batteries. *J. Mater. Chem.* 15, 3362–3379. doi: 10.1039/b501961c

Williams, M. L., Jercinovic, M. J., and Hetherington, C. J. (2007). Microprobe monazite geochronology: understanding geologic processes by integrating composition and chronology. *Annu. Rev. Earth Planet. Sci.* 35, 137–175. doi: 10.1146/annurev.earth.35.031306.140228

Wu, X., Kang, F., Duan, W., and Li, J. (2019). Density functional theory calculations: a powerful tool to simulate and design high-performance energy storage and conversion materials. *Proc. Nat. Sci. Mater.* 29, 247–255. doi: 10.1016/j.pnsc.2019.04.003

Wuensch, B. (2000). Connection between oxygen-ion conductivity of pyrochlore fuel-cell materials and structural change with composition and temperature. *Solid State Ion* 129, 111–133. doi: 10.1016/S0167-2738(99)00320-3

Xia, X.-L., Ouyang, J.-H., and Liu, Z.-G. (2010). Electrical properties of gadolinium-europium zirconate eramics. *J. Am. Ceram.* 93, 1074–1080. doi: 10.1111/j.1551-2916.2009.03505.x

Yamada, A., Koizumi, H., Nishimura, S.-I., Sonoyama, N., Kanno, R., Yonemura, M., et al. (2006). Room-temperature miscibility gap in Li_xFePO_4. *Nat. Mater.* 5, 357–360. doi: 10.1038/nmat1634

Yamamura, H. (2003). Electrical conductivity anomaly around fluorite-pyrochlore phase boundary. *Solid State Ion.* 158, 359–365. doi: 10.1016/S0167-2738(02)00874-3

Zakaria, Z., Abu Hassan, S. H., Shaari, N., Yahaya, A. Z., and Boon Kar, Y. (2020). A review on recent status and challenges of yttria stabilized zirconia modification to lowering the temperature of solid oxide fuel cells operation. *Int. J. Energy Res.* 44, 631–650. doi: 10.1002/er.4944

Zhang, C., Li, C.-J., Zhang, G., Ning, X.-J., Li, C.-X., Liao, H., et al. (2007). Ionic conductivity and its temperature dependence of atmospheric plasma-sprayed yttria stabilized zirconia electrolyte. *Mater. Sci. Eng. B* 137, 24–30. doi: 10.1016/j.mseb.2006.10.005

Zhao, X., and Vanderbilt, D. (2002). Phonons and lattice dielectric properties of zirconia. *Phys. Rev. B* 65:075105. doi: 10.1103/PhysRevB.65.075105

Zhou, F., Maxisch, T., and Ceder, G. (2006). Configurational electronic entropy and the phase diagram of mixed-valence oxides: the case of Li_xFePO_4. *Phys. Rev. Lett.* 97:155704. doi: 10.1103/PhysRevLett.97.155704

Zhu, Y.-M., Ruan, Z.-W., Tang, S.-Z., and Thangadurai, V. (2014). Research status in preparation of $FePO_4$: a review. *Ionics* 20, 1501–1510. doi: 10.1007/s11581-014-1241-x

Conflict of Interest: The authors declare that the research was conducted in the absence of any commercial or financial relationships that could be construed as a potential conflict of interest.

frontiers in Energy Research

ORIGINAL RESEARCH
published: 13 April 2021
doi: 10.3389/fenrg.2021.609070

A Data-Driven Framework for the Accelerated Discovery of CO_2 Reduction Electrocatalysts

*Ali Malek[1], Qianpu Wang[1], Stefan Baumann[2], Olivier Guillon[2,3], Michael Eikerling[3,4,5] and Kourosh Malek[1,4]**

[1]NRC Energy, Mining and Environment(EME), Vancouver, BC, Canada, [2]Institute of Energy and Climate Research, IEK-1: Materials Synthesis and Processing, Forschungszentrum Jülich, Jülich, Germany, [3]Jülich Aachen Research Alliance: JARA-Energy, Jülich, Germany, [4]Institute of Energy and Climate Research, IEK-13: Theory and Computation of Energy Materials, Forschungszentrum Jülich, Jülich, Germany, [5]Chair of Theory and Computation of Energy Materials, Division of Materials Science and Engineering, RWTH Aachen University, Aachen, Germany

Searching for next-generation electrocatalyst materials for electrochemical energy technologies is a time-consuming and expensive process, even if it is enabled by high-throughput experimentation and extensive first-principle calculations. In particular, the development of more active, selective and stable electrocatalysts for the CO_2 reduction reaction remains tedious and challenging. Here, we introduce a material recommendation and screening framework, and demonstrate its capabilities for certain classes of electrocatalyst materials for low or high-temperature CO_2 reduction. The framework utilizes high-level technical targets, advanced data extraction, and categorization paths, and it recommends the most viable materials identified using data analytics and property-matching algorithms. Results reveal relevant correlations that govern catalyst performance under low and high-temperature conditions.

Keywords: CO_2 reduction, high and low temperature, machine learning, artificial intelligence, materials discovery, data analytics, classification

OPEN ACCESS

Edited by:
Kai S. Exner,
Sofia University, Bulgaria

Reviewed by:
Guangfeng Wei,
Tongji University, China
Venkatasubramanian Viswanathan,
Carnegie Mellon University,
United States

****Correspondence:***
Kourosh Malek
koroush.malek@nrc-cnrc.gc.ca

Specialty section:
This article was submitted to Electrochemical Energy Conversion and Storage, a section of the journal Frontiers in Energy Research

Received: *22 September 2020*
Accepted: *29 January 2021*
Published: *13 April 2021*

Citation:
Malek A, Wang Q, Baumann S, Guillon O, Eikerling M and Malek K (2021) A Data-Driven Framework for the Accelerated Discovery of CO_2 Reduction Electrocatalysts. Front. Energy Res. 9:609070. doi: 10.3389/fenrg.2021.609070

INTRODUCTION

CO_2 emissions are the main cause of human-made global warming (Al-Ghussain, 2019). To avert the direst consequences of this global change, the Paris Agreement calls for a net 80–95% reduction of CO_2 emissions by 2050 (Rogelj et al., 2015). The rapid development of sustainable energy sources and environmentally benign storage and conversion technologies is thus a foremost goal in scientific research and technology development, pursued collectively in countries around the world.

CO_2 can be used as a renewable feedstock for the production of synthetic fuels or fuel precursors such as CO, CH_3OH, and CH_4, addressing the problem of the intermittency of renewably generated energy from wind turbines and solar cells (Qiao et al., 2014; Lu and Jiao, 2016; Zhu et al., 2016; Liu et al., 2017; Wang et al., 2017). This energy storage pathway renders the CO_2 reduction reaction (CO_2RR) a crucial and extensively researched electrochemical process (Lin et al., 2020; Mandal, 2020).

CO_2RR processes inside an electrochemical cell require stable, cost-effective and highly performing electrocatalyst materials. The challenge of optimizing catalytic materials, electrodes and devices for the CO_2RR, calls for further investigation into factors that control their catalytic activity and stability. The electrocatalytic media are usually heterogeneous composites that embed the active material into a host medium with suitable transport properties for gaseous reactants, liquid

products, dissolved ions, and electrons. These media can undergo significant changes in structure and composition under operation through various phenomena such as Ostwald ripening, particle detachment or coagulation in nanoparticle-based catalyst layers; surface reconstruction, oxidation or passivation by irreversible adsorption; or electrolyte disintegration. Besides, inhibited mass transport due to non-optimal wetting of the porous electrode could cause additional voltage loss or limit the current density (CD) that a cell could attain.

A recently performed cost-benefit analysis has shown that electrochemical CO_2 conversion processes need to be economically viable at the system level, while the faradaic efficiency (FE) and energy efficiency (EF) must be maximized at the component and cell levels (Kibria et al., 2019; Lin et al., 2020). The hydrogen evolution reaction (HER) is an unwanted parallel process in CO_2 reduction cells, which impacts the yield of synthetic fuel or fuel precursor production (Goyal et al., 2020). Minimization of hydrogen production requires electrocatalyst materials that are highly selective in terms of the reaction pathway to support.

The integration, testing and qualification of new catalyst materials is a tedious and time-consuming process as there are limitations even for the best catalysts due to specific compatibilities that are required with other components in a membrane electrode assembly (MEA), single cell or stack of the electrochemical device. Challenges in this context involve reactant and product transport as well as water and heat balances. These phenomena are coupled across multiple components and interfaces in a cell, and they determine 3D distributions of local reaction conditions in active electrode media. Assessing the impact of a new catalyst material on performance at cell and stack levels is thus a complex undertaking. An electrocatalyst material may show markedly improved activity and selectivity in a well-defined lab set-up under precisely controlled reaction conditions; but this improvement may not transpire when the material is incorporated into a real cell and tested under realistic conditions.

Complex electrocatalytic media cannot be studied solely with computational studies based on density functional theory (DFT). Usually, the complexity of materials, components and physicochemical phenomena to be considered as well as the interplay of solvation effects, charge transfer, and electric field effects at the interface, warrant a well-devised hierarchical framework in modeling and simulation. This framework should interweave computational approaches, including DFT as well as classical simulations, microkinetic modeling of reaction mechanisms, interface and charge transfer theory, and continuum modeling of transport processes at the electrode level, to rationalize local reaction conditions, decipher reaction mechanisms and calculate reaction rates. Considering all of these aspects, the theory-driven approach towards the development of highly active, selective, and stable electrocatalysts for the CO_2RR remains a highly challenging task (Elouarzaki et al., 2019; Ju et al., 2019).

The discovery and scale-up of integrated materials, i.e., those materials that are integrated into a component, cell, and device to fulfill certain functionalities at the device level, require significant capacities for characterization, testing, and optimization at all structural levels. The discovery-to-demonstration pipeline of new electrocatalyst materials, including fabrication scale-up and integration with other cell components is thus more complex to follow through than it is for simpler, so-called "molecular materials," where *minimal* integration and optimization is required beyond materials properties (Elouarzaki et al., 2019; Ju et al., 2019). Apart from performance metrics related to activity, yield and selectivity, the degradation of cell components, overall system durability and overall cell lifetime present essential issues to be addressed, which are related to the stability of a catalyst material for relevant environmental conditions and operating regimes.

The key attributes of successful design of CO_2 reduction cells include high mass activity of electrocatalysts to perform well at low overpotential and reasonable materials cost, catalyst layer microstructure to facilitate charge and mass transfer, well-attuned wettabilities of porous transport media to optimize the water distribution across the cell, and mechanical and chemical durability. New approaches in materials design and integration are needed to realize the selective transformation of CO_2 into desired products in scale-up pilot or industrial setups.

Numerous investigations have recently been made to design, synthesize and develop new CO_2RR electrocatalysts (Lu and Jiao, 2016; Liu et al., 2019). Machine learning (ML) and data-driven methods provide a powerful set of methods and tools to accelerate materials discovery (De Luna et al., 2017; Cao et al., 2018). Fundamentally, ML is the practice of using statistical algorithms to parse data, learn from a set of indicators (performance metrics) and then make a fast determination or a prediction of target performance properties of any new data sets. ML in materials science is mostly concerned with supervised learning. One must realize that the selection of high-quality (accurate) datasets in addition to an appropriate set of descriptors is more important than the selection of the ML algorithm itself. The former would be considered as the first step for building any ML application. The suitable ML model, denoted as classification, regression, or rank ordering model, depends on the desired outcome (Elouarzaki et al., 2019).

Describing all the complexities of the electrochemical interface within a DFT model, considering the number and type of components (catalyst, solvent molecules, ions, etc.), as well as the fundamental physics involved (electric fields, solvation free energy, charge transfer kinetics etc.), is challenging due to computational limitations.

Classification models are designed to allocate a substance to a given number of categories such as *active* and *inactive catalysts*; they can be used to separate groups of molecules or materials according to the presence or absence of a target property. For instance, CO_2RR electrocatalysts can be classified based on their Faradaic efficiency or product selectivity. In this context, several statistical tools, in particular, regression models attempt to determine a function that can represent a continuous hypersurface to relate indicator variance to observable electrocatalytic properties. Regression models are used where prediction and discovery of a missing physico-chemical property such as performance or selectivity are needed

(Varnek et al., 2007). Ranking models put out the order of electrocatalysts for a specific property; they are highly useful for electrocatalyst design and discovery, where the priority of one property over another is more important than its exact value (Goldsmith et al., 2018; Lamoureux et al., 2019; Schleder et al., 2019).

Recent self-learning algorithms have greatly influenced catalysis research due to the availability of ML analysis tools, e.g., Python Scikit-learn, TensorFlow and workflow management tools such as ASE (Larsen et al., 2017) or Atomate (Mathew et al., 2017), and the proliferation of large public materials databases, including Materials Project (Jain et al., 2013), Novel Materials Discovery Laboratory (Draxl and Scheffler, 2019), Citrination (Citrine Informatics, 2013), CatApp (Hummelshøj et al., 2012), and AiiDA (Pizzi et al., 2016) and advancement of applied statistical algorithms and models.

ML models have been utilized in a variety of energy material applications to design and discover novel electrocatalyst materials with superior performance (e.g., higher energy density and higher energy conversion efficiency) (Meyer et al., 2018; Zahrt et al., 2019). Such models can have a transformative impact on the development of low cost CO_2RR catalysts with high product selectivity and maximal performance (Goldsmith et al., 2018; Kitchin, 2018; Schlexer Lamoureux et al., 2019; Gusarov et al., 2020; Smith et al., 2020). For instance, ML models have been used to disentangle catalyst-adsorbate interactions for various reactions, including CO_2RR (Ma et al., 2015; Tran and Ulissi, 2018). A combination of advanced optimization tools based on ML and other conventional approaches has been developed to predict electrocatalyst performance for CO_2 reduction and H_2 evolution (Tran and Ulissi, 2018).

In this work, we demonstrate a data-driven framework for materials screening, which is particularly applied to low and high temperate catalysts for CO_2 reduction (Garza et al., 2018; Kibria et al., 2019; Malek et al., 2019; Chou et al., 2020). A viable electrocatalyst for the CO_2RR must satisfy performance metrics related to current density, faradaic efficiency, energy efficiency, overpotential, production rate, and chemical stability. Correlations among these performance metrics at low or high temperature remain largely unknown and require extensive data analytics.

Our data-driven methodology is designed with the objective of integrating domain-specific data sources in order to eliminate difficulties in data collection and interpretation from multiple sources and data types. The integration process consists of a combination of "modular" sub-processes to build "standardized energy materials data" in real-time with advanced filtering, scale-up and cognitive insights, ML, and fundamental data analytics functionalities, including visualization and big-data management tools. The recommendation system and decision module utilize high-level technical targets as input data, which can be displayed in the form of radar (or spider) charts; advanced data extraction and categorization using deep learning techniques; property-matching algorithms to search for the best viable materials that satisfy selected high-level technical targets; and finally a multi-parameter optimization to recommend top choices in connection with ML algorithms.

METHODOLOGY

Application-Driven Architecture

In order to offer scale-bridging capabilities to connect crucial steps in materials design-to-device integration, an application-driven architecture has been introduced and demonstrated (Malek et al., 2019). The central part of this architecture is an embedded master data lake, consisting of large-scale metadata for electrocatalyst materials, which is assembled from various types and sources of materials data. Key technical targets such as activity (i.e., the faradaic efficiency), stability, and selectivity are usually defined at cell and device level and may also correlate differently at low or high temperatures with physicochemical properties of electrocatalysts and the operating conditions at cell or device levels (Chan and Li, 2014; Nitopi et al., 2019).

Figure 1 illustrates the functional layers of the ML-enabled data analytics approach and its underlying workflow. The workflow comprises various layers including user-defined or default data sources and databases, analytics modules, and self-driving algorithms, which are commonly used in materials discovery approaches, regardless of the corresponding field of application. The complexity with scale-up and discovery of integrated materials also implies the need for ad hoc communication among parallel or series of synthesis and characterization steps or equipment, in-device component integration, and device testing or validation. This all-embracing workflow along the complete development pipeline can enhance data communication and promote understanding of correlations among structure, functional properties, and performance indicators at all scales from materials discovery to device performance and optimization.

Master Data Lakes

A vital prerequisite for any type of ML application is the provision of a suitable dataset for a given domain. The search for new electrocatalyst materials essentially needs a minimal and sufficient set of performance indicators from the "chemical domain" and the "property domain" of different electrocatalyst materials (Flores-Leonar et al., 2020).

The master database is built from materials datasets collected from a wide range of sources and user-types, namely 1) unpublished records of academic researchers, 2) published articles, and 3) other public records and industry reports. The details of the data retrieval from images, tables and texts are described in ref Malek et al. (2019). The resulting database is stored in excel or CSV format with predefined and standardized headers that include metadata preprocessing and cleaning.

In this article, the CO_2RR experimental databases were generated from literature sources on the basis of seven input variables: electrocatalyst type, faradaic efficiency, applied potential, current density, type of electrolyte, major product, and temperature. Each experimental data point is characterized by a set of performance indicators for catalyst formulation and reaction conditions, either as continuous values (such as current density) or as categorical values (such as catalyst type). The ranges of the corresponding input variables are summarized in **Table 1**.

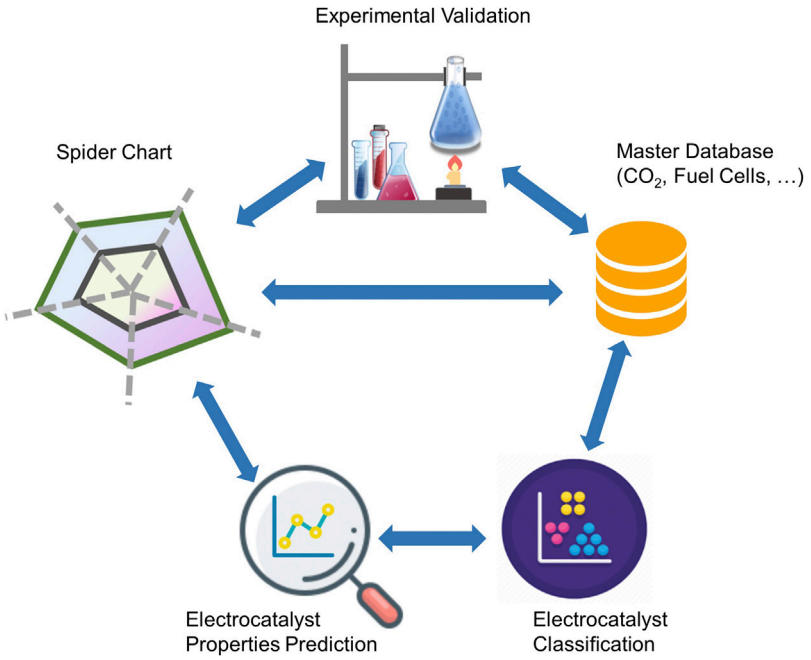

FIGURE 1 | The workflow of the cognitive material identification system.

TABLE 1 | Key performance indicators and their types or range of values as being set in the data extraction process.

Descriptors	Range or types	Units
Catalyst	Cu, Ag, Ni, Ti	
Applied potential	−1.45 to 5.3	V
Current density	0.00058–856	mA/cm^2
Faradaic efficiency	0 to100	—
Type of electrolyte	KOH, KCl $KHCO_3$, $CsHCO_3$, YSZ, Li_2O-Li_2CO_3	
Major products	CO, H_2, CH_3COOH C_2H_5OH, C_3H_7OH	
Temperature	25–900	°C

Machine Learning Algorithms

ML classification models could be used to identify and classify materials or map them in terms of their properties (descriptors), which is the first essential requirement prior to any ML-based prediction. We use the Scikit-learn package in the ML modules (Pedregosa et al., 2011).

The ML algorithms employed for classification of electrocatalyst and product type include logistic regression (LR), linear discriminant analysis (LDA), k-nearest neighbors (KNN) classifier, and random forest (RF) classifier. In addition, we tried to classify groups of products by putting all possible products into two or three different larger groups of products. In order to compare the predictability of different models for finding missing data, four ensembles of ML algorithms were evaluated. The regression algorithms include Bagging Regression (BR), Gradient Boosting Regression (GBR), Random Forest Regression (RFR), and Extra Trees Regression (ETR). BR is an ensemble method that fits regressors on random subsets of the original dataset and makes a final decision based on aggregated prediction. The bagging method increases the robustness of the original set of models by introducing randomness during the training process and then ensembling their predictions. GBR builds a model in a forward stage-wize style, which enables optimization on any differentiable loss function. RF is a typical ensemble learning model that operates by building a set of decision trees and yielding average predictions of a separate tree. Random decision forests are superior to decision trees due to the ability to solve the over-fitting issue. Finally, extra trees implement a meta-estimator that fits several random decision trees on different sub-samples of the dataset and utilizes the mean of trees to boost the predictive performance and reduce the variance. ETR and RFR models have shown to be promising in the modeling of chemical systems. Each algorithm was trained on the training data for the CO_2 reduction reaction. The algorithms were then implemented to predict faradaic efficiency, applied potential (AP), and current density for the test dataset. We used the ML hyperparameter optimization module to tune hyperparameters automatically.

The accuracy score (%) (i.e., the ratio of correct predictions to the total number of predictions) is used as a performance metric for the evaluation of each classification algorithm. The performance of each ML algorithm for prediction was evaluated by using several statistical indicators such as the mean squared errors (MSE), the root mean squared error (RMSE), and the coefficient of determination (R^2),

$$MSE(y,\hat{y}) = \frac{1}{n}\sum_{i=0}^{n-1}(y_i - \hat{y}_i)^2 \quad (1)$$

$$RMSE(y,\hat{y}) = \sqrt{\frac{1}{n}\sum_{i=0}^{n-1}(y_i - \hat{y}_i)^2} \quad (2)$$

$$R^2 = \frac{\sum_{i=0}^{n-1}(\hat{y}_i - \bar{y}_i)^2}{\sum_{i=0}^{n-1}(y_i - \bar{y}_i)^2} \quad (3)$$

in which y_i and $\hat{y}_i$ are the true and predicted values, respectively, $\bar{y}_i$ is the mean of the true values, and n is the number of samples.

Modular Design

The complexity of the materials design-to-device integration calls upon a modular approach, in which various data management tasks and data analytics tools are built and tested in isolation, as stand-alone-modules. The suitable modules are then called and integrated into the main platform depending upon the application area, required analysis tools, and type of meta-data that the user needs for the analysis. In the following, we describe the adaptation of each module and their inter-dependencies for the analysis of electrocatalytic materials for the CO_2RR.

Classification and Materials Data Extraction

This module utilizes a classification algorithm that categorizes catalyst materials in the form of performance range (e.g., potential or current density) or selectivity or type of products. The reference values for high-level technical targets are based on a "performance matrix" that is provided as the default for a particular field of application or as a user-entry table for the target values. These initial values can be seen as the first set of keywords for data mining and data discovery from the literature for a given material application field or sub-classes therein such as low-temperature catalysts or high-temperature catalysts. The extracted data is then mapped on these key technical parameters and other crucial measurement conditions for each class of materials.

Materials Property Prediction

This module can predict a specific electrocatalytic property such as the faradaic efficiency as a function of input or exploratory variables using embedded ML models. The results of these ML prediction models can refine the usefulness and relevance of the user input variables. The module also helps fill missing data points related to performance indicators or target properties in the database and thus enriches the master database. In this context, electrode type, current density, voltage, polarization resistance, conductivity, electrolyte type and composition, temperature, type of product, and (rarely) faradaic efficiency are among the key factors that can influence CO_2RR performance.

Recommendation System and Decision Models

The performance tuning algorithm is the first layer of the recommendation module that uses the complete dataset to find the best electrocatalyst material based on performance and stability metrics' target values. It displays the information using standard visualization tools, for example, using a radar chart. A radar chart is a typical visualization tool employed in benchmarking electrocatalyst materials for the purpose of quality and performance improvement of a system of materials or an electrochemical device (Basu, 2004). The use of radar charts makes two significant contributions: first, it provides a simple 2D visual representation of multiple performance indicators without the need of using dimensionality reduction on multivariate data; second, the enclosed area, formed by spikes (or axes), can be considered as an intuitive electrocatalyst performance indicator.

The ML-powered recommendation module uses the power of regression modeling to predict values for the missing data as accurately as possible. **Supplementary Table S1** shows the sample data statistics used to train the regression models for predicting the missing data, specifically for applied potential, current density, and faradaic efficiency. Datapoints for four types of electrocatalyst material were selected, as there was not enough data for predicting other variables in the CO_2 experimental database.

Data Matching and Validation

The ultimate criterion for ML-based predictive capabilities is experimental validation, which demonstrates how computer algorithms lead to real discoveries. After predicting the best candidate electrocatalyst material, the prediction can be validated by direct comparison to experimental data for the same or almost the same set of conditions and materials specifications (Malek et al., 2019).

In our predictive algorithm, CO_2 electrocatalyst materials are generally categorized into three main groups: metallic, non-metallic, and molecular catalysts. Each category of electrocatalyst materials exhibits distinct physicochemical and electrocatalytic properties. Therefore, it is possible that the performance of an electrocatalyst material is restricted and limited to the group of catalyst materials it belongs to. Here, we used ML classification models to sort different electrocatalyst materials into different groups based on their performance. The numerical data are normalized between 0 and 1, and we encoded the categorical data using "*OneHotEncoder*" from the Scikit-learn data preprocessing module (Pedregosa et al., 2011).

Most of the data in our Master database at low temperature are for Cu electrocatalyst, with the key properties of AP, CD, and FE, type of electrolyte, and type of product. Material properties predictions thus focus on these attributes.

RESULTS AND DISCUSSION

Materials Recommendation

Figure 2 shows the workflow of material recognition. In order to identify an electrocatalyst material for a given electrochemical process, it is expected that the performance metrics of the chosen electrocatalyst meet or exceed the target values set by the user. For this purpose, one needs to consider the key performance metrics, i.e., faradaic efficiency, current density, applied potential, selectivity, and production rate, to select the best electrocatalyst material.

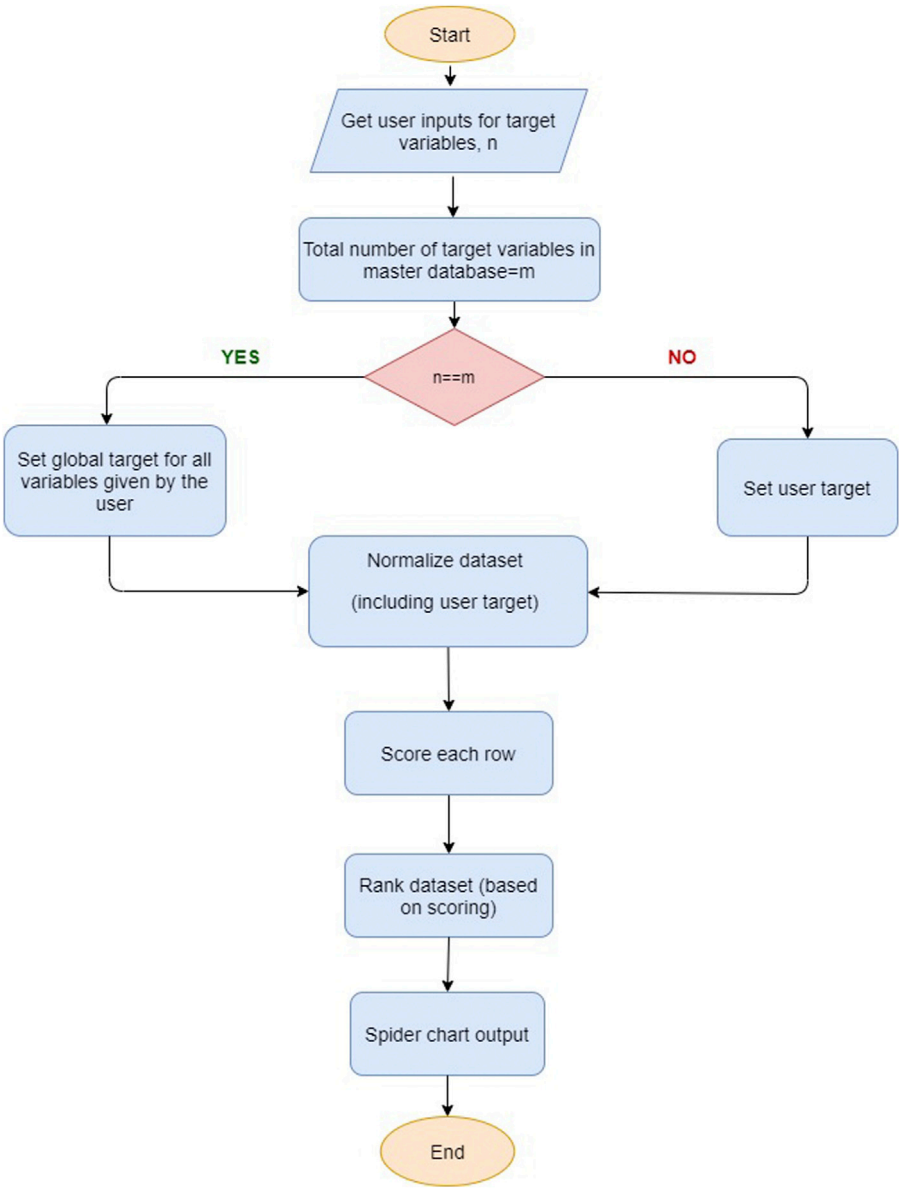

FIGURE 2 | Flowchart of material identification framework.

In practice, keeping track of all variables and establishing correlations among optimization parameters in an electrochemical reaction path is a difficult task; once a set of properties is set to the optimum values, other properties of the catalyst can have values which are below user requirements. We attempt to address this challenge by introducing a penalty function for any value less than the desired value for a target application variable.

The recommendation process shown in **Figure 2** initially takes input from the user-specified target values. The recommendation then selects the "best" electrocatalyst or recommends electrocatalyst materials primarily based on the targets for the set of performance metrics defined by the user. Global target values are provided as default if no user-entry target values are available. In order to minimize the optimization effort and for fast and better identification criteria, the user is provided with one of the following identification schemes: 1) find any electrocatalyst material for some desired value of a metric, with any chemical product; 2) find any electrocatalyst material for target value metrics for a specific set of chemical products; 3) find some desired performance metrics, within specific electrocatalyst material groups, with any product; 4) find some desired properties within specific electrocatalyst material groups, for a certain set of chemical products. The user is given target values for selected metrics, electrocatalyst type, and chemical products, where a user is able to filter data based on products and electrocatalyst material or simply select all the possibilities. If the user provides target values for all metrics, the recommendation algorithm selects an electrocatalyst material with

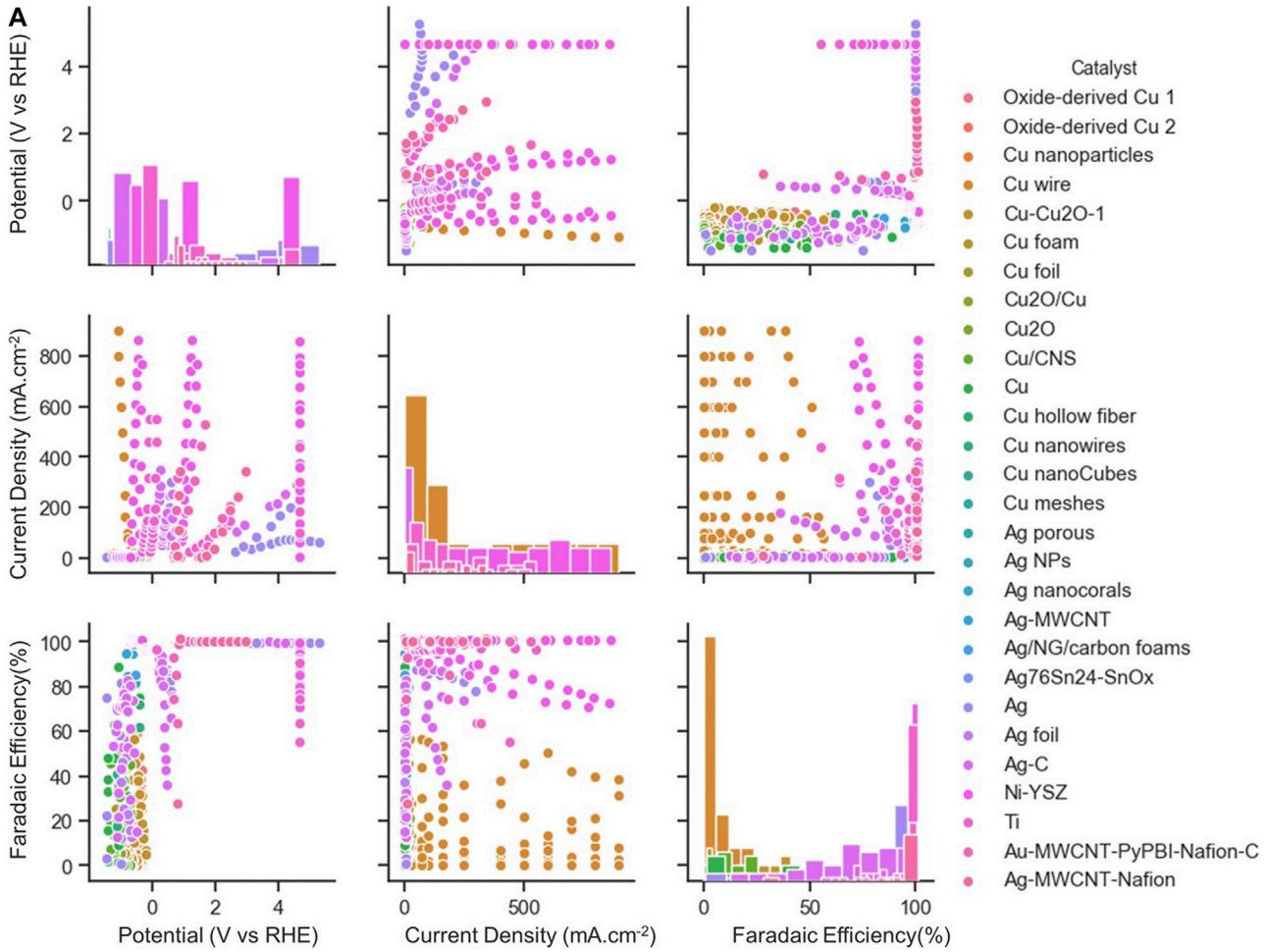

FIGURE 3 | Scatter plot matrix showing the data distribution for **(A)** both High-T and low-T **(B)** High-T, **(C)** Low-T of CO_2RR according to three performance metrics. The elements in the diagonal (upper left to lower right) represent the respected range of data points for each catalyst type.

properties equal (with less than 10% deviation) or better than the user target. If the user provides target values for a few properties and not all the properties, then the algorithm uses default global target values for those target properties that are not provided by the user.

Here, a simplified, yet straightforward method for selecting an electrocatalyst material is employed by using a radar chart to identify the material, which encloses the graph's maximum area. Although this heuristic method can be seen as practically useful, it may lead to a biased selection with few performance indicators at high values, while others remain at low values. It ignores the ranking and importance of different variables.

Our optimization algorithm employs a special scoring factor where it scores positive values for properties that are higher or equal to the user target values and penalize properties that are less than the user target values. The value of the penalty function becomes more valuable for performance indicators that significantly less than the actual target values. This sub-routine recommends catalyst materials that exhibit high values in one or multiple attributes from the performance matrix table.

The scoring factor is defined by,

$$Score_i = \sum_{m=1}^{m=k} difference_{im} \qquad (4)$$
$$i: \ is\ the\ number\ of\ row$$

where k is the number of target properties (P). If $P_{ij} \geq P_{User\ Targetj}$

$$difference_{ij} = P_{ij} - P_{User\ Targetj}$$

If $P_{ij} < P_{User\ Targetj}$

$$difference_{ij} = 5^{(P_{ij} - P_{User\ Targetj})} - 1$$

Here P_{ij} is the default target value of property j for row number i and $P_{User\ Targetj}$ is the user defined target value for property j.

The constraint for the penalty function is set at 5, representing the maximum error tolerated. Once the scoring factors for each row in the database are calculated, the algorithm recommends electrocatalyst materials with high score values, as illustrated in **Supplementary Figure S1**.

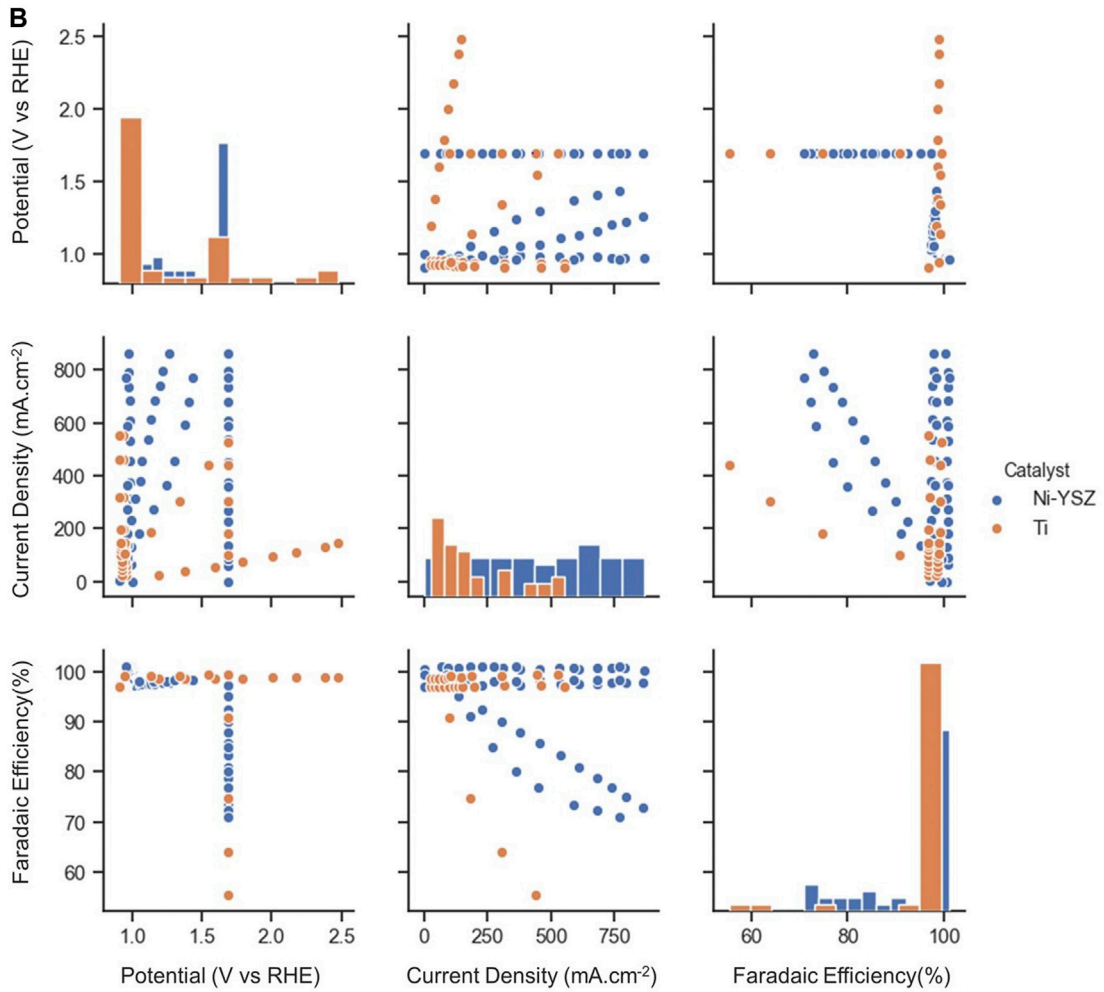

FIGURE 3 | (Continued).

Low-Temperature Electrocatalyst Materials

Figure 3 shows the visualization of data, which is distributed among applied potential, current density, and faradaic efficiency for different types of electrocatalysts at low- or high-temperature. The diagonal graphs represent the density plot of each respective feature, providing useful information by giving a density of plots in the form of bar charts. Among the possible choices of electrocatalysts at low temperature, mainly four types of Cu-based electrocatalysts are used for the classification task. The dataset is divided into training and test datasets. The dataset consists of 228 different Cu electrocatalyst materials, among which training and test datasets account for 183 and 45 data points, respectively. Each data point consists of a set of properties for a given material. The same material may appear in different data points with different operating conditions. The materials space is then scanned using a set of descriptors, such as selectivity for a given product or performance indicators against a reference target range. The latter is performed using machine learning techniques. Model performance for classification of the type of electrocatalyst and type of products was evaluated through the calculation of an accuracy score.

As illustrated in **Table 2**, the key indicators (AP, CD, FE, Product selectivity) have high cross-validation scores, which can vary according to the ML algorithms. The LR and LDA classifiers are found to return the highest accuracy score of 81%, determining the type of electrocatalyst. QDA classifier has an accuracy score of 32%, which is remarkably lower than that for other classifiers.

As shown in **Table 3**, the indicators of AP, CD, FE, and type of electrocatalyst yield a higher accuracy for classification of a group of two products (CH_4, C_2H_5OH) in comparison with two other groups, each consisting of three different products. RF and LDA classifiers return value of 1 and 0.93, respectively, for the accuracy score of all test cases. In general, RF classifier has the best performance among other algorithms for the classification of the type of products regardless of the number of products.

LR, LDA, QDA, and GNB algorithms were unable to distinguish and single out one group of products, including

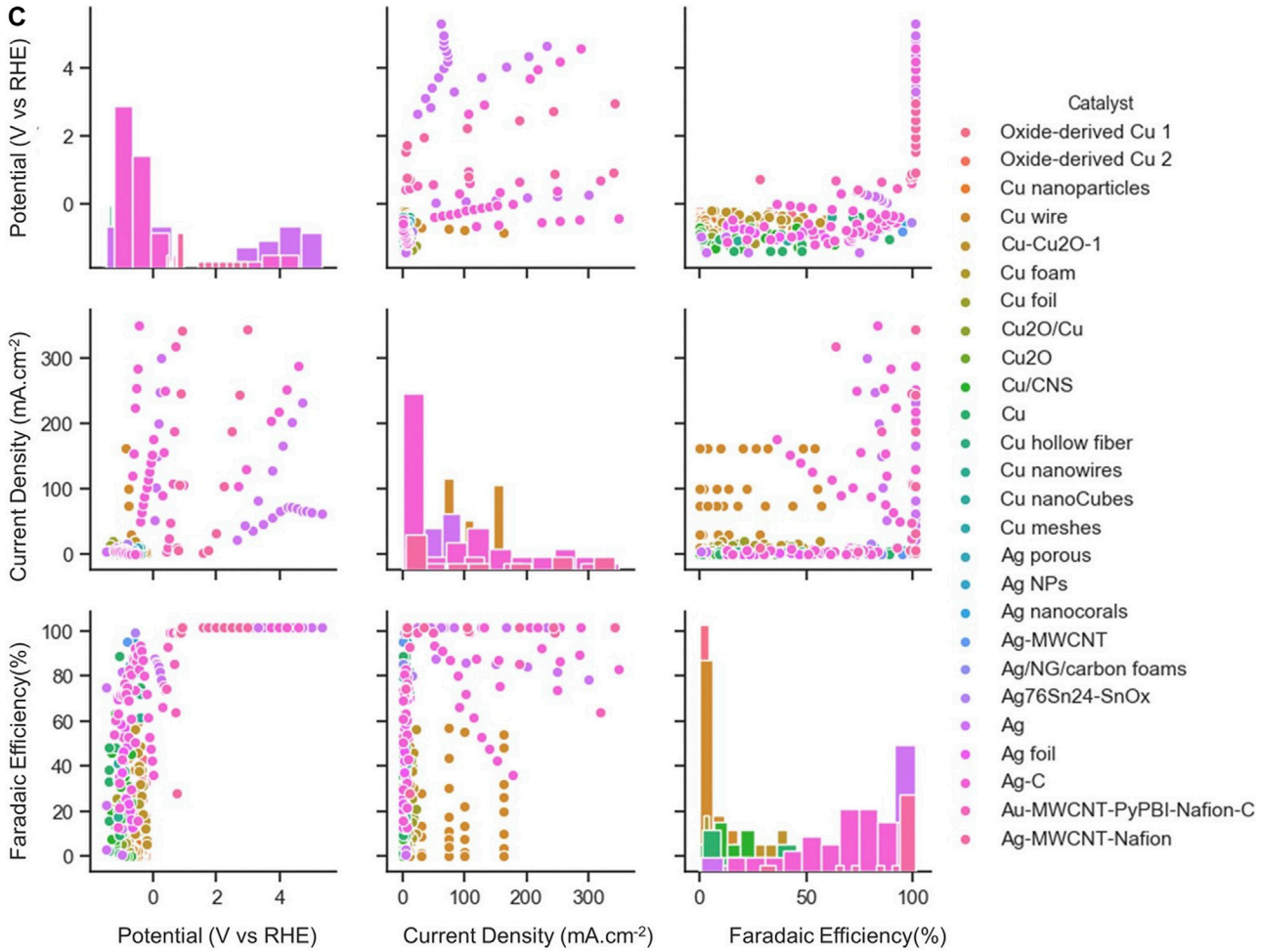

FIGURE 3 | (Continued).

those with three different products. Additionally, GNB returns an accuracy score of 26%, the lowest of all six algorithms. It is obvious that better performance of ML algorithms can be achieved for the group with two products than for the groups with three different products. The latter can be understood from the comparison of the values of accuracy score for classification of the type of electrocatalyst or products reported in **Table 2** and **Table 3**. One would need more indicators such as the reaction conditions (pH, mass loading of catalyst, production rate, and concentration) for each reaction in order to have a better performance with the classification scheme.

Table 4 lists the performance of predictive analytics using MSE for various experimental numerical values, i.e., AP, CD, and FE. ETR is seen to have a better predictive capability with a minimum error, which is considered more accurate than other algorithms. In order to quantitively obtain a prediction model for FE, AP and CD, we employed the BR, GBR, ETR, and RFR

TABLE 2 | The results of cross-validation with six different classification algorithms against low-temperature catalyst types in four classes (Cu wire, Oxide-derived Cu 1, Oxide-derived Cu 2, Cu nanoparticles).

Catalysts: Cu wire, oxide-derived Cu 1, oxide-derived Cu 2, Cu nanoparticles	
ML algorithms	**Average score (%)**
Logistic regression (LR)	0.81
Linear discriminant analysis (LDA)	0.81
Quadratic discriminant analysis (QDA)	0.32
k-nearest neighbors classifier (KNN)	0.68
Random forest classifier (RFC)	0.71
Gaussian NB (GNB)	0.61

TABLE 3 | The results of cross-validation with six different classification algorithms against the type of products in three classes [a group of (CH_4, C_2H_4, C_2H_5OH) (CH_4, C_2H_5OH, C_3H_7OH), and (CH_4, C_2H_5OH)].

	Average score (%)		
ML algorithms	**CH_4, C_2H_4, C_2H_5OH**	**CH_4, C_2H_5OH, C_3H_7OH**	**CH_4, C_2H_5OH**
Logistic regression (LR)	0.39	0.20	0.80
Linear discriminant analysis (LDA)	0.52	0.15	0.93
Quadratic discriminant analysis (QDA)	0.43	0.51	0.60
k-Nearest neighbors classifier (KNN)	0.48	0.65	0.73
Random forest classifier (RFC)	0.70	0.71	1
Gaussian NB (GNB)	0.52	0.45	0.26

algorithms. Models were based on the training data (80% of the full dataset), where 20% of is used to evaluate the test data.

The scatter plots of the outputs vs. the actual values for the training, testing, and overall data sets using RFR and ETR algorithms are presented in **Figure 4**. The coefficient of determination (R^2) indicates a strong correlation between outputs for CD and AP and actual values. The AP, CD, and FE results clearly show excellent agreement between the actual values and RFR, GBR, and ETR predictions, with $R^2 > 0.90$ and MSE < 0.008 for all of the ensemble modeling cases. The R^2 and MSE of test data for faradaic efficiency with ETR and RFR have better performance than that for other regressors.

Success with ML depends on the number of descriptors and their correlations, as well as available large training data. The true benefit of structure-property relationships revealed through ML models lies in the multi-variant correlations and their interpretation in terms of the fundamental materials properties.

The missing values in the primary database can nonetheless be filled with values extrapolated from ML by building a model that relates known indicators of materials to target properties. Our ML model has successfully predicted different properties like FE or CD, or classification of the type of electrocatalyst, or major products related to specific type of catalyst. The latter process has been carried out iteratively. After filling missing values, the database is ready to screen the electrocatalyst performance through means of analytical and visualization tools.

Utilizing all available and supplemented databases, rapid screening of electrocatalyst materials was carried out, while the user would be able to specify target values for various properties. The optimization algorithm proposed in this work uses a scoring factor based on a rank-ordering approach. The best electrocatalyst material for selected chemical products was then estimated for a class of materials or products. **Figure 5** shows the radar charts of the best electrocatalyst materials based on the target attributes selected by users or directly from a global target, which is set as a default. The figure indicates that Pt is the catalyst of choice when no specific fuel products are considered.

High-Temperature Electrocatalyst Materials

Despite recent advances in electrolytic systems for CO_2 conversion at high temperature (>800°C), the overall efficiency and performance of the system remain far from being sufficiently understood for commercialization and practical usage (Gorte et al., 2000). Among the technological shortcomings are low conversion efficiency and high degradation rates of materials and components, including membrane and electrocatalysts. The latter is mainly due to the fact that the high catalytic conversion will inherently result in low electrochemical stability of catalyst materials at higher temperatures. The fundamental understanding of the elementary kinetic processes involved in CO_2 electrochemical conversion at high temperature is a subject of ongoing research (Tran and Ulissi, 2018). Notably, the cost-effectiveness of catalytic processes at high temperature primarily depends upon the trade-off between the system efficiency and

TABLE 4 | Evaluation of predictive algorithms for applied potential, faradic efficiency and current density.

	Statistical technique	**Bagging regression (BR)**		**Random forest regression (RFR)**		**Gradient boosting regression (GBR)**		**Extra trees regression (ETR)**	
Features	**n/a**	**Training**	**Test**	**Training**	**Test**	**Training**	**Test**	**Training**	**Test**
Applied potential (V vs. RHE)	MSE	1.17E-03	6.15E-03	5.30E-04	3.18E-03	8.14E-04	2.96E-03	6.31E-06	2.66E-03
	R^2	0.97	0.88	0.98	0.94	0.98	0.94	0.99	0.94
Current density (mA.cm^{-2})	MSE	9.30E-04	7.06E-03	9.76E-04	5.87E-03	1.11E-03	5.42E-03	4.45E-08	4.82E-03
	R^2	0.98	0.88	0.98	0.90	0.98	0.91	0.99	0.91
Faradaic efficiency (%)	MSE	2.44E-03	7.30E-03	1.86E-03	6.22E-03	7.17E-03	8.35E-03	2.56E-31	5.38E-03
Overall	R^2	0.98	0.95	0.98	0.96	0.95	0.94	1	0.96

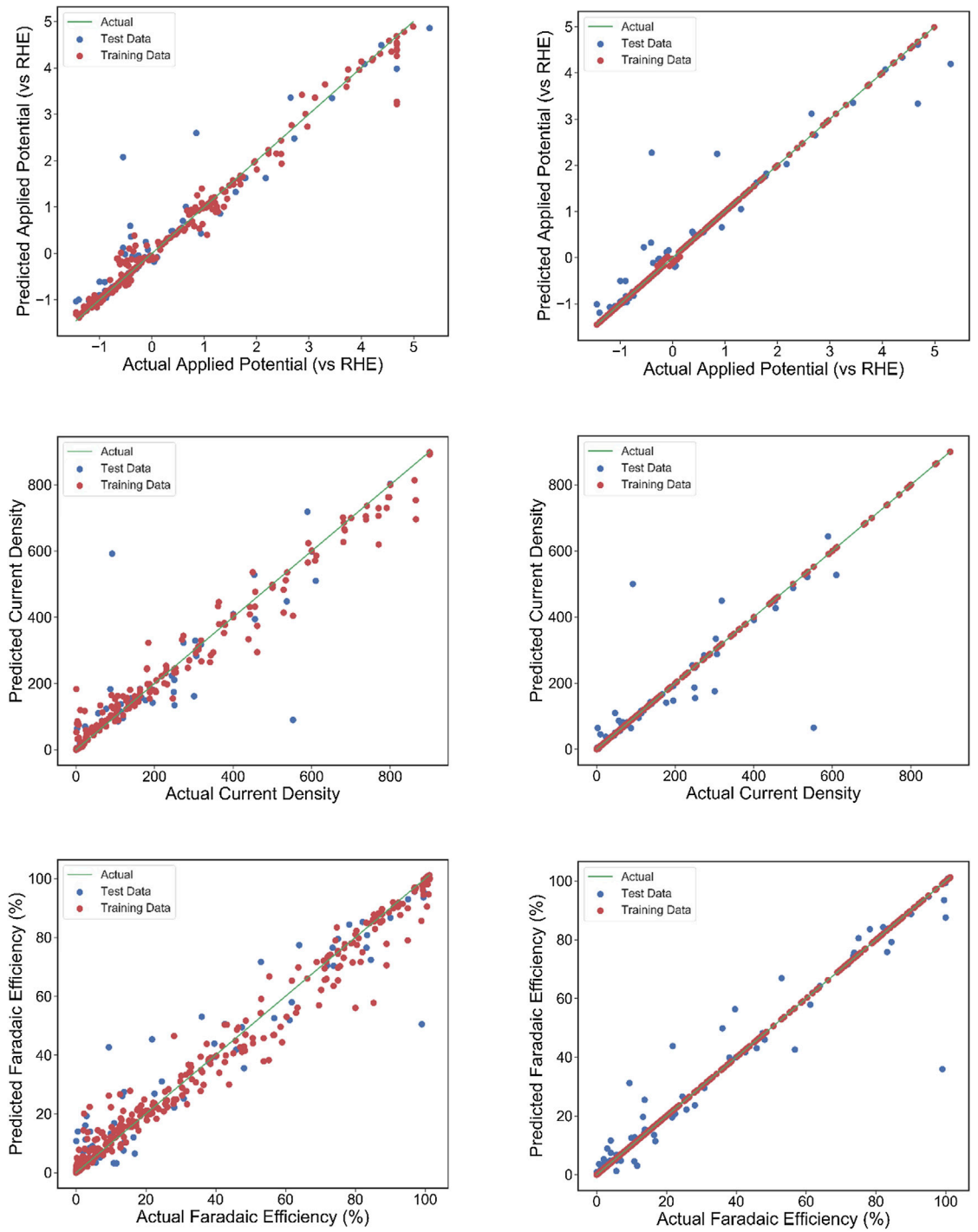

FIGURE 4 | The actual Faradaic efficiency, applied potential, and Current density values compared with the predicted values using Random Forest regression and Extra Tree regression models. The coefficient of determination (R^2) and mean squared error (MSE) are computed to estimate the prediction errors. The test and training points are shown in blue and red, respectively. The perfect correlation line is included for reference as a green line.

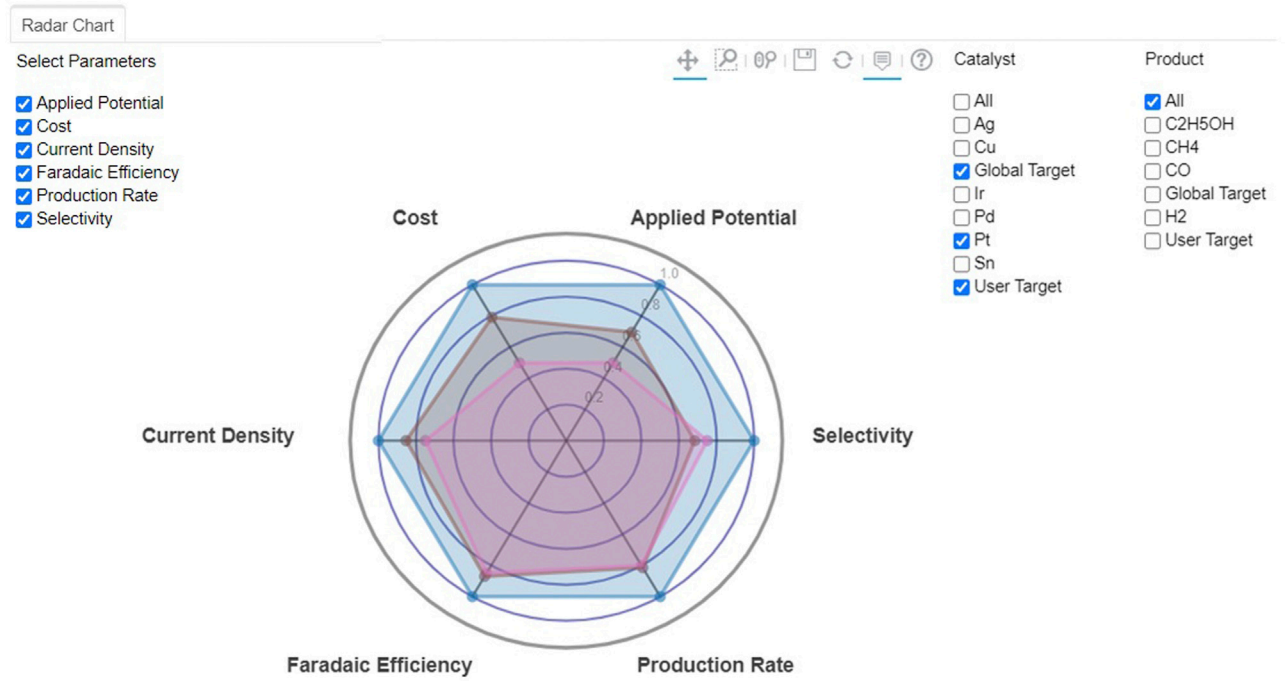

FIGURE 5 | Screenshot of radar chart for CO_2 reduction to fuels of Pt-based on different classification of electrocatalysts and selected target values by default global (blue) or user-entry (brown) targets.

production cost of the fuel, while the operating condition of the solid oxide electrolyzer cells (SOECs) remains very narrow due to high heat requirements and the sensitivity to temperature fluctuations (Ma et al., 2015). CO is the major product as all other competing chemical reaction products are desorbed from the surface to produce CO at high temperatures. Therefore, additional down-stream processes need to be performed in order to achieve other products such as methanol. For co-electrolysis of CO_2 and H_2O, SOEC provides high flexibility in the carbon to hydrogen ratio (C/H) and, thus, state-of-the-art

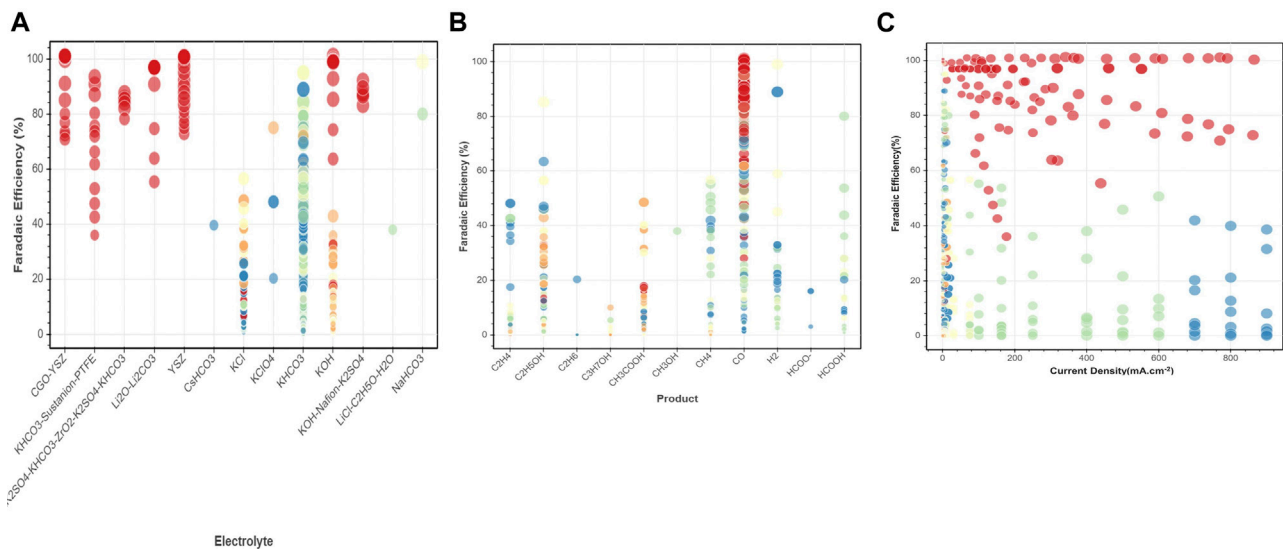

FIGURE 6 | Binary correlations among key attributes **(A)** FE-electrolyte, **(B)** FE-product, **(C)** FE-current density for sample extracted datasets of electrocatalyst materials at low and high temperature.

technologies such as Fischer Tropsch (FT) synthesis can be utilized downstream for achieving high product flexibility (Zhang et al., 2017; Zheng et al., 2017).

Here, we present preliminary results and a discussion for a data-driven analysis of selected electrocatalyst systems in SOECs that address a few of the above technological challenges. In high-temperature electrolysis of CO_2, the co-electrolysis process in the presence of steam is taking place at temperatures >600°C. High-temperature CO_2 electrochemical conversion using SOEC generally has a better selectivity compared to that at low temperatures. Correlations among AP, CD and FE at low or high temperature are not known yet and require extensive data analytics.

State-of-the-art high-temperature electrocatalyst materials in SOECs contain Ni-YSZ. A key factor for the stability and activity of these materials at high-temperatures is Ni% in the range of 40–60%. This range is required to fulfill the catalytic reforming and satisfies the matching requirement of the thermal expansion coefficients of the catalyst layer and the YSZ electrolyte (Gorte et al., 2000). Similar to solid oxide fuel cell (SOFC) electrodes, electrocatalytic reactions in SOECs take place at the triple phase boundary (TPB) where the Ni phase provides electrons, and YSZ particles offer the required oxygen ion vacancies for the reduction of adsorbed CO_2 and the removal of oxygen ions, respectively.

Recent progress suggests that the electrochemical reduction of CO_2 in solid oxide electrolysis cells takes place at high current densities. Degradation rates are higher in electrolysis mode compared to those in fuel cell mode based on enhanced effects of metal particle migration and/or oxidation, carbon deposition, grain coarsening, and contamination by impurities. This adds complexity to the choice of electrocatalyst materials and, thus drives significant research activity. In particular, electrochemical reduction of CO_2 in the temperature range of 573–873 K is worth exploring in order to match the temperature levels of electrolysis with required downstream FT-processes; however, there are no proper material systems for electrodes and electrolytes in that temperature regime at the current stage.

Here we consider a few conventional classes of electrode materials and explore the impact of Ni or Ti addition in various proportions on the overall catalytic activity *via* extensive data analytics. **Figure 3B** provides scatter plots and distributed values for applied potential, current density, and faradaic efficiency for Ti and Ni-YSZ catalyst systems. Ti-based electrocatalyst exhibits different dependencies for applied potential and faradaic efficiency compared to that for the Ni-YSZ system, while both catalyst materials are relatively similar in view of current densities. Overall, the Ti-based catalytic system shows high correlations among FE and CD, in particular in the range of data obtained at higher applied potentials (>2 V). **Figures 3A**,**B** clearly reveal differences in the correlations among key attributes such as FE and AP for catalysts at low and high temperatures. The correlations are more pronounced among FE and AP for high-temperature electrocatalysts, whereas CD and AP are the main indicators at low temperature. Among all electrocatalyst materials studied at high temperatures, Ni-YSZ shows the highest correlation between FE and AP, although the correlation factors can vary depending upon Ni ratios and type of electrolytes or products, as illustrated in the binary correlations in **Figure 6**.

The dataset for high-temperature catalysts consists of 180 test data points distributed among five different catalyst types. This amount of data is insufficient for accurate prediction of missing properties in the data set, and thus further predictions using ML techniques and identification thereof are not feasible based on the existing size of the dataset. Moreover, the atomic ratios of the composite electrocatalysts are not taken into consideration in these databases. The current results, however, will be expanded in the future to generate further insights for the correlation of key attributes at high-temperatures using larger and more diverse training and test data sets.

Recommendation and Decision System

Here, we only focused on high-level correlations among selected indicators. **Supplementary Table S2** provides the complete test data and other operational conditions that are assumed for each data point. The type of electrolyte is another important factor to be considered as it influences the extend of correlations among FE and AP for various high-temperature electrolysis technologies and the respective electrocatalysts. In particular, future work can include the analysis for the following use cases and comparison based on phase ratios and catalyst types such as Ag, Ni|YSZ or Ag|YSZ and for at least one cell configuration such as Ag/GDC|YSZ|YSZ/LSM|LSM [La 0.8 Sr 0.2 Cr 0.5 Mn 0.5 O 3 $-\delta$(LSCM)]. Further analysis is still ongoing to improve the test and training databases for high-temperature catalysts and provide a robust recommendation framework for this system. Here, the analysis is primarily built upon existing and extracted historical data. There is an emerging need for employing sophisticated decision algorithms and recommendation systems to "close-the-loop." Such algorithms will emerge from predictive models of key materials properties under different experimental conditions or modeling assumptions. They also identify weighting factors that govern specifications and limitations imposed at the components and device-level. Such algorithms are trained over time as more historical data and use cases become available.

CONCLUSION

The discovery and optimization of electrocatalyst materials are driven in large part by collecting and analyzing experimental data. The ML-assisted development of electrocatalysts is still an emerging field despite its success in molecular and material science; it cannot yet lead directly to novel electrocatalyst materials.

In this article, we proposed a recommendation framework for the benchmarking of existing electrocatalyst materials. A multi-attribute decision process was adopted, which was mapped on radar charts, from which the analysis of best-performed electrocatalyst is carried out based on user-entry or global technological targets. This recommendation framework provides the choice of dimensions, indicators, and appropriate correlations for benchmarking purposes and materials screenings process, purely based on historical data. With the availability of reliable process and materials economic data,

the latter can lead to comprehensive techno-economic insights into what performance levels are required for commercially viable electrocatalyst materials for the use in electrochemical energy conversion and storage devices.

We used ML to supplement missing data in CO_2RR databases prior to deploying ML algorithms to identify the best catalytic system. The ML module is primarily built for the classification and prediction of electrocatalyst materials. Different models for classification of the type of electrocatalyst materials and chemical products are used with reasonable accuracy within the limit of available test and training data. Among different regression algorithms, the Random Forest model showed a better capability for the prediction of electrochemical attributes. The proposed recommendation system provides interactive visual analysis of different indicators for the exploration of uploaded electrocatalyst data. High-level correlation analytics was also provided for catalyst materials at high temperatures, and the intensity of correlations was compared to that for catalyst materials at low temperature.

Finally, rapid screening and benchmarking studies of electrocatalysts material *via* data-driven visualization can significantly reduce the discovery time for the best materials and to understand or compare vital performance trends and correlations for given classes of materials, from initial discovery to component or device integration and for full-scale component or device production. The major limitations of the framework presented here are the incompleteness of datapoints, un-clarity or lack of consistency around key numerical or categorical attributes, and missing values for the attributes that are collected from the literature. The framework, however, can be applied to other sustainable electrochemical processes such as electrochemical NH_3 synthesis through N_2 and H_2O electrolysis.

The interactive visualization tools assist researchers in discovering trends and patterns hidden with the electrocatalyst material based on historical experimental and modeling data. Further ML and analytics functionalities are currently under development, which will offer higher accuracy and better inter-operability of the recommendation framework for idea-creation and the screening of electrocatalyst materials for various applications.

DATA AVAILABILITY STATEMENT

The original underlying data presented in the study are included in the article/**Supplementary Material**, further inquiries for access to Github can be directed to the corresponding author.

AUTHOR CONTRIBUTIONS

All authors contributed to the writing and editing of this manuscript. KM and ME contributed equally to the design of the initial concept and implementation of the research method. AM, KM, and ME collectively led and designed the underlying data analytics concept and ML methodology, and backbone of the data visualization and analysis tools.

FUNDING

This work was supported by the German-NRC collaboration project.

ACKNOWLEDGMENTS

KM and QW would like to thank NRC international office and NRC's Materials for Fuel Challenge program for their financial support. The authors also greatly acknowledge researchers in IEK-13 and IEK-1 at the Forschungszentrum Jülich for valuable insights and contributions to this project. Contribution from Gagandeep Singh Bajwa at NRC-EME for the extraction, cleaning, and analysis of CO_2RR databases is greatly acknowledged. ME acknowledges the support from the Forschungszentrum Jülich GmbH.

SUPPLEMENTARY MATERIAL

The Supplementary Material for this article can be found online at: https://www.frontiersin.org/articles/10.3389/fenrg.2021.609070/full#supplementary-material.

REFERENCES

Al-Ghussain, L. (2019). Global warming: review on driving forces and mitigation. *Environ. Prog. Sustain. Energ.* 38, 13–21. doi:10.1002/ep.13041

Basu, R. (2004). *Implementing quality: a practical guide to tools and techniques: enabling the power of operational excellence*. Boston, MA: Cengage Learning EMEA.

Cao, B., Adutwum, L. A., Oliynyk, A. O., Luber, E. J., Olsen, B. C., Mar, A., et al. (2018). How to optimize materials and devices via design of experiments and machine learning: demonstration using organic photovoltaics. *ACS Nano* 12, 7434–7444. doi:10.1021/acsnano.8b04726

K.-Y. Chan and C.-Y. V. Li (2014). *Electrochemically enabled sustainability: devices, materials and mechanisms for energy conversion*. Boca Raton, FL: CRC Press.

Chou, T.-C., Chang, C.-C., Yu, H.-L., Yu, W.-Y., Dong, C.-L., Velasco-Vélez, J.-J., et al. (2020). Controlling the oxidation state of the Cu electrode and reaction intermediates for electrochemical CO_2 reduction to ethylene. *J. Am. Chem. Soc.* 142, 2857–2867. doi:10.1021/jacs.9b11126

Citrine Informatics (2013). Available at: https://citrination.com (Accessed March 10, 2021).

De Luna, P., Wei, J., Bengio, Y., Aspuru-Guzik, A., and Sargent, E. (2017). Use machine learning to find energy materials. *Nature* 552, 23–27. doi:10.1038/d41586-017-07820-6

Draxl, C., and Scheffler, M. (2019). The NOMAD laboratory: from data sharing to artificial intelligence. *J. Phys. Mater.* 2, 036001. doi:10.1088/2515-7639/ab13bb

Elouarzaki, K., Kannan, V., Jose, V., Sabharwal, H. S., and Lee, J. M. (2019). Recent trends, benchmarking, and challenges of electrochemical reduction of CO_2 by molecular catalysts. *Adv. Energ. Mater.* 9, 1900090. doi:10.1002/aenm.201900090

Flores-Leonar, M. M., Mejía-Mendoza, L. M., Aguilar-Granda, A., Sanchez-Lengeling, B., Tribukait, H., Amador-Bedolla, C., et al. (2020). Materials acceleration platforms: on the way to autonomous experimentation. *Curr. Opin. Green Sustain. Chem.* 25, 100370. doi:10.1016/j.cogsc.2020.100370

Garza, A. J., Bell, A. T., and Head-Gordon, M. (2018). Mechanism of CO_2 reduction at copper surfaces: pathways to C_2 products. *ACS Catal.* 8, 1490–1499. doi:10.1021/acscatal.7b03477

Goldsmith, B. R., Esterhuizen, J., Liu, J. X., Bartel, C. J., and Sutton, C. (2018). Machine learning for heterogeneous catalyst design and discovery. *AIChe J.* 64 (7), 2311–2323. doi:10.1002/aic.16198

Gorte, R. J., Park, S., Vohs, J. M., and Wang, C. (2000). Anodes for direct oxidation of dry hydrocarbons in a solid-oxide fuel cell. *Adv. Mater.* 12, 1465–1469. doi:10.1002/1521-4095(200010)12:19<1465::aid-adma1465>3.0.co;2-9

Goyal, A., Marcandalli, G., Mints, V. A., and Koper, M. T. M. (2020). Competition between CO_2 reduction and hydrogen evolution on a gold electrode under well-defined mass transport conditions. *J. Am. Chem. Soc.* 142, 4154–4161. doi:10.1021/jacs.9b10061

Gusarov, S., Stoyanov, S. R., and Siahrostami, S. (2020). Development of fukui function based descriptors for a machine learning study of CO_2 reduction. *J. Phys. Chem. C* 124, 10079–10084. doi:10.1021/acs.jpcc.0c03101

Hummelshøj, J. S., Abild-Pedersen, F., Studt, F., Bligaard, T., and Nørskov, J. K. (2012). CatApp: a web application for surface chemistry and heterogeneous catalysis. *Angew. Chem. Int. Ed.* 51, 272–274. doi:10.1002/anie.201107947

Jain, A., Ong, S. P., Hautier, G., Chen, W., Richards, W. D., Dacek, S., et al. (2013). Commentary: the materials project: a materials genome approach to accelerating materials innovation. *APL Mater.* 1, 011002. doi:10.1063/1.4812323

Ju, H., Kaur, G., Kulkarni, A. P., and Giddey, S. (2019). Challenges and trends in developing technology for electrochemically reducing CO_2 in solid polymer electrolyte membrane reactors. *J. CO_2 Utilization* 32, 178–186. doi:10.1016/j.jcou.2019.04.003

Kibria, M. G., Edwards, J. P., Gabardo, C. M., Dinh, C. T., Seifitokaldani, A., Sinton, D., et al. (2019). Electrochemical CO_2 reduction into chemical feedstocks: from mechanistic electrocatalysis models to system design. *Adv. Mater.* 31, 1807166. doi:10.1002/adma.201807166

Kitchin, J. R. (2018). Machine learning in catalysis. *Nat. Catal.* 1, 230–232. doi:10.1038/s41929-018-0056-y

Lamoureux, P. S., Winther, K. T., Torres, J. a. G., Streibel, V., Zhao, M., Bajdich, M., et al. (2019). Machine learning for computational heterogeneous catalysis. *ChemCatChem* 11 (16), 3581–3601. doi:10.1002/cctc.201900595

Larsen, A. H., Mortensen, J. J., Blomqvist, J., Castelli, I. E., Christensen, R., Dułak, M., et al. (2017). The atomic simulation environment—a Python library for working with atoms. *J. Phys. Condens. Matter* 29, 273002. doi:10.1088/1361-648X/aa680e

Lin, R., Guo, J., Li, X., Patel, P., and Seifitokaldani, A. (2020). Electrochemical reactors for CO_2 conversion. *Catalysts* 10, 473. doi:10.3390/catal10050473

Liu, X., Xiao, J., Peng, H., Hong, X., Chan, K., and Nørskov, J. K. (2017). Understanding trends in electrochemical carbon dioxide reduction rates. *Nat. Commun.* 8, 1–7. doi:10.1038/ncomms15438

Liu, Y., Leung, K. Y., Michaud, S. E., Soucy, T. L., and Mccrory, C. C. L. (2019). Controlled substrate transport to electrocatalyst active sites for enhanced selectivity in the carbon dioxide reduction reaction. *Comments Inorg. Chem.* 39, 242–269. doi:10.1080/02603594.2019.1628025

Lu, Q., and Jiao, F. (2016). Electrochemical CO_2 reduction: electrocatalyst, reaction mechanism, and process engineering. *Nano Energy* 29, 439–456. doi:10.1016/j.nanoen.2016.04.009

Ma, X., Li, Z., Achenie, L. E. K., and Xin, H. (2015). Machine-learning-augmented chemisorption model for CO_2 electroreduction catalyst screening. *J. Phys. Chem. Lett.* 6, 3528–3533. doi:10.1021/acs.jpclett.5b01660

Malek, A., Eslamibidgoli, M. J., Mokhtari, M., Wang, Q., Eikerling, M. H., and Malek, K. (2019). Virtual materials intelligence for design and discovery of advanced electrocatalysts. *Chemphyschem.* 20, 2946–2955. doi:10.1002/cphc.201900570

Mandal, M. (2020). CO_2 electroreduction to multicarbon products. *ChemElectroChem.* 7 (18), 3712–3715.doi:10.1002/celc.202000798

Mathew, K., Montoya, J. H., Faghaninia, A., Dwarakanath, S., Aykol, M., Tang, H., et al. (2017). Atomate: a high-level interface to generate, execute, and analyze computational materials science workflows. *Comput. Mater. Sci.* 139, 140–152. doi:10.1016/j.commatsci.2017.07.030

Meyer, B., Sawatlon, B., Heinen, S., Von Lilienfeld, O. A., and Corminboeuf, C. (2018). Machine learning meets volcano plots: computational discovery of cross-coupling catalysts. *Chem. Sci.* 9, 7069–7077. doi:10.1039/c8sc01949e

Nitopi, S., Bertheussen, E., Scott, S. B., Liu, X., Engstfeld, A. K., Horch, S., et al. (2019). Progress and perspectives of electrochemical CO_2 reduction on copper in aqueous electrolyte. *Chem. Rev.* 119, 7610–7672. doi:10.1021/acs.chemrev.8b00705

Pedregosa, F., Varoquaux, G., Gramfort, A., Michel, V., Thirion, B., Grisel, O., et al. (2011). Scikit-learn: machine learning in Python. *J. Machine Learn. Res.* 12, 2825–2830. doi:10.5555/1953048.2078195

Pizzi, G., Cepellotti, A., Sabatini, R., Marzari, N., and Kozinsky, B. (2016). AiiDA: automated interactive infrastructure and database for computational science. *Comput. Mater. Sci.* 111, 218–230. doi:10.1016/j.commatsci.2015.09.013

Qiao, J., Liu, Y., Hong, F., and Zhang, J. (2014). A review of catalysts for the electroreduction of carbon dioxide to produce low-carbon fuels. *Chem. Soc. Rev.* 43, 631–675. doi:10.1039/c3cs60323g

Rogelj, J., Schaeffer, M., and Hare, B. (2015). *Timetables for zero emissions and 2050 emissions reductions: state of the science for the ADP agreement*. Berlin, Germany: Climate Analytics.

Schleder, G. R., Padilha, A. C., Acosta, C. M., Costa, M., and Fazzio, A. (2019). From DFT to machine learning: recent approaches to materials science–a review. *J. Phys. Mater.* 2, 032001. doi:10.1088/2515-7639/ab084b

Schlexer Lamoureux, P., Winther, K. T., Garrido Torres, J. A., Streibel, V., Zhao, M., Bajdich, M., et al. (2019). Machine learning for computational heterogeneous catalysis. *ChemCatChem.* 11, 3581–3601. doi:10.1002/cctc.201900595

Smith, A., Keane, A., Dumesic, J. A., Huber, G. W., and Zavala, V. M. (2020). A machine learning framework for the analysis and prediction of catalytic activity from experimental data. *Appl. Catal. B: Environ.* 263, 118257. doi:10.1016/j.apcatb.2019.118257

Tran, K., and Ulissi, Z. W. (2018). Active learning across intermetallics to guide discovery of electrocatalysts for CO_2 reduction and H_2 evolution. *Nat. Catal.* 1, 696–703. doi:10.1038/s41929-018-0142-1

Varnek, A., Kireeva, N., Tetko, I. V., Baskin, I. I., and Solov'ev, V. P. (2007). Exhaustive QSPR studies of a large diverse set of ionic liquids: how accurately can we predict melting points? *J. Chem. Inf. Model.* 47, 1111–1122. doi:10.1021/ci600493x

Wang, Y., Liu, J., Wang, Y., Al-Enizi, A. M., and Zheng, G. (2017). Tuning of CO_2 Reduction selectivity on metal electrocatalysts. *Small* 13, 1701809. doi:10.1002/smll.201701809

Zahrt, A. F., Henle, J. J., Rose, B. T., Wang, Y., Darrow, W. T., and Denmark, S. E. (2019). Prediction of higher-selectivity catalysts by computer-driven workflow and machine learning. *Science* 363, eaau5631. doi:10.1126/science.aau5631

Zhang, X., Song, Y., Wang, G., and Bao, X. (2017). Co-electrolysis of CO_2 and H_2O in high-temperature solid oxide electrolysis cells: recent advance in cathodes. *J. Energ. Chem.* 26, 839–853. doi:10.1016/j.jechem.2017.07.003

Zheng, Y., Wang, J., Yu, B., Zhang, W., Chen, J., Qiao, J., et al. (2017). A review of high temperature co-electrolysis of H_2O and CO_2 to produce sustainable fuels using solid oxide electrolysis cells (SOECs): advanced materials and technology. *Chem. Soc. Rev.* 46, 1427–1463. doi:10.1039/c6cs00403b

Zhu, D. D., Liu, J. L., and Qiao, S. Z. (2016). Recent advances in inorganic heterogeneous electrocatalysts for reduction of carbon dioxide. *Adv. Mater.* 28, 3423–3452. doi:10.1002/adma.201504766

Conflict of Interest: The authors declare that the research was conducted in the absence of any commercial or financial relationships that could be construed as a potential conflict of interest.

frontiers in Energy Research

REVIEW
published: 04 May 2021
doi: 10.3389/fenrg.2021.654460

The Sabatier Principle in Electrocatalysis: Basics, Limitations, and Extensions

Hideshi Ooka[1], Jun Huang[2] and Kai S. Exner[3,4]**

[1] Center for Sustainable Resource Science (CSRS), RIKEN, Wako, Japan, [2] Institute of Theoretical Chemistry, Ulm University, Ulm, Germany, [3] Faculty of Chemistry, Theoretical Inorganic Chemistry, University Duisburg-Essen, Essen, Germany, [4] Cluster of Excellence RESOLV, Bochum, Germany

The Sabatier principle, which states that the binding energy between the catalyst and the reactant should be neither too strong nor too weak, has been widely used as the key criterion in designing and screening electrocatalytic materials necessary to promote the sustainability of our society. The widespread success of density functional theory (DFT) has made binding energy calculations a routine practice, turning the Sabatier principle from an empirical principle into a quantitative predictive tool. Given its importance in electrocatalysis, we have attempted to introduce the reader to the fundamental concepts of the Sabatier principle with a highlight on the limitations and challenges in its current thermodynamic context. The Sabatier principle is situated at the heart of catalyst development, and moving beyond its current thermodynamic framework is expected to promote the identification of next-generation electrocatalysts.

Keywords: electrocatalysis, Sabatier principle, thermodynamics, kinetics, theory

OPEN ACCESS

Edited by:
Soorathep Kheawhom, Chulalongkorn University, Thailand

Reviewed by:
Mingchuan Luo, Leiden University, Netherlands
Supareak Praserthdam, Chulalongkorn University, Thailand

****Correspondence:***
Hideshi Ooka
hideshi.ooka@riken.jp
Kai S. Exner
kai.exner@uni-due.de

Specialty section:
This article was submitted to Electrochemical Energy Conversion and Storage, a section of the journal Frontiers in Energy Research

Received: *16 January 2021*
Accepted: *26 March 2021*
Published: *04 May 2021*

Citation:
Ooka H, Huang J and Exner KS (2021) The Sabatier Principle in Electrocatalysis: Basics, Limitations, and Extensions. Front. Energy Res. 9:654460. doi: 10.3389/fenrg.2021.654460

INTRODUCTION

Electrocatalysis is gaining widespread attention as a critical technology to enhance the sustainability of human society. Core technology for the hydrogen economy, such as fuel cells and water electrolysis, rely on efficient electrocatalysts to perform the interconversion between water and hydrogen (Mehta and Cooper, 2003). The electrochemical synthesis of next-generation fuels, derived from atmospheric CO_2 rather than from fossil fuels, is also under intensive investigation (Zhang et al., 2018). Even the carbon footprint of the artificial nitrogen cycle can be improved using electrocatalysis, because the Haber-Bosch process used to synthesize ammonia and chemical fertilizers requires vast amounts of hydrogen, which are mainly produced from fossil fuels (Smith et al., 2020). Therefore, the development of electrocatalysts, especially those based on earth-abundant elements, is currently a central topic in chemistry and energy research.

However, the parameter space to search for new catalytic materials is massive. For example, oxides, such as the dimensionally stable anodes in the chlor-alkali industry (Karlsson and Cornell, 2016) or the iridium oxides in electrolyzers (Carmo et al., 2013), are a widely used family of catalysts. Based on the periodic table of elements, a chemist may choose from approximately 40 elements with which to make a single metal oxide. However, if the material candidates are expanded to binary, ternary, or even more complex mixed oxides, the possibility of materials expands massively ($40^4 > 2$ million), especially if dopants are considered. Furthermore, every elemental composition

has multiple possible atomic orientations in the bulk and the surface (Ulissi et al., 2017). Surface reconstruction, which can potentially occur during catalysis, are an additional contribution to the huge parameter space of materials (Fabbri et al., 2017; Li et al., 2019), leading to a combinatorial explosion of the possible candidate materials. In order to identify next-generation catalysts within this massive parameter space, a design principle which connects the chemical structure to catalytic activity is needed.

Nowadays, this role is fulfilled by the Sabatier principle (Sabatier, 1913; Che, 2013). This principle states that "an ideal catalyst must bind to the reactant at an intermediate strength which is neither too weak nor too strong." This concept is based on the notion that if the bond is too weak, the catalyst and the reactant will hardly interact with each other, whereas if the bond is too strong, the reactant will not desorb from the catalyst surface, effectively inhibiting further reactions. This principle was first proposed in 1913 by the Nobel laureate, Paul Sabatier, based on empirical observations (Sabatier, 1913; Che, 2013). At that time, there was no method to directly obtain the binding energy, and therefore, other experimentally accessible parameters, such as hydride (Trasatti, 1972) or chelate formation energies (Rootsaert and Sachtler, 1960), were used to quantitatively assess the interaction between the catalyst and the reactant. A century later, however, it is now the norm to directly evaluate the binding energy of intermediate states using *in silico* computation (Nørskov et al., 2004; Rossmeisl et al., 2005; Rossmeisl et al., 2007b). In particular, the widespread accessibility of density functional theory (DFT) has made it almost every-day practice to predict the activity of a potential candidate prior to performing actual experiments (Greeley et al., 2006). Recent computational studies are further supplemented by machine-learning techniques to reduce computational costs (Back et al., 2019a,b; Li et al., 2020; Ulissi et al., 2016, 2017). In the following section, we will provide a brief, conceptual overview of the Sabatier principle in its current form, which has been widely employed to evaluate catalysts *in silico*. In section "CHALLENGES OF THE SABATIER PRINCIPLE AND APPROACHES FORWARD," its challenges and limitations will be highlighted, along with ongoing approaches to overcome these bottlenecks. The main question addressed in this review is "what is the (theoretical) requirement for active electrocatalysts?", not "which material satisfies these conditions?" For the reader with an interest in the progress of state-of-the-art materials, we would like to recommend several excellent reviews published recently (Xiao et al., 2015; Tahir et al., 2017; Song et al., 2020; Theerthagiri et al., 2020).

THE SABATIER PRINCIPLE AND ITS THERMODYNAMIC INTERPRETATION

The Ideal Free-Energy Landscape

The free-energy difference between the initial (reactant) and final (product) states is defined by thermodynamics and is independent of the actual catalyst. When the applied electrode potential (U) is the same as the half-cell potential U_0, the free energies of the reactant and product are equal, and the system is in equilibrium. The reaction can proceed once the electrode potential is shifted away from the half-cell potential, such that the free energy of the product state becomes lower than that of the reactants. The difference between the applied potential and the half-cell potential is known as the applied overpotential, $\eta = U - U_0$. A positive overpotential is required for anodic (oxidation) processes, such as the chlorine evolution reaction (CER), whereas a negative overpotential is necessary for cathodic (reduction) reactions, such as the hydrogen evolution reaction (HER). However, the word "overpotential" is used to refer to absolute values in the following sections for simplicity, and hence "a larger overpotential" should be interpreted as the reaction becoming more thermodynamically favorable.

Within this framework, the role of the catalyst is to tune the free-energy landscape between the reactant and the product in a way that is beneficial for the catalytic process (Koper, 2011b). For a two-step reaction, such as the CER (Trasatti, 1987; Exner, 2020b) or HER (Gerischer and Gerischer, 1956; Parsons, 1958; Nørskov et al., 2005; Zeradjanin et al., 2016; Exner, 2020e), there is only one reaction intermediate, whose free energy depends on the catalyst surface to which it is adsorbed to (**Figure 1A**; Koper, 2011b, 2013a). The free energy of this reaction intermediate with respect to the reactant at equilibrium potential is denoted as ΔG_{RI}. Currently, the general consensus of an ideal free-energy landscape is one where this reaction intermediate has the same free energy as the reactant and the product at equilibrium. In other words, $\Delta G_{RI} = 0$ is the criterion for an ideal catalyst (Koper, 2011b, 2013a; Laursen et al., 2012), and ΔG_{RI} can be considered as a "descriptor" for catalytic activity (Greeley and Nørskov, 2007; Peterson and Nørskov, 2012; Dubouis and Grimaud, 2019).

The reason behind why thermoneutral bonding ($\Delta G_{RI} = 0$) is considered ideal is shown in **Figure 1**. If the reaction intermediate is bound too weakly ($\Delta G_{RI} > 0$), the first step is thermodynamically unfavorable (**Figure 1A**, blue lines). On the other hand, if the intermediate is bound too strongly ($\Delta G_{RI} < 0$), the second step is thermodynamically unfavorable (**Figure 1B**, green lines). If we assume that the efficiency of the overall reaction is determined by the most thermodynamically unfavorable step, a thermoneutral landscape where no elementary step is thermodynamically unfavorable corresponds to the ideal situation (**Figure 1A**, red lines). This is often discussed quantitatively using the concept of the thermodynamic overpotential (η_{TD}), introduced by Nørskov, Rossmeisl, and co-workers (Nørskov et al., 2004). η_{TD} is defined as the minimum overpotential necessary to make all elementary reaction steps either thermoneutral or exergonic (Rossmeisl et al., 2005; Rossmeisl et al., 2007b). A smaller value of η_{TD} implies higher activity, and η_{TD} is commonly used to compare and rationalize the activity of various materials. In the case of a two-step reaction, $\eta_{TD} = |\Delta G_{RI}|/e$ with e = elementary charge, and therefore, a thermoneutral landscape ($\Delta G_{RI} = 0$) yields $\eta_{TD} = 0$ V. For this reason, the thermodynamically ideal catalyst is

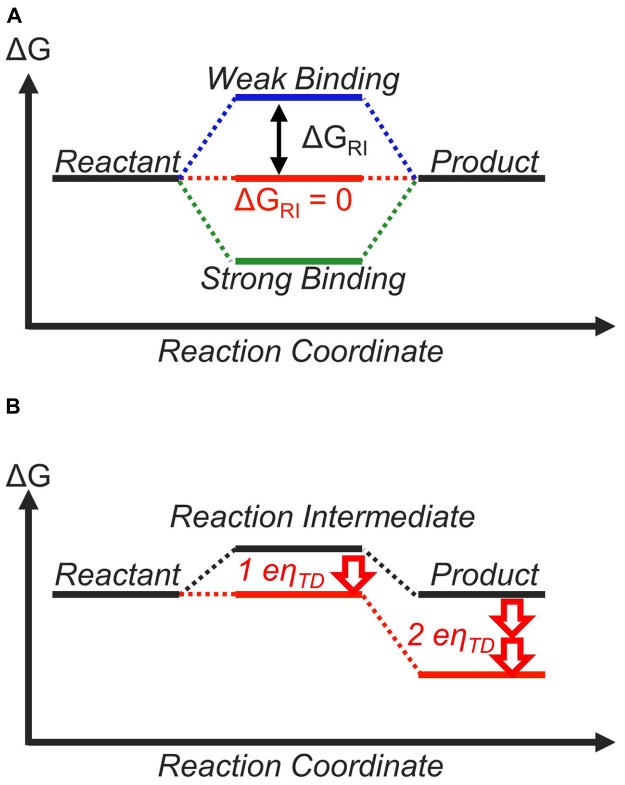

FIGURE 1 | The thermodynamic free-energy landscape of a catalytic reaction with one reaction intermediate. **(A)** indicates the free-energy landscape for different binding strengths (ΔG_{RI}) of the reaction intermediate. **(B)** shows the free-energy landscape for a catalyst that binds the reaction intermediate weakly ($\Delta G_{RI} > 0$ at equilibrium, black). By applying an overpotential of $\eta = \eta_{TD}$, all elementary reaction steps become thermoneutral or downhill in free energy (red).

sometimes referred to as the "zero overpotential catalyst" (Koper, 2011b, 2013a; Craig et al., 2019). This discussion is based on purely thermodynamic considerations and does not explicitly differentiate between outer-sphere and inner-sphere electron transfer mechanisms. However, all electrocatalytic reactions involve the rearrangement of chemical bonds, suggesting they can be considered as inner-sphere processes (Bard, 2010; Schmickler and Santos, 2010).

Nowadays, the free-energy landscape of an electrocatalyst can be calculated using computational techniques, such as density functional theory (DFT). Nørskov and co-workers introduced the computational hydrogen electrode (CHE) model, which substitutes the free energy of an electron-proton pair with that of half a hydrogen molecule at $U = 0$ V *vs.* RHE (reversible hydrogen electrode) (Nørskov et al., 2004). Using this method, it is possible to determine the free energies of reaction intermediates as a function of the applied electrode potential and pH by *a posteriori* analysis. Once the free energies of reaction intermediates are determined by DFT at zero electrode potential and pH zero conditions, they can be shifted to any electrochemical condition based on the CHE model (Calle-Vallejo and Koper, 2012). In principle, this method can also be used to determine the free energies of charged reaction intermediates (Craig et al., 2019), although in practice, most studies focus on non-charged intermediates (Calle-Vallejo and Koper, 2012) due to the large computational errors for charged intermediate states on solid surfaces. Regardless of these limitations, the CHE model and the thermodynamic overpotential (η_{TD}) are by far the most popular way to evaluate electrocatalytic activity *in silico*. To date, many experimental trends have been rationalized and new materials have been identified based on this simple framework (Hinnemann et al., 2005; Greeley et al., 2006; Diaz-Morales et al., 2016; Seitz et al., 2016).

Practical Application and Linear Scaling Relationships

From a thermodynamic viewpoint, the free-energy landscape should be completely flat at equilibrium to obtain the ideal catalyst. This notion holds true even when the mechanism involves more than two elementary steps. In practice, however, it is much easier to tune the landscape for two-electron transfer reactions, such as the HER and CER, compared to reactions which transfer more electrons, such as the oxygen evolution and reduction reactions (OER and ORR: $2\ H_2O \leftrightarrow O_2 + 4H^+ + 4e^-$). This is reflected in the experimental literature, as some HER/HOR catalysts, such as Pt, are so active that practically no overpotential is visible in the cyclic voltammogram and the current density increases exponentially as soon as an overpotential is applied (Auinger et al., 2011; Durst et al., 2014). Other examples include a Pd-based catalyst which also exhibits almost no overpotential to catalyze the two-electron transfer reaction between CO_2 and formic acid (Kortlever et al., 2015a). In contrast, even the most active OER/ORR catalysts require overpotentials of several hundred mV to obtain current densities in the order of mA/cm^2 (Suntivich et al., 2011a,b; Diaz-Morales et al., 2016; Seitz et al., 2016; Chen et al., 2017). The reason why it is difficult to realize thermodynamically ideal catalysts for reactions with more than two electrons transferred has been rationalized due to the so-called scaling relationships, which impose physical limitations on how the free-energy landscape can be tuned. Let us take the OER as an example.

The OER is a four-electron process, in which water molecules are transformed into gaseous oxygen according to equation (1):

$$2H_2O_{(aq)} \rightarrow O_{2(g)} + 4H^+ + 4e^-,\ U_0 = 1.23\text{V}\ \textit{vs.}\ \text{RHE} \quad (1)$$

Rossmeisl et al. (2005, 2007b) calculated the OER free-energy landscape according to a pathway, which assumes the OH, O, and OOH adsorbates as reaction intermediates. Each step was assumed to proceed via concerted proton-electron transfer steps. This was originally due to technical reasons, namely to maintain charge neutrality (cf. Section "Stepwise Proton-Electron Transfer and Charged Intermediates") (Rossmeisl et al., 2005, 2007b), but this mechanism is still adopted in the recent literature

(Halck et al., 2014; Busch et al., 2016; Dickens and Nørskov, 2017; Hajiyani and Pentcheva, 2018).

$$H_2O_{(l)} + S \rightarrow S\text{-}OH + H^+ + e^- \quad \Delta G_1 \quad (2)$$

$$S - OH \rightarrow S\text{-}O + H^+ + e^- \quad \Delta G_2 \quad (3)$$

$$S - O + H_2O_{(l)} \rightarrow S\text{-}OOH + H^+ + e^- \quad \Delta G_3 \quad (4)$$

$$S - OOH \rightarrow S + O_{2(g)} + H^+ + e^- \quad \Delta G_4 \quad (5)$$

In equations (2) – (5), S denotes the active site of an OER catalyst. In order to realize an ideal catalyst, every step must be thermoneutral at the equilibrium potential. In other words, when the free-energy change of the i^{th} step is denoted as ΔG_i, the criterion of a thermodynamically ideal catalyst is: $\Delta G_1 = \Delta G_2 = \Delta G_3 = \Delta G_4 = 0$ eV at $U = 1.23$ V *vs.* RHE (**Figure 2**, blue lines). This results in $\Delta G_1 = \Delta G_2 = \Delta G_3 = \Delta G_4 = 1.23$ eV at $U = 0$ V *vs.* RHE (**Figure 2**, black lines), which corresponds to the usual conditions of DFT calculations within the CHE framework.

In reality however, no electrode material that fulfills the requirements of a thermodynamically ideal catalyst has been identified so far. This is because the binding energies of structurally similar intermediates are difficult to tune independently. For example, the binding energies of the OH and OOH adsorbates are known to exhibit a linear correlation. This relationship is often referred to as a linear scaling relationship (Man et al., 2011; Viswanathan et al., 2012), and is given by equation (6):

$$\Delta G_2 + \Delta G_3 = 3.2\ \text{eV} \quad (6)$$

The number 3.2 eV is the value that has been reported for planar metal oxides (Rossmeisl et al., 2005; Man et al., 2011; Viswanathan et al., 2012). The values in more recent studies span a range of about 2.8 eV – 3.4 eV (Calle-Vallejo et al., 2013; Viswanathan and Hansen, 2014; Tao et al., 2019; Exner, 2020a), suggesting that different classes of materials may follow different scaling relationships.

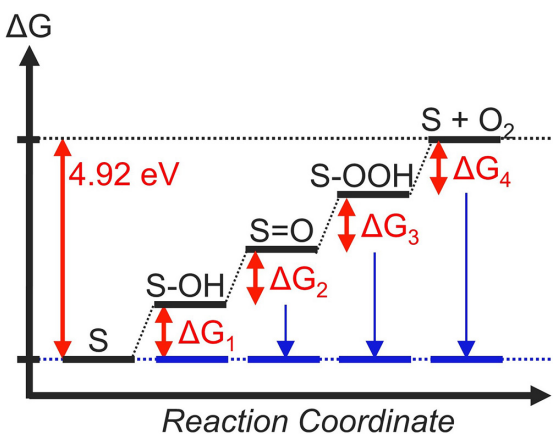

FIGURE 2 | The thermodynamic landscape of an ideal OER catalyst at $U = 0$ V (black lines) and $U = 1.23$ V (blue lines). Relative energies are indicated in red letters.

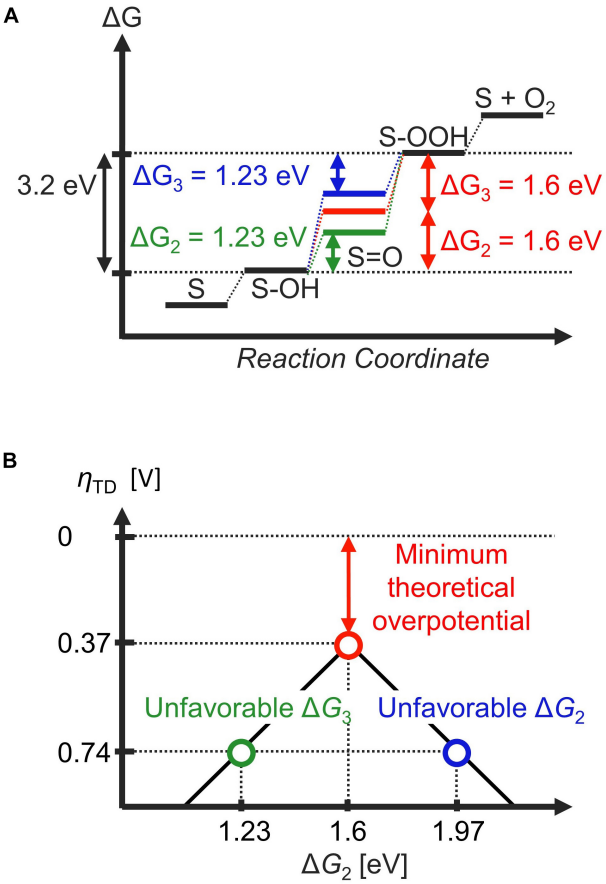

FIGURE 3 | The effect of the scaling relation on the thermodynamic free-energy landscape for the oxygen evolution reaction (OER), assuming the participation of OH, O, and OOH adsorbates within the catalytic cycle. **(A)** Due to the linear scaling relationship between the OH and OOH adsorbates ($\Delta G_2 + \Delta G_3 = 3.2$ eV), it is not possible to adjust both ΔG_2 and ΔG_3 to 1.23 eV simultaneously (blue and green pathways). The minimum thermodynamic (theoretical) overpotential is realized when $\Delta G_2 = \Delta G_3 = 1.6$ eV; that is, the free-energy penalty due to the scaling relations is shared equally between these two elementary steps. **(B)** The thermodynamic overpotential is plotted as a function of ΔG_2 in the form of a volcano plot.

In any case, the scaling relationship directly implies that a thermodynamically ideal catalyst cannot be realized. For example, if a certain electrocatalyst exhibits ideal thermodynamics for the second step ($\Delta G_2 = 1.23$ eV at $U = 0$ V), the scaling relationships indicate that the third step cannot be thermodynamically ideal due to: $\Delta G_3 = 3.2$ eV – 1.23 eV = 1.97 eV (**Figure 3A**, green line). On the other hand, setting ΔG_3 to 1.23 eV leads to a scenario where ΔG_2 is unfavorable (**Figure 3B**, blue line). In other words, optimizing either ΔG_2 or ΔG_3 leads to the other deviating from the thermodynamic ideal. If the most thermodynamic unfavorable reaction step dictates catalytic activity, the best compromise is to distribute the free-energy penalty from the scaling relationship into equal parts; that is, $\Delta G_2 = \Delta G_3 = 3.2$ eV / 2 = 1.6 eV (Man et al., 2011). In this case, the thermodynamic overpotential amounts to $\eta_{TD} = 1.60$ V – 1.23 V = 0.37 V

(**Figure 3A**, red line), which is significantly smaller than η_{TD} = 1.97 V – 1.23 V = 0.74 eV which results by making either the second step or third step thermodynamically ideal (**Figure 3A**, blue and green lines). In terms of the volcano plot, electrocatalysts with optimum ΔG_2 or ΔG_3 are located at the leg of the volcano because they bind the O adsorbate either too strongly or too weakly, respectively, such that the other step becomes thermodynamically prohibitive. This leads to a minimum thermodynamic overpotential, also denoted as minimum theoretical overpotential, of 0.37 V for the OER (**Figure 3B**). This value is roughly consistent with the experimental overpotential necessary to reach a current density of 10 mA/cm^2, a benchmark for the solar-cell community (Suntivich et al., 2011b; Diaz-Morales et al., 2016; Seitz et al., 2016). However, some recent materials have overpotentials below 200 mV to sustain of 10 mA/cm^2 (Kim et al., 2017; Su et al., 2018; Retuerto et al., 2019; Hao et al., 2020), indicating that η_{TD} is not necessarily a quantitatively accurate descriptor of electrocatalytic activity (Exner, 2021a). This discrepancy is most likely because the thermodynamic overpotential and the experimental overpotential have different definitions, and thus have no direct physical correlation: while η_{TD} is a purely thermodynamic indicator of activity based on the free-energy landscape at equilibrium (zero overpotential), the experimental overpotential η must be evaluated at some non-zero current density, and is thus always influenced by the kinetics. However, the concept of η_{TD} does offer at least a qualitative explanation why the OER is a more difficult process compared to the HER and other two-electron processes, where the thermodynamics is not restrained by any scaling relationships.

Examples for the Application of the Sabatier Principle in Practice

The Sabatier principle and its thermodynamic interpretation have been successfully applied for the development of new catalysts. For example, Greeley et al. used ΔG_{RI} to screen alloy catalysts for the HER (Greeley et al., 2006), and identified a Bi-Pt surface alloy with higher electrocatalytic activity than platinum. Similarly, Hinnemann et al. (2005) identified MoS_2 nanoparticles as a potential HER electrocatalyst by applying the Sabatier principle in its thermodynamic form. The work of Seitz et al. is another example, where the highly active $IrO_x/SrIrO_3$ catalyst for the OER was predicted based on the framework of scaling relations and η_{TD} discussed in the previous section (Seitz et al., 2016). These works, among others, contributed to the fact that *in silico* screening procedures became extremely popular in electrocatalysis and, nowadays, are broadly used for the discovery of catalytic materials (Yao et al., 2019; Yang et al., 2020).

More recently, the rise of data science has promoted the usage of the Sabatier principle for materials' screening (Basdogan et al., 2020a; Toyao et al., 2020). For example, Ulissi et al. used a neural network-based surrogate model to reduce the number of explicit DFT calculations by an order of magnitude, allowing them to extensively screen active sites for CO_2 reduction (Ulissi et al., 2017). Machine-learning has also been beneficial to obtain more accurate binding energies across wider configurations (Back et al., 2019a).

Application of the Sabatier Principle to Enzymes, Molecular Catalysts, and Beyond

The Sabatier principle has also been successfully applied to enzymes and homogeneous catalysts. For example, biological OER and ORR enzymes were compared with their artificial counterparts, and their higher activity was rationalized by their lower η_{TD} (Rossmeisl et al., 2007a; Kjaergaard et al., 2010). These enzymes deviate from the linear scaling relationships reported for planar metal oxides (Man et al., 2011). Therefore, this finding has stimulated various studies aiming to find strategies to break scaling relations (Li and Sun, 2016; Pegis et al., 2017; Huang et al., 2019). However, breaking the scaling relationship in itself is not a sufficient condition to realize active materials, because it does not guarantee a lower η_{TD} as the recent literature has shown (Govindarajan et al., 2018; Exner, 2020f; Piqué et al., 2020).

More recently, Kari et al. (2018) demonstrated experimentally that enzymes also follow a Sabatier-type trend. The Michaelis-Menten constant K_m is a quantitative measure of the substrate-enzyme interaction and was used as a substitute for the binding energy to construct volcano plots of various cellulases. The maximum rate was observed at intermediate values of K_m, suggesting that an intermediate interaction strength between the catalyst and the reactant may also be important to enhance enzymatic activity.

Scaling relations and volcano plots have also been introduced into the field of organometallic chemistry. For example, the thermodynamics of Suzuki coupling catalysts was rationalized based on linear scaling relationships and free-energy changes (Busch et al., 2015, 2016; Wodrich et al., 2018). Catalysts known to be active from experiments appear near the top of the volcano plot, suggesting the Sabatier principle may also help in the understanding of organometallic catalysts.

The Sabatier principle was also transferred to the field of lithium-ion batteries in order to study the intercalation of lithium-ions into spinel lithium titanate electrodes (Exner, 2018, 2019e). While the conventional Sabatier principle only considers activity by analyzing binding energies, stability was introduced as a second performance parameter to rationalize experimental trends by the construction of activity-stability volcano plots. The volcano plots indicate that an intermediate lithium binding strength is the best compromise between enhanced energy density while maintaining stability, thus building a bridge between the catalysis and battery science communities (Exner, 2018, 2019e). This may be the reason why the idea of an intermediate binding strength in conjunction with the volcano notion has found entrance for the screening of electrode materials in batteries (Pande and Viswanathan, 2019). The advanced framework of activity-stability volcano curves can also be employed to electrocatalytic processes such as the CER (Exner, 2019a).

CHALLENGES OF THE SABATIER PRINCIPLE AND APPROACHES FORWARD

The simplicity of the Sabatier principle and its thermodynamic interpretation has led to its widespread application so far. At the same time, however, this simplicity implies limitations where theory does not match with experiments. This can be due to issues at multiple levels.

For example, the binding energy estimated from the CHE model may not reflect the true binding energy without a more extensive treatment of factors such as solvation or the effective electrochemical potential in the double layer. In this case, the discrepancy between theory and experiments is a matter of accuracy which can be resolved by sufficient technical advancement. The Sabatier principle itself is not the problem if a more accurate binding energy can yield predictions consistent with experiments.

In other cases, the issue may be rooted deeper in the theory. For example, the Sabatier principle has its basis on the thermodynamics because the binding energy is in essence an equilibrium constant between the adsorption and desorption of a reactant. However, thermodynamics alone cannot explain how quickly electron-transfer reactions occur. Conventionally, kinetic factors such as activation barrier heights are assumed to scale universally with the thermodynamics. However, if this assumption is not valid, activity trends can no longer be predicted from thermodynamic criteria such as the thermodynamic overpotential, binding energies, or scaling relations. This is an issue which is beginning to attract more attention, stimulating recent microkinetic studies (Ooka and Nakamura, 2019; Exner, 2020c,e) which have attempted to expand the Sabatier principle (Exner, 2019d, 2021b) by the incorporation of overpotential and kinetic factors.

Finally, there are some chemical processes which the Sabatier principle does not consider at all. The Sabatier principle predicts the intrinsic activity of a material, but in some cases, the observed electrocatalytic behavior is not purely due to the intrinsic activity. For example, mass transport is well known to influence electrode kinetics, such as in the case of the CO_2 reduction reaction (Ringe et al., 2020). The electrochemically active surface area is another consideration which cannot be determined by DFT calculations due to the usage of simplified slab models.

Proper comparison between theoretical and experimental activities requires calculation of the full free-energy landscape including the kinetics, which is computationally expensive. This is the reason why theoretical and experimental activities are often evaluated at the level of material trends by comparing the thermodynamics (theory) with the kinetics (experiment). A more rigorous and critical verification based on a direct quantitative comparison would be beneficial to improve the accuracy of theoretical predictions. In the following sections, we have attempted to sort the existing challenges of the Sabatier principle and the CHE model in order to provide a guideline of possible approaches beyond the current thermodynamic framework.

Challenges to Accurately Predict the Binding Energy

Influence of the Electrolyte: Beyond the CHE Model

Electrocatalysis is in general a phenomenon which is also dependent on the electrolyte. The most famous example for pH dependence may be the HER on platinum, which is more active in acid compared to alkaline conditions (Sheng et al., 2010). However, the CHE model treats the electrolyte ion concentrations of protons and hydroxides based on the Nernst equation, and thus, the thermodynamic overpotential η_{TD} is independent of the pH. As η_{TD} is the common theoretical measure for electrocatalytic activity, this is a direct contradiction with experiments. Other ions besides protons and hydroxides in the electrolyte may also influence electrocatalytic activity (Xue et al., 2018; Garcia et al., 2019; Shinagawa et al., 2019), yet such factors are not considered in the CHE model.

Although the influence of the electrolyte can be ascribed to multiple factors, at least part of the reason is due to the binding energy being electrolyte dependent. The electrolyte determines the double-layer structure surrounding the adsorbate (Ledezma-Yanez et al., 2017), which has direct implications on the stability of intermediates on the electrode.

The double layer structure is also influenced by the electrochemical potential, and thus the binding energy may also deviate from the Nernstian behavior assumed in the CHE model when the electrode potential or pH is changed (Hörmann et al., 2019, 2020). There are several recent studies which have attempted to explain the pH dependence of Pt in the HER by considering the binding energies to be pH dependent (Kunimatsu et al., 2007; Sheng et al., 2010, 2015; Zheng et al., 2016; Ledezma-Yanez et al., 2017; Zhu et al., 2020). Yet, such effects are not considered in most theoretical studies, which tacitly assume the binding energy to be a material-specific value which is pH independent (Nørskov et al., 2005, 2009).

The above-highlighted challenges could potentially be overcome if the electrolyte solution, consisting of all ions and solvent molecules, is explicitly modeled in the theoretical framework. This, however, requires computationally expensive ab initio molecular dynamics (AIMD) simulations (Kenmoe et al., 2018; Sakong and Groß, 2020). The cell sizes that can be treated by AIMD (Groß, 2020) so far are too small to simulate the dependency of binding energies on electrolyte concentrations (Groß, 2020). Although a steep increase in the computational power is needed to accurately determine the binding energies as a function of electrolyte composition, the effect of the electrolyte solution on the binding energy of an intermediate is significant, nonetheless. For example, explicit consideration of a solvent bilayer was found to change the DFT-obtained binding energy of adsorbed hydroxyl (OH_{ads}) on Pt(111) by −0.5 eV, and assuming the same solvation configuration for different metals resulted in errors exceeding 0.2 eV (He et al., 2017). This is the same order of magnitude compared to typical DFT errors (Nørskov et al., 2009), indicating that proper modeling of solvation within the available methods is indispensable for the computational design of electrocatalysts.

Currently, continuum solvation models such as Vaspsol (Mathew et al., 2014, 2019), COSMO (Klamt and Schüürmann, 1993), or Jaguar (Bochevarov et al., 2013) are commonly used to describe solvation at the electrode/electrolyte interface (Abidi et al., 2020; Basdogan et al., 2020b; Groß, 2020). However at least in the case of the intermediates relevant to the ORR and CO_2 reduction reactions on Cu, Au, and Pt, the widely used continuum solvation models did not improve the accuracy of binding energies compared to the respective calculations in vacuum (Heenen et al., 2020). Due to the complexity and computational costs of AIMD, solvation models by the inclusion of machine-learning techniques have been developed (Basdogan et al., 2020b), which are a promising alternative to continuum solvation models.

Another shortcoming of the CHE model refers to the fact that this approach relies on a canonical ensemble, in which the charge is fixed. Experimental conditions, however, correspond to a grand canonical ensemble where the electrode potential is fixed instead of the charge. Recent progress in this field put forth grand canonical models beyond the CHE method (Hansen and Rossmeisl, 2016; Hörmann et al., 2019, 2020; Abidi et al., 2020), allowing the electrode potential to be explicitly included into the DFT calculations (Govind Rajan et al., 2020; Groß, 2020). Yet, a limitation of this approach is that the outcome may severely depend on the chosen value for the proton/hydrogen work function, for which values between 3.9 eV and 4.7 eV have been reported in the literature (Busch et al., 2020; Bhattacharyya et al., 2021).

Influence of Surface Charge

Another challenge in the accurate evaluation of the binding energy is the influence of the surface charge density on the electrode. Adsorbates on the electrode surface are usually charged due to the partial charge transfer in the chemisorption process. For instance, halogen ions adsorbed to a metal surface still carry a significant fraction of its negative charge after adsorption (Ávila et al., 2020) leading to the formation of surface dipole moments. The free energy of these surface dipoles depends on the local electric field, which is further modulated by the electrode surface charge. Therefore, the binding energy of reaction intermediates usually depends on the electrode surface charge. Furthermore, the electrode surface charge determines the local reaction conditions, such as the reactant concentration and the driving force at the reaction plane, thus having a pronounced effect on electrocatalytic activity. A recent example is the peroxodisulfate reduction on Pt, which has been shown to be inhibited when the surface charge density is negative (Martnez-Hincapié et al., 2018). This result could be explained by incorporating effects of the electrochemical double layer on electron transfer kinetics described using the Marcus–Hush–Chidsey theory (Zhang and Huang, 2020).

In order to incorporate double layer effects, an explicit model of the interface between the electrode and the electrolyte is necessary. When a reaction intermediate is adsorbed to the electrode surface, this is usually concurrent with the desorption of a solvent molecule. The displacement of the solvent molecule is rarely modeled explicitly due to the fact that conventional DFT studies are commonly performed in vacuum or with implicit solvation models. However, it has been proposed that this process is a possible origin of the pH-dependent HER activity of Pt (Sheng et al., 2015; Zheng et al., 2016; Ledezma-Yanez et al., 2017). If the chemisorbed intermediate possesses a dipole moment such as OH_{ads}, this intermediate contributes to the electrical field at the electrode surface (Ávila et al., 2020). The electrical field is dependent on the coverage of the intermediates, which is in turn dependent on the electrochemical potential, thus making the modeling of the double layer's potential dependency a non-trivial task.

The normal potential of zero charge (PZC) is defined for ideally polarizable electrodes, at which variation of the metal potential only alters the distribution of the electron spillover without resulting in electron transfer from or onto ions and molecules in the solution. This is not the case for electrocatalytic interfaces, at which ions and molecules may adsorb onto the electrode surface, forming chemical bonds. The chemisorption dramatically changes the structure of the electric double layer.

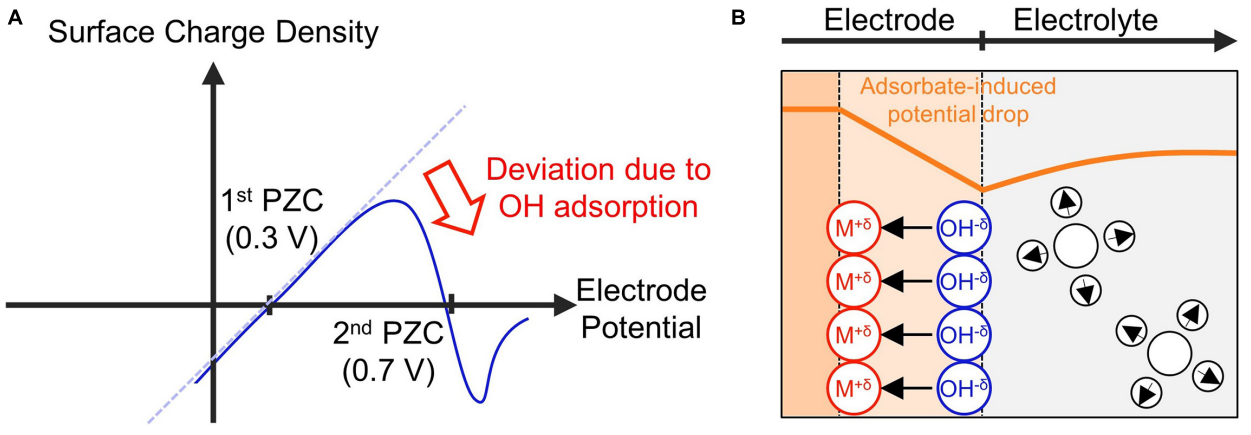

FIGURE 4 | Schematic illustrations of **(A)** the surface charge density with respect to the potential and **(B)** the structure of the electrode – electrolyte interface near the second PZC.

One known effect is associated with surface dipole moments that arise from partially charged chemisorbates. The chemisorption-induced surface dipole moments generate a significant potential drop on the electrode surface. This additional surface potential drop will change the surface charging behavior of the electrode, resulting in a second PZC in the potential region where chemisorption occurs.

In the case of Pt (111) in 0.1 M $HClO_4$, the normal PZC is around 0.3 V vs RHE, and shifting the electrode potential to more positive potentials should lead to an increase in the surface charge (**Figure 4A**). However, at potentials above 0.6 V *vs*. RHE, water dissociation leads to the chemisorption of negatively charged OH^-, forming an inward surface dipole moment (**Figure 4B**, the direction of a dipole moment is from negative to positive charge). This effectively neutralizes the potential-dependent increase of the surface charge, resulting in a nonmonotonic surface charging relation as can be seen from the second PZC in the OH_{ads} potential region (Huang et al., 2016b; Huang et al., 2018).

In general, when there is a net dipole change upon displacing the solvent with an adsorbate, there is a possibility for a second PZC, and therefore, this phenomenon is most likely not unique to the combination of platinum and OH intermediates (Frumkin and Petrii, 1975; Martnez-Hincapié et al., 2018). In addition to the ORR (Huang et al., 2016a; Zhang et al., 2019; Zhou et al., 2020), the double layer model above has been used successfully to model the formic acid oxidation (Zhu and Huang, 2019), and peroxodisulfate reduction (PDSR) reactions (Zhang and Huang, 2020) at Pt(111).

Stepwise Proton-Electron Transfer and Charged Intermediates

Another challenge to obtain accurate binding energies is the involvement of charged intermediate species. The CHE model avoids charged intermediates by assuming that the proton and electron are always transferred together in a single step, also denoted as concerted proton-electron transfer (CPET). This is partially justified because the CPET mechanism is in general thermodynamically more favorable compared to stepwise proton-electron transfer (SPET) (Hammes-Schiffer and Stuchebrukhov, 2010; Warren et al., 2010; Koper, 2013c). However, there is experimental evidence suggesting decoupled electron-proton transfer steps are involved in reactions such as CO_2 reduction on copper (Kortlever et al., 2015b) and gold (Wuttig et al., 2016), or the ORR on gold (Rodriguez and Koper, 2014). If so, this implies that some intermediates are charged, and evaluating their free energies accurately is necessary to construct the free-energy landscape for the electrocatalytic process. In fact, from a purely thermodynamic standpoint, the pH dependence of many electrocatalytic reactions already suggests the participation of SPET within the reaction mechanism (Hammes-Schiffer and Stuchebrukhov, 2010; Koper, 2013b; Sakaushi et al., 2020). Furthermore, the theoretical model by Koper suggests SPET may even be beneficial in some cases because modulating the driving force of electrochemical and non-electrochemical steps separately may lead to higher activity or selectivity (Koper, 2013b). The pH dependent selectivity regulation of nitrite reduction on MoS_2 is a direct support to this theoretical model (He et al., 2018, 2020). SPET pathways have also been proposed for other electrocatalytic processes, including the OER and ammonia oxidation reaction (Katsounaros et al., 2016; Saveleva et al., 2018; Exner and Over, 2019).

To date, the energetics of SPET pathways has been assessed theoretically for some molecular catalysts, and it has been shown that charged intermediates are indeed preferred during reactions such as CO_2 reduction (Göttle and Koper, 2017) or the OER (Craig et al., 2019). Thorough treatment of CPET and SPET pathways by quantum chemical considerations can be found in the works of Hammes-Schiffer and coworkers, who have developed computational protocols for the calculation of concerted or decoupled proton-electron transfers for biological enzymes and bio-inspired molecules (Goings and Hammes-Schiffer, 2020; Sayfutyarova and Hammes-Schiffer, 2020; Warburton et al., 2020). Although direct calculation of charged intermediates using DFT tends to be avoided due to their large errors, moving beyond the conventional picture of uncharged intermediate states within the CHE model is of particular importance to the electrocatalysis community. First steps for molecular catalysts have been made, whereas the description of charged species on solid-state surfaces is still in its early stages (Kastlunger et al., 2018; Lindgren et al., 2020).

Coverage Dependence of the Binding Energy

When evaluating the binding energy of intermediate species, it is also important to account for the chemical environment of the adsorbate. For example, the hydrogen binding energy on Pt(111) was shown to shift from strong-binding to weak-binding when the coverage was increased (Skúlason et al., 2010). The hydrogen binding energy also increases with the coverage of CO on metals such as Cu or Mo, which has been used to explain why Cu favor CO_2 reduction of HER when the two are in competition (Zhang et al., 2014). The CER on RuO_2(110) is another example which is influenced by the coverage (Exner et al., 2016). The active site under typical CER conditions consists of a surface oxygen atom, O_{ads}, on which chloride anions from the electrolyte solution adsorb under formation of an OCl_{ads} precursor (Exner et al., 2014). The binding strength of chlorine to the underlying oxygen atoms is stronger if there is a neighboring OH group instead of an oxygen atom, due to the attractive interaction between the adsorbed chlorine and the neighboring hydrogen atom in the OH group.

In order to calculate the binding energy more accurately, it is desirable to resolve not only the active site but also its surrounding environment under typical reaction conditions. One approach is to use DFT to construct surface Pourbaix diagrams (Hansen et al., 2008; Sumaria et al., 2018; Vinogradova et al., 2018). These diagrams indicate the thermodynamically most favorable surface structure as a function of the applied electrode potential and pH (Gossenberger et al., 2020), and by assuming that this surface corresponds to the active surface, it is possible to predict the coverage of intermediates and adsorbates. However, this approach is purely thermodynamic in nature, and cannot be used if the surface structure in experiments deviates from the most energetically favorable one. The gap

between thermodynamics and kinetics is discussed in detail in the following section, and some of the methods discussed therein may allow the construction of more accurate Pourbaix diagrams which include not only thermodynamic but also kinetic information.

Thermodynamics and Kinetics

The BEP Relationship

The previous section has focused on challenges to obtain accurate binding energies. However, even if the free energy of reaction intermediates could be obtained without any error, there is still a conceptual gap between the Sabatier principle and the activity in real experiments. This is because the traditional interpretation of the Sabatier principle is based on pure thermodynamic considerations, whereas experiments always contain the influence of kinetics.

A framework based on pure thermodynamic considerations has historically been rationalized by the Brønsted (Bell) – Evans – Polanyi (BEP) relationship, which states that the free-activation energy ($\Delta G_{RI}^{\#}$) is linearly correlated with the reaction free energy (ΔG_{RI}) (Bligaard et al., 2004; Cheng et al., 2008). In other words, $\Delta G_{RI}^{\#} = \beta \Delta G_{RI}$, where β denotes the so-called BEP coefficient ($0 < \beta < 1$) (Van Santen et al., 2009).

An example for a two-electron reaction, such as the HER, is shown in **Figure 5**. For a weak-binding catalyst (**Figure 5A**), the first step should have a higher transition-state free energy compared to the second because the first step is uphill in free energy. In contrast, for a strong-binding catalyst (**Figure 5B**), the BEP relation predicts that the second elementary reaction step would have a higher transition-state free energy than the first step. The optimum situation corresponds to a thermoneutral catalyst (**Figure 5C**) because in this case, the transition-state free energies of both elementary reactions are at the same height, and the highest transition state within the entire landscape would be lower than that of the weak-binding and strong-binding catalysts. In general, the positive nature of β ensures that a thermodynamically unfavorable step would have unfavorable kinetics due to a higher transition state. Based on this logic, the thermodynamically ideal (zero-overpotential) catalyst should also be the kinetically optimum catalyst, in agreement with the discussion in Section 2.1. Following the pioneering work of Parsons from the 1950s (Parsons, 1951, 1958), the reaction intermediates preceding the highest transition state can be considered to be in quasi-equilibrium, and the rate of the entire reaction (**Figure 5**) is governed by the free energy difference between the intermediate with smallest free energy and the transition state with highest free energy (Exner et al., 2018).

On the other hand, there are examples in the literature where the binding energy and the activity do not seem to correlate. For example, thermodynamic DFT calculations analyzed in terms of the BEP relationship for the ORR predict an activity trend of Pt > Ir > Rh, although the experimental trend is Pt > Rh > Ir (**Figure 6A**; Zhou et al., 2020). This discrepancy persists despite the experiments being performed using single crystals and even after diffusion effects are compensated, suggesting

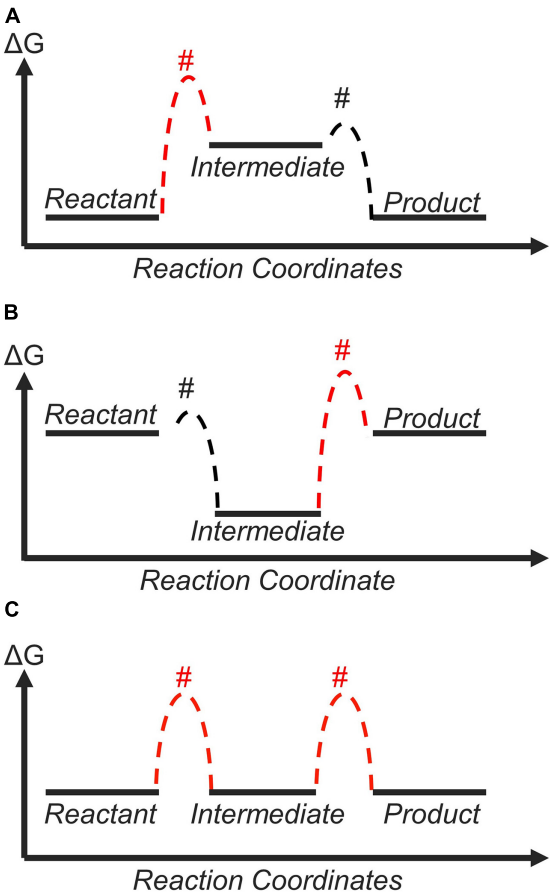

FIGURE 5 | The free-energy landscape of a two-step electrocatalytic process in equilibrium. The heights of transition states indicated by # were drawn assuming a constant BEP coefficient: **(A)** weak-binding catalyst; **(B)** strong-binding catalyst; **(C)** thermoneutral catalyst. The highest transition state, shown in red, occurs at the reaction step with the least favorable thermodynamics. Therefore, the thermodynamically ideal catalyst **(C)** should also be the kinetically ideal catalyst.

that the binding energy alone cannot predict the activity of electrocatalysts. A discrepancy between theory and experiment is observed even within different single crystal facets of Pt (**Figure 6B**; Gómez-Marín et al., 2014). There are also examples where the activity trend is reversed when the overpotential is increased; that is, a material which is less active than another electrocatalyst at low overpotentials can become more active at large overpotentials (Exner, 2019d). These discrepancies are mainly because the experimental activity is evaluated by the current density (kinetics) whereas theoretical trends are evaluated based on the thermodynamics (cf. Section "The Ideal Free-Energy Landscape") (Exner, 2021b).

Validity of the BEP Relationship

First, it is important to note that the BEP relationship is in direct contradiction to the Marcus theory of electron transfer, and therefore, in some cases, it does not depict the free-energy landscape accurately. Although the BEP relationship states a

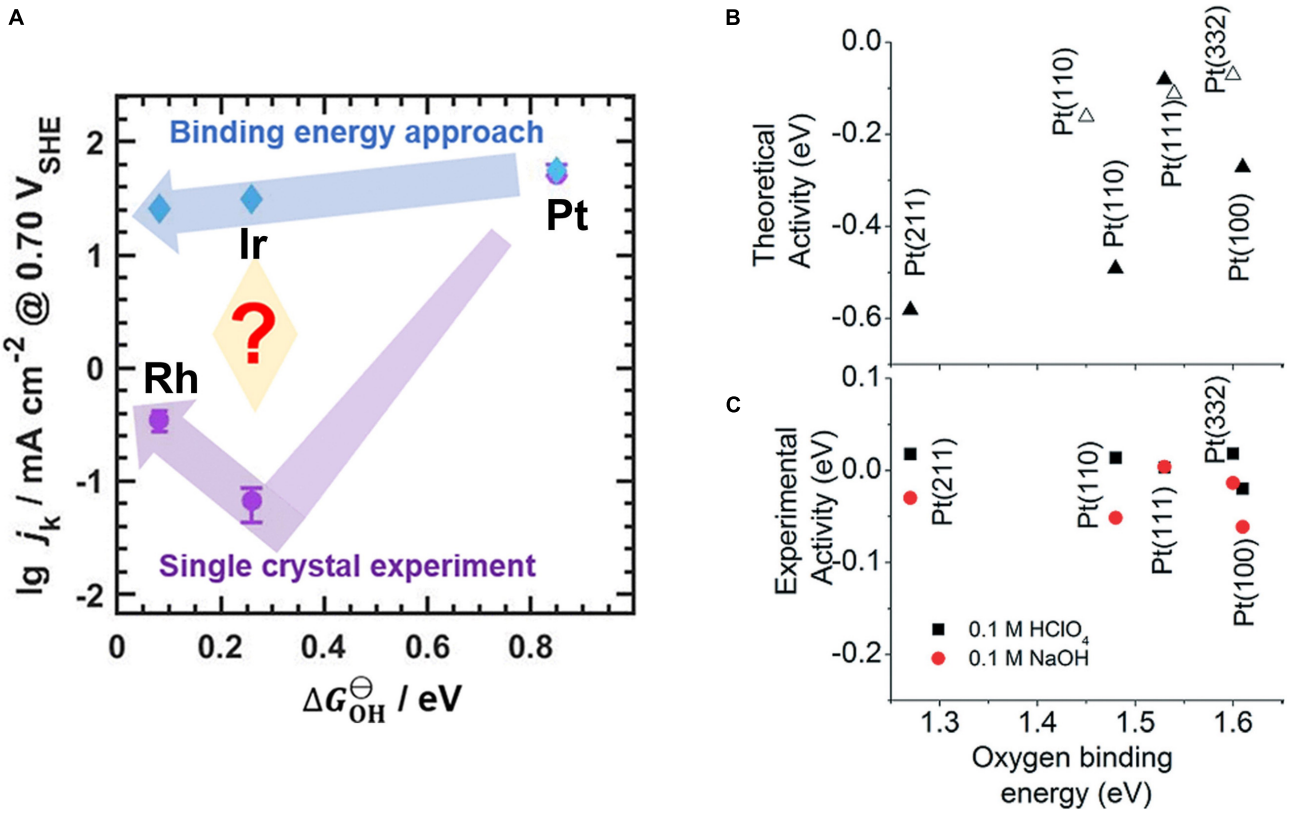

FIGURE 6 | (A) Theoretical (blue) and experimental (purple) ORR activity trends on Pt, Ir, and Rh single-crystal (111) rotating disk electrodes. **(B,C)** A theoretical and experimental volcano plot of ORR on different facets of platinum. Reproduced from Zhou et al. (2020) and Gómez-Marín et al. (2014) with permission. Copyright 2020 American Chemical Society, 2014 Royal Society of Chemistry.

linear relationship between the free energy of activation and the reaction free energy ($\Delta G_{RI}{}^{\#} = \beta \Delta G_{RI}$), the Marcus theory states a quadratic relationship ($\Delta G_{RI}{}^{\#} = \frac{(\lambda + \Delta G_{RI})^2}{4\lambda}$). This is a direct consequence of how these two theories modeled the free-energy landscape: while Brønsted, Evans, and Polanyi assumed the free energy to be a linear function of the reaction coordinate, Marcus assumed it to be quadratic. As these assumptions are fundamental to both theories, the applicability of these theories depends on the validity of these presumptions, which should ideally be tested on a system-by-system basis. As a general guideline, the discrepancy between the two is less apparent near equilibrium as the non-linearity, predicted by the Marcus theory, is less important. However, the predictions from the two theories diverge when the overpotential is increased. The most iconic example is the Marcus inverted region (Hammes-Schiffer, 2009; Parada et al., 2019), where once the overpotential is increased beyond a certain point, the free energy of activation starts to increase. This corresponds to a negative BEP coefficient, which is a direct contradiction to the assumption of $0 < \beta < 1$.

As for the value of the BEP coefficient, $\beta = 0.5$ is a frequent assumption, although there is no physical basis for why β should be 0.5 or why it should be independent of the material (Koper, 2011a; Akhade et al., 2018). There is also no basis for why β should be constant throughout the various elementary steps of a multistep electrocatalytic reaction. $\beta = 0.5$ is only a convenient assumption for theoretical analysis and should be treated as such.

Overpotential Effects on the BEP Relationship

So far, the entire discussion connecting thermodynamic and kinetics via the BEP relationship is based on the free-energy landscape at equilibrium (zero overpotential). Experimentally, however, electrocatalytic turnover can only be observed if a non-zero overpotential is applied to make the overall reaction exergonic (cf. Section "The Ideal Free-Energy Landscape"). Therefore, there is a discrepancy in the condition between theory ($\eta = 0$) and experiments ($\eta > 0$) (Exner, 2019a, 2020c, 2019b).

How can the applied overpotential be introduced in the analysis of the free-energy changes (thermodynamics) within the reaction mechanism? For a two-electron process, Exner suggested analyzing the potential dependency of the reaction intermediates in the free-energy landscape, $|\Delta G_{RI}(\eta)|$ (Exner, 2019d, 2021b). $|\Delta G_{RI}(\eta)|$ is an overpotential-dependent activity descriptor, reaching its maximum at the overpotential η_{target} that fulfills $|\Delta G_{RI}(\eta_{target})| = 0$ eV. As a consequence, thermoneutral bonding of the reaction intermediate at the targeted overpotential, η_{target}, has been identified as a design criteria for active electrocatalysts (Exner, 2020d). This is in contrast to the conventional approach which aims for

thermoneutral bonding at zero overpotential (cf. Section "The Ideal Free-Energy Landscape"), and has been coined as the extended Sabatier principle (Exner, 2021b).

Accounting for the overpotential dependency in predicting activity trends appears to be especially important for the evaluation of active catalysts located near the top of the volcano plot (Exner, 2020a). The conventional volcano analysis with the thermodynamic overpotential as the activity descriptor predicts IrO_2 > RuO_2 in both CER and OER (Briquet et al., 2017; Krishnamurthy et al., 2018), although once the overpotential dependence of the free-energy landscape is considered, the experimental activity trend of RuO_2 > IrO_2 could be reproduced (Exner, 2020d). This suggests that the link between the thermodynamics and kinetics via the BEP relationship should not be set at $\eta = 0$ V, but rather at the target overpotential ($\eta > 0$ V) based on typical reaction conditions in experiments. While the targeted overpotential may be about 50 – 100 mV for a two-electron process such as the HER and CER, a larger value of 300 – 400 mV is more realistic for sluggish four-electron processes such as the OER (Exner, 2019c).

A major consequence of the extended Sabatier principle is the shift in the optimum binding energy with increasing driving force (Exner, 2019d, 2020c). In Section "The BEP Relationship," it was demonstrated that the thermodynamically ideal free-energy landscape for a two-electron process is one which is completely flat at equilibrium ($\Delta G_{RI} = 0$ eV at $\eta = 0$ V). However, this may no longer be ideal if an overpotential is applied. The criterion for the optimum landscape according to the overpotential-dependent description refers to thermoneutral bonding of the reaction intermediate at the target overpotential (Exner, 2020c). Applying the CHE scheme, the free energy of the reaction intermediate at zero overpotential is described by the relation $\Delta G_{RI} = e|\eta_{target}| > 0$ eV, and hence the optimum binding energy of the reaction intermediate shifts to weak bonding with increasing overpotential (**Figure 7**), in which ΔG_{RI} of about 100 – 200 meV has been recognized as the ideal situation for a two-electron process. It is noteworthy that only the extended Sabatier principle can explain the high activities of Pt ($\Delta G_{RI} = 0.21$ eV), MoS_2 ($\Delta G_{RI} = 0.20$ eV), and Mo_2C ($\Delta G_{RI} = 0.13$ eV) in the HER (Tang and Jiang, 2016; Handoko et al., 2019; Lindgren et al., 2020) as well as the high activity of RuO_2 ($\Delta G_{RI} = 0.13$ eV) in the CER (Exner, 2019b, 2021b). In contrast, the conventional Sabatier approach would not consider these materials as highly active electrocatalysts, because they are not located at the top ($\Delta G_{RI} = 0$ eV) of the volcano plot at $\eta = 0$ V.

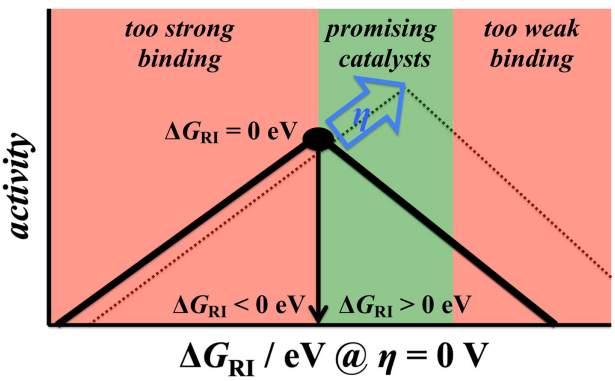

FIGURE 7 | The extended Sabatier principle purports a positive shift of the reaction intermediate's optimum binding energy with increasing driving force for a two-electron process. As such, electrocatalysts that bind the intermediate slightly weakly (by about 100 – 200 meV) are the most promising materials. Reproduced from Exner (2020c) with permission. Copyright 2020 John Wiley and Sons.

So far, the overpotential dependence for the free energy of the reaction intermediate relating to a simple two-electron process has been discussed. In case of a four-electron process, the situation is more complex since three reaction intermediates need to be considered in the analysis (cf. Section "Practical Application and Linear Scaling Relationships"). The common approach to assess electrocatalytic activity for multiple-electron processes relies on the notion of the thermodynamic overpotential, η_{TD}, assuming that the highest free-energy change at the equilibrium potential governs the catalytic performance. It was already recognized by Calle-Vallejo and coworkers that the assessment of a single free-energy change to approximate electrocatalytic activity is too simplistic (Govindarajan et al., 2018; Piqué et al., 2020). These authors put forth an alternate activity descriptor, the electrochemical-step symmetry index (ESSI), which in contrast to η_{TD} analyzes the entire free-energy landscape at zero overpotential. As such, the ESSI is a more balanced activity descriptor than η_{TD} and provides better results in the sorting of highly active electrocatalysts (Exner, 2020f; Piqué et al., 2020). Yet, the ESSI does not contain any overpotential effects in its framework. Recently, Exner derived an overpotential-dependent activity descriptor for multiple-electron processes, denoted $G_{max}(\eta)$ (Exner, 2020g). In a similar fashion to the descriptor $|\Delta G_{RI}(\eta)|$ for a two-electron process, $G_{max}(\eta)$ analyzes the thermodynamics of the reaction intermediates at the target overpotential, but at the same time makes use of the free-energy span model (Kozuch and Shaik, 2011; Kozuch, 2012) by assessing the free-energy difference between the intermediate with smallest free energy and the intermediate with highest free energy in the free-energy landscape. This is achieved by a dedicated procedure of renumbering the electron-proton transfer steps with increasing overpotential, as illustrated in **Figure 8**.

The concept of $G_{max}(\eta)$ as activity descriptor goes far beyond the assessment of a single free-energy change, as encountered with η_{TD}. It is noteworthy that the application of $G_{max}(\eta)$ to OER electrocatalysts predicts that the volcano apex is situated at about $\Delta G_2 = 1.40$ eV (Exner, 2020g). Following the discussion in Section "Practical Application and Linear Scaling Relationships," the thermodynamic analysis at zero overpotential in terms of η_{TD} purports $\Delta G_2 = 1.60$ eV as the optimum situation in the OER, indicating a shift of the volcano top by about 200 meV. Thus, the displacement of the volcano apex with increasing driving force is in the same order of magnitude as observed for a two-electron process (**Figure 7**), whereas the direction of the shift is toward stronger bonding of the oxygen adsorbate (smaller value of ΔG_2). The move of the volcano top to stronger oxygen

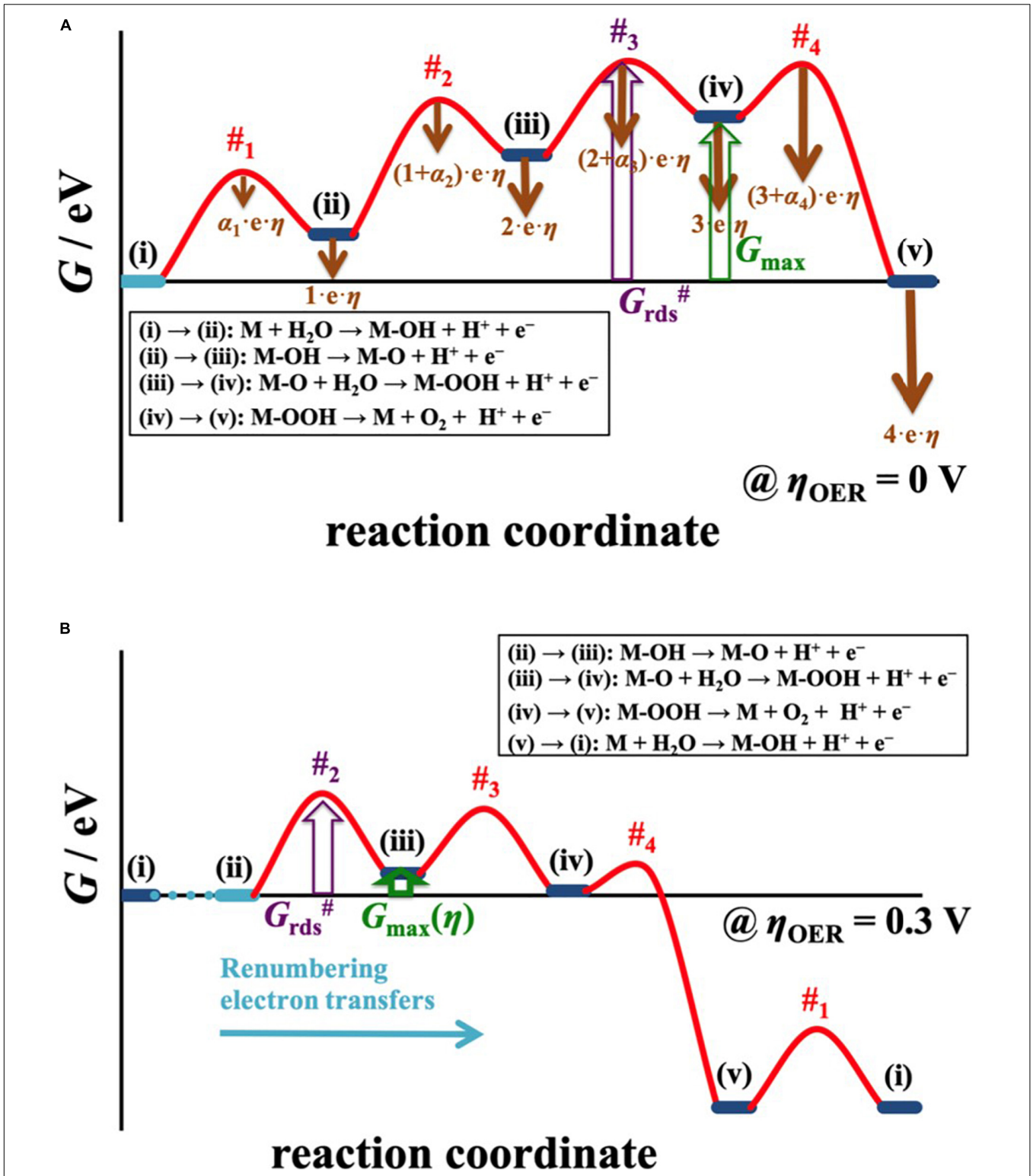

FIGURE 8 | (A) The free-energy span model is applied to determine the distance between the intermediate with smallest free energy and the intermediate with highest free energy in the OER landscape, described by the descriptor G_{max}. By accounting for the overpotential dependency of the elementary reaction steps, indicated by brown arrows in a), the free-energy diagram is translated to an applied overpotential of 300 mV in **(B)** to evaluate $G_{max}(\eta)$. Herein, the electron-proton transfer steps are renumbered in that the reaction always commences from the intermediate with smallest free energy. The peculiarity of the overpotential-dependent descriptor $G_{max}(\eta)$, albeit of thermodynamic nature, is that this activity measure directly scales with the kinetics of the reaction, which is governed by the transition state with highest free energy ($G_{rds}^{\#}$) in the free-energy diagram. Reproduced with permission from Exner (2020g). Copyright 2020 American Chemical Society.

bonding is further corroborated by a unifying screening approach which considers not only binding energies but also the applied overpotential, rate-determining steps, and catalytic symmetry, and reports $\Delta G_2 = 1.30$ eV as the optimum situation at an OER overpotential of 400 meV (Exner, 2019c).

Consideration of the applied overpotential for the approximation of electrocatalytic activity by the thermodynamics is of crucial importance when analyzing free-energy changes to comprehend trends in a class of materials. The concept of the extended Sabatier principle by connecting the thermodynamics to the kinetics at the target overpotential of the reaction is recognized as a valuable tool to distinguish between active and inactive electrode materials, particularly since it has been shown that the approximation of electrocatalytic activity by a single free-energy change, as encountered with the notion of η_{TD}, is insufficient (Exner, 2021c). Yet, this framework cannot entirely close the gap between theory and model experiments. This is also related to the fact that the kinetics is only partly covered in this theory, motivating the following discussion on kinetic effects.

Kinetic Effects Beyond the BEP Relationship

Under the assumption that the reaction intermediates preceding the transition state with highest free energy are in quasi-equilibrium (Parsons, 1951, 1958), the rate of an electrocatalytic process is governed by the transition state with the highest free energy in the free-energy landscape (cf. **Figure 8**). It should be noted that the transition-state free energy consists of a coverage term [(i) → (iii) in **Figure 8A**] as well as a free-energy barrier [(iii) → #$_3$ in **Figure 8A**], in which the transition state with highest free energy can change upon increasing the overpotential (cf. **Figure 8B**). However, such a switch in the transition state with highest free energy cannot be predicted solely by thermodynamic considerations, leading to potential discrepancies between thermodynamics and kinetics.

The transition state with highest free energy in the free-energy landscape is connected with the experimentally measurable current density, governing electrocatalytic activity (Parsons, 1951, 1958; Exner et al., 2018). Experiments commonly assess the relation between the current and electrode potential by measuring the Tafel plot, in which the applied overpotential is depicted as a function of the logarithm of the current density. This graph facilitates quantifying the so-called Tafel slope (Hu et al., 2004; Guidelli et al., 2014; Shinagawa et al., 2015), which is a measure for the electrocatalyst's sensitivity to the applied electrode potential. The Tafel slope, b, indicates by how many mV the applied overpotential needs to be enhanced to yield an increase of the current density by one order of magnitude:

$$b = \frac{\partial \eta}{\partial \log_{10} j} \tag{7}$$

In equation (7), η and j denote the applied overpotential and current density, respectively. Some catalysts are extremely sensitive to the applied overpotential. For instance, a Tafel slope of 40 mV/dec. is obtained for HER on Pt in acid at low overpotentials, whereas the Tafel slope increases to about 120 mV/dec. at higher overpotentials. In alkaline solutions, a single Tafel slope with $b = 120$ mV/dec. is observed (Sheng et al., 2010). In general, a smaller Tafel slope is desirable because a slight increase in the overpotential can significantly increase the current and thus, the observed electrocatalytic activity.

The different Tafel slopes of 40 mV/dec. and 120 mV/dec. can be ascribed to differences in the location of the highest transition state in the free-energy landscape (Parsons, 1951, 1958). The Tafel slope can be expressed in terms of the apparent transfer coefficient, β, which is given by Exner et al. (2018):

$$b = \frac{RT \ln 10}{F\beta} = \frac{59}{\beta}\text{mV/dec} \tag{8}$$

In case of $\beta = 0.5$, the Tafel slope amounts to 120 mV/dec., whereas for $\beta = 1.5$ a Tafel slope of 40 mV/dec. is obtained. This finding directly indicates that different transition states govern the rate of the HER over platinum in acidic or alkaline environment at small overpotentials. The apparent transfer coefficient is related to the transfer coefficient for the highest transition state (α) and the number of electrochemical reaction steps consisting of a charge transfer preceding it (n) as follows:

$$\beta = n + \alpha \tag{9}$$

Commonly, the assumption $\alpha = 0.5$ is used, even if deviations from this notion have been reported in the literature (Fang and Liu, 2014; Rojas-Carbonell et al., 2018; Exner and Over, 2019). Now, it becomes clear that $n = 0$ results in $\beta = ½$, and thus $b = 120$ mV/dec., whereas $n = 1$ yields ß = 1.5 and $b = 40$ mV/dec. As a result, when the first or second elementary reaction step governs the rate, the Tafel slope amounts to 120 mV/dec. or 40 mV/dec., respectively. It shall be noted that these different Tafel slopes can be obtained even if the thermodynamic landscape is the same, which is illustrated in **Figure 9** for a two-electron process.

Recently, there have been several attempts to bridge the gap between the thermodynamics and kinetics, at least for two-electron processes such as the HER. For example, a microkinetic study by Koper has explicitly shed light on the relationship between thermodynamic and kinetic free-energy landscapes, and has shown how the thermodynamic landscape may overestimate the catalytic rate due to unfavorable kinetics (Koper, 2013a). A recent study by Ooka and Nakamura demonstrates that the optimum binding energy in terms of maximizing reaction rates may not be thermoneutral as expected from the traditional thermodynamic framework (cf. Section "The Ideal Free-Energy Landscape"). Instead, the optimum binding energy is dependent on the kinetic rate constants, and higher rates are achieved if the binding energy of the reaction intermediate shifts to weak or strong bonding with increasing driving force (Ooka and Nakamura, 2019). Exner has taken the analysis one step further to propose the direction of the binding energy's shift by combining microkinetics with the characteristics of the free-energy diagram in electrocatalysis, pointing out that a shift to strong bonding can be fairly excluded (Exner, 2020e). Rather, displacement of the optimum binding energy to weak bonding is observed for a two-electron process, coinciding with the theory of the extended Sabatier principle (cf. Section "Validity of the BEP Relationship") (Exner, 2019d, 2020c). In addition to these and many other

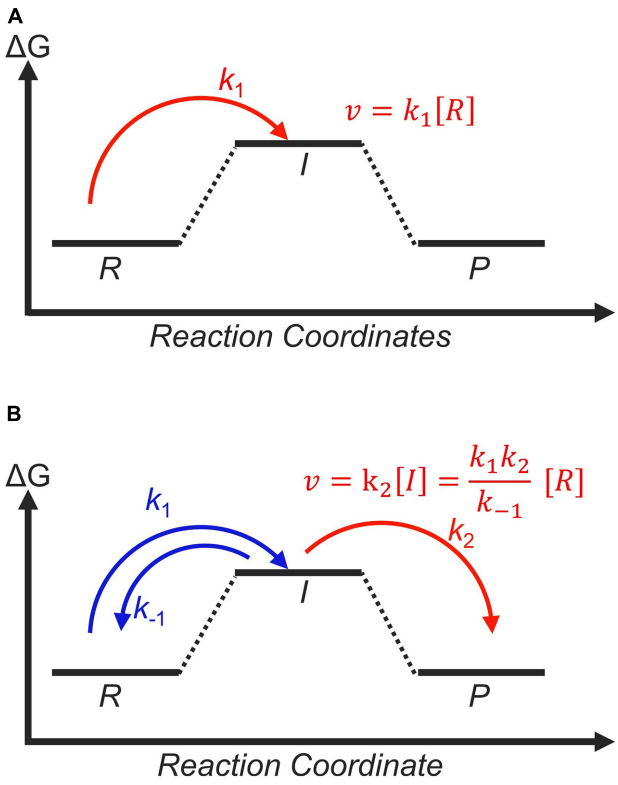

FIGURE 9 | Catalysts with the same thermodynamic free-energy landscapes can still yield different experimental activities, depending on whether the first **(A)** or the second **(B)** step determines the catalytic rate. This is governed by the transition state with highest free energy, indicated in red. The corresponding rate equation are shown in both panels, with [R] and [I] corresponding to the concentrations of the reactant and intermediate, respectively. Rate constants are according to usual nomenclature, where k_1 is for the formation of the intermediate, k_2 is for the formation of the product, and negative signs indicate reverse reactions.

studies based on microkinetic considerations in the steady-state approximation (Wang et al., 2009; Holewinski and Linic, 2012; Marshall and Vaisson-Béthune, 2015; Shinagawa et al., 2015; Tao et al., 2019; Mefford et al., 2020; Tichter et al., 2020; Zhang et al., 2020), Dauenhauer and coworkers directly calculated the time-dependent kinetics of electrochemical processes, proposing that an oscillation in the driving force may lead to an enhancement in the reaction rate compared to the steady state (Ardagh et al., 2019; Shetty et al., 2020). This is because temporal oscillations allow a single catalytic material to exhibit multiple free-energy landscapes, which promote different parts of the reaction.

Chemical Processes Outside the Scope of the Sabatier Principle

Finally, in this section, we will consider factors which influence the observed electrocatalytic performance in ways which are beyond the scope of the Sabatier principle. The Sabatier principle is useful to predict the intrinsic activity of a material. However, in some cases, the intrinsic activity is not the limiting factor of the catalysis.

Mass Transport and Reactant Availability

A prominent example where mass transport and reactant availability significantly influence the observed electrocatalytic reaction is CO_2 reduction (Gattrell et al., 2006; Ooka et al., 2017; Lum and Ager, 2018). It has been demonstrated both experimentally and theoretically that the availability of CO_2, protons, and other electrolyte ions at the electrode heavily influences the selectivity of this reaction (Hori et al., 1989; Murata and Hori, 1991; Varela et al., 2016; Pérez-Gallent et al., 2017; Ringe et al., 2020). While it is difficult to understand the effect of each ion directly from experiments, it is possible to resolve trends of different ions qualitatively using theoretical approaches (Ringe et al., 2019). This requires multi-scale modeling bridging different time and length scales, which accounts for factors such as surface charging, the potential of zero charge, and the double layer capacitance (cf. Section "Challenges to Accurately Predict the Binding Energy").

Another difficulty of CO_2 reduction is the change of the pH during the reaction. For example, the bicarbonate ion inside the electrolyte, either added intentionally or formed as a result from the equilibrium with CO_2, acts as a pH buffer, thus influencing the pH (Gattrell et al., 2006; Gupta et al., 2006). The buffering effect changes as the reaction progresses because there is a gradual accumulation of products inside the reactor. Although gaseous products, such as CO, CH_4, and C_2H_4, have no buffering capacity, oxygenated products such as HCOOH and acetate also have protonation equilibria of their own, and hence are expected to influence the pH. As CO_2 reduction is known to be highly sensitive to the pH (Bumroongsakulsawat and Kelsall, 2014; Schouten et al., 2014; Gao et al., 2015; Birdja et al., 2019), this effect would directly impact electrocatalytic activity and selectivity. It is possible to steer the selectivity of electrochemical reactions by manipulating the local concentrations of substrates, as has been shown experimentally in the case of CO_2 reduction *vs.* HER (Ooka et al., 2017) or the CER *vs.* OER (Vos et al., 2018; Wintrich et al., 2019).

Surface Area

The surface area and the availability of active sites on the electrocatalyst surface are other factors which influences the observed activity in ways independent from the intrinsic activity. Although the number of active sites can be estimated theoretically from simplified slab models, there is no direct access to the electrochemically active surface area. From an experimental point of view, the surface area is a critical factor to design new electrodes because the activity is usually evaluated based on the geometric area. For this reason, many reports of active materials are based on porous substrates, such as carbon felt or Pt/Ti mesh, compared with glassy carbon or conductive glass substrates (Park et al., 2012; Xie et al., 2017; Kang et al., 2019).

The surface area may also indirectly influence diffusion at the vicinity of the electrode as a rough surface would disrupt the diffusion layer. Although most studies so far assume the concentration of chemical species within the diffusion layer to be dependent only on the distance from the electrode, a more accurate prediction may be obtained by taking the roughness of the electrode into account (Pajkossy and Nyikos, 1989;

Louch and Pritzker, 1993; Kant, 1994). This is especially important for cascade reaction systems, where the intermediate must reach the next catalyst before it diffuses into the bulk solution (Lum and Ager, 2018; Gurudayal et al., 2019). So far, both the electrochemically active surface area and the roughness of the electrode are difficult to describe using DFT, indicating another limitation for the comparison between experiment and theory, which is particularly pronounced when surface blocking or roughness effects govern electrocatalytic activity.

CONCLUSION

The present review has summarized the key concepts of the Sabatier principle, which is widely used today to guide catalyst development. From traditional materials science to the most advanced machine learning studies, there is a general consensus that the binding energy of reaction intermediates is a critical parameter to predict electrocatalytic activity. This descriptor-based approach has also been recently transferred to the surrounding fields of homogeneous catalysis and enzyme catalysis.

Since the concept of the binding energy and the Sabatier principle are central in the current electrocatalysis theory, it is important to highlight not only its usefulness, but also its challenges and shortcomings in a critical light. This may help not only to prevent misleading analyses, but also to clarify what steps need to be taken next. To this end, we have attempted to accentuate at which level issues can arise. Some matters are technical in nature and can be overcome if the accuracy of binding energy calculations is enhanced. On the other hand, some aspects are not an issue of computational accuracy and are more fundamental in nature, such as the bridge between the thermodynamics and kinetics by the Brønsted – Evans – Polanyi relationship or the influence of electrolyte, surface charging and mass transport effects, which require the application of multi-scale frameworks. While the simplicity of the CHE model has led to its widespread success and application, more comprehensive approaches which include a grand canonical description of the electrochemical double layer as well as an explicit treatment of the overpotential and its influence on kinetic barriers may be the next step forward. Increasing the model complexity can be promoted considering the emergence of new techniques such as machine learning, which can be used to reduce computational costs.

The theoretical advancement based on the CHE model and the Sabatier principle in its thermodynamic form has been a major driving force behind the advancement of electrocatalysis in the last fifteen years. Building upon and expanding our current framework is critical to promote the identification of next-generation electrocatalysts, and to realize a truly sustainable society.

AUTHOR CONTRIBUTIONS

All authors listed have made a substantial, direct, and intellectual contribution to the work and approved it for publication.

FUNDING

HO is grateful to the support from the RIKEN Special Postdoctoral Researcher Program and to the grant-in-aid for scientific research (No. 20K15387) from the Japan Society for the Promotion of Science. JH appreciates the support from the National Natural Science Foundation of China (No. 21802170). KE gratefully acknowledges funding from the Alexander von Humboldt Foundation. KE is associated with the CRC/TRR247: "Heterogeneous Oxidation Catalysis in the Liquid Phase" (Project number 388390466-TRR 247). KE is associated with the RESOLV Cluster of Excellence, funded by the Deutsche Forschungsgemeinschaft (DFG, German Research Foundation) under Germany's Excellence Strategy – EXC 2033 – 390677874 – RESOLV. The contribution of KE is based upon the work from COST Action 18234, supported by COST (European Cooperation in Science and Technology).

REFERENCES

Abidi, N., Lim, K. R. G., Seh, Z. W., and Steinmann, S. N. (2020). Atomistic modeling of electrocatalysis: are we there yet? *WIRES Comput. Mol. Sci.* doi: 10.1002/wcms.1499 [Epub ahead of print],

Akhade, S. A., Nidzyn, R. M., Rostamikia, G., and Janik, M. J. (2018). Using brønsted-evans-polanyi relations to predict electrode potential-dependent activation energies. *Catal. Tod.* 312, 82–91. doi: 10.1016/j.cattod.2018.03.048

Ardagh, M. A., Abdelrahman, O. A., and Dauenhauer, P. J. (2019). Principles of dynamic heterogeneous catalysis: surface resonance and turnover frequency response. *ACS Catal.* 9, 6929–6937. doi: 10.1021/acscatal.9b01606

Auinger, M., Katsounaros, I., Meier, J. C., Klemm, S. O., Biedermann, P. U., Topalov, A. A., et al. (2011). Near-surface ion distribution and buffer effects during electrochemical reactions. *Phys. Chem. Chem. Phys.* 13, 16384–16394. doi: 10.1039/C1CP21717H

Ávila, M., Juárez, M. F., and Santos, E. (2020). Role of the partial charge transfer on the chloride adlayers on Au (100). *ChemElectroChem* 7, 4269–4282. doi: 10.1002/celc.202001228

Back, S., Tran, K., and Ulissi, Z. W. (2019a). Toward a design of active oxygen evolution catalysts: insights from automated density functional theory calculations and machine learning. *ACS Catal.* 9, 7651–7659. doi: 10.1021/acscatal.9b02416

Back, S., Yoon, J., Tian, N., Zhong, W., Tran, K., and Ulissi, Z. W. (2019b). Convolutional neural network of atomic surface structures to predict binding energies for high-throughput screening of catalysts. *J. Phys. Chem. Lett.* 10, 4401–4408. doi: 10.1021/acs.jpclett.9b01428

Bard, A. J. (2010). Inner-sphere heterogeneous electrode reactions. Electrocatalysis and photocatalysis: the challenge. *J. Am. Chem. Soc.* 132, 7559–7567. doi: 10.1021/ja101578m

Basdogan, Y., Groenenboom, M. C., Henderson, E., De, S., Rempe, S. B., and Keith, J. A. (2020a). Machine learning-guided approach for studying solvation environments. *J. Chem. Theory Comput.* 16, 633–642. doi: 10.1021/acs.jctc.9b00605

Basdogan, Y., Maldonado, A. M., and Keith, J. A. (2020b). Advances and challenges in modeling solvated reaction mechanisms for renewable fuels and chemicals. *WIRES Comput. Mol. Sci.* 10:e1446. doi: 10.1002/wcms.1446

Bhattacharyya, K., Poidevin, C., and Auer, A. A. (2021). Structure and reactivity of IrO X nanoparticles for the oxygen evolution reaction in electrocatalysis: an electronic structure theory study. *J. Phys. Chem. C* 125, 4379–4390. doi: 10.1021/acs.jpcc.0c10092

Birdja, Y. Y., Pérez-Gallent, E., Figueiredo, M. C., Göttle, A. J., Calle-Vallejo, F., and Koper, M. T. (2019). Advances and challenges in understanding the electrocatalytic conversion of carbon dioxide to fuels. *Nat. Energ.* 4, 732–745. doi: 10.1038/s41560-019-0450-y

Bligaard, T., Nørskov, J. K., Dahl, S., Matthiesen, J., Christensen, C. H., and Sehested, J. (2004). The Brønsted–Evans–polanyi relation and the volcano curve in heterogeneous catalysis. *J. Catal.* 224, 206–217. doi: 10.1016/j.jcat.2004.02.034

Bochevarov, A. D., Harder, E., Hughes, T. F., Greenwood, J. R., Braden, D. A., Philipp, D. M., et al. (2013). Jaguar: a high-performance quantum chemistry software program with strengths in life and materials sciences. *Int. J. Quantum Chem.* 113, 2110–2142. doi: 10.1002/qua.24481

Briquet, L. G., Sarwar, M., Mugo, J., Jones, G., and Calle-Vallejo, F. (2017). A new type of scaling relations to assess the accuracy of computational predictions of catalytic activities applied to the oxygen evolution reaction. *ChemCatChem* 9, 1261–1268. doi: 10.1002/cctc.201601662

Bumroongsakulsawat, P., and Kelsall, G. (2014). Effect of solution pH on CO: formate formation rates during electrochemical reduction of aqueous CO2 at Sn cathodes. *Electrochim. Acta* 141, 216–225. doi: 10.1016/j.electacta.2014.07.057

Busch, M., Halck, N. B., Kramm, U. I., Siahrostami, S., Krtil, P., and Rossmeisl, J. (2016). Beyond the top of the volcano?–A unified approach to electrocatalytic oxygen reduction and oxygen evolution. *Nano Energ.* 29, 126–135. doi: 10.1016/j.nanoen.2016.04.011

Busch, M., Laasonen, K., and Ahlberg, E. (2020). Method for the accurate prediction of electron transfer potentials using an effective absolute potential. *Phys. Chem. Chem. Phys.* 22, 25833–25840. doi: 10.1039/D0CP04508J

Busch, M., Wodrich, M. D., and Corminboeuf, C. (2015). Linear scaling relationships and volcano plots in homogeneous catalysis–revisiting the suzuki reaction. *Chem. Sci.* 6, 6754–6761. doi: 10.1039/C5SC02910D

Calle-Vallejo, F., and Koper, M. T. (2012). First-principles computational electrochemistry: achievements and challenges. *Electrochim. Acta* 84, 3–11. doi: 10.1016/j.electacta.2012.04.062

Calle-Vallejo, F., Martnez, J., Garcá-Lastra, J., Abad, E., and Koper, M. (2013). Oxygen reduction and evolution at single-metal active sites: comparison between functionalized graphitic materials and protoporphyrins. *Surf. Sci.* 607, 47–53. doi: 10.1016/j.susc.2012.08.005

Carmo, M., Fritz, D. L., Mergel, J., and Stolten, D. (2013). A comprehensive review on PEM water electrolysis. *Int. J. Hyd. Energ.* 38, 4901–4934. doi: 10.1016/j.ijhydene.2013.01.151

Che, M. (2013). Nobel prize in chemistry 1912 to sabatier: organic chemistry or catalysis? *Catal. Tod.* 218, 162–171. doi: 10.1016/j.cattod.2013.07.006

Chen, X., Yu, L., Wang, S., Deng, D., and Bao, X. (2017). Highly active and stable single iron site confined in graphene nanosheets for oxygen reduction reaction. *Nano Energ.* 32, 353–358. doi: 10.1016/j.nanoen.2016.12.056

Cheng, J., Hu, P., Ellis, P., French, S., Kelly, G., and Lok, C. M. (2008). Brønsted- evans- polanyi relation of multistep reactions and volcano curve in heterogeneous catalysis. *J. Phys. Chem. C* 112, 1308–1311. doi: 10.1021/jp711191j

Craig, M. J., Coulter, G., Dolan, E., Soriano-López, J., Mates-Torres, E., Schmitt, W., et al. (2019). Universal scaling relations for the rational design of molecular water oxidation catalysts with near-zero overpotential. *Nat. Commun.* 10, 1–9. doi: 10.1038/s41467-019-12994-w

Diaz-Morales, O., Raaijman, S., Kortlever, R., Kooyman, P. J., Wezendonk, T., Gascon, J., et al. (2016). Iridium-based double perovskites for efficient water oxidation in acid media. *Nat. Commun.* 7, 1–6. doi: 10.1038/ncomms12363

Dickens, C. F., and Nørskov, J. K. (2017). A theoretical investigation into the role of surface defects for oxygen evolution on RuO2. *J. Phys. Chem. C* 121, 18516–18524. doi: 10.1021/acs.jpcc.7b03481

Dubouis, N., and Grimaud, A. (2019). The hydrogen evolution reaction: from material to interfacial descriptors. *Chem. Sci.* 10, 9165–9181. doi: 10.1039/C9SC03831K

Durst, J., Siebel, A., Simon, C., Hasche, F., Herranz, J., and Gasteiger, H. (2014). New insights into the electrochemical hydrogen oxidation and evolution reaction mechanism. *Energ. Environ. Sci.* 7, 2255–2260. doi: 10.1039/C4EE00440J

Exner, K. S. (2018). Activity–stability volcano plots for the investigation of nano-sized electrode materials in lithium-ion batteries. *ChemElectroChem* 5, 3243–3248. doi: 10.1002/celc.201800838

Exner, K. S. (2019a). Activity-stability volcano plots for material optimization in electrocatalysis. *ChemCatChem* 11, 3234–3241. doi: 10.1002/cctc.201900500

Exner, K. S. (2019b). Beyond the traditional volcano concept: overpotential-dependent volcano plots exemplified by the chlorine evolution reaction over transition-metal oxides. *J. Phys. Chem. C* 123, 16921–16928. doi: 10.1021/acs.jpcc.9b05364

Exner, K. S. (2019c). Design criteria for oxygen evolution electrocatalysts from first principles: introduction of a unifying material-screening approach. *ACS Appl. Energ. Mater.* 2, 7991–8001. doi: 10.1021/acsaem.9b01480

Exner, K. S. (2019d). Is thermodynamics a good descriptor for the activity? Re-investigation of Sabatier's principle by the free energy diagram in electrocatalysis. *ACS Catal.* 9, 5320–5329. doi: 10.1021/acscatal.9b00732

Exner, K. S. (2019e). Recent advancements towards closing the gap between electrocatalysis and battery science communities: the computational lithium electrode and activity–stability volcano plots. *ChemSusChem* 12, 2330–2344. doi: 10.1002/cssc.201900298

Exner, K. S. (2020a). Comparison of the conventional volcano analysis with a unifying approach: material screening based on a combination of experiment and theory. *J. Phys. Chem. C* 124, 822–828. doi: 10.1021/acs.jpcc.9b10860

Exner, K. S. (2020b). Design criteria for the competing chlorine and oxygen evolution reactions: avoid the OCl adsorbate to enhance chlorine selectivity. *Phys. Chem. Chem. Phys.* 22, 22451–22458. doi: 10.1039/D0CP03667F

Exner, K. S. (2020c). Does a Thermoneutral Electrocatalyst correspond to the apex of a volcano plot for a simple two-electron process? *Angew. Chem. Int. Ed.* 22, 10236–10240. doi: 10.1002/anie.202003688

Exner, K. S. (2020d). Overpotential-dependent volcano plots to assess activity trends in the competing chlorine and oxygen evolution reactions. *ChemElectroChem* 7, 1448–1455. doi: 10.1002/celc.202000120

Exner, K. S. (2020e). Paradigm change in hydrogen electrocatalysis: the volcano's apex is located at weak bonding of the reaction intermediate. *Int. J. Hyd. Energ.* 45, 27221–27229. doi: 10.1016/j.ijhydene.2020.07.088

Exner, K. S. (2020f). Recent progress in the development of screening methods to identify electrode materials for the oxygen evolution reaction. *Adv. Funct. Mater.* 30:2005060. doi: 10.1002/adfm.202005060

Exner, K. S. (2020g). A universal descriptor for the screening of electrode materials for multiple-electron processes: beyond the thermodynamic overpotential. *ACS Catal.* 10, 12607–12617. doi: 10.1021/acscatal.0c03865

Exner, K. S. (2021a). Boosting the stability of RuO2 in the acidic oxygen evolution reaction by tuning oxygen-vacancy formation energies: a viable approach beyond noble-metal catalysts? *ChemElectroChem* 8, 46–48. doi: 10.1002/celc.202001465

Exner, K. S. (2021b). Hydrogen electrocatalysis revisited: weak bonding of adsorbed hydrogen as design principle for active electrode materials. *Curr. Opin. Electrochem.* 26:100673. doi: 10.1016/j.coelec.2020.100673

Exner, K. S. (2021c). Why approximating electrocatalytic activity by a single free-energy change is insufficient. *Electrochim. Acta* 375:137975. doi: 10.1016/j.electacta.2021.137975

Exner, K. S., Anton, J., Jacob, T., and Over, H. (2014). Controlling selectivity in the chlorine evolution reaction over RuO2-based catalysts. *Angew. Chem. Int. Ed.* 53, 11032–11035. doi: 10.1002/anie.201406112

Exner, K. S., Anton, J., Jacob, T., and Over, H. (2016). Full kinetics from first principles of the chlorine evolution reaction over a RuO2 (110) model electrode. *Angew. Chem. Int. Ed.* 55, 7501–7504. doi: 10.1002/anie.201511804

Exner, K. S., and Over, H. (2019). Beyond the rate-determining step in the oxygen evolution reaction over a single-crystalline IrO2 (110) model electrode: kinetic scaling relations. *ACS Catal.* 9, 6755–6765. doi: 10.1021/acscatal.9b01564

Exner, K. S., Sohrabnejad-Eskan, I., and Over, H. (2018). A universal approach to determine the free energy diagram of an electrocatalytic reaction. *ACS Catal.* 8, 1864–1879. doi: 10.1021/acscatal.7b03142

Fabbri, E., Nachtegaal, M., Binninger, T., Cheng, X., Kim, B.-J., Durst, J., et al. (2017). Dynamic surface self-reconstruction is the key of highly active perovskite nano-electrocatalysts for water splitting. *Nat. Mater.* 16, 925–931. doi: 10.1038/nmat4938

Fang, Y.-H., and Liu, Z.-P. (2014). Tafel kinetics of electrocatalytic reactions: from experiment to first-principles. *ACS Catal.* 4, 4364–4376. doi: 10.1021/cs501312v

Frumkin, A., and Petrii, O. (1975). Potentials of zero total and zero free charge of platinum group metals. *Electrochim. Acta* 20, 347–359. doi: 10.1016/0013-4686(75)90017-1

Gao, D., Wang, J., Wu, H., Jiang, X., Miao, S., Wang, G., et al. (2015). pH effect on electrocatalytic reduction of CO2 over Pd and Pt nanoparticles. *Electrochem. Commun.* 55, 1–5. doi: 10.1016/j.elecom.2015.03.008

Garcia, A. C., Touzalin, T., Nieuwland, C., Perini, N., and Koper, M. T. (2019). Enhancement of oxygen evolution activity of nickel oxyhydroxide by electrolyte alkali cations. *Angew. Chem. Int. Ed.* 58, 12999–13003. doi: 10.1002/anie.201905501

Gattrell, M., Gupta, N., and Co, A. (2006). A review of the aqueous electrochemical reduction of CO2 to hydrocarbons at copper. *J. Electroanal. Chem.* 594, 1–19. doi: 10.1016/j.jelechem.2006.05.013

Gerischer, R., and Gerischer, H. (1956). Über die Katalytische Zersetzung Von Wasserstoffsuperoxyd an metallischem platin. *Z. Phys. Chem.* 6, 178–200. doi: 10.1524/zpch.1956.6.3_4.178

Goings, J. J., and Hammes-Schiffer, S. (2020). Nonequilibrium dynamics of proton-coupled electron transfer in proton wires: concerted but asynchronous mechanisms. *ACS Cent. Sci.* 6, 1594–1601. doi: 10.1021/acscentsci.0c00756

Gómez-Marín, A. M., Rizo, R., and Feliu, J. M. (2014). Oxygen reduction reaction at Pt single crystals: a critical overview. *Catal. Sci. Technol.* 4, 1685–1698. doi: 10.1039/C3CY01049J

Gossenberger, F., Juarez, F., and Groß, A. (2020). Sulfate, bisulfate, and hydrogen co-adsorption on Pt (111) and Au (111) in an electrochemical environment. *Front. Chem.* 8:634. doi: 10.3389/fchem.2020.00634

Göttle, A. J., and Koper, M. T. (2017). Proton-coupled electron transfer in the electrocatalysis of CO2 reduction: prediction of Sequential Vs. Concerted pathways using DFT. *Chem. Sci.* 8, 458–465. doi: 10.1039/C6SC02984A

Govind Rajan, A., Martirez, J. M. P., and Carter, E. A. (2020). Why do we use the materials and operating conditions we use for heterogeneous (Photo) electrochemical water splitting? *ACS Catal.* 10, 11177–11234. doi: 10.1021/acscatal.0c01862

Govindarajan, N., García-Lastra, J. M., Meijer, E. J., and Calle-Vallejo, F. (2018). Does the breaking of adsorption-energy scaling relations guarantee enhanced electrocatalysis? *Curr. Opin. Electrochem.* 8, 110–117. doi: 10.1016/j.coelec.2018.03.025

Greeley, J., Jaramillo, T. F., Bonde, J., Chorkendorff, I., and Nørskov, J. K. (2006). Computational high-throughput screening of electrocatalytic materials for hydrogen evolution. *Nat. Mater.* 5, 909–913. doi: 10.1038/nmat1752

Greeley, J., and Nørskov, J. K. (2007). Large-scale, density functional theory-based screening of alloys for hydrogen evolution. *Surf. Sci* 601, 1590–1598. doi: 10.1016/j.susc.2007.01.037

Groß, A. (2020). "Theory of solid/electrolyte interfaces," in *Surface and Interface Science: Volume 8: Interfacial Electrochemistry*, ed. K. Wandelt (Weinheim: Wiley-VCH Verlag GmbH & Co. KGaA).

Guidelli, R., Compton, R. G., Feliu, J. M., Gileadi, E., Lipkowski, J., Schmickler, W., et al. (2014). Defining the transfer coefficient in electrochemistry: an assessment (Iupac Technical Report). *Pure Appl. Chem.* 86, 245–258. doi: 10.1515/pac-2014-5026

Gupta, N., Gattrell, M., and MacDougall, B. (2006). Calculation for the cathode surface concentrations in the electrochemical reduction of CO2 in KHCO3 solutions. *J. Appl. Electrochem.* 36, 161–172. doi: 10.1007/s10800-005-9058-y

Gurudayal, D. P., Malani, S., Lum, Y., Haussener, S., and Ager, J. W. (2019). Sequential cascade electrocatalytic conversion of carbon dioxide to C–C coupled products. *ACS Appl. Energ. Mater.* 2, 4551–4559. doi: 10.1021/acsaem.9b00791

Hajiyani, H., and Pentcheva, R. (2018). Surface termination and composition control of activity of the CoxNi1–xFe2O4 (001) surface for water oxidation: insights from DFT + U calculations. *ACS Catal.* 8, 11773–11782. doi: 10.1021/acscatal.8b00574

Halck, N. B., Petrykin, V., Krtil, P., and Rossmeisl, J. (2014). Beyond the volcano limitations in electrocatalysis–oxygen evolution reaction. *Phys. Chem. Chem. Phys.* 16, 13682–13688. doi: 10.1039/C4CP00571F

Hammes-Schiffer, S. (2009). Theory of proton-coupled electron transfer in energy conversion processes. *Acc. Chem. Res.* 42, 1881–1889. doi: 10.1021/ar9001284

Hammes-Schiffer, S., and Stuchebrukhov, A. A. (2010). Theory of coupled electron and proton transfer reactions. *Chem. Rev.* 110, 6939–6960. doi: 10.1021/cr1001436

Handoko, A. D., Steinmann, S. N., and Seh, Z. W. (2019). Theory-guided materials design: two-dimensional mxenes in electro-and photocatalysis. *Nanoscale Horiz.* 4, 809–827. doi: 10.1039/C9NH00100J

Hansen, H. A., Rossmeisl, J., and Nørskov, J. K. (2008). Surface pourbaix diagrams and oxygen reduction activity of Pt, Ag and Ni (111) surfaces studied by DFT. *Phys. Chem. Chem. Phys.* 10, 3722–3730. doi: 10.1039/B803956A

Hansen, M. H., and Rossmeisl, J. (2016). pH in grand canonical statistics of an electrochemical interface. *J. Phys. Chem. C* 120, 29135–29143. doi: 10.1021/acs.jpcc.6b09019

Hao, S., Liu, M., Pan, J., Liu, X., Tan, X., Xu, N., et al. (2020). Dopants fixation of ruthenium for boosting acidic oxygen evolution stability and activity. *Nat. Commun.* 11, 1–11. doi: 10.1038/s41467-020-19212-y

He, D., Li, Y., Ooka, H., Go, Y. K., Jin, F., Kim, S. H., et al. (2018). Selective electrocatalytic reduction of nitrite to dinitrogen based on decoupled proton–electron transfer. *J. Am. Chem. Soc.* 140, 2012–2015. doi: 10.1021/jacs.7b12774

He, D., Ooka, H., Kim, Y., Li, Y., Jin, F., Kim, S. H., et al. (2020). Atomic-scale evidence for highly selective electrocatalytic N- N coupling on metallic MoS2. *Proc. Natl. Acad. Sci. U.S.A.* 117, 31631–31638. doi: 10.1073/pnas.2008429117

He, Z.-D., Hanselman, S., Chen, Y.-X., Koper, M. T. M., and Calle-Vallejo, F. (2017). Importance of solvation for the accurate prediction of oxygen reduction activities of pt-based electrocatalysts. *J. Phys. Chem. Lett.* 8, 2243–2246. doi: 10.1021/acs.jpclett.7b01018

Heenen, H. H., Gauthier, J. A., Kristoffersen, H. H., Ludwig, T., and Chan, K. (2020). Solvation at metal/water interfaces: an Ab initio molecular dynamics benchmark of common computational approaches. *J. Chem. Phys.* 152:144703. doi: 10.1063/1.5144912

Hinnemann, B., Moses, P. G., Bonde, J., Jørgensen, K. P., Nielsen, J. H., Horch, S., et al. (2005). Biomimetic hydrogen evolution: MoS2 nanoparticles as catalyst for hydrogen evolution. *J. Am. Chem. Soc.* 127, 5308–5309. doi: 10.1021/ja0504690

Holewinski, A., and Linic, S. (2012). Elementary mechanisms in electrocatalysis: revisiting the ORR tafel slope. *J. Electrochem. Soc.* 159:H864. doi: 10.1149/2.022211jes

Hori, Y., Murata, A., and Takahashi, R. (1989). Formation of hydrocarbons in the electrochemical reduction of carbon dioxide at a copper electrode in aqueous solution. *J. Chem. Soc.* 85, 2309–2326. doi: 10.1039/F19898502309

Hörmann, N. G., Andreussi, O., and Marzari, N. (2019). Grand canonical simulations of electrochemical interfaces in implicit solvation models. *J. Chem. Phys.* 150:041730. doi: 10.1063/1.5054580

Hörmann, N. G., Marzari, N., and Reuter, K. (2020). Electrosorption at metal surfaces from first principles. *NPJ Comput. Mater.* 6, 1–10. doi: 10.1038/s41524-020-00394-4

Hu, J.-M., Zhang, J.-Q., and Cao, C.-N. (2004). Oxygen evolution reaction on IrO2-based DSA type electrodes: kinetics analysis of tafel lines and EIS. *Int. J. Hyd. Energ.* 29, 791–797. doi: 10.1016/j.ijhydene.2003.09.007

Huang, J., Malek, A., Zhang, J., and Eikerling, M. H. (2016a). Non-monotonic surface charging behavior of platinum: a paradigm change. *J. Phys. Chem. C* 120, 13587–13595. doi: 10.1021/acs.jpcc.6b03930

Huang, J., Zhang, J., and Eikerling, M. (2016b). Theory of electrostatic phenomena in water-filled Pt nanopores. *Faraday Disc.* 193, 427–446. doi: 10.1039/C6FD00094K

Huang, J., Zhang, J., and Eikerling, M. (2018). Unifying theoretical framework for deciphering the oxygen reduction reaction on platinum. *Phys. Chem. Chem. Phys.* 20, 11776–11786. doi: 10.1039/C8CP01315B

Huang, Z.-F., Song, J., Dou, S., Li, X., Wang, J., and Wang, X. (2019). Strategies to break the scaling relation toward enhanced oxygen electrocatalysis. *Matter* 1, 1494–1518. doi: 10.1016/j.matt.2019.09.011

Kang, Y. S., Jo, S., Choi, D., Kim, J. Y., Park, T., and Yoo, S. J. (2019). Pt-Sputtered Ti mesh electrode for polymer electrolyte membrane fuel cells. *Int. J. Precis* 6, 271–279. doi: 10.1007/s40684-019-00077-6

Kant, R. (1994). Can one electrochemically measure the statistical morphology of a rough electrode? *J. Phys. Chem.* 98, 1663–1667. doi: 10.1021/j100057a020

Kari, J., Olsen, J. P., Jensen, K., Badino, S. F., Krogh, K. B., Borch, K., et al. (2018). Sabatier principle for interfacial (Heterogeneous) enzyme catalysis. *ACS Catal.* 8, 11966–11972. doi: 10.1021/acscatal.8b03547

Karlsson, R. K., and Cornell, A. (2016). Selectivity between oxygen and chlorine evolution in the chlor-alkali and chlorate processes. *Chem. Rev.* 116, 2982–3028. doi: 10.1021/acs.chemrev.5b00389

Kastlunger, G., Lindgren, P., and Peterson, A. A. (2018). Controlled-potential simulation of elementary electrochemical reactions: proton discharge on metal surfaces. *J. Phys. Chem. C* 122, 12771–12781. doi: 10.1021/acs.jpcc.8b02465

Katsounaros, I., Chen, T., Gewirth, A. A., Markovic, N. M., and Koper, M. T. (2016). Evidence for decoupled electron and proton transfer in the electrochemical oxidation of ammonia on Pt (100). *J. Phys. Chem. Lett.* 7, 387–392. doi: 10.1021/acs.jpclett.5b02556

Kenmoe, S., Lisovski, O., Piskunov, S., Bocharov, D., Zhukovskii, Y. F., and Spohr, E. (2018). Water adsorption on clean and defective anatase Tio2 (001) nanotube surfaces: a surface science approach. *J. Phys. Chem. B* 122, 5432–5440. doi: 10.1039/C9CP06584A

Kim, J., Shih, P.-C., Tsao, K.-C., Pan, Y.-T., Yin, X., Sun, C.-J., et al. (2017). High-performance pyrochlore-type yttrium ruthenate electrocatalyst for oxygen evolution reaction in acidic media. *J. Am. Chem. Soc.* 139, 12076–12083. doi: 10.1021/jacs.7b06808

Kjaergaard, C. H., Rossmeisl, J., and Nørskov, J. K. (2010). Enzymatic versus inorganic oxygen reduction catalysts: comparison of the energy levels in a free-energy scheme. *Inorg. Chem.* 49, 3567–3572. doi: 10.1021/ic900798q

Klamt, A., and Schüürmann, G. (1993). COSMO: a new approach to dielectric screening in solvents with explicit expressions for the screening energy and its gradient. *J. Chem. Soc. Perkin Trans. II* 5, 799–805. doi: 10.1039/P29930000799

Koper, M. T. (2011a). Structure sensitivity and nanoscale effects in electrocatalysis. *Nanoscale* 3, 2054–2073. doi: 10.1039/C0NR00857E

Koper, M. T. (2011b). Thermodynamic theory of multi-electron transfer reactions: implications for electrocatalysis. *J. Electroanal. Chem.* 660, 254–260. doi: 10.1016/j.jelechem.2010.10.004

Koper, M. T. (2013a). Analysis of electrocatalytic reaction schemes: distinction between rate-determining and potential-determining steps. *J. Solid State Electrochem.* 17, 339–344. doi: 10.1007/s10008-012-1918-x

Koper, M. T. (2013b). Theory of multiple proton–electron transfer reactions and its implications for electrocatalysis. *Chem. Sci.* 4, 2710–2723. doi: 10.1039/C3SC50205H

Koper, M. T. (2013c). Theory of the transition from sequential to concerted electrochemical proton–electron transfer. *Phys. Chem. Chem. Phys.* 15, 1399–1407. doi: 10.1039/c2cp42369c

Kortlever, R., Balemans, C., Kwon, Y., and Koper, M. T. (2015a). Electrochemical CO2 reduction to formic acid on a Pd-based formic acid oxidation catalyst. *Catal. Tod.* 244, 58–62. doi: 10.1016/j.cattod.2014.08.001

Kortlever, R., Shen, J., Schouten, K. J. P., Calle-Vallejo, F., and Koper, M. T. (2015b). Catalysts and reaction pathways for the electrochemical reduction of carbon dioxide. *J. Phys. Chem. Lett.* 6, 4073–4082. doi: 10.1021/acs.jpclett.5b01559

Kozuch, S. (2012). A refinement of everyday thinking: the energetic span model for kinetic assessment of catalytic cycles. *WIRES Comput. Mol. Sci.* 2, 795–815. doi: 10.1002/wcms.1100

Kozuch, S., and Shaik, S. (2011). How to conceptualize catalytic cycles? The energetic span model. *Acc. Chem. Res.* 44, 101–110. doi: 10.1021/ar1000956

Krishnamurthy, D., Sumaria, V., and Viswanathan, V. (2018). Maximal predictability approach for identifying the right descriptors for electrocatalytic reactions. *J. Phys. Chem. Lett.* 9, 588–595. doi: 10.1021/acs.jpclett.7b02895

Kunimatsu, K., Senzaki, T., Samjeské, G., Tsushima, M., and Osawa, M. (2007). Hydrogen adsorption and hydrogen evolution reaction on a polycrystalline Pt electrode studied by surface-enhanced infrared absorption spectroscopy. *Electrochim. Acta* 52, 5715–5724. doi: 10.1016/j.electacta.2006.12.007

Laursen, A. B., Varela, A. S., Dionigi, F., Fanchiu, H., Miller, C., Trinhammer, O. L., et al. (2012). Electrochemical hydrogen evolution: Sabatier's principle and the volcano plot. *J. Chem. Educ.* 89, 1595–1599. doi: 10.1021/ed200818t

Ledezma-Yanez, I., Wallace, W. D. Z., Sebastián-Pascual, P., Climent, V., Feliu, J. M., and Koper, M. T. (2017). Interfacial water reorganization as a pH-dependent descriptor of the hydrogen evolution rate on platinum electrodes. *Nat. Energ.* 2, 1–7. doi: 10.1038/nenergy.2017.31

Li, Y., Du, X., Huang, J., Wu, C., Sun, Y., Zou, G., et al. (2019). Recent progress on surface reconstruction of earth-abundant electrocatalysts for water oxidation. *Small* 15:1901980. doi: 10.1002/smll.201901980

Li, Y., and Sun, Q. (2016). Recent advances in breaking scaling relations for effective electrochemical conversion of CO2. *Adv. Energ. Mater.* 6:1600463. doi: 10.1021/jp077210j

Li, Z., Achenie, L. E., and Xin, H. (2020). An adaptive machine learning strategy for accelerating discovery of perovskite electrocatalysts. *ACS Catal.* 10, 4377–4384. doi: 10.1021/acscatal.9b05248

Lindgren, P., Kastlunger, G., and Peterson, A. A. (2020). A challenge to the G ∼0 interpretation of hydrogen evolution. *ACS Catal.* 10, 121–128. doi: 10.1021/acscatal.9b02799

Louch, D. S., and Pritzker, M. D. (1993). Transport to rough electrode surfaces: part 2: perturbation solution for two-dimensional steady state transport to an arbitrary surface under mixed diffusion-kinetic control. *J. Electroanal. Chem.* 346, 211–237. doi: 10.1016/0022-0728(93)85014-8

Lum, Y., and Ager, J. W. (2018). Sequential catalysis controls selectivity in electrochemical CO2 reduction on Cu. *Energ. Environ. Sci.* 11, 2935–2944. doi: 10.1039/C8EE01501E

Man, I. C., Su, H.-Y., Calle-Vallejo, F., Hansen, H. A., Martinez, J. I., Inoglu, N. G., et al. (2011). Universality in oxygen evolution electrocatalysis on oxide surfaces. *ChemCatChem* 3, 1159–1165. doi: 10.1002/cctc.201000397

Marshall, A. T., and Vaisson-Béthune, L. (2015). Avoid the quasi-equilibrium assumption when evaluating the electrocatalytic oxygen evolution reaction mechanism by tafel slope analysis. *Electrochem. Commun.* 61, 23–26. doi: 10.1016/j.elecom.2015.09.019

Martnez-Hincapié, R., Climent, V., and Feliu, J. M. (2018). Peroxodisulfate reduction as a probe to interfacial charge. *Electrochem. Commun.* 88, 43–46. doi: 10.1016/j.elecom.2018.01.012

Mathew, K., Kolluru, V. C., Mula, S., Steinmann, S. N., and Hennig, R. G. (2019). Implicit self-consistent electrolyte model in plane-wave density-functional theory. *J. Chem. Phys.* 151:234101. doi: 10.1063/1.5132354

Mathew, K., Sundararaman, R., Letchworth-Weaver, K., Arias, T., and Hennig, R. G. (2014). Implicit solvation model for density-functional study of nanocrystal surfaces and reaction pathways. *J. Chem. Phys.* 140:084106. doi: 10.1063/1.4865107

Mefford, J. T., Zhao, Z., Bajdich, M., and Chueh, W. C. (2020). Interpreting Tafel behavior of consecutive electrochemical reactions through combined thermodynamic and steady state microkinetic approaches. *Energ. Environ. Sci.* 13, 622–634. doi: 10.1039/C9EE02697E

Mehta, V., and Cooper, J. S. (2003). Review and analysis of PEM fuel cell design and manufacturing. *J. Power Sources* 114, 32–53. doi: 10.1016/S0378-7753(02)00542-6

Murata, A., and Hori, Y. (1991). Product selectivity affected by cationic species in electrochemical reduction of CO2 and CO at a Cu electrode. *Bull. Chem. Soc. Jpn.* 64, 123–127. doi: 10.1246/bcsj.64.123

Nørskov, J. K., Bligaard, T., Logadottir, A., Kitchin, J., Chen, J. G., Pandelov, S., et al. (2005). Trends in the exchange current for hydrogen evolution. *J. Electrochem. Soc.* 152:J23. doi: 10.1149/1.1856988

Nørskov, J. K., Bligaard, T., Rossmeisl, J., and Christensen, C. H. (2009). Towards the computational design of solid catalysts. *Nat. Chem.* 1, 37–46. doi: 10.1038/nchem.121

Nørskov, J. K., Rossmeisl, J., Logadottir, A., Lindqvist, L., Kitchin, J. R., Bligaard, T., et al. (2004). Origin of the overpotential for oxygen reduction at a fuel-cell cathode. *J. Phys. Chem. B* 108, 17886–17892. doi: 10.1021/jp047349j

Ooka, H., Figueiredo, M. C., and Koper, M. T. (2017). Competition between hydrogen evolution and carbon dioxide reduction on copper electrodes in mildly acidic media. *Langmuir* 33, 9307–9313. doi: 10.1021/acs.langmuir.7b00696

Ooka, H., and Nakamura, R. (2019). Shift of the optimum binding energy at higher rates of catalysis. *J. Phys. Chem. Lett.* 10, 6706–6713. doi: 10.1021/acs.jpclett.9b01796

Pajkossy, T., and Nyikos, L. (1989). Diffusion to fractal surfaces? II. Verification of theory. *Electrochim. Acta* 34, 171–179. doi: 10.1016/0013-4686(89)87082-3

Pande, V., and Viswanathan, V. (2019). Computational screening of current collectors for enabling anode-free lithium metal batteries. *ACS Energy Lett.* 4, 2952–2959. doi: 10.1021/acsenergylett.9b02306

Parada, G. A., Goldsmith, Z. K., Kolmar, S., Rimgard, B. P., Mercado, B. Q., Hammarström, L., et al. (2019). Concerted proton-electron transfer reactions in the marcus inverted region. *Science* 364, 471–475. doi: 10.1126/science.aaw4675

Park, S., Lee, J.-W., and Popov, B. N. (2012). A review of gas diffusion layer in PEM fuel cells: materials and designs. *Int. J. Hyd. Energ.* 37, 5850–5865. doi: 10.1016/j.ijhydene.2011.12.148

Parsons, R. (1951). General equations for the kinetics of electrode processes. *Trans. Faraday Soc.* 47, 1332–1344. doi: 10.1039/TF9514701332

Parsons, R. (1958). The rate of electrolytic hydrogen evolution and the heat of adsorption of hydrogen. *Trans. Faraday Soc.* 54, 1053–1063. doi: 10.1039/TF9585401053

Pegis, M. L., Wise, C. F., Koronkiewicz, B., and Mayer, J. M. (2017). Identifying and breaking scaling relations in molecular catalysis of electrochemical reactions. *J. Am. Chem. Soc.* 139, 11000–11003. doi: 10.1021/jacs.7b05642

Pérez-Gallent, E., Marcandalli, G., Figueiredo, M. C., Calle-Vallejo, F., and Koper, M. T. (2017). Structure-and potential-dependent cation effects on CO reduction at copper single-crystal electrodes. *J. Am. Chem. Soc.* 139, 16412–16419. doi: 10.1021/jacs.7b10142

Peterson, A. A., and Nørskov, J. K. (2012). Activity descriptors for CO2 electroreduction to methane on transition-metal catalysts. *J. Phys. Chem. Lett.* 3, 251–258. doi: 10.1021/jz201461p

Piqué, O., Illas, F., and Calle-Vallejo, F. (2020). Designing water splitting catalysts using rules of thumb: advantages, dangers and alternatives. *Phys. Chem. Chem. Phys.* 22, 6797–6803. doi: 10.1039/D0CP00896F

Retuerto, M., Pascual, L., Calle-Vallejo, F., Ferrer, P., Gianolio, D., Pereira, A. G., et al. (2019). Na-doped ruthenium perovskite electrocatalysts with improved oxygen evolution activity and durability in acidic media. *Nat. Commun.* 10, 1–9. doi: 10.1038/s41467-019-09791-w

Ringe, S., Clark, E. L., Resasco, J., Walton, A., Seger, B., Bell, A. T., et al. (2019). Understanding cation effects in electrochemical CO2 reduction. *Energ. Environ. Sci.* 12, 3001–3014. doi: 10.1039/C9EE01341E

Ringe, S., Morales-Guio, C. G., Chen, L. D., Fields, M., Jaramillo, T. F., Hahn, C., et al. (2020). Double layer charging driven carbon dioxide adsorption limits the rate of electrochemical carbon dioxide reduction on gold. *Nat. Commun.* 11, 1–11. doi: 10.1038/s41467-019-13777-z

Rodriguez, P., and Koper, M. T. (2014). Electrocatalysis on gold. *Phys. Chem. Chem. Phys.* 16, 13583–13594. doi: 10.1039/C4CP00394B

Rojas-Carbonell, S., Artyushkova, K., Serov, A., Santoro, C., Matanovic, I., and Atanassov, P. (2018). Effect of pH on the activity of platinum group metal-free catalysts in oxygen reduction reaction. *ACS Catal.* 8, 3041–3053. doi: 10.1021/acscatal.7b03991

Rootsaert, W., and Sachtler, W. (1960). Interaction of formic acid vapour with tungsten. *Z. Phys. Chem.* 26, 16–26. doi: 10.1524/zpch.1960.26.1_2.016

Rossmeisl, J., Dimitrievski, K., Siegbahn, P., and Nørskov, J. K. (2007a). Comparing electrochemical and biological water splitting. *J. Phys. Chem. C* 111, 18821–18823.

Rossmeisl, J., Logadottir, A., and Nørskov, J. K. (2005). Electrolysis of water on (Oxidized) metal surfaces. *Chem. Phys.* 319, 178–184. doi: 10.1016/j.chemphys.2005.05.038

Rossmeisl, J., Qu, Z.-W., Zhu, H., Kroes, G.-J., and Nørskov, J. K. (2007b). Electrolysis of water on oxide surfaces. *J. Electroanal. Chem.* 607, 83–89. doi: 10.1016/j.jelechem.2006.11.008

Sabatier, P. (1913). *La Catalyse en Chimie Organique, Encyclopédie de Science Chimique Appliquée*. Dunham, QC: Ch. Béranger.

Sakaushi, K., Kumeda, T., Hammes-Schiffer, S., Melander, M. M., and Sugino, O. (2020). Advances and challenges for experiment and theory for multi-electron multi-proton transfer at electrified solid–liquid interfaces. *Phys. Chem. Chem. Phys.* 22, 19401–19442. doi: 10.1039/D0CP02741C

Sakong, S., and Groß, A. (2020). Water structures on a Pt (111) electrode from Ab initio molecular dynamic simulations for a variety of electrochemical conditions. *Phys. Chem. Chem. Phys.* 22, 10431–10437.

Saveleva, V. A., Wang, L., Teschner, D., Jones, T., Gago, A. S., Friedrich, K. A., et al. (2018). Operando evidence for a universal oxygen evolution mechanism on thermal and electrochemical iridium oxides. *J. Phys. Chem. Lett.* 9, 3154–3160. doi: 10.1021/acs.jpclett.8b00810

Sayfutyarova, E. R., and Hammes-Schiffer, S. (2020). Excited state molecular dynamics of photoinduced proton-coupled electron transfer in anthracene–phenol–pyridine triads. *J. Phys. Chem. Lett.* 11, 7109–7115. doi: 10.1021/acs.jpclett.0c02012

Schmickler, W., and Santos, E. (2010). *Interfacial Electrochemistry*. Berlin: Springer Science & Business Media.

Schouten, K. J. P., Gallent, E. P., and Koper, M. T. (2014). The influence of pH on the reduction of CO and CO2 to hydrocarbons on copper electrodes. *J. Electroanal. Chem.* 716, 53–57. doi: 10.1016/j.jelechem.2013.08.033

Seitz, L. C., Dickens, C. F., Nishio, K., Hikita, Y., Montoya, J., Doyle, A., et al. (2016). A highly active and stable IrOx/SrIrO3 catalyst for the oxygen evolution reaction. *Science* 353, 1011–1014. doi: 10.1126/science.aaf5050

Sheng, W., Gasteiger, H. A., and Shao-Horn, Y. (2010). Hydrogen oxidation and evolution reaction kinetics on platinum: acid Vs Alkaline electrolytes. *J. Electrochem. Soc.* 157:B1529. doi: 10.1149/1.3483106

Sheng, W., Zhuang, Z., Gao, M., Zheng, J., Chen, J. G., and Yan, Y. (2015). Correlating hydrogen oxidation and evolution activity on platinum at different pH with measured hydrogen binding energy. *Nat. Commun.* 6, 1–6. doi: 10.1038/ncomms6848

Shetty, M., Walton, A., Gathmann, S. R., Ardagh, M. A., Gopeesingh, J., Resasco, J., et al. (2020). The catalytic mechanics of dynamic surfaces: stimulating methods for promoting catalytic resonance. *ACS Catal.* 10, 12666–12695. doi: 10.1021/acscatal.0c03336

Shinagawa, T., Garcia-Esparza, A. T., and Takanabe, K. (2015). Insight on tafel slopes from a microkinetic analysis of aqueous electrocatalysis for energy conversion. *Sci. Rep.* 5:13801. doi: 10.1038/srep138012015

Shinagawa, T., Obata, K., and Takanabe, K. (2019). Switching of kinetically relevant reactants for the aqueous cathodic process determined by mass-transport coupled with protolysis. *ChemCatChem* 11, 5961–5968. doi: 10.1002/cctc.201901459

Skúlason, E., Tripkovic, V., Björketun, M. E., Gudmundsdottir, S., Karlberg, G., Rossmeisl, J., et al. (2010). Modeling the electrochemical hydrogen oxidation and evolution reactions on the basis of density functional theory calculations. *J. Phys. Chem. C* 114, 18182–18197. doi: 10.1021/jp1048887

Smith, C., Hill, A. K., and Torrente-Murciano, L. (2020). Current and future role of haber–bosch ammonia in a carbon-free energy landscape. *Energ. Environ. Sci.* 13, 331–344. doi: 10.1039/C9EE02873K

Song, J., Wei, C., Huang, Z.-F., Liu, C., Zeng, L., Wang, X., et al. (2020). A review on fundamentals for designing oxygen evolution electrocatalysts. *Chem. Soc. Rev.* 49, 2196–2214. doi: 10.1039/C9CS00607A

Su, J., Ge, R., Jiang, K., Dong, Y., Hao, F., Tian, Z., et al. (2018). Assembling ultrasmall copper-doped ruthenium oxide nanocrystals into hollow porous polyhedra: highly robust electrocatalysts for oxygen evolution in acidic media. *Adv. Mater.* 30:1801351. doi: 10.1002/adma.201801351

Sumaria, V., Krishnamurthy, D., and Viswanathan, V. (2018). Quantifying confidence in DFT predicted surface pourbaix diagrams and associated reaction pathways for chlorine evolution. *ACS Catal.* 8, 9034–9042. doi: 10.1021/acscatal.8b01432

Suntivich, J., Gasteiger, H. A., Yabuuchi, N., Nakanishi, H., Goodenough, J. B., and Shao-Horn, Y. (2011a). Design principles for oxygen-reduction activity on perovskite oxide catalysts for fuel cells and metal–air batteries. *Nat. Chem.* 3, 546–550. doi: 10.1038/nchem.1069

Suntivich, J., May, K. J., Gasteiger, H. A., Goodenough, J. B., and Shao-Horn, Y. (2011b). A perovskite oxide optimized for oxygen evolution catalysis from molecular orbital principles. *Science* 334, 1383–1385. doi: 10.1126/science.1212858

Tahir, M., Pan, L., Idrees, F., Zhang, X., Wang, L., Zou, J.-J., et al. (2017). Electrocatalytic oxygen evolution reaction for energy conversion and storage: a comprehensive review. *Nano Energ.* 37, 136–157. doi: 10.1016/j.nanoen.2017.05.022

Tang, Q., and Jiang, D.-E. (2016). Mechanism of hydrogen evolution reaction on 1T-MoS2 from first principles. *ACS Catal.* 6, 4953–4961. doi: 10.1021/acscatal.6b01211

Tao, H. B., Zhang, J., Chen, J., Zhang, L., Xu, Y., Chen, J. G., et al. (2019). Revealing energetics of surface oxygen redox from kinetic fingerprint in oxygen electrocatalysis. *J. Am. Chem. Soc.* 141, 13803–13811. doi: 10.1021/jacs.9b01834

Theerthagiri, J., Lee, S. J., Murthy, A. P., Madhavan, J., and Choi, M. Y. (2020). Fundamental aspects and recent advances in transition metal nitrides as electrocatalysts for hydrogen evolution reaction: a review. *Curr. Opin. Solid State Mater. Sci.* 24:100805. doi: 10.1016/j.cossms.2020.100805

Tichter, T., Schneider, J., and Roth, C. (2020). Finite heterogeneous rate constants for the electrochemical oxidation of Vo2+ at glassy carbon electrodes. *Front. Energ. Res.* 8:155. doi: 10.3389/fenrg.2020.00155

Toyao, T., Maeno, Z., Takakusagi, S., Kamachi, T., Takigawa, I., and Shimizu, K. (2020). Machine learning for catalysis informatics: recent applications and prospects. *ACS Catal.* 10, 2260–2297. doi: 10.1021/acscatal.9b04186

Trasatti, S. (1972). Work function, electronegativity, and electrochemical behaviour of metals: III. Electrolytic hydrogen evolution in acid solutions. *J. Electroanal. Chem. Interfacial Electrochem.* 39, 163–184. doi: 10.1016/S0022-0728(72)80485-6

Trasatti, S. (1987). Progress in the understanding of the mechanism of chlorine evolution at oxide electrodes. *Electrochim. Acta* 32, 369–382. doi: 10.1016/0013-4686(87)85001-6

Ulissi, Z. W., Singh, A. R., Tsai, C., and Nørskov, J. K. (2016). Automated discovery and construction of surface phase diagrams using machine learning. *J. Phys. Chem. Lett.* 7, 3931–3935. doi: 10.1021/acs.jpclett.6b01254

Ulissi, Z. W., Tang, M. T., Xiao, J., Liu, X., Torelli, D. A., Karamad, M., et al. (2017). Machine-learning methods enable exhaustive searches for active bimetallic facets and reveal active site motifs for CO2 reduction. *ACS Catal.* 7, 6600–6608. doi: 10.1021/acscatal.7b01648

Van Santen, R. A., Neurock, M., and Shetty, S. G. (2009). Reactivity theory of transition-metal surfaces: a Brønsted- evans- polanyi linear activation energy-free-energy analysis. *Chem. Rev.* 110, 2005–2048. doi: 10.1021/cr9001808

Varela, A. S., Ju, W., Reier, T., and Strasser, P. (2016). Tuning the catalytic activity and selectivity of Cu for CO2 electroreduction in the presence of halides. *ACS Catal.* 6, 2136–2144. doi: 10.1021/acscatal.5b02550

Vinogradova, O., Krishnamurthy, D., Pande, V., and Viswanathan, V. (2018). Quantifying confidence in DFT-predicted surface pourbaix diagrams of transition-metal electrode–electrolyte interfaces. *Langmuir* 34, 12259–12269. doi: 10.1021/acs.langmuir.8b02219

Viswanathan, V., and Hansen, H. A. (2014). Unifying solution and surface electrochemistry: limitations and opportunities in surface electrocatalysis. *Top. Catal.* 57, 215–221. doi: 10.1007/s11244-013-0171-6

Viswanathan, V., Hansen, H. A., Rossmeisl, J., and Nørskov, J. K. (2012). Universality in oxygen reduction electrocatalysis on metal surfaces. *ACS Catal.* 2, 1654–1660. doi: 10.1021/cs300227s

Vos, J. G., Wezendonk, T. A., Jeremiasse, A. W., and Koper, M. T. (2018). MnOx/IrOx as selective oxygen evolution electrocatalyst in acidic chloride solution. *J. Am. Chem. Soc.* 140, 10270–10281. doi: 10.1021/jacs.8b05382

Wang, J. X., Uribe, F. A., Springer, T. E., Zhang, J., and Adzic, R. R. (2009). Intrinsic kinetic equation for oxygen reduction reaction in acidic media: the double tafel slope and fuel cell applications. *Faraday Disc.* 140, 347–362. doi: 10.1039/B802218F

Warburton, R. E., Hutchison, P., Jackson, M. N., Pegis, M. L., Surendranath, Y., and Hammes-Schiffer, S. (2020). Interfacial field-driven proton-coupled electron transfer at graphite-conjugated organic acids. *J. Am. Chem. Soc.* 142, 20855–20864. doi: 10.1021/jacs.0c10632

Warren, J. J., Tronic, T. A., and Mayer, J. M. (2010). Thermochemistry of proton-coupled electron transfer reagents and its implications. *Chem. Rev.* 110, 6961–7001. doi: 10.1021/cr100085k

Wintrich, D., Öhl, D., Barwe, S., Ganassin, A., Möller, S., Tarnev, T., et al. (2019). Enhancing the selectivity between oxygen and chlorine towards chlorine during the anodic chlorine evolution reaction on a dimensionally stable anode. *ChemElectroChem* 6, 3108–3112. doi: 10.1002/celc.201900784

Wodrich, M. D., Sawatlon, B., Busch, M., and Corminboeuf, C. (2018). On the generality of molecular volcano plots. *ChemCatChem* 10, 1586–1591. doi: 10.1002/cctc.201701709

Wuttig, A., Yaguchi, M., Motobayashi, K., Osawa, M., and Surendranath, Y. (2016). Inhibited proton transfer enhances Au-catalyzed CO2-to-fuels selectivity. *Proc. Natl. Acad. Sci. U.S.A.* 113, E4585–E4593. doi: 10.1073/pnas.16029 84113

Xiao, P., Chen, W., and Wang, X. (2015). A review of phosphide-based materials for electrocatalytic hydrogen evolution. *Adv. Energ. Mater.* 5:1500985. doi: 10.1002/aenm.201500985

Xie, C., Wang, Y., Yan, D., Tao, L., and Wang, S. (2017). In situ growth of cobalt at cobalt-borate core–shell nanosheets as highly-efficient electrocatalysts for oxygen evolution reaction in alkaline/neutral medium. *Nanoscale* 9, 16059–16065. doi: 10.1039/C7NR06054H

Xue, S., Garlyyev, B., Watzele, S., Liang, Y., Fichtner, J., Pohl, M. D., et al. (2018). Influence of alkali metal cations on the hydrogen evolution reaction activity of Pt, Ir, Au, and Ag electrodes in alkaline electrolytes. *ChemElectroChem* 5, 2326–2329. doi: 10.1002/celc.201800690

Yang, T., Zhou, J., Song, T. T., Shen, L., Feng, Y. P., and Yang, M. (2020). High-throughput identification of exfoliable two-dimensional materials with active basal planes for hydrogen evolution. *ACS Energy Lett.* 5, 2313–2321. doi: 10.1021/acsenergylett.0c00957

Yao, S., Zhang, X., Chen, A., Zhang, Z., Jiao, M., and Zhou, Z. (2019). Algorithm screening to accelerate discovery of 2d metal-free electrocatalysts for hydrogen evolution reaction. *J. Mat. Chem. A* 7, 19290–19296. doi: 10.1039/C9TA06286F

Zeradjanin, A. R., Grote, J.-P., Polymeros, G., and Mayrhofer, K. J. (2016). A critical review on hydrogen evolution electrocatalysis: re-exploring the volcano-relationship. *Electroanalysis* 28, 2256–2269. doi: 10.1002/elan.201600270

Zhang, J., Tao, H. B., Kuang, M., Yang, H. B., Cai, W., Yan, Q., et al. (2020). Advances in thermodynamic-kinetic model for analyzing the oxygen evolution reaction. *ACS Catal.* 10, 8597–8610. doi: 10.1021/acscatal.0c01906

Zhang, L., and Huang, J. (2020). Understanding surface charge effects in electrocatalysis. Part I: peroxodisulfate reduction at Pt (111). *J. Phys. Chem. C* 124, 16951–16960. doi: 10.1021/acs.jpcc.0c02824

Zhang, W., Hu, Y., Ma, L., Zhu, G., Wang, Y., Xue, X., et al. (2018). Progress and perspective of electrocatalytic CO2 reduction for renewable carbonaceous fuels and chemicals. *Adv. Sci.* 5:1700275. doi: 10.1002/advs.201700275

Zhang, Y., Zhang, J., and Huang, J. (2019). Potential-dependent volcano plot for oxygen reduction: mathematical origin and implications for catalyst design. *J. Phys. Chem. Lett.* 10, 7037–7043.

Zhang, Y.-J., Sethuraman, V., Michalsky, R., and Peterson, A. A. (2014). Competition between CO2 reduction and H2 evolution on transition-metal electrocatalysts. *ACS Catal.* 4, 3742–3748. doi: 10.1021/cs5012298

Zheng, J., Sheng, W., Zhuang, Z., Xu, B., and Yan, Y. (2016). Universal dependence of hydrogen oxidation and evolution reaction activity of platinum-group metals on pH and hydrogen binding energy. *Sci. Adv.* 2:e1501602. doi: 10.1021/jacs.0c01104

Zhou, D., Wei, J., He, Z.-D., Xu, M.-L., Chen, Y., and Huang, J. (2020). Combining single crystal experiments and microkinetic modeling in disentangling thermodynamic, kinetic and double-layer factors influencing oxygen reduction. *J. Phys. Chem. C* 124, 13672–13678. doi: 10.1021/acs.jpcc.0c01621

Zhu, S., Qin, X., Yao, Y., and Shao, M. (2020). pH-dependent hydrogen and water binding energies on platinum surfaces as directly probed through surface-enhanced infrared absorption spectroscopy. *J. Am. Chem. Soc.* 142, 8748–8754.

Zhu, X., and Huang, J. (2019). Modeling electrocatalytic oxidation of formic acid at platinum. *J. Electrochem. Soc.* 167:013515. doi: 10.1149/2.0152001JES

Conflict of Interest: The authors declare that the research was conducted in the absence of any commercial or financial relationships that could be construed as a potential conflict of interest.

Advantages of publishing in Frontiers

OPEN ACCESS
Articles are free to read for greatest visibility and readership

FAST PUBLICATION
Around 90 days from submission to decision

HIGH QUALITY PEER-REVIEW
Rigorous, collaborative, and constructive peer-review

TRANSPARENT PEER-REVIEW
Editors and reviewers acknowledged by name on published articles

Frontiers
Avenue du Tribunal-Fédéral 34
1005 Lausanne | Switzerland

Visit us: www.frontiersin.org
Contact us: frontiersin.org/about/contact

REPRODUCIBILITY OF RESEARCH
Support open data and methods to enhance research reproducibility

DIGITAL PUBLISHING
Articles designed for optimal readership across devices

FOLLOW US
@frontiersin

IMPACT METRICS
Advanced article metrics track visibility across digital media

EXTENSIVE PROMOTION
Marketing and promotion of impactful research

LOOP RESEARCH NETWORK
Our network increases your article's readership